

Synthesis of mechanisms with prescribed elastic load-displacement characteristics

Radaelli, Giuseppe

DOI

[10.4233/uuid:d518b379-462a-448f-83ef-5ba0e761c578](https://doi.org/10.4233/uuid:d518b379-462a-448f-83ef-5ba0e761c578)

Publication date

2017

Document Version

Final published version

Citation (APA)

Radaelli, G. (2017). *Synthesis of mechanisms with prescribed elastic load-displacement characteristics*. [Dissertation (TU Delft), Delft University of Technology]. <https://doi.org/10.4233/uuid:d518b379-462a-448f-83ef-5ba0e761c578>

Important note

To cite this publication, please use the final published version (if applicable). Please check the document version above.

Copyright

Other than for strictly personal use, it is not permitted to download, forward or distribute the text or part of it, without the consent of the author(s) and/or copyright holder(s), unless the work is under an open content license such as Creative Commons.

Takedown policy

Please contact us and provide details if you believe this document breaches copyrights. We will remove access to the work immediately and investigate your claim.

SYNTHESIS OF MECHANISMS
WITH
PRESCRIBED ELASTIC
LOAD-DISPLACEMENT
CHARACTERISTICS



GIUSEPPE
RADAELLI

Synthesis of mechanisms with prescribed elastic load-displacement characteristics

Proefschrift

ter verkrijging van de graad van doctor
aan de Technische Universiteit Delft,
op gezag van de Rector Magnificus prof. ir. K.C.A.M. Luyben,
voorzitter van het College voor Promoties,
in het openbaar te verdedigen op
vrijdag 15 september 2017 om 10:00 uur

door

Giuseppe RADAELLI

Master of Science in Mechanical Engineering,
Technische Universiteit Delft, Delft, Netherland,
geboren te Padua, Italië.

Dit proefschrift is goedgekeurd door de promotor:

Prof. dr. ir. J.L. Herder

Samenstelling promotiecommissie:

| | |
|--|---|
| Rector Magnificus, Prof. dr. ir. J.L. Herder, | voorzitter Technische Universiteit Delft |
|--|---|

Onafhankelijke leden:

| | |
|-----------------------------|-------------------------------|
| Prof. dr. ir. F. van Keulen | Technische Universiteit Delft |
| Prof. dr. C. Bisagni | Technische Universiteit Delft |
| Prof. dr. S.D. Guest | University of Cambridge |
| Prof. dr. ir. D.M. Brouwer | Universiteit Twente |
| Prof. dr. ir. D. Lefeber | Vrije Universiteit Brussel |
| Dr. C.J. Kim | Bucknell University |



This work is part of the research programme HTSM-2012 with project number 12814, which is (partly) financed by the Netherlands Organisation for Scientific Research (NWO).

Keywords: Nonlinear spring synthesis, Compliant shell mechanisms, Static balancing, Potential energy fields

Printed by: Gildeprint

Front image: By Noemi Papa: Oil painting of a shell-balancer where the stresses are visualized using the photoelastic effect.

Copyright © 2017 by G. Radaelli
Author email: g.radaelli@tudelft.nl;

All rights reserved. No part of the material protected by this copyright notice may be reproduced or utilized in any form or by any other means, electronic or mechanical, including photocopying, recording, or by any other information storage and retrieval system, without the prior permission of the author.

ISBN 978-94-6186-840-4

An electronic version of this dissertation is available at
<http://repository.tudelft.nl/>.

"Love and do what you will."

St. Augustine (354-430)

Contents

| | |
|---|------------|
| Summary | vii |
| Samenvatting | ix |
| Preface | xi |
| 1 Introduction | 1 |
| I Torsion spring mechanisms | 13 |
| 2 Static balancing of an inverted pendulum with prestressed torsion bars | 15 |
| 3 Design of a compact gravity equilibrator with an unlimited range of motion | 33 |
| II Curved compliant mechanisms | 47 |
| 4 Shape optimization and sensitivity of compliant beams for prescribed load-displacement response | 49 |
| 5 A carbon fibre beam balancing a pendulum: experimental evaluation | 73 |
| 6 A monolithic compliant large-range gravity balancer | 79 |
| 7 Design and Optimization of a General Planar Zero Free Length Spring | 95 |
| 8 Design and Characterization of a Linear Elastic Isotropic Metamaterial with Zero Poisson's Ratio over Large Strains Using a Spring Lattice | 107 |
| 9 Potential energy fields of systems with torsion stiffness | 117 |
| 10 A lumped compliant statically balanced self-guiding straight-line mechanism | 125 |
| 11 A potential energy field (PEF) approach to the design of a compliant self-guiding statically-balanced straight-line mechanism | 129 |
| III Compliant shell mechanisms | 151 |
| 12 Gravity balanced compliant shell mechanisms | 153 |

| | |
|--|------------|
| 13 Pseudo Rigid Body Modeling of a single vertex compliant-facet origami mechanism (SV-COFOM) | 175 |
| 14 A design tool for a single vertex compliant-facet origami mechanism (SV-COFOM) including torsional hinge lines | 183 |
| 15 Study on the large-displacement behavior of a spiral spring with variations of cross-section, orthotropy and prestress | 189 |
| IV Application examples | 207 |
| 16 Application examples | 209 |
| V Conclusion | 219 |
| 17 Conclusion | 221 |
| Acknowledgements | 227 |
| References | 229 |
| Contribution to each chapter | 249 |
| Curriculum Vitæ | 251 |
| List of Publications | 253 |

Summary

In this dissertation a collection of concepts to synthesise nonlinear springs is presented. Such springs can be useful in various application domains where, e.g., multi-stability or static balancing is desired. These behaviors are often sought to alleviate the effort required for actuation. The explored concepts are presented by showing the design methods, numerical or analytical models, and assessing their viability with experimental evaluations.

In part I two concepts show how the linear moment characteristic of torsion bars can be reshaped into a nonlinear one. Torsion bars are often suitable energy storage elements because they can be conveniently integrated within the hinge of a mechanism. In both examples the synthesised nonlinear characteristic is determined such that it counteracts the moment of a turning pendulum. The way how the characteristic is reshaped is, however, very different. In the first concept multiple springs are employed, but activated or deactivated by mechanical stops in order to create a piecewise linear characteristic. In the second concept the characteristic is reshaped by a set of non-circular gears. These gears are arranged in a planetary way to obtain a compact transmission.

In part II the focus is on planar compliant mechanisms that by virtue of their optimized shape exhibit the desired behavior. A few examples demonstrate that, even with relatively simple topologies, complex characteristics can be synthesised accurately. For example, a single beam clamped at one end and pivoted at the other end, is able to match a sinusoidal moment characteristic for a half period. In a second example we were able to produce a constant force by a doubly clamped optimally shaped beam. The constant force of this minimalistic design can be applied to balance a weight over a range of motion approximately equal to the largest dimension of the design. In another example it is shown that an optimized beam shape can emulate the behavior of zero free-length springs. These springs have ideal properties but are in practice difficult to make. We also show that a meta-material constituted by a lattice of zero free-length springs, exhibits very peculiar properties as zero Poisson's ratio, isotropy, and constant Young's modulus, up to large strains. Obtaining the required spring behaviour at such small scale would become possible by the use of optimally shaped beam springs. In the last example of part II a design consisting of four symmetric beams that move over a straight line of continuous static equilibrium is shown. As an aid to the design process, a representation of the elastokinematic behavior is introduced, based on the potential energy field (PEF). The PEFs characterise the behavior of compliant systems not only instantaneously, but over an area of possible displacement locations of the endpoint of the system.

Part III of this dissertation is dedicated to compliant shell mechanisms. The design of compliant mechanisms as spatial, thin walled, and possibly double curved

structures has some interesting and promising aspects. Because of their inherent nonlinear behavior, for example, they lend themselves good for synthesising the nonlinear equilibrium path. With compliant shell mechanisms it is also possible to conveniently create anisotropic stiffness, such that some motion directions are travelled much easier with respect to others. This type of effects can be tailored to create a desired kinematic function. In applications as wearable devices and interactive structures, compliant shell mechanisms can yield to slender, lightweight, aesthetically pleasing, and highly functional solutions. In this dissertation some progresses are made in this infant field of research. As a showcase, in the first chapter of this part, a self-balanced shell is designed. The optimized doubly curved shape of this shell is in continuous equilibrium with its own weight over a fairly large range of motion. In the subsequent two chapters, a tailored moment-angle characteristic is realized by optimizing the parameters of a basic origami mechanism. In the last chapter of this part a spiral spring with various cross-sections is analyzed to understand the anisotropic stiffness behaviors that can be achieved. In particular, the out-of-plane spatial behavior is studied. This is done by using the PEFs, for the first time in three dimensions.

In part IV two application examples are shown. First a shell mechanism, designed to provide a constant force, is applied to the tip of a heart ablation catheter. The constant force at the tip of the catheter helps maintaining contact with the heart wall while preventing dangerously high forces. The second example shows the concept of a large scale collapsible wall, consisting of a doubly curved shell that balances its own weight. Such wall, employed as e.g. a sound barrier, could be hidden flat when not in use, and be lifted upright when it is needed.

The concepts presented in this dissertation are applied to selected examples. However, they can be applied to synthesise a broader scope of desired characteristics. Also, the ideas can be generalised by moving from springs to mechanisms, i.e. where input and output have distinct locations. A step even further is to apply distributed actuation, sensing, and control on the deforming bodies such to obtain real automata, where advantage is taken of the synthesised elastic behavior. It is also advisable to direct future research into the use of composites as spring material. It can be expected that their high strength, their tailorable anisotropy, and the possibility to deliberately introduce prestress will lead to springs with increased performance and improved control of the behavior. Future research should also be directed towards improving the available design aids, including PEFs, for compliant mechanism designers. Furthermore, it is expected that the developments of this dissertation can be beneficially applied in an increasing number of application areas.

Samenvatting

In dit proefschrift wordt een verzameling aan concepten voor de synthese van niet-lineaire veren gepresenteerd. Dergelijke veren kunnen bruikbaar zijn in verscheidene toepassingsgebieden waarin bijvoorbeeld multi-stabiliteit of statisch balanceren gewenst is. Dit soort gedrag is vaak gewild om de inspanning van de actuatie te verlichten. De onderzochte concepten worden gepresenteerd door de ontwerpmethododes, numerieke en analytische modellen, en experimentele validaties te tonen.

In deel I demonstreren twee concepten hoe een lineaire moment karakteristiek omgevormd kan worden tot een niet-lineaire karakteristiek. Torsiestaven zijn vaak geschikte energieopslagelementen omdat ze gemakkelijk kunnen worden geïntegreerd in het scharnier van een mechanisme. In beide voorbeelden wordt de niet-lineaire karakteristiek zo ontworpen dat het moment van een roterende pendulum wordt tegengewerkt. In het eerste concept worden meerdere veren gebruikt, die steeds ge(de)activeerd worden door middel van mechanische aanslagen zodat een stuksgewijs lineaire karakteristiek ontstaat. In het tweede concept wordt de karakteristiek omgevormd door een compacte planetair stelsel van niet-ronde tandwielen.

In deel II ligt de nadruk op flexibele mechanismen die middels hun geoptimaliseerde vorm het gewenste gedrag vertonen. Een aantal voorbeelden tonen aan dat, zelfs met relatief simpele topologieën, complexe karakteristieken nauwkeurig gesynthetiseerd kunnen worden. Als voorbeeld wordt een enkele balk gegeven, die aan een uiteinde is ingeklemd en aan de andere uiteinde scharniert om een vast punt, die een sinusvormige momentkarakteristiek kan genereren. In een tweede voorbeeld konden we een constante kracht genereren door een dubbel ingeklemde balk waarvan de vorm is geoptimaliseerd. De constante kracht van dit minimalistisch ontwerp kan worden gebruikt om een gewicht te balanceren over een bewegingsbereik ongeveer zo groot als de grootste dimensie van het ontwerp. In een ander voorbeeld wordt aangetoond dat een geoptimaliseerde balkvorm het gedrag van nul vrije-lengte veren (ideale veren) kan emuleren. Deze veren hebben ideale eigenschappen maar zijn in de praktijk moeilijk te maken. We tonen ook aan dat een meta-materiaal, bestaand uit een raster van ideale veren, zeer bijzondere eigenschappen vertoont zoals nul Poisson ratio, isotropie en constante elasticiteitsmodulus, tot op grote rek waarden. Het verkrijgen van het vereiste veergedrag op zulk een kleine schaal kan mogelijk worden gemaakt door het gebruik van balken met geoptimaliseerde vorm. In het laatste voorbeeld van deel II wordt een ontwerp getoond die bestaat uit vier symmetrische balken die over een rechte lijn kunnen bewegen waarover een continu statisch evenwicht heerst. Als hulpmiddel bij het ontwerpproces wordt een representatie van het elastokinematisch gedrag op basis van het potentiële energieveld (PEF) geïntroduceerd. De PEFs karakteriseren het gedrag van flexibele systemen niet alleen in een instantane positie, maar over een heel gebied van mogelijke verplaatsingen van het eindpunt van het systeem.

Deel III van dit proefschrift is gewijd aan flexibele schaalmechanismen (compliant shell mechanisms). Het ontwerpen van flexibele mechanismen als ruimtelijke, dunwandige en eventueel dubbelgekromde structuren heeft een aantal interessante en veelbelovende aspecten. Vanwege hun inherente nietlineariteit, bijvoorbeeld, lenen ze zich goed voor het synthetiseren van het niet-lineair evenwichtspad. Met flexibele schaalmechanismen is het ook mogelijk om relatief makkelijk anisotrope stijfheid te creëren. Daarmee wordt de beweging in bepaalde bewegingsrichtingen veel lichter ten opzichte van andere richtingen. Dit soort effecten kunnen worden gebruikt om een gewenste kinematische functie te realiseren. Bij toepassingen zoals draagbare ondersteuning en interactieve structuren kunnen flexibele schaalmechanismen leiden tot dunne, lichtgewicht, esthetische en functionele oplossingen. In dit proefschrift zijn een aantal stappen gezet in dit jong onderzoeksgebied. Als toonvoorbeeld is in het eerste hoofdstuk van dit deel een zelfbalancerende schaalconstructie ontworpen. De geoptimaliseerde dubbelgekromde vorm zorgt ervoor dat deze schaal in een continu evenwicht is met zijn eigengewicht over een groot bewegingsbereik. In de daaropvolgende twee hoofdstukken wordt een naar wens bepaalde moment karakteristiek gerealiseerd door de parameters van een basis origami mechanisme te optimaliseren. In het laatste hoofdstuk van dit deel wordt een spiraalveer met verschillende dwarsdoorsneden geanalyseerd om begrip te vormen over het anisotroop stijfheidsgedrag dat verkregen kan worden. In het bijzonder wordt het ruimtelijk gedrag bestudeerd. Dit wordt gedaan door voor het eerst gebruik te maken van ruimtelijke PEF visualisaties.

In deel IV worden twee toepassingsvoorbeelden getoond. Eerst wordt een schaalmechanisme die ontworpen is om een constante kracht te genereren gebruikt als tip van een hartablatiekatheter. De constante kracht op de tip van de katheter helpt om contact te behouden met de hartwand en om grote gevaarlijke krachten te vermijden. Het tweede voorbeeld toont een grootschalige inklapbare wand, bestaande uit een dubbelgekromde schaal die zijn eigengewicht in balans houdt. Een dergelijke wand, toegepast bijvoorbeeld als geluidsbarrière, kan plat worden gemaakt wanneer het niet in gebruik is en rechtop worden geheven wanneer het weer nodig is.

De concepten in dit proefschrift worden toegepast op gekozen voorbeelden. Zij kunnen echter ook worden toegepast voor de synthese van andere gewenste karakteristieken. Ook kunnen de ideeën gegeneraliseerd worden door over te gaan van veren naar mechanismen, dus met in- en uitgang op verschillende punten. Nog een stap verder is het toepassen van verdeelde actuatie, sensing en aansturing op de vervormende elementen. Op deze manier ontstaan ware automaten waarin voordeel wordt behaald uit het gesynthetiseerd elastisch gedrag. Het is ook aan te raden om toekomstig onderzoek te richten op het gebruik van composieten als veermateriaal. Het is te verwachten dat hun hoge sterkte, hun beïnvloedbare anisotropie en de mogelijkheid om gecontroleerd voorspanningen te introduceren zal leiden tot veren met betere prestaties en een betere beheersing van het gedrag. Vervolgonderzoek zou ook gericht moeten worden op het verbeteren van hulmidelen (inclusief PEFs) voor ontwerpers van flexibele mechanismen. Verder wordt verwacht dat de ontwikkelingen uit dit proefschrift voordelig kunnen worden toegepast in een groeiend aantal toepassingsgebieden.

Preface

/ˈpɹɛfəs/

from *prae* "before" + *fari* "speak", meaning "to say beforehand". I must admit that in my case I am writing this preface rather afterwards, when everything is done, submitted, accepted, etc.

But it makes sense. Preface is about expressing gratitude. And usually we are grateful for what has been. Therefore I will spend a few words on expressing my sincere gratitude towards all the people that supported (italians may confuse this with *sopportato* = "endured") me during the past eight years.

Yet at this moment my gratitude, rather than looking back, is directed towards the present and future. The introductory prayer of the Catholic Mass, also called Preface, starts with "It is truly right and just, our duty and our salvation, always and everywhere to give you thanks, Lord...". So give thanks. Always. I am grateful for the upcoming times, for the opportunities that are given to me, for the challenges I will face, for seeing my children grow up, for not knowing what will be next. For knowing that whatever will be next, it will be good.

The last couple of years, of which this thesis is only a minor sideproduct, have taught me to appreciate everything I don't know and cannot foresee. I could not have foreseen that a temporary job of a few months at InteSpring would extend to eight years working on exoskeletons. I thank Rogier, Wouter and Boudewijn. I could not foresee that from a bistable shirt clip on, there has always been some interesting stuff to work on: SPISTA, Elasticom, -K, X-arm, ShellMech. I thank Just for continuously believing in me. I could not have foreseen, or maybe I could, such a lively life with my wife. I thank Noemi for her crazy choice. I could not have foreseen the growth of my support team at home. I thank God for his crazy choices. I thank my kids: They are my chance not to live for myself. Cristina, with only half of her vitality I would have finished my PhD two years ago. Monica, small and profound. Giovanni, only half of his dedication would have saved me another two years. Daniela, the cutest being. Antonio, wake him up in the middle of the night: He'll smile!

I owe a particular debt of gratitude to all students I supervised and collaborated with. Not only because of their important contributions, help and insights, but also because I enjoy(ed) all the speculations, discussions, mutual corrections, and the achievements. Thank you Wouter, Freeke, Boaz, Albert, Bob, Jesse, Jelle, Hoessein, Rik, Roriko, Josella, Arnoud, Joep, Jelmer, Barend, and Floris. A special thanks also to the people I collaborated with in various projects: Werner, Nauzef, Micha, Awaz, Emile, Milton, Annechien, and Mike. I also want to thank all the guys and girls at the TUDelft, Holland Container Innovations, InteSpring, and Laevo. I name a few by their names, with excuses for the ones I don't: Juan, Nima, Gert, Gerard, Rob, Simon, Gunawan, Hanneke, Rianne, Amber, Davood, Patrice, Reinier, Freek, Niranjan, Stefan, Wan.

To end, I thank my parents, my family (excuse me for not listing you all), my church community, and friends, because doctor or no doctor, they have been and will be close to me no matter what.

Giuseppe Radaelli
Delft, August 2017

1

Introduction

1.1. Synthesising nonlinearity in elastic systems

In many engineering and scientific disciplines the convenient choice is often made to assume linearity. In mechanical engineering, and in particular structural mechanics, this choice implies the assumption of small deflections, linear elastic materials, no friction, no contacts, etc. The convenience gained from these assumptions is significant. They allow to apply proportionality (double load gives double deflection [1, Chapter 10]), superposition of response to loads, modal superposition [2], etc. Moreover, it is possible to use the solutions to eigenvalue problems for, e.g., eigenfrequency analysis and linear buckling [3]. In practice, maybe the most relevant advantage is that solving a linear system of equations does not require the use of iterative schemes, e.g., the Newton-Raphson method, which often make a prohibitive claim on time and computing resources.

Even though nonlinear analysis is certainly not new and within reach of most engineers, nonlinearity is often tried to be avoided. This is not only because of the difficulties regarding the analysis of a nonlinear case, but also because it is often associated with failure rather than with function. Buckling, cracking, friction, plasticity, etc., are phenomena that are generally avoided. Therefore, traditionally, nonlinear structural mechanics is focussed on analyzing the nonlinear phenomena in order to be able to understand, predict, and eventually prevent their occurrence.

But nonlinearity in elastic mechanical systems also represents a great opportunity. It is not just about using nonlinearity for a better representation of the physical reality, but rather to exploit it by making it functional. The ability to synthesize the nonlinear load-displacement characteristic of elastic systems opens new avenues to the design of mechanisms.

1.2. Types of load-displacement functions

The static equilibrium path of a conservative system describes the relation between an applied load and a chosen displacement quantity. We limit this discourse more specifically to springs, defined by Veihar [4] as “mechanisms with coincident input and output points”, thus where the equilibrium path represents the relation between a load and the corresponding displacement of its point of application.

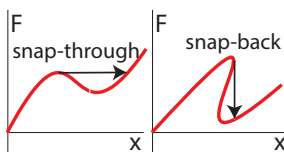


Figure 1.1:
Snap-through and snap-back

In an equilibrium path it is possible that one load value corresponds to multiple displacements. In such cases, one or more maxima or minima are encountered for which a small increment in the load results in a large displacement, i.e. snap-through (Fig. 1.1a).

Another possible case is that one displacement value corresponds to multiple load values. The equilibrium path exhibits a turning point for which a small change in the displacement results in a sudden change in the load, i.e. snap-back (Fig. 1.1a). In this thesis, where we choose to focus on quasi-static conditions, the last type of behavior is kept out of consideration since it usually goes accompanied by dynamic effects.

To get an overview and understanding of the possible types of equilibrium

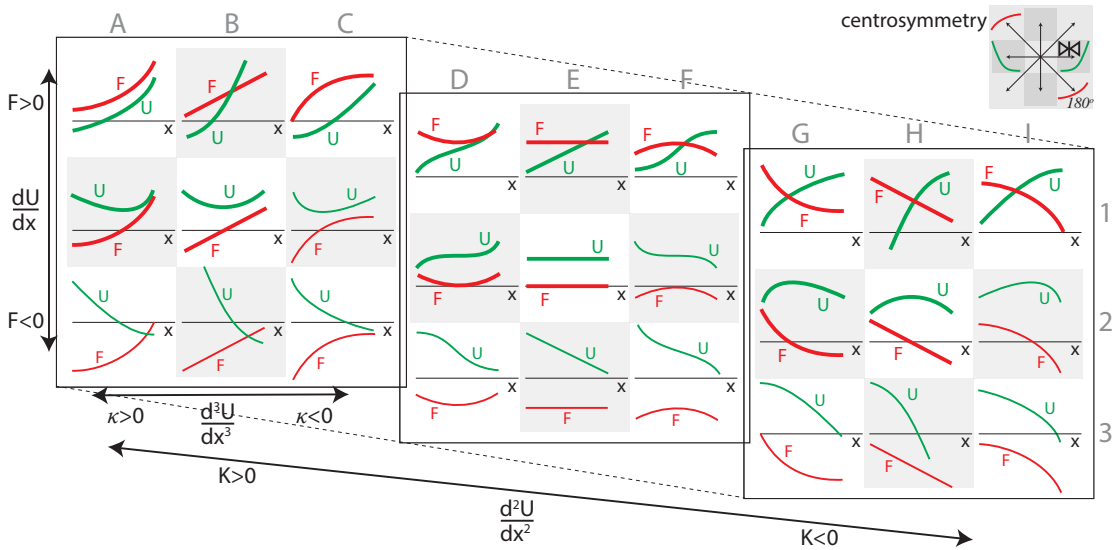


Figure 1.2: Schematic overview of possible nonlinear equilibrium path-segments (F-x,red) with corresponding energy graphs (U-x,green). The categorisation is according to the first, second and third derivative of the potential energy, corresponding to the dimensions of the 3D-array. Equivalent behaviors appear in centrosymmetric fashion and are shown with thinner lines. Note that the energy levels can be freely chosen, thus the crossings with the x-axis have no particular meaning.

paths, consider the scheme in Fig. 1.2. A general equilibrium path can consist of multiple consecutive path-segments. In this scheme, short segments of the load-displacement curve and the corresponding energy-displacement curve are illustrated, categorized according to the first, second, and third derivative of the potential energy which can be positive, zero, or negative. These quantities, that correspond to the force, the stiffness, and the curvature of the equilibrium path, are shown in a 3D-array with every quantity related to a dimension of the array. The curve segments can either lie above, cross, or lie underneath the zero force axis; have a positive, zero, or negative slope; and have a positive, zero, or negative curvature. That a general equilibrium path consists of possibly many of the represented curve segments does not mean that it can be created by simply concatenating the physical systems that exhibit the short segment paths. But understanding the nature of the sought equilibrium path helps the designer to identify the challenges associated with it and the physical phenomena that can be exploited to achieve it.

In the shown 3D-array the dimensions are ordered such that equivalent behavior due to symmetry is easily identified. If an equilibrium path can be obtained by rotating another path by 180° about a point on the zero force axis, then the same behavior can be obtained by turning the physical system by 180° (Fig. 1.3). The behaviors are therefore considered equivalent in the sense that they are not fundamentally different and can supposedly be achieved by similar design principles. From the

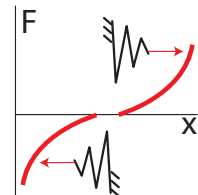


Figure 1.3: Equivalent behavior.

perspective of potential energy, a system is equivalent if a vertical symmetry can be identified. In the array in Fig. 1.2, the equivalent systems are located in a centrosymmetric manner in the three squares. Of every equivalent couple, only one is highlighted. This reduces the number of possible path-segment types from twentyseven to fifteen.

Some observations can be made about how to achieve certain equilibrium paths. Naturally, an unstressed system made of an hookean material has a linear force-displacement relation with positive slope within small displacement ranges. At large deflections nonlinearities start to arise. The sources of nonlinearity in structural mechanics can be categorized as material, geometric, force boundary conditions, and displacement boundary conditions [5]. A progressive characteristic is not rare. Consider a horizontal cantilever beam loaded by a vertical force. As the force increases it aligns more and more with the beam, causing a transition from a prevalent bending load case to a prevalent tension load case, which is much stiffer. Degressive characteristics are often encountered in material-related nonlinearities and in buckling-like conditions. In the first type, the equilibrium path is dictated by the nonlinear stress-strain relation belonging to the material at hand. The buckling-like softening is abrupt, and the precise course of the equilibrium path is not easy to predict because it is very sensitive to imperfections. That holds for example for a straight column compressed by a vertical force. In the case of an intentionally imperfect column, e.g. asymmetric or non straight, the softening becomes less abrupt and the course of the equilibrium path is easier to reproduce [1, 6]. A degressive characteristic can be the ramp up to a constant force path. Therefore, a constant force is to be regarded as a nonlinear path. In fact, strictly speaking, a constant force other than zero is not linear because it does not obey to proportionality between force and displacement, i.e. the straight line does not cross the origin. Related thereto, it is noted that a non-positive slope cannot be obtained without applying some form of preload or prestress to the system. The system must be brought in a stressed state with higher potential energy w.r.t. the unstressed system. This can be done by tracing an initial positive segment of the equilibrium path until a negative slope is reached, or alternatively by, e.g., connecting elements during assembly, by applying preload on a secondary input port of the system, by applying dead loads such as weight, or by introducing residual stresses such as thermal stresses.

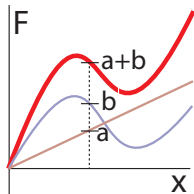


Figure 1.4:
Parallel coupling

It is possible to synthesise a desired equilibrium path by combining multiple elements in parallel, series or a combination of both. The parallel case is straightforward. Parallel elements share the same applied displacement value. Therefore, their equilibrium paths are simply added (Fig. 1.4). For instance, a constant force can be used to adjust the load level of another function. Another frequent practice is to combine a linear positive path with a linear negative portion of a path in order to achieve a constant value. Interestingly, shifting the paths horizontally with respect to each other can be used to tune the level of the constant line [7, 8]. There are also other examples where the stiffness of a parallel system is tuned by shifting two nonlinear paths horizontally with respect to each other [9, 10].

In the 3D array of Fig. 1.2 it is possible to choose two opposing elements across every dimension: The sum of both equals the element in-between, but with doubled amplitude. It so becomes useful to find combinations of systems that yield a desired path. For example, a parallel coupling of the progressive positive stiffness (upper-left corner A-1) and the degressive negative stiffness (upper right I-1) result in a constant force (upper middle E-1).

Serial connections are a little more intricate. Two elements connected in series share the same force value but different displacements. Therefore, the behavior is obtained by adding the displacement and using the load as the argument. In Fig. 1.5 this is illustrated by switching the load and the displacement axis, before taking the sum of the curves. As we see happening at point $a+c$, in serial connections there is a good chance to obtain snap-back behavior. This happens for instance if for a given load the magnitude of the negative stiffness of one system exceeds the magnitude of the positive stiffness of the other system.

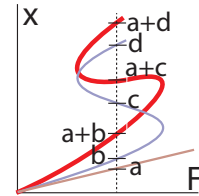


Figure 1.5:
Serial coupling

1.3. Application areas

In this section we will go through some application domains of nonlinear springs. Particular attention in this thesis is given to degressive, zero and negative stiffness. Although these behaviors are often not the first to be associated with nonlinear springs, many applications can take profit from them and the ability to synthesize them is valuable. This overview is by no means a complete review of achievements found in literature, but rather an illustration of how broad the domain of possible applications is.

Degressive, or softening, characteristics (Fig. 1.6) are of interest in applications where the energy storage must be optimized. The energy contained in a spring, which equals the area under the load-displacement function, is more in a degressive spring than in a linear spring with the same end-load and displacement. Also, because of the lowered stiffness after a certain load, degressive springs are used in vibration isolation mounts [11–13] and in MEMS resonators [14].

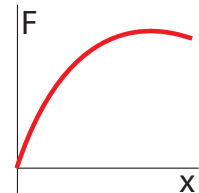


Figure 1.6:
Degressive.

Multistable systems (Fig. 1.7), i.e. those with more than one stable equilibrium position, can be found in many application domains. The main reason to use multistability is because it allows to passively keep a mechanism in multiple configurations. Only the switching between configurations requires an external input, but holding it in position requires no effort. Familiar examples of multistable systems are light switches, the lid of shampoo bottles, hair clips, and bistable bracelets. Many examples can also be found in the micro mechanism domain as valves [15–18],

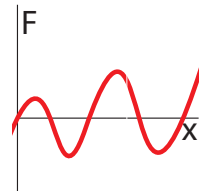


Figure 1.7:
Multistable

switches [19–23], actuators [24], mechanical memory [25, 26] and vibration energy harvesters [27, 28]. At a larger scale, multistability is often proposed for deployable and morphing structures with applications in, e.g., space and defence [29–31], and medicine (stent) [32].

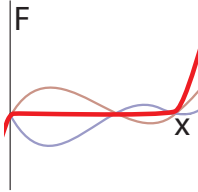


Figure 1.8:
Continuous equilibrium

Mechanisms that have a continuous equilibrium over a range of position are called statically balanced mechanisms (Fig. 1.8). This type of mechanisms get particular attention in this work because of some clear advantages they possess. A major advantage is the reduction of actuation forces that results in small actuators or the possibility of manual operation. Another one is that holding a position requires negligible forces, implying small brakes and inherent safety. Moreover, eigenfrequencies are close to zero which is useful for, e.g., vibration isolation [33]. Statically balanced mechanisms can also be identified in literature in terms of the related properties of zero-stiffness, neutral stability, and constant potential energy [34].

The ability to synthesise general shapes of equilibrium paths is useful because often statically balanced mechanisms are designed by seeking the inverse match of a given equilibrium path. In the most common case the given system has a positive stiffness and the goal is to find a matching negative stiffness profile. But the path of the given system can also be nonlinear and contain transitions between the cells of Fig. 1.2. It is sometimes not evident which part of the system is the balancer and which one is balanced [35]. It is emphasized that the connection of multiple systems that neutralize their stiffness requires a preload step.

There are some elegant examples of systems where prestress is applied to the system in a distributed fashion. It so can happen that a single element is inherently balanced so that it is even harder to attribute the balancing contribution at subsystem level. Guest describes a remarkable shell structure that has zero stiffness along a cyclic twisting path [36]. Schenk and Guest also show a prestressed annular rod with a neutrally stable twisting motion [34]. Seffen, from the same group, shows a circle-based hyperboloid with concentric corrugations that, although not explicitly mentioned, has zero stiffness behavior [37]. Lamacchia illustrates how an annular plate becomes neutrally stable by applying circumferentially distributed moments [38]. These remarkable structures are not associated to particular application possibilities.

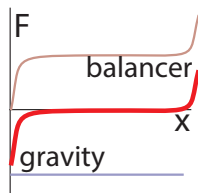


Figure 1.9:
Gravity balancing

A special class of statically balanced mechanisms are gravity balancers. A gravity balancer generates a constant force upward that is always in equilibrium with the weight (Fig. 1.9). Gravity balancing can be found in products of various type and scale. Examples of manually operated systems include furniture and household objects [39–41]. At a larger scale the weight of walls and panels can be balanced [42]. In orthosis and exoskeletons it is possible to balance the weight of parts of the body [43–

45]. Furthermore, gravity balancing can be found in many automated systems like robots [46, 47]. Constant force mechanisms are also sometimes used for other applications as, e.g., overload protection [48, 49] and maintaining contact irrespectively of disturbances or imperfections [49–52].

1.4. Problem statement

Nonlinearity in mechanical systems is extensively treated in many fields of research. Most of it focuses on analysing particular effects (buckling, cracks, plasticity), and numerical methods to simulate them. However, we observe sporadic attention to the synthesis of nonlinearity as a functional benefit [53–56]. Moreover, there is a scarcity of methods to synthesise the nonlinearity accurately for a given desired equilibrium path. This holds especially if the path is specified for relatively large range of motion. It would be beneficial to the mechanism designer to have a set of available tools, including conceptual principles, models and design methods, that aid them to obtain a desired equilibrium path accurately.

1.5. Objective

The objective of this thesis is to present novel concepts to synthesise the equilibrium path of elastic systems. Concepts as intended in this context are distinct ways and principles by which nonlinearity is achieved. As will be elaborated in Section 1.6 the presented concepts appertain to the three categories *Torsion spring mechanisms*, *Curved compliant mechanism*, and *Compliant shell mechanisms*. The concepts are made usable for designers by presenting related design methods, numerical simulations and experimental validations. The purpose of every design is to match a particular equilibrium path with good accuracy. Special attention is given to systems with decreasing, zero, or negative stiffness, and where the path is specified for large ranges of motion. The concepts are applied to examples with a chosen behavior, but in most cases they are more broadly applicable to other desired responses. Each concept has distinct benefits, among which being efficient, compact, minimalistic, scalable, or organically shaped.

1.6. Concepts

There are many factors that can influence the equilibrium path of spring systems: topology, shape, constraints, material, transmission, contact, etc. We investigate a selection of interesting basic concepts to manipulate the equilibrium path of spring systems, divided over the categories: *torsion spring mechanisms*, *curved compliant mechanisms*, and *compliant shell mechanisms*. The presented concepts are tools with distinct possible advantages and application domains.

1.6.1. Torsion spring mechanisms

Using torsion springs as alternative to extension springs has a couple of advantages. Especially, the space they occupy does not change significantly while loaded. For example, a torsion bar can be integrated along the hinge line of a door to exert

a moment on it whereas an extension spring would need to cross the free space to do so (Fig. 1.10). This has functional advantages because the crossed space becomes available, but also in terms of aesthetics and safety because the spring can more easily be covered. Examples of products that can take advantage of these benefits are foldable sea containers [42] where the side walls are balanced by a torsion spring along the lower hinge line. It is essential that the inner space of the container remains available for freight. Hinged doors and panels that could benefit from elegantly integrated spring systems can also be found in furniture, cars, deployable systems and the like.

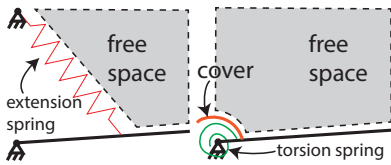


Figure 1.10: Space advantage of torsion springs.

While in literature the design of nonlinearity with extension springs is extensively treated, and specifically for static balancing, it is incomplete in terms of solutions involving torsion springs [57–61].

1.6.2. Curved compliant mechanisms

An exceptional role when discussing synthesis of nonlinear elasticity is taken by compliant mechanisms. Compliant mechanisms are an increasingly popular class of mechanisms that take advantage of the flexibility of their members to achieve motion [62]. The absence of kinematic pairs gives compliant mechanisms most of its well-praised advantages [62]: no friction, no wear, no stick-slip, no backlash, no need for lubrication, part count reduction, noise reduction, and vibration reduction.

A major drawback of compliant mechanisms is that their deflection is always associated with a restoring force. In some cases this restoring force is beneficial, for instance to create a stable pose [63], a spring action (maintain contact, elastic support) [64] or unidirectional actuation (e.g. cable driven) [65–67]. In other cases the restoring force is undesired because it results in larger actuators, high energy consumption, and reduced tactile feedback perception [68]. An explored solution to this problem is to apply static balancing. The resulting mechanisms, statically balanced compliant mechanisms (SBCM) [69], have a constant potential energy and thus have the advantages of compliant mechanisms as well as those of statically balanced ones.

In terms of exploiting the nonlinearities, compliant mechanisms offer many opportunities because of their ample design freedom. The load-displacement of a compliant mechanism is influenced by aspects of material (combinations), topology, shape, contact, and stress state. While all these aspects have been elucidated to some extent before [53, 70, 71], the full potential of synthesising specific load-displacements in an accurate manner has not been fully exploited yet. Of particular interest is exploiting the shape of compliant mechanism members. Many compliant mechanisms consist of combinations of (sometimes many) straight flexural members, in some rare cases with a curvature. But shaping flexural members freely has the potential of creating enhanced functionality at no higher cost of material volume, number of elements or complexity of the construction, yet resulting in elegant,

simple-looking solutions. With increased freedom of shape in modern manufacturing facilities (additive manufacturing, computer aided manufacturing), restricting a compliant mechanism design to just combinations of straight beams or well defined basic shapes seems like an unnecessary limitation.

The planar compliant solutions to the synthesis problems in this thesis are mostly based on finding optimal shapes of compliant members. This resulted in minimalistic designs with accurately matched equilibrium paths.

1.6.3. Compliant shell mechanisms

Compliant shell mechanisms are a relatively unexplored class of compliant mechanisms with an enhanced potential with respect to the tailorability of their load response. Seffen [37] defines compliant shell mechanisms as “open, thin-walled, discretely corrugated structures, with flat facets or curved regions of shell interconnected by folds or hinge lines”, or “discretely corrugated structures, capable of undergoing large, reversible displacements”. Because corrugations, folds and hinge lines impose an unnecessary restriction on the class, in this thesis we redefine the term compliant shell mechanisms from a contraction of Farshad’s definition of shells [72] and Howell’s definition of compliant mechanism [62]: *Compliant shell mechanisms are spatially curved thin-walled structures able to transfer or transform motion, force or energy through elastic deflection.*

Distinctive for compliant shell mechanisms is hence their being spatially curved. A double curvature is often the cause of nonlinear effects. Double curvature (or non-zero Gaussian curvature) can cause a coupling between deformation modes. If the deformations are large, this often implies a nonlinear load-deformation characteristic.

For instance, if a shell dome (Fig. 1.11) is bent inwards, the curvature transverse to that loading becomes flatter. The more it gets flat, the more the stiffness diminishes. If bent outwards the transverse curvature increases, causing a stiffening behavior. In general, when a double curvature

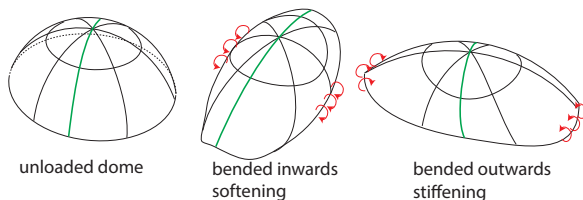


Figure 1.11: Coupled deformations that cause nonlinearity.

causes the coupling of deformation modes, this results in substantial shape changes that alter the stiffness. It is thus an opportunity to exploit the freedom of shape of a shell can thus be exploited to influence its nonlinear equilibrium path.

Compliant shell mechanisms are also well-suited to obtain anisotropic stiffness of the end-effector of a mechanism [37, 73]. The preference to move in a certain direction or along a certain path becomes more accentuated due to the stiffness contrast in different directions. As such, shell mechanisms could be made suitable as kinematic elements, i.e. path-generators. Understanding, modelling, characterising and optimizing compliant shell mechanisms with the purpose to exploit the described benefits is a worthwhile research endeavour that could lead to surpris-

ingly integrated, simple and aesthetically pleasing mechanisms. To the eye of most people such a mechanism will not even look like one. In an age where interaction of machines with humans is intensifying (prostheses, orthoses, exoskeletons, collaborative robots), and where the success of a product highly depends on its aesthetic appeal, the importance of aesthetics of mechanisms should not be underestimated.

Besides the ability to synthesize nonlinearity, anisotropy and the aesthetic argument, other reasons to advocate this relatively new field of research are

- the ability of shells to efficiently carry large loads relative to their material volume [72], and at the same time the ability to undergo large deformations;
- the possibility to shape shells around the contours of the human body, useful for creating inconspicuous wearable devices;
- the ability to synthesise complex kinematic functions, e.g., remote centres of motion;
- the possibility to use fibre-reinforced plastics which lend themselves well to the fabrication of complex curved shells. These materials can have superior properties in the combination of stiffness, toughness and elastic energy absorption capability;
- as a consequence of the latter, the ability to tailor the behavior by optimizing fibre orientation, stack sequence and prestress;
- the possibility to apply distributed actuation spread over the shell's geometry;

This thesis contributes in laying a foundation to this field by developing proof of principles that can stimulate the implementation of compliant shell mechanisms in actual products.

1.7. Outline

The remainder of this book is structured as follows. The body is subdivided in four parts. Part I treats ways to tailor the moment-angle characteristic of torsion systems applied to the balancing of a pendulum. This is done in Chapter 2 by using mechanical stops and prestress to (de)activate torsion springs, such to obtain a piecewise linear moment-angle characteristic. In Chapter 3 the reciprocating rotation of a bundle of linear torsion bars is converted into a continuous rotation by a planetary gear system with noncircular gears. The torsion bars can therefore be used to balance the sinusoidal moment-angle characteristic of a pendulum over an unlimited rotation range.

In part II the focus is on planar compliant mechanisms. In Chapters 4 and 5 it is shown how the shape of a compliant mechanism can be optimized to obtain complex moment-angle characteristic with a relatively simple topology consisting of a single beam. This beam is preloaded by displacing its endpoint and then pivot it about its new position. Shape optimization of a single beam clamped at both ends and loaded in the middle is used in Chapter 6 to obtain a monolithic large range

gravity balancer. Chapter 7 presents the emulation of a zero free length spring (ZFLS) behavior by an optimized beam geometry, developed for different endpoint conditions. This type of behavior is desirable because it is essential to many static balancing principles for rigid body mechanisms. This compliant beam alternative opens up the opportunity to create monolithic versions of conventional balanced mechanisms. On top of that, one of the optimized shapes is applied in Chapter 8 as an element in a lattice of a meta-material with the unique combination of linear isotropy with large strains and zero Poisson's ratio. In Chapters 9, 10 and 11 a characterisation approach for elastic systems is presented that can aid the synthesis of nonlinear responses. The elastokinematic behavior is characterised on a large range of motion by representing the potential energy field (PEF) of the whole system corresponding to the displacement field of the endpoint. The approach is illustrated by a design that consists of four equal and symmetrically arranged springs that are in balance with each other throughout a linear displacement.

Part III collects the chapters that are related to spatial compliant mechanism, i.e. origami and shells. In Chapter 12 the remarkable design of a doubly curved optimized shell shape is presented. This shell is in equilibrium with its own weight and a small payload while deforming from standing upright to laying flat. Chapters 13 and 14 are dedicated to a single vertex origami mechanism including the bending of the facets which results in a nonlinear moment-angle output. A simple and accurate model is presented and some specific nonlinear functions are designed. In Chapter 15 the spatial behavior of spiral springs is investigated by the use of spatial PEFs. The anisotropic stiffness of the inner endpoint of the spiral is influenced by varying the cross-section shape, the anisotropy of the material and applied prestress conditions.

Part IV touches upon some application examples. These examples illustrate the potential of compliant shell mechanisms to obtain extremely simple designs with special functionalities at different size scales. The first example regards a constant force tip for a heart ablation catheter. The constant force is needed to maintain contact with the moving heart wall. At a totally different scale, the second example regards a sound barrier, to be used for instance along a train track, that can be erected upright and flattened down with minimal actuation effort.

1.8. Readers guide

This thesis is a collection of scientific articles, published or submitted, on which the author has a director's role. It is chosen to add some articles in a shortened format, highlighting the main contributions that are supporting the objective and the message of the thesis. Some of these articles are co-authored by the author of this thesis and are based on the graduation theses of supervised MSc students. A detailed overview of the author's contribution in every chapter is provided in Chapter [Contribution to each chapter](#).

I

Torsion spring mechanisms

2

Static balancing of an inverted pendulum with prestressed torsion bars

This chapter presents a method for the design of a statically balanced inverted pendulum. The nonlinear moment-rotation characteristic of the pendulum's weight is approximated by a piecewise linear characteristic. Each transition is realized by engaging or disengaging one or more torsion bars, by means of mechanical stops. The set of torsion bars is located along the hinge axis of the pendulum. A prototype with three parallel torsion bars was built. Experimental evaluation of the prototype revealed a 99% work reduction of the balanced pendulum with respect to the unbalanced one.

This chapter has been published in Mechanism and Machine Theory (2017) [74], and in the conference proceedings of the 13th World Congress in Mechanism and Machine Science, Juanajuato (Mexico), June 2011 [75].

2.1. Introduction

In order to alleviate the operating forces of mechanical devices, it is possible to apply static balancing to counteract the weight of the system and/or its payload [35]. The result is a more manageable device in the case that it is human-operated, and less powerful actuators in the case that the device is powered. Other advantages of static balancing include intrinsic safety [46], intuitive man-machine interaction [76, 77], backlash reduction due to prestress, and weight reduction of motors and brakes [57]. Because of these advantages static balancing of weight has been proposed in numerous applications, especially in the fields of robotics [78–82], orthotics and assistive devices [83–85], and consumer products [39].

Most static balancing techniques involve the use of counter-masses [86], which have the disadvantage of increasing the overall mass and inertia of the system. A common alternative is to use extension springs [35], which have the disadvantage that the volume they occupy increases when the spring is loaded. In addition, most spring-based balancing techniques rely on the use of a special type of spring, namely a zero-free-length spring (ZFLS), which is not a common off-the-shelf component. Some authors have presented ways to circumvent the need for ZFLS proposing alternative balancing methods that are based on conventional springs with non-zero free-length [83, 87–90].

Both kind of extension springs often have the disadvantage that the volume they occupy crosses the empty space between the elements of the device, which implies that the space is not available for other purposes. Think for example of an application where static balancing is to be applied in a foldable structure, such as a foldable sea container [91], to compensate the weight of the members of the structure. If there were extension springs crossing the free space inside the structure, this space would not be available for goods. Therefore more compact solutions that only occupy space near the hinges are sought.

Koser [92] present a cam mechanism in combination with a compression spring that is designed as a compact unit at the base of a robotic manipulator. However, the assessment of the practical applicability of the concept is not completed up to the level of component design and physical evaluation. In practice, the high forces on the cam system combined with the very small design space may reveal as the limiting factors.

Shieh [93] presents a balancing mechanism that does not cross the free space by applying a Scotch Yoke spring mechanism which can be integrated within the link. Friction in the sliding parts are probably affecting the performance of balancing significantly, but the authors make no mention of this possible issue.

The employment of torsion springs at the hinges of a linkage would eliminate the named disadvantages. Torsion springs, namely, act at the point of rotation between two bodies and thus do not elongate when loaded. Very little work has been found that includes torsion springs for the purpose of balancing weights.

Gopalswamy [57] balances the weight of a parallelogram linkage with a single torsion spring with a linear characteristic. The range where the balance applies, however, is limited to the part of the sine characteristic that can be approximated as linear.

Trease [58] developed a gravity balanced four-bar linkage. An optimization procedure was used to obtain a constant potential energy of the masses and the open-cross compliant joints, a type of torsional springs. As the authors state, the presented solution is a specific one limited to the given parameter set only. A similar result was obtained by Radaelli [94], who developed a general design method for approximate static balancing of linkages with torsion springs. In one of the examples, a pendulum is balanced by an additional double link, obtaining in fact a four bar linkage with a balanced weight. In both cases the links that are added to balance the pendulum occupy a considerable amount of space. Therefore, in this regard, these solutions do not offer enough advantage with respect to the helical spring balancers.

In the present chapter the case is considered of a body, modelled by a point mass connected by a weightless link to a revolute joint in an inverted pendulum arrangement, representing, e.g., a side wall of a foldable sea container. The pendulum moves over ninety degrees from the upright vertical position to a horizontal position. The weight will be balanced with torsion springs, specifically torsion bars. Torsion bars have the advantage that they occupy approximately the same space loaded as well as unloaded. Moreover, normally the bars are situated at the hinge in the direction perpendicular to the plane of motion of the pendulum. This is especially advantageous for pendulums with large out-of-plane width, such as the side wall of the container.

Since normal torsion springs have a linear moment-angle characteristic, they can only linearly approximate the sinusoidal moment-angle characteristic of the weight. We propose the judicious employment of mechanical stops and prestress for the sequential activation or deactivation of different torsion bars in order to obtain a piecewise linear moment characteristic. This piecewise linear characteristic can give better approximations of the nonlinear degressive characteristic of the weight.

Eshelman [59] describes an invention where a multi-rate torsion bar is employed for vehicle suspensions. An increased torsional stiffness is obtained with two serial torsion bars with one mechanical stop. Also Fader [95] describes a similar torsion bar for vehicle suspensions, where more mechanical stops are used to affect the total torsion stiffness of the bar. In his invention, Castrilli [60] obtains nonlinearity in the torsion characteristic of a bar with a continuous contact profile along the length of the bar. This system can be regarded as an infinite number of bars of infinitesimal length in series, all with their own contact point.

All mentioned inventions concern torsion bars with increasing stiffness. A degressive stiffness, however, can only be obtained if the stops make contact initially and loses contact afterwards, i.e. if one or more bars are prestressed. Claus [96] designed such a system for static balancing of the walls of a foldable container. In a small-scale prototype he used a configuration of two serial torsion bars with one mechanical stop. No other examples of torsion spring systems with positive but degressive stiffness were found in literature.

The goal of this chapter is to propose a method for balancing an inverted pendulum by a piecewise linear approximation of the nonlinear characteristic, obtained by the sequential (de-)activation of torsion springs. The design approach allows for

unlimited number of linear segments. This number is only limited by the physical implementation of the torsion bars.

The outline of this chapter is as follows. In Section 2.2 the design methodology is described. Section 2.3 illustrates the design of the physical prototype, while in Section 2.4 the testing procedure and the test results are provided. Finally the discussion and conclusions are found in Sections 2.5 and 2.6, respectively.

2.2. Method

The present section starts with a description of the technical problem and the conceptual solution. After that the design method will be discussed.

2.2.1. Problem description

Consider the system depicted in Fig. 2.1a. A point mass m is attached to a weightless rigid link at a distance l from a hinge. The pendulum is allowed to move between its upright vertical position a , and 90 degrees clockwise, to the horizontal position b , thus $[a, b] = [0, \frac{\pi}{2}]$ rad. The weight of the pendulum produces a negative sinusoidal moment-angle characteristic at the hinge. Friction and other non-conservative forces are neglected. To maintain the system in equilibrium at every position, a system with a positive sinusoidal moment characteristic is needed to counteract the weight, see Fig. 2.1b. Focusing on the given range of motion it is required that the balancing system possesses a nonlinear, positive and decreasing stiffness.

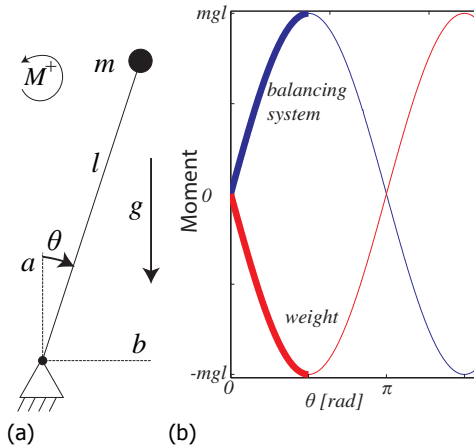


Figure 2.1: (a) Inverted pendulum, (b) moment-angle of pendulum and of ideal balancer.

A given design requirement is that the balancing system occupies as little space as possible around the hinge. In a sea container, the direction out of the plane of motion is along the hinge of the wall, thus along this hinge there is space available for the balancing system. This requirement practically excludes the employment of extension springs.

2.2.2. Effect of contact and prestress

Obtaining a changing stiffness in a controlled manner can be done by the subsequent employment of multiple springs and mechanical stops. The mechanical stops serve to activate or deactivate a spring such to obtain a different compound of active springs, resulting in a non-constant stiffness, see [97]. The employed springs can be connected in series or in parallel or in a combination of both, as will be explained next.

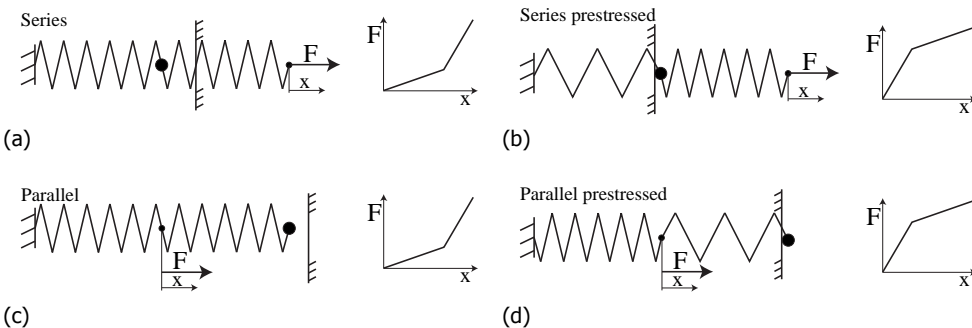


Figure 2.2: Variable stiffness with mechanical stops in extension springs. (a) series making contact, (b) prestressed series releasing contact, (c) parallel making contact, (d) prestressed parallel releasing contact.

Series

Assume two extension springs in serial are fixed at one end and loaded at the other end, with a mechanical stop at the connection point of both springs, see Fig. 2.2a. The mechanical stop is not making contact. Increasing the applied load will cause the mechanical stop to make contact. Now one spring is allowed to deform further, while the other one keeps its current deformation and no longer contributes to the stiffness at the endpoint. The resulting stiffness is higher than before.

Series prestressed

Consider now the other way around. The same two springs are prestressed in such a way that the mechanical stop makes contact initially, see Fig. 2.2b. One of the springs will initially not deform and therefore not contribute to the stiffness. When the load exceeds the prestress force the mechanical stop loses contact. Now both springs start to contribute to the stiffness, making the total stiffness lower than before.

Parallel

Analogous reasoning can be applied to parallel springs. Consider two parallel springs. One spring is connected to ground at one end and at a common load point at the other end. The other spring is connected to the load point at one end and is initially loose at the other end, see Fig 2.2c. When the load increases

the second spring makes contact and starts contributing to the stiffness, yielding a higher stiffness.

2

Parallel prestressed

In the fourth case the mechanical stop is initially active, thus with a certain prestress force holding the contact. Once the load equals the prestress force the contact gets lost and the second spring does not contribute to the stiffness any more. In fact, the second spring will have only a rigid-body motion from that point on. Since in parallel systems the stiffnesses add together, the result is a lower stiffness after contact is lost.

Extrapolating from this fundamental idea, it becomes possible to approximate different nonlinear curves by piecewise-linear curves possibly involving two or more linear segments, obtained by one or more mechanical stops. The explanation with the extension springs, which is more easily illustrated, also holds for torsion springs or any other analogous situation with potential energy storage elements.

2.2.3. Design method

The present subsection describes the linear approximation of the sine curve that can be obtained by a single linear torsion spring. It is followed by a description of the piecewise-linear approximation obtained by the passive (de-)activation of different prestressed linear torsion springs with mechanical stops. The result is an improved approximation of the sine curve with two equilibrium points for every additional spring.

Linear approximation

Consider a single torsion spring, or any combination of springs with a linear moment characteristic. If employed as balancing system for an inverted pendulum, the balance will always be approximate and a finite number of static equilibrium positions can be obtained. The best fit between a linear segment and the segment of the sine depends on the choice of the objective function. For example, the maximum difference between both curves could be minimized to suppress high peak forces. Alternatively one could take the integral of the squared difference between both curves over the range of motion. This would lead to a lower work done over the whole range of motion. The choice is related to the application of the balanced system. With no specific application at hand, in this chapter the second objective is arbitrarily chosen. The dimensionless difference Δ between the sine and the line (normalized by amplitude $mgL = 1$) is given by

$$\Delta = \sin(\theta) - (K\theta + M), \quad (2.1)$$

where K is the slope of the line and M is the level of the line at $\theta = 0$. The objective is the integral of the squared difference over the range of motion, as

$$f = \min_{K,M} \int_a^b \Delta^2 d\theta, \quad (2.2)$$

where K and M are varied to obtain the best fit. The optimization is performed with the aid of the Matlab[®] tool *slmengine*, which can perform a piecewise linear fitting to any dataset by least squares optimization.

The sine curve in the range $a = 0$, $b = \pi/2$, the fitted line and the resulting error curve are provided in Fig. 2.3a. The optimized value for f is 0.0062. The optimized parameters K and M are 0.66 and 0.11, respectively. The system can be made with a torsional spring with stiffness $k = KmgL$ and neutral angle

$$\alpha = -\frac{M}{K}. \quad (2.3)$$

The maximum rotation which the spring undergoes is

$$\theta = b - \alpha. \quad (2.4)$$

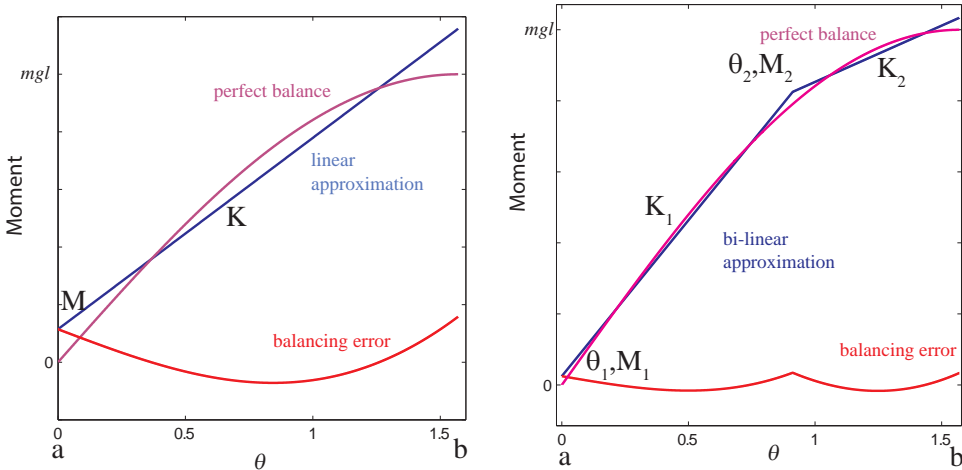


Figure 2.3: (a) Linear approximation of perfect balancer, with balancing error. (b) Bi-linear approximation of perfect balancer, with balancing error.

Bi-linear approximation

For an improved approximation the sine can be fitted with two linear segments, see Fig. 2.3b. Both line segments can be described by their slopes K_1 and K_2 , and their starting point defined by the coordinates θ_1, M_1 , and θ_2, M_2 . θ_1 is defined by the starting point of the range of motion a , in this case $\theta_1 = 0$. Moreover, M_2 is determined by the first line segment and the intersection angle θ_2 . The set of remaining independent optimization parameters includes K_1, K_2, M_1 and θ_2 . The dimensionless difference between the piecewise approximation and the sine is now given by

$$\Delta = \begin{cases} \sin(\theta) - (K_1\theta + M_1) & a \leq \theta < \theta_2 \\ \sin(\theta) - (K_2\theta + M_2) & \theta_2 \leq \theta < b \end{cases}, \quad (2.5)$$

and the objective becomes

$$f = \min_{K_1, K_2, M_1, \theta_2} \int_a^b \Delta^2 d\theta. \quad (2.6)$$

The values obtained from the optimization are

$$\begin{aligned} [K_1, K_2, M_1, M_2, \theta_2] = \\ [0.88, 0.32, 0.02, 0.83, 0.91], \end{aligned} \quad (2.7)$$

and the obtained value of the objective is $f = 3.2647e - 4$.

Series springs

If both springs are in series, then in the first segment only one spring is active, and in the second segment also the other spring becomes active. The first spring thus must have the stiffness $k_1 = K_1 mgl$ and neutral angle $\alpha_1 = -\frac{M_1}{K_1}$ while the second spring has stiffness

$$k_2 = \frac{K_1 \cdot K_2}{K_1 - K_2} mgl, \quad (2.8)$$

and neutral angle

$$\alpha_2 = -\frac{M_2}{k_2} mgl. \quad (2.9)$$

Parallel springs

In the case that the springs are parallel the stiffness of the first spring is

$$k_1 = (K_1 - K_2) mgl, \quad (2.10)$$

while the stiffness of the second bar is simply $k_2 = K_2 mgl$. The neutral angles of the two springs are

$$\alpha_1 = \theta_2, \quad (2.11)$$

$$\alpha_2 = \theta_2 - \frac{M_2}{K_2}. \quad (2.12)$$

Multi-linear approximation

The procedure above can in principle be extended for any number of serial or parallel springs. Combinations of serial and parallel springs are also possible, but will not be considered here. For n number of linear segments, there are $2n$ free parameters to optimize. These are the slopes K_1, K_2, \dots, K_n , the height of the first intersection point M_1 and the angles of the following intersection points $\theta_2, \theta_3, \dots, \theta_n$, see Fig. 2.4. The difference function and the objective function are given by

$$\Delta = \begin{cases} \sin(\theta) - (K_1\theta + M_1) & a \leq \theta < \theta_2 \\ \sin(\theta) - (K_2\theta + M_2) & \theta_2 \leq \theta < \theta_3 \\ \vdots & \\ \sin(\theta) - (K_n\theta + M_n) & \theta_n \leq \theta < b \end{cases}, \quad (2.13)$$

and

$$f = \min_{\mathbf{x}} \int_a^b \Delta^2 d\theta, \quad (2.14)$$

with

$$\mathbf{x} = [K_1 \cdots K_n, M_1, \theta_2 \cdots \theta_n]. \quad (2.15)$$

2

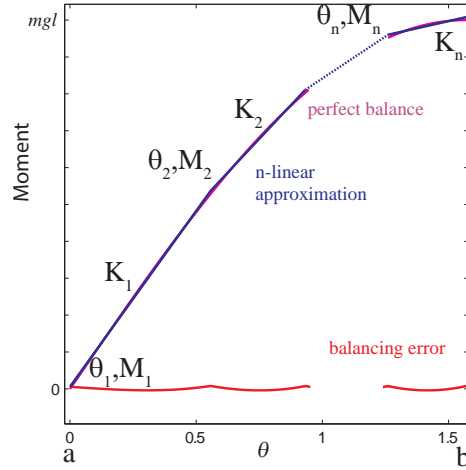


Figure 2.4: n-piece linear approximation of perfect balancer.

Series springs

In the case of a serial configuration, the spring parameters are obtained with

$$\begin{aligned} k_i &= K_i mgl & i &= 1 \\ k_i &= \frac{K_{i-1} K_i}{K_{i-1} - K_i} mgl & i &= 2 \dots n \end{aligned} \quad (2.16)$$

$$\alpha_i = -\frac{M_i}{k_i} mgl \quad i = 1 \dots n \quad (2.17)$$

The maximum rotation undergone by the springs is

$$\theta_i = \frac{M_b}{k_i} mgl \quad i = 1 \dots n \quad (2.18)$$

where M_b is the normalized moment at point b , that can be derived by

$$M_b = M_n + K_n (b - \theta_n). \quad (2.19)$$

Parallel springs

The spring parameters in the case of a parallel configuration of springs are obtained with

$$\begin{aligned} k_i &= (K_i - K_{i+1}) mgl & i &= 1 \dots n - 1 \\ k_i &= K_i mgl & i &= n \end{aligned} \quad (2.20)$$

$$\begin{aligned} \alpha_i &= \theta_{i+1} & i &= 1 \dots n - 1 \\ \alpha_i &= \theta_i - \frac{M_i}{K_i} & i &= n \end{aligned} \quad (2.21)$$

The maximum rotation undergone by the springs is

$$\begin{aligned}\Theta_i &= \theta_i & i &= 1 \dots n-1 \\ \Theta_i &= b - \alpha_i & i &= n\end{aligned}\quad (2.22)$$

2.2.4. Number of bars

Evidently, the more linear segments are used, the better the approximation to the sine curve is. However, the advantage in fitting result may in practical cases not weight against the added complexity of a high number of springs. Therefore a trade-off should be made between complexity and accuracy, which is highly dependent on the intended application. Figure 2.5 shows the results of optimized objective function f as a function of the number of linear segments on a logarithmic scale. It can be observed that the advantage in accuracy is decreasing as the number of segments increases.

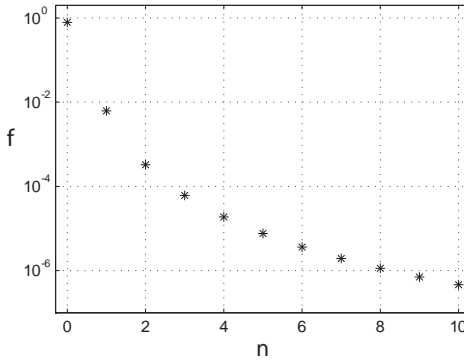


Figure 2.5: Result of optimization for different number of segments on logarithmic scale. Improvement in result is getting smaller as number of bars increases.

2.2.5. Choice between parallel and series

It is again dependent on what the intended application of the balanced system is whether to prefer a serial configuration or a parallel one. However, some guidance can be found in the metric given next.

The potential energy required to lift the pendulum is independent from the configuration of springs. But due to prestress, there is more energy stored in the springs than strictly required. Therefore, the sum of the maximum strain energy that is stored in the separate springs can be used as an indicator for the efficiency of the system. The maximum energy storage U in the single springs is given by

$$U_i = \frac{1}{2} k_i \theta_i^2, \quad (2.23)$$

and the sum of the strain energy over all springs is

$$U_{tot} = \sum_{i=1}^n U_i. \quad (2.24)$$

| Nr. segments | 1 | 2 | 3 | 4 | 5 |
|--------------|------|------|------|------|------|
| series | 1.01 | 1.69 | 2.48 | 3.29 | 4.11 |
| parallel | 1.01 | 1.92 | 2.82 | 3.69 | 4.54 |

Table 2.1: Sum of maximum strain energy in every bar, for different number of bars. Pendulum parameters are normalized to $mgl = 1$.

Table 2.1 gives some comparative values of total strain energy for series and parallel springs. It can be seen that the energy efficiency, as defined above, is worse for parallel systems because the energy metric is increasing faster w.r.t. serial systems.

2.3. Prototype

For the illustration and evaluation of the presented design approach, a prototype has been designed, constructed and tested. In the presented prototype, as an example for above mentioned possibilities, three parallel torsion bars are used to approximate static balancing of an inverted pendulum. The choice of three bars and the parallel configuration is arbitrary and is not related to the efficiency metric discussed above. A trilinear approximation of the first quarter-period of a sine function gives 2 orders of magnitude error reduction with respect to a linear approximation, see Fig. 2.5.

2.3.1. Torsion bars

The spring type selected for this prototype are torsion bars. Torsion bars can occupy very narrow spaces along the hinge axis. Moreover, torsion bars have an efficient energy storage per material volume as compared to springs that are loaded in bending [97], e.g., spiral springs and helical torsion springs.

For the dimensioning of torsion bars the material properties shear modulus G and maximum shear strength τ_{max} are needed. Given a circular cross-section of the bars, the length L_i and diameter d_i must satisfy the following relation in order to obtain the desired stiffness k_i

$$L_i = \frac{J_i G}{k_i}, \quad (2.25)$$

where J is the polar moment of inertia, given by

$$J_i = \frac{\pi d_i^4}{32}. \quad (2.26)$$

Moreover, as the maximum shear stress τ may not be exceeded, the following inequality must be satisfied

$$L_i \geq \frac{d_i G \theta_i}{2\tau_{max}}. \quad (2.27)$$

To use as little material as possible, one might want to chose the values for d and L for which this inequality is just fulfilled. However, for practical reasons, a round-off

| Parameter | units | value |
|---------------------------------|--------------------|---------------------------|
| m, g, l | $[kg, ms^{-2}, m]$ | 5, 9.81, 0.5 |
| K_1, K_2, K_3 | $[rad^{-1}]$ | 22.82, 14.79, 5.09 |
| a, θ_2, θ_3, b | $[rad]$ | 0, 0.68, 1.15, 1.57 |
| M_1, M_2, M_3, M_b | $[-]$ | 0.26, 15.81, 22.74, 24.88 |
| k_1, k_2, k_3 | $[Nmrad^{-1}]$ | 8.03, 9.70, 5.09 |
| $\alpha_1, \alpha_2, \alpha_3$ | $[rad]$ | 0.68, 1.15, -3.32 |
| $\Theta_1, \Theta_2, \Theta_3,$ | $[rad]$ | 0.68, 1.15, 4.89 |
| d_1, d_2, d_3 | $[m]$ | 0.004, 0.005, 0.006 |
| L_1, L_2, L_3 | $[m]$ | 0.247, 0.500, 1.975 |

Table 2.2: Design parameters

value of the diameter would be beneficial for the ease of purchasing the bar. With the material properties $G = 79 \text{ GPa}$ and $\tau_{max} = 600 \text{ MPa}$ (alloy steel DIN 1.8159) the resulting design parameters are given in Table 2.2. The moment characteristic of the pendulum, the balancing system and both together are plotted in Fig. 2.6.

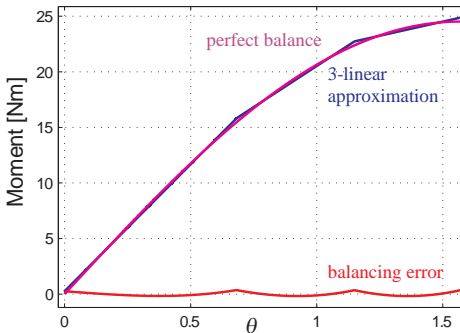


Figure 2.6: Tri-linear approximation applied on the prototype.

2.3.2. Construction

A picture of the entire prototype is provided in Fig. 2.7. Some details of the construction are discussed next. The three bars have an L-shaped hook at one end, and are fixed to the same aluminium block in such a way to impede relative rotation, see Fig 2.8a. This part is connected to a bearing and to the pendulum, with masses at adjustable distances. The longest torsion bar is positioned centrally with respect to the other two bars. It is assumed that the influence of the offset of the two short bars from the axis of rotation is negligible.

At the free end of the two short bars a wing-shaped part is fixed. The wings can make contact with a perpendicular bolt at every side such to impede further rotation, see Fig. 2.8b. This system is the mechanical stop that makes the bar active only in a certain range of motion. Due to the bending stiffness of the bars it is not needed to support them at this end.

Figure 2.7: Picture of entire prototype. Three torsion bars with an arrangement of mechanical stops serve as gravity balancing system for an inverted pendulum.

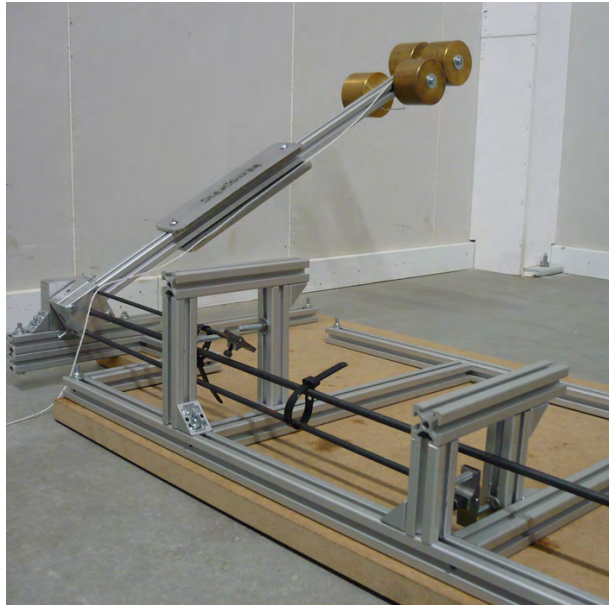
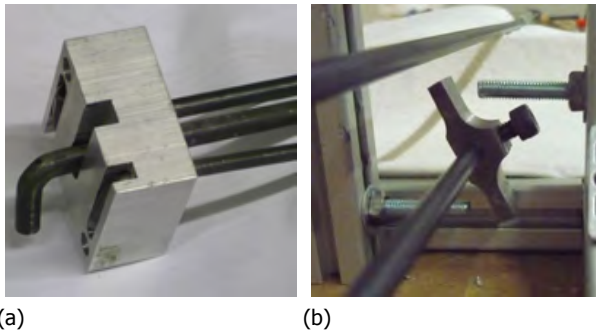


Figure 2.8: Prototype details pictures. (a) L-shaped bar ends clamped, (b) mechanical stops, the wings touch the bolts impeding rotation from then on.



2.4. Evaluation

The testing of the prototype and the results from the measurements are discussed in the present section. The mass of the pendulum and the distance of the centre of mass from the rotation axis, for which the best results were found experimentally, are

$$m_{real} = 5.0 \text{ kg}, \quad (2.28)$$

$$l_{real} = 0.487 \text{ m}. \quad (2.29)$$

The distance is 0.013 m smaller than the optimized value.

2.4.1. Equilibrium positions

The system is expected to exhibit six equilibrium positions within the given range of motion, three stable ones and three unstable ones. The pendulum is positioned in

| Nr | Stable/Unstable | Model [deg] | Prototype [deg] |
|----|-----------------|-------------|-----------------|
| 1 | U | 9.3 | 4 |
| 2 | S | 31.8 | 38 |
| 3 | U | 45.1 | 43 |
| 4 | S | 60.4 | 60.5 |
| 5 | U | 71.0 | 69 |
| 6 | S | 84.9 | 84 |

Table 2.3: Equilibrium positions, prediction and measurements.

proximity of the expected equilibrium positions. In the case of the stable equilibria, the system will spontaneously approach the state of equilibrium. In the case of unstable equilibria, the point is searched manually by feeling where the reaction force and the tendency to deviate from that position are minimal. Once the pendulum is positioned at these positions, the angle is measured with a bevel protractor. The results of this test are tabulated in Table 2.3.

2.4.2. Moment-angle measurements

The next test aims to get a precise moment-angle characteristic of the prototype over the given range of motion. The measurements are performed with a vertical tensile bench. The load cell is connected by a wire to an aluminium disc with 30mm diameter. The disc, which is supported by a separate ball-bearing, is connected to the balancing system with a pin connection between the axis of the disc and the hollow axis of the balancing system. On the disc a counter-mass is attached through a wire over a pulley to make all forces tensile and thus measurable with this setup. This weight was later subtracted from the measurement result.

Two separate measurements are performed. One in which only the disc with the mass and the pulley are connected, and one also including the pendulum with its balancing system. Subtracting both measurements from each other gives the moment contribution of the balanced pendulum. The measurements are performed two ways, from 0° to 90° and back from 90° to 0°. This way, a hysteresis loop is obtained. Taking the mean of the values for both directions at every angle gives an estimate of what the force would be in the absence of friction. This estimate is based on the assumption that the contribution of friction at every angle is equal in both directions. Figure 2.9a gives the measurements results of the setup (red), the setup with the balanced pendulum (green), and the difference between both (blue). Also the mean value between the upper and lower part of the last hysteresis loop is plotted (black). This moment-angle characteristic is compared to the modelled one in Fig. 2.9b.

Two comparative parameters will be provided to evaluate the fit between the modelled curve and the measured curve: the root mean squared error $RMSE$ and the correlation coefficient ρ . These parameters, however, do not quantify the balancing quality. To this end we take the ratio R between the work done by the balanced pendulum over the work done by the unbalanced pendulum in one way

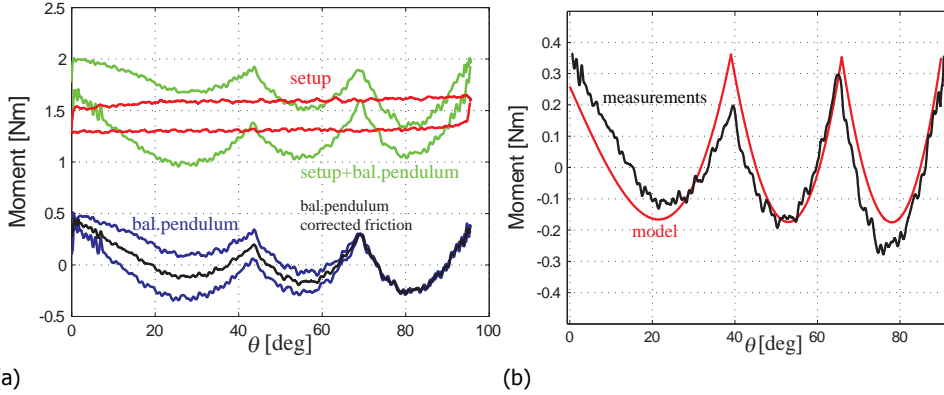


Figure 2.9: (a) Moment-angle measurements. The measurements with the system and the measurements setup are corrected with measurements of the setup alone. The results are corrected for friction. The black line is considered to come from the balanced pendulum itself. (b) Measurements compared with the model.

over the range of motion

$$R = \frac{W_{bal\ pendulum}}{W_{pendulum}} = \frac{W_{bal\ pendulum}}{g \cdot m_{real} \cdot l_{real}}. \quad (2.30)$$

The results are

$$\begin{aligned} RMSE &= 0.0868\ Nm, \\ \rho &= 0.8288, \end{aligned} \quad (2.31)$$

$$R = \frac{0.1996J}{23.8874J} = 0.89\%. \quad (2.32)$$

2.5. Discussion

2.5.1. Design approach

The presented design approach based on a piece-wise linear approximation of a sine curve through multiple torsion bars with preload and mechanical stops seems to be a powerful and easy tool for the design of statically balanced inverted pendulums. The present design concerns a range of motion of 90 degrees. The design approach, however, can be applied for different ranges of motion and potentially also for other types of nonlinear moment characteristics. Yet, it is not possible to obtain a negative stiffness with a compound of positive stiffness springs.

It is possible, but left for future work, to combine series and parallel springs together. This might be beneficial for the material and space-efficiency of the system. Also it must be investigated what type of nonlinearities are possible to achieve. For example, is it possible to combine progressive and degressive slopes consecutively?

2.5.2. Measurements

The measurement results are quite satisfactory. The difference with the modelled results are small and qualitatively the behavior is as expected. This can be verified with the number and location of the equilibria and the location of the transition points, i.e. where contact conditions change. The amount of work reduction of about 99% is also very satisfactory. Regarding the measurements themselves, the amount of measured hysteresis is considered as high. As seen in Fig. 2.9a, however, most of the hysteresis stems from the measurements setup, the disc and pulley, and not from the balancing system. It is also noticed that significantly higher friction is present near the upright position of the pendulum. This is presumably the effect of misalignment of the bearings.

2.5.3. Material

The design of the balancing system is developed for a mass of 5kg on a distance of 0.5m . To obtain the best results in the prototype, however, a mass of 5kg was fixed at a distance of 0.487m . This difference of 2.6% is most probably due to variations in the shear modulus of the material. For employment of such a balancing mechanism in real-life applications either good tests beforehand should reveal the exact properties of the material, or the mechanism should be able to accommodate for adjustment of the torsional rigidity of the bars or one of the other design parameters.

2.5.4. Construction

The presented construction of the prototype revealed some interesting features.

The absence of bearings for the two contacting bars combines a reduction in complexity and an improvement in terms of friction losses. In this case the bending stiffness of the bars suffices to sustain themselves and to guide themselves against the contacting points of the mechanical stops.

The distance of the two short bars with respect to the axis of rotation does not compromise the energy storage properties of the bars noticeably. This is because their bending stiffness and their deflection are relatively small.

2.6. Conclusion

This chapter presents a design approach for static balancing of an inverted pendulum. The design approach is based on a piecewise linear approximation of the nonlinear moment characteristic of the pendulum, obtained with sequential (de-)activation of torsion springs using mechanical stops and prestress in a variety of arrangements. In the optimization procedure, the area between the original curve and the approximation is minimized, resulting in a system that requires minimal work for operation.

The design method is a tool to approximate balance with torsion springs in series and parallel configurations up to an unlimited number of springs, limited only by physical construction constraints.

The method is used to approximate a sinusoidal curve, but can potentially be

used for the approximation of other types of nonlinear moment characteristics. For example, in a more complex linkage system subject to gravity, the effect of the weight can be translated into a needed moment characteristic at one or more hinges of the system.

A trilinear approximation of the first quarter-period of a sine function gives a factor 100 error reduction with respect to a linear approximation. A prototype with three parallel torsion bars was constructed and tested. As compared to the unbalanced pendulum, less than 1% of the work is needed to turn the pendulum 90° from upright to horizontal.

3

Design of a compact gravity equilibrators with an unlimited range of motion

Bob G. Bijlsma, **Giuseppe Radaelli**, Just L. Herder

Current spring-to-mass gravity equilibrators are limited in their range of motion as a result of constructional limitations. An increment of the range of motion is desired to expand the field of applications. The goal of this chapter is to present a compact one degree of freedom mechanical gravity equilibrators that can statically balance a rotating pendulum over an unlimited range of motion. Static balance over an unlimited range of motion is achieved by a coaxial gear train that uses non-circular gears. These gears convert the continuous rotation of the pendulum into a reciprocating rotation of the torsion bars. The pitch curves of the non-circular gears are specifically designed to balance a rotating pendulum. The gear train design and the method to calculate the parameters and the pitch curves of the non-circular gears are presented.

A prototype is designed, built and experimentally validated. A work reduction of 87% compared to an unbalanced pendulum is achieved, and the hysteresis in the mechanism is 36%.

This chapter is a short version of a paper published in the Journal of Mechanisms and Robotics (2017) [98], and in the proceedings of the ASME IDETC 2016 40th Mechanisms and Robotics conference [99].

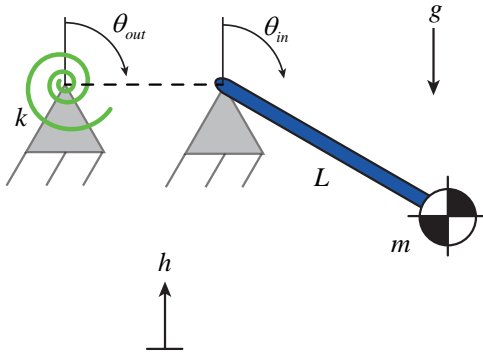


Figure 3.1: An exploded view of the different components to distinguish the parameters of the gravity equilibrator. On the left a torsion spring of which the angle of rotation is defined by θ_{out} and on the right a rotating mass on an arm, that is defined by the angle θ_{in} .

3.1. Introduction

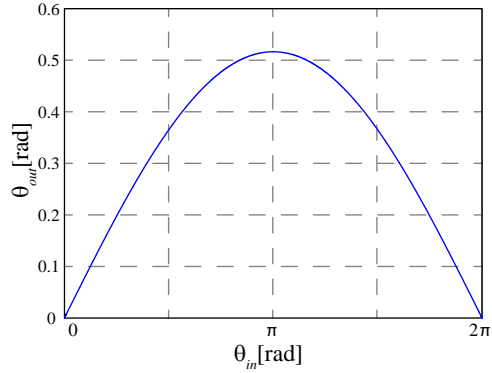
The purpose of a gravity equilibrator is designed to counterbalance a weight [100]. The advantage of such a system is that the operating effort to move the mass is greatly reduced [35]. This property is based on the principle of constant potential energy. Normally, a system tends to converge to a state where the potential energy is at a relative minimum. When a system exhibits constant potential energy, there is no such state. The result is that any preferred position is eliminated. In order to achieve constant potential energy a counterweight or a spring can be added to the system. A spring is preferable over a counterweight in terms of weight, dimensions and inertia forces [101].

A disadvantage of current spring-to-mass balancers is that helical springs are used. The spring crosses the working space of the mass and a zero-free-length spring is required to achieve perfect balance, Carwardine [102]. These springs are not readily available off-the-shelf.

Claus [96] designed a one degree of freedom (DoF) bottom hinged gravity equilibrator where a cluster of torsion bars is placed near the pivot point of the rotating mass, such that the working space of the pendulum is free of components. Radaelli [74] applies similar principles with multiple prestressed torsion bars to obtain a multi-linear approximation of the moment characteristic. Osch [61] applies a nonlinear transmission between the cluster of bars and the mass. This transmission is established by a Double Cam Transmission (DCT) which consists of two cams with varying radii that are placed side by side. A string wrapped around both cams transmits the torque. The main disadvantage of these designs is that the rotating mass is limited in its range of motion which is $0 \leq \theta_{in} \leq \pi/2$ rad. For a larger range, the radii of the cams are converging to the extrema; one radius becomes zero and one radius becomes maximal. This will result in extreme forces on the cams.

Another disadvantage of introducing the DCT is that the rotation axis of the mass and the rotation axis of the cluster of torsion bars are not coaxial. Not only does this lead to an increase in required space, it also causes an imbalance of forces. The result of this imbalance is that the structure around the mechanism is subjected to resultant forces, causing the whole structure to deform. This deformation is undesired in terms of alignment and energy storage.

Figure 3.2: The relation between θ_{in} and θ_{out} to obtain a statically balanced system. For increasing θ_{in} , θ_{out} first increases and then decreases again.



The goal of this chapter is to present a new gravity equilibrator that is able to statically balance a rotating mass over an unlimited range of motion which can be made more compact than the state of the art.

3.2. Method

The gravity equilibrator from Fig. 3.1 contains a mass and an energy storage element, i.e. a spring. The mass m rotates at a distance L from the pivot point and is connected to the input axis. The position of the mass is defined by the angle θ_{in} . The height h of the mass is measured from the datum plane $h = 0$. This reference plane can be chosen arbitrarily. The spring has a stiffness k and its deformation is defined by the angle θ_{out} .

The principle of constant potential energy is used to design the gravity equilibrator. It states that the sum of the potential energies in the system must be constant for all configurations:

$$V_g(\theta_{in}) + V_e(\theta_{out}) = C, \quad (3.1)$$

where V_g is the potential energy due to gravitational forces and V_e is the potential energy due to elastic forces. This results in the following condition to be met:

$$mgh(\theta_{in}) + \frac{1}{2}k\theta_{out}^2 = C. \quad (3.2)$$

The parameter h is chosen such that the height of the mass is equal to zero when the pendulum is at π rad. Therefore h equals $L(1 + \cos(\theta_{in}))$. Rearranging Eq. 3.2 gives θ_{out} as a function of θ_{in}

$$\theta_{out} = \sqrt{\frac{2mgL}{k}} \cdot \sqrt{1 - \cos(\theta_{in})}. \quad (3.3)$$

Eq. 3.3 gives the relation between θ_{in} and θ_{out} such that the rotating mass is balanced for every angle, see Fig. 3.2.

For increasing θ_{in} , θ_{out} first increases to a maximum and after that it decreases to its initial value. It can be stated that in order to achieve a perfectly balanced

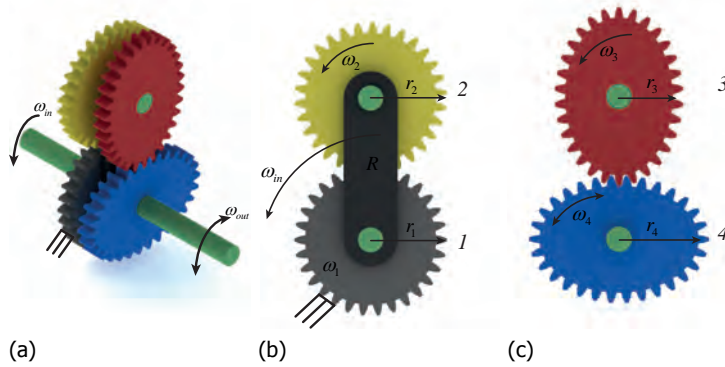


Figure 3.3: A schematic representation of the gear train: (a) A three dimensional representation of the gear train to visualize the topology, (b) the first gear set which consists of two circular gears, (c) the second gear set which consists of two non-circular gears, visualized by oval gears.

system, the input axis has to make a continuous rotation while the output axis has to make a reciprocating rotation. The assumption is made that the system acts quasi-statically, such that kinetic energy and dynamic forces can be neglected.

3.3. Conceptual design

In order to achieve perfect balance over an unlimited range of motion a transmission is introduced. This transmission converts a continuous rotation of the input axis into a reciprocating rotation of the output axis as depicted by Fig. 3.2. Figure 3.3 is a schematic representation of a transmission, adapted from [103], that converts a continuous rotation of the input into a reciprocating rotation of the output. This transmission consists of two gear sets. Gear set #1, see Fig. 3.3b, consists of two gears with constant pitch curves. Gear set #2, see Fig. 3.3c, consists of two gears with changing pitch curves, called non-circular gears. They are represented by oval gears. Next, the relation between the angular velocities ω_{in} and ω_{out} of the mechanism is derived in two steps.

3.3.1. Gear set #1

The first gear set consists of two gears which are both circular. There are three angular velocities to be distinguished, ω_{in} , ω_1 and ω_2 , which are the angular velocities of the rotating mass, gear 1 and gear 2 respectively. Gear 1 is rigidly connected to the world, such that ω_1 is 0 rad/s. Gear 2 is connected to the arm R which rotates with angular velocity ω_{in} , defined positive counterclockwise. Gear 2 meshes with gear 1 and because the latter is fixed, gear 2 is forced to rotate. The angular velocity of gear 2 is

$$\omega_2 = \left(1 + \frac{r_1}{r_2}\right) \cdot \omega_{in}, \quad (3.4)$$

where r_1 and r_2 are the radii of gear 1 and gear 2 respectively. These radii are both constant and positive.

3.3.2. Gear set #2

The connection between the first and the second gear set is established by gear 2 and 3 which are rigidly connected such that

$$\omega_3 = \omega_2. \quad (3.5)$$

Gear 4 is connected to the output axis. The angular velocity ω_{out} of gear 4 is a weighted combination of ω_{in} and ω_3 . The factor of ω_{in} is derived in the same way as was done for the configuration of the first gear set. The factor of ω_3 is derived by the ratio r_3/r_4 between the two gears. The derivation of ω_{out} is

$$\omega_{out} = \left(1 + \frac{r_3}{r_4}\right) \cdot \omega_{in} - \frac{r_3}{r_4} \cdot \omega_3. \quad (3.6)$$

By substituting Eq. 3.4 and 3.5 in Eq. 3.6, ω_{out} is expressed as a function of ω_{in}

$$\omega_{out} = \left(1 - \frac{r_1 \cdot r_3}{r_2 \cdot r_4}\right) \cdot \omega_{in}. \quad (3.7)$$

The transmission ratio is defined by the ratio between ω_{out} and ω_{in}

$$\frac{\omega_{out}}{\omega_{in}} = 1 - \frac{r_1 \cdot r_3}{r_2 \cdot r_4}. \quad (3.8)$$

The fraction of the four radii can be chosen in such a way that ω_{out}/ω_{in} is either positive, negative or equal to zero. When the fraction of radii is smaller than one, the transmission ratio is positive and θ_{out} increases for increasing θ_{in} . A negative transmission ratio is obtained when the fraction of radii is larger than one and θ_{out} decreases for increasing θ_{in} . When the combination of radii is equal to one, the output angle is stationary for increasing θ_{in} .

In this mechanism the second gear set consists of two non-circular gears. The radii r_3 and r_4 are variable. With changing radii the transmission ratio also changes. The radii are changed such that the output angle θ_{out} is tuned. To achieve perfect balance, θ_{out} first has to increase from zero to a certain angle and then decreases to zero as depicted in Fig. 3.2.

3.3.3. Concept alternatives

The concept of obtaining a reciprocating motion from a continuous one is explained by using external gears. However, as shown in Fig. 3.4, it is also possible to obtain the same behavior by replacing gears 1 and 4 by gears with internal teeth. This alternative results in a smaller outer diameter of the system. Therefore, this alternative is chosen for further elaboration.

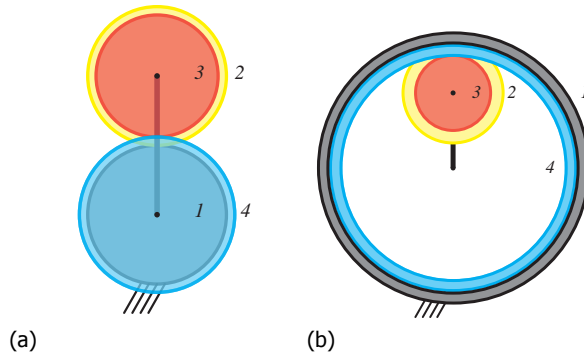


Figure 3.4: Two concept alternatives: (a) the original concept where all four gears have external toothing, (b) the concept where both gear 1 and 4 are replaced by gears with internal teeth.

3.4. Dimensional design

With concept 3.4b chosen, the design is worked out in detail. This process is divided in the calculation of the pitch curves of gear set #1 and gear set #2, the extension from the two dimensional plane to the three dimensional space, the determination of the exact teeth profiles and the calculations on the energy storing element.

3.4.1. Pitch curves of gear set #1

Gear set #1 consists of two gears with constant pitch curves. Gear 1 has internal tothing and is fixed. Gear 2 has external tothing and rotates inside gear 1. The relation between ω_2 and ω_{in} is

$$\omega_2 = \left(1 - \frac{r_1}{r_2}\right) \omega_{in}. \quad (3.9)$$

In order to achieve a periodic rotation the fraction r_1/r_2 has to be an integer and $r_1 > r_2$. The choice of the radii is arbitrary.

3.4.2. Pitch curves of gear set #2

Gear set #2 consists of two gears with non-circular pitch curves. The radii of these two gears are determined by differentiating Eq. 3.3 with respect to time to obtain the angular velocity of the output axis

$$\omega_{out} = \frac{d\theta_{out}}{dt} = \left(\frac{\sqrt{\frac{2mgL}{k}} \cdot \sin(\theta_{in})}{2\sqrt{1 - \cos(\theta_{in})}} \right) \cdot \omega_{in}. \quad (3.10)$$

The transmission ratio between ω_{out} and ω_{in} is equal to

$$\frac{\omega_{out}}{\omega_{in}} = \frac{\sqrt{\frac{2mgL}{k}} \cdot \sin(\theta_{in})}{2\sqrt{1 - \cos(\theta_{in})}}. \quad (3.11)$$

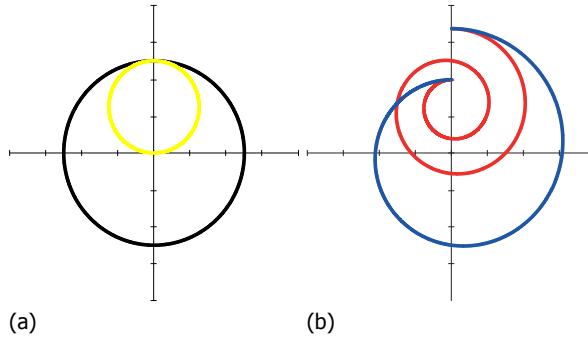


Figure 3.5: The pitch curves of: (a) gearset #1, (b) gearset #2. Black: gear 1, Yellow: gear 2, Red: gear 3, Blue: gear 4.

The transmission ratio of the gear mechanism is already determined in Eq. 3.8. By combining Eq. 3.8 and 3.11 the relation between the radius r_3 and θ_{in} is derived

$$1 - \frac{r_1 \cdot r_3}{r_2 \cdot r_4} = \frac{\sqrt{\frac{2mgL}{k}} \cdot \sin(\theta_{in})}{2\sqrt{1 - \cos(\theta_{in})}}. \quad (3.12)$$

Because the teeth of gear 3 and 4 have to mesh, r_4 can be expressed as $r_4 = r_3 + R$, where R is the length of the arm as depicted in Fig. 3.3b. With θ_{in} ranging from 0 to 2π , r_3 and r_4 are derived. The pitch curves of the four gears are visualized in Fig. 3.5. The radius of gear 1 is twice the radius of gear 2. The radius of gear 3 ranges between two extrema as well as the radius of gear 4.

Figure 3.6 visualises the relative positions of the four gears for one revolution of the input axis.

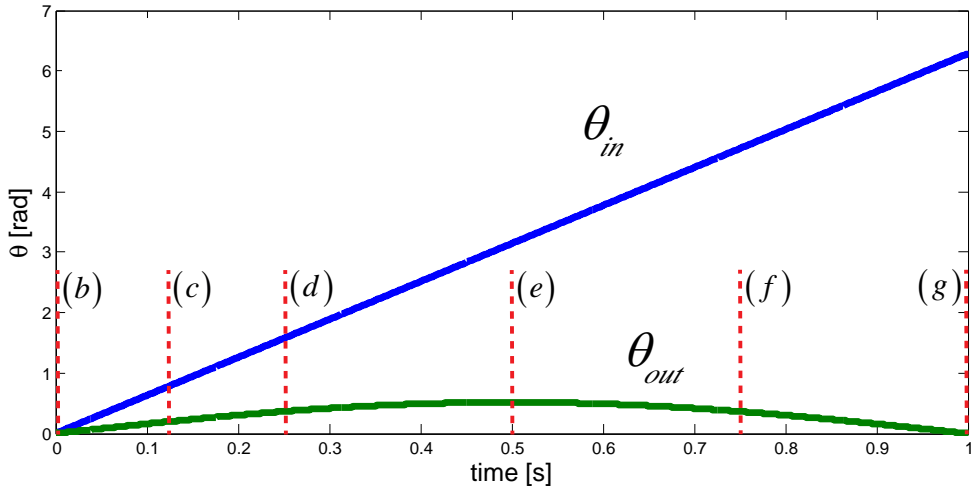
3.4.3. Three dimensional design

From Fig. 3.5b it is seen that the pitch curve of gear 3 makes a rotation of 4π rad. This is independent of the fraction of radii. If the pitch curve is designed in the two dimensional plane, the pitch curves of gear 3 and gear 4 intersect and the gear train cannot function. Therefore it is necessary to build the gears in the three dimensional space with a pitch that is equal or larger than the width of the teeth such that interference is avoided.

3.4.4. Generation of teeth profile

The teeth profiles are derived by the rack-cutter method [104]. This method generates the teeth profile by using a rack that unrolls around the pitch curve. Because the pitch curves of gear 1 and 2 have a constant radius, all teeth are equal.

The generation of the teeth on the non-circular gears differs from the circular gears. These gears have changing pitch curves and the shape of the teeth depends



(a)

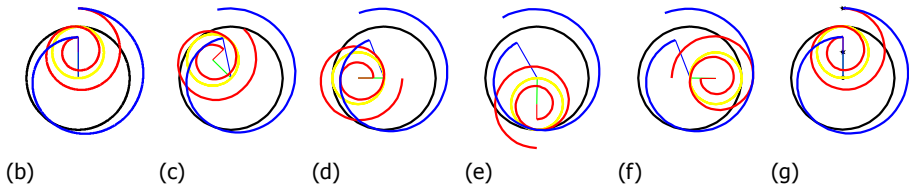


Figure 3.6: A visualization of the positions of the gears at different moments. These moments are referred to in (a): (a) the graph where the angle θ_{in} and θ_{out} are plotted, (b) the initial position where θ_{in} and θ_{out} are zero, (c), (d) other moments where both θ_{in} and θ_{out} are increasing, (e) at this moment θ_{out} is maximal, (f) a moment where θ_{in} increases and θ_{out} decreases, (g) the initial position which is equal to (a).

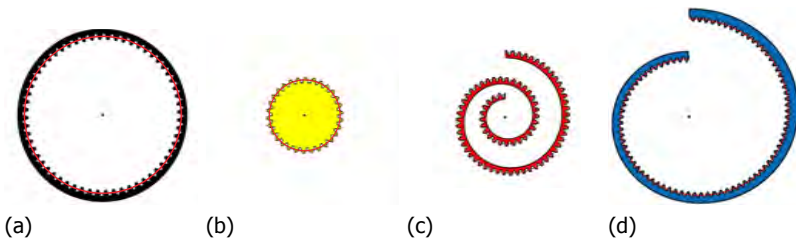


Figure 3.7: The pitch curves of the four gears with the teeth: (a) the pitch curve of gear 1 and the internal teeth, (b) the pitch curve of gear 2 and the external teeth, (c) the pitch curve of gear 3 and the external teeth, (d) the pitch curve of gear 4 and the internal teeth.

| Parameter | Symbol | Value |
|------------------------|---------|-----------|
| Number of torsion bars | n | 3 [-] |
| Shape coefficient | β | 0.333 [-] |
| Shear modulus | G | 78 [GPa] |
| Width | b | 18 [mm] |
| Thickness | t_s | 1 [mm] |
| Length | l | 200 [mm] |

Table 3.1: The parameters of the torsion bars that are required to balance a mass.

on the curvature of the pitch curve. Therefore each tooth is different [105]. In Fig. 3.7 the teeth are shown on the four pitch curves.

3.4.5. Energy storing elements

A torsion bar is chosen as the energy storage element because torsion bars have a high energy to volume ratio. The bar has only one large dimension which is the length. A rectangular torsion bar can be clamped to create a form closed connection, such that a torque can be applied without the need of additional measures to prevent slip. The stiffness is [106, 107]

$$k = \frac{n \cdot \beta \cdot G \cdot b \cdot t_s^3}{l}, \quad (3.13)$$

where n is the number of torsion bars, β is the shape coefficient, G is the Shear modulus, b , t_s and l are the width, thickness and length of the torsion bar respectively.

The parameters n , b , t_s and l are given in Table 3.1 and are chosen such that enough energy can be stored to balance the mass but the rotation of the spring is within the material yield limits.

3.5. Prototype

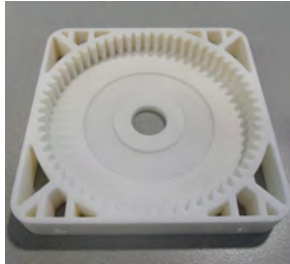
A prototype is built in order to validate the design of the gravity equilibrator. An overview of the prototype together with the main components is shown in Fig. 3.8. The design of the prototype and the evaluation of the preliminary experiments are treated.

3.5.1. Design

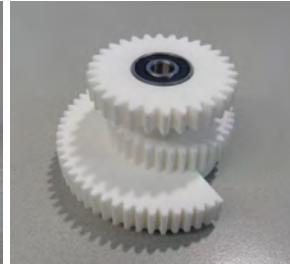
The gears are made of polyamide which is used for fully functional prototypes with high mechanical qualities and are constructed with a rapid prototyping technique called *Selective Laser Sintering (SLS)* [108]. Figure 3.8a gives the full picture of the prototype. The mass connected to the arm is visible in the foreground. On the back the torsion bars are visible. Figure 3.8b shows internal gear 1 which is rigidly connected to the ground. In Fig. 3.8c gears 2 and 3 are shown which are made up from one single part. Figure 3.8d shows gear 4 with internal toothing and which is



(a)



(b)



(c)



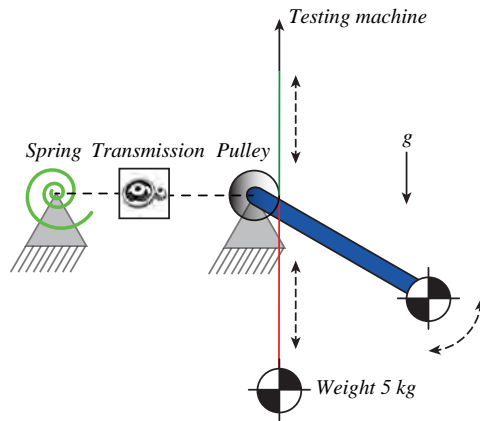
(d)



(e)

Figure 3.8: Pictures of the prototype: (a) a general overview, (b) fixed internal gear 1, (c) gear 2 and gear 3 combined, (d) output gear 4, (e) the structure that connects the multiple parts.

Figure 3.9: A schematic overview of the measurement setup. A pulley is attached to the pendulum. Two different cables are attached to this pulley. One of these cables is connected to the testing machine and one cable is connected to a counterweight of 5 kg.



connected to the torsion bars. Figure 3.8e shows the input axis and the structure that constraints gear 2 and 3 and supports gear 4.

3.5.2. Measurement results

The prototype is tested on a universal testing machine M250-2.5 CT of Testometric. The testing machine can make a vertical translation and measure the pulling force. A pulley is placed at the pivot point such that the testing machine can exert a moment on the pendulum. When the pendulum is perfectly balanced, the required moment to move the pendulum fluctuates around 0 Nm . Because the cable between the pulley and the testing machine can only be subjected to a pulling force a counterweight is added to the mechanism. This counterweight is a mass of 5 kg that is connected via a cable to the pulley which causes a constant moment on the input axis. A schematic overview is shown in Fig. 3.9.

Three consecutive measurements are performed of the total system. The input axis is rotated 4π rad counterclockwise, and 4π rad clockwise. The constant moment exerted by the counterweight is subtracted from the measurement values. The results of these measurements are shown in Fig. 3.10.

The behavior of the gear transmission is measured separately by removing the pendulum and the torsion bars. The results of these measurements are shown in Fig. 3.11. The data is smoothed in order to filter the peaks that occur due to the high measurement frequency. The green line in Fig. 3.10 represents the mean value of the moment of the unbalanced pendulum, which is used to determine the efficiency. The average required moment of the three measurements is shown in red, which is the hysteresis loop. The mean value between the upper and lower part of this hysteresis loop is plotted in black. This black line gives an estimation of the required moment if friction were absent. The assumption is made that the magnitude of the friction for the way up and way back is equal at every position.

The mechanism is analyzed by two different criteria. These criteria are a measure of the performance of the mechanism.

The first criterion is the balancing quality. This is defined by the work W_{bal}

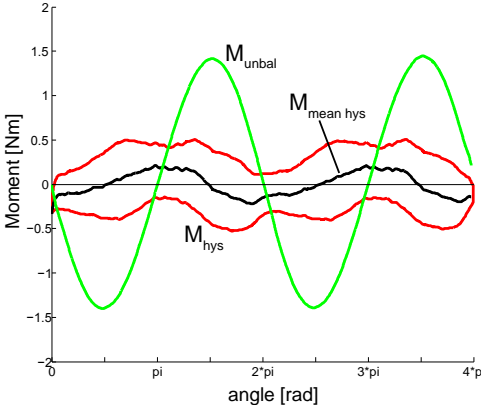


Figure 3.10: The measurement results of three consecutive measurements from 0 to 4π rad and back. The hysteresis loop is shown in red, the mean value of the hysteresis loop is shown in black. The mean value of the moment exerted by the unbalanced pendulum is shown in green.

that is required to rotate the balanced pendulum over the work W_{unbal} to rotate an unbalanced pendulum. The work is determined by taking the Riemann sum of the absolute values of the moment M_{bal} and M_{unbal} . The criterion is expressed in the efficiency η_{bal} and is determined by

$$\eta_{bal} = \left(1 - \frac{W_{bal}}{W_{unbal}}\right) \cdot 100. \quad (3.14)$$

With $W_{bal} = 1.5J$ and $W_{unbal} = 11J$, the criterion yields a value of $\eta_{bal} = 87\%$.

The second criterion is the hysteresis. A quantification of the hysteresis is given by the ratio of the peak to peak amplitude of the moment M_{hys} that is lost due to hysteresis over the peak to peak amplitude of the moment M_{unbal} that the unbalanced pendulum exerts:

$$R_{hys} = \frac{M_{hys}}{M_{unbal}} \cdot 100\%. \quad (3.15)$$

From 0 to 4π rad the peak moment to move the balanced pendulum is $0.5 Nm$. On the way back from 4π to 0 rad the peak moment is $-0.5 Nm$. The hysteresis amplitude is therefore $1.0 Nm$. The peak to peak amplitude of the moment from the unbalanced pendulum is equal to $2.8 Nm$. This yields for the second criterion a value of $R_{hys} = 36\%$.

3.6. Discussion

The hysteresis in the system is considered to be large when compared to the maximal moment that the unbalanced pendulum exerts in the pivot point. There are various sources of friction that can be pointed out. One is the accuracy of the rapid manufacturing method. Since the teeth of the gears do not perfectly mesh, a considerable resistance is created. Another source is the misalignment of the elements, partly do to the flexibility of the element that connects the gears, Fig. 3.8e. The misalignment causes a cyclic frustration resulting in high forces at the interface of the gears. In the measurements, a cyclic variation of the hysteresis can be identified. A third source of friction is present in the unintended sliding between the

Figure 3.11: The hysteresis in the gear transmission which is not loaded by the torsion bars. Only the counterweight is added to the mechanism for the measurements. The hysteresis in the unloaded system is around 0.

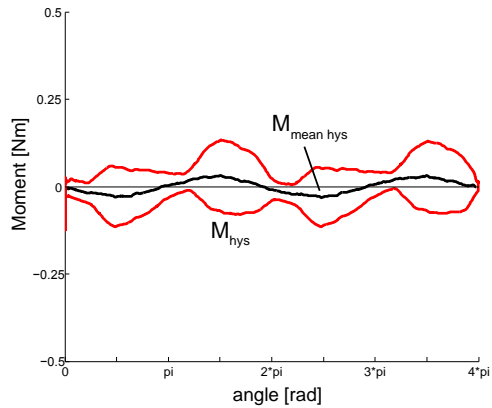
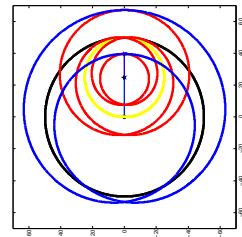


Figure 3.12: The pitch curves when the angle θ_{out} can also becomes negative. It is seen that the pitch curves of gear 3 (red) and gear 4 (blue) are now continuous but have multiple loops. This configuration of gears is impossible without having intersecting gears.



connecting element and (Fig. 3.8e) and gear 1 and 4. Wear is observed on the surface of these components.

It is expected that a detailed system redesign, using tooling steel and preciser manufacturing techniques, can reduce the hysteresis drastically.

During the dimensional design the pitch curves of the non-circular gears were obtained. The pitch curves of these gears have a discontinuity at the moment that the pendulum is at 0 rad . It was not possible to smooth this jump such that the pitch curves would be continuous again. Angle θ_{out} changes discontinuously when θ_{in} is $i \cdot 2\pi \text{ rad}$, with $i = \mathbb{Z}$. This discontinuity in θ_{out} is caused by $\sqrt{1 - \cos(\theta_{in})}$ in Eq. 3.3. θ_{out} can never become negative, but has the largest steepness at the moment that $\sqrt{1 - \cos(\theta_{in})}$ is zero.

Theoretically, θ_{out} could also be negative, because the same energy is achieved when the torsion bars are rotated in the other direction. When this is implemented, the pitch curves of gear 3 and 4 become indeed continuous, see Fig. 3.12. The problem that now occurs is that there are four loops present in gear 3 and two loops in gear 4. It becomes virtually impossible to create gears that can function without intersecting.

3.7. Conclusion

A gravity equilibrator is designed that can theoretically balance a rotating pendulum with a single degree of freedom over an unlimited range of motion using a geared transmission and torsion bars.

A general method is presented to calculate the shape of the pitch curves of the non-circular gears such that perfect balance is achieved. The shape can be adjusted by choosing different parameters for the mass, the length of the arm, and the stiffness of the torsion bars.

Different masses can be balanced by changing the active length of the torsion bars or the number of torsion bars.

Preliminary experiments with a rapid-prototyped gear set reveal a work reduction of 87% over a rotation of 4π rad when compared to an unbalanced pendulum.

The hysteresis in the mechanism is 36%, other manufacturing methods and improvements in the prototype are needed to reduce the hysteresis in the system.

II

Curved compliant mechanisms

4

Shape optimization and sensitivity of compliant beams for prescribed load-displacement response

This chapter presents the shape optimization of a compliant beam for prescribed load-displacements response. The analysis of the design is based on the isogeometric analysis framework for an enhanced fidelity between designed and analyzed shape. The sensitivities used for an improved optimization procedure are derived analytically, including terms due to the use of nonlinear state equations and nonlinear boundary constraint equations. A design example is illustrated where a beam shape is found that statically balances a pendulum over a range of 180° with good balancing quality. The analytical sensitivities are verified by comparison with finite difference sensitivities.

4.1. Introduction

Mechanism synthesis can be thought of as finding a mechanism with a certain force transmission, a certain motion transmission, or both. For conventional mechanisms the analysis and synthesis of motion and forces can be performed separately. This does not hold in general for compliant mechanisms. In compliant mechanisms, which move due to deformation of slender segments [62], every motion is associated to a restoring force. If a certain force and motion combination is desired at a part of the mechanism which is input and output at the same time, such mechanism is sometimes called a spring [4]. Not limited to the conventional coil springs, where a motion over a straight path produces a linear force characteristic, a general spring mechanism can potentially exhibit infinite types of nonlinear load-displacement responses when moved along a general trajectory, which may be non-straight. A load-displacement response, in this context, is defined as the force/moment exerted by the spring given a series of applied boundary displacements/rotations.

Applications of nonlinear springs can be found in many design disciplines including prosthetics, assistive devices, MEMS and user products. Often nonlinear springs are applied as balancing mechanisms where either an external load, e.g. a weight, or an intrinsic stiffness, e.g. in a compliant mechanism, is counteracted by such nonlinear spring [110–112]. Types of nonlinearity that are typically interesting are constant force mechanism, bi-stable or multi-stable mechanisms and negative stiffness mechanisms [113–115].

A way of obtaining nonlinear spring behavior is by optimization of the shape of a chosen topology of elements such as rods, beams, shells etc. Other means are to manipulate the topology of a system [116, 117] or the material properties.

In tailoring the load-response of structures and, more in general, when dealing with large deflections the nonlinearity of the equilibrium equations makes optimization more challenging. The optimization procedure, which is an iterative scheme, includes at every step the solution of a nonlinear set of equations, on their turn also iterative. Clear disadvantages are the complexity of the procedure and increased computation time, but also the smoothness of the optimization function space is often compromised due to e.g. singularities and bifurcations in the solution.

Eriksson [118] proposes a method where tracing the nonlinear equilibrium at every optimisation iteration is not needed. This is done by augmenting the system of equilibrium equations such that the unknowns include the displacements and design variables, including a load parameter. By keeping the load parameter constant a sequence of responses to that loading can be obtained for different designs, without computing the whole nonlinear equilibrium every time.

Similarly, in the concept of simultaneous analysis and design (SAND) [119] the analysis unknowns, e.g., the displacements, and the design variables are all treated equivalently as optimization variables. Since equilibrium is not required at every iteration step, also tracing the nonlinear equilibrium path is not needed every time. At the end of the procedure equilibrium is hopefully satisfied, and the design optimized [120].

Also in the compliant mechanisms community several approaches have been proposed to deal with geometrical nonlinearities, often present in compliant mechanisms [117, 121, 122].

In the majority of the cases the goal is to optimize the design for the situation where the full load is applied. If, however, the nonlinear load-response itself is what must be optimized, the problem gets more involved. Examples of shape and/or topology optimization where the whole load-response or part of it is optimized can be found in [53–55, 70, 123]

In this work we focus on shape optimization and, as such, a simple given topology is assumed. Topology and material optimization are not considered in this work. In the context of shape optimization of structures there is an increasing interest in the isogeometric analysis (IGA) paradigm [124]. This can be considered as an alternative to finite element analysis (FEA) with some peculiar additional advantages. There is an enhanced fidelity between designed shape and analyzed shape. This comes from the use of B-splines as basis functions for the computer aided geometric design (CAGD) as well as for the structural analysis. This preserves the original shapes and guarantees a high level of continuity between elements [125].

Having the same geometrical formulation at the basis of design and analysis also gives the advantage that there is no need to spend much effort in meshing, which is done repeatedly in an optimization procedure. Instead there are some well-performing and efficient refinement algorithms that are applied in order to work with a finer discretisation of the shape for the analysis.

A third advantage is that sensitivity properties are derivable in an analytical fashion, which supposedly can improve the efficiency of an optimization procedure [126, 127]. Also, the derivable shape sensitivities are more accurate [128], leading to preciser results.

While the work done on isogeometric shape optimization is widespread [129, 130], specific attention to nonlinear settings is scarce [128, 131]. Moreover, while typical problems where the stiffness, the weight, the volume or stresses are optimized have been analyzed extensively [127, 132, 133], there is no work known by the authors where the load-displacement of a nonlinear spring is optimized within the IGA framework.

The rotationless character of the degrees of freedom in the used isogeometric formulation gives a complication with respect to the application of rotation constraints on the beam. These constraints, imposed here by nonlinear equations on the control points by Lagrange multipliers, have a relevant impact on the derivation of the sensitivity. Together with the nonlinearity of the equilibrium equations and the unusual type of objective function, this leads to a few non-trivial problems to be dealt with in this chapter.

In previous work [134] the authors have applied isogeometric shape optimization to obtain a flexible beam with a rotational load-displacement response that matches a sine. This moment-angle characteristic can be used to balance a pendulum which has a similar but opposite moment-angle characteristic.

The current work is dedicated to the derivation of the sensitivities needed for the shape optimization of a flexible beam with prescribed load-displacement. This procedure is demonstrated on the same case study of the balanced pendulum. This case study is a comprehensible but not trivial case: it requires the stiffness to go from positive, through zero, to negative. The contribution of this chapter is to enhance the procedure by adding the sensitivity analysis. Special attention is paid to the formulation of an objective function for general load-displacement tracing cases and to the application of general boundary conditions as nonlinear constraint equations. Putting together these pieces in one work is a contribution that has not been found in literature, but is believed to be helpful for designers of nonlinear springs.

The rest of the chapter is structured as follows: After a brief introduction to the IGA framework, Section 4.2 is dedicated to the derivation of the objective function and the terms needed for the sensitivity analysis. Section 4.3 shows a comparison of two optimization runs on a given example problem with various optimization algorithms, with and without use of gradient information. Section 4.4 shows the result of a validation by comparing the analytical sensitivities with the numerically approximated sensitivities.

4.2. Method

The present section starts with the problem description of a compliant mechanism with tailored load-displacement response formulated as the minimization of the difference between a desired and an obtained energy-path. Following, a brief explanation is given of the basic concepts of isogeometric analysis (IGA), needed for this chapter. There are many literature sources about this method. The reader is referred to [124] for more information. In the remainder all components needed for the evaluation of the sensitivity of the objective function are treated.

4.2.1. Problem description and objective formulation

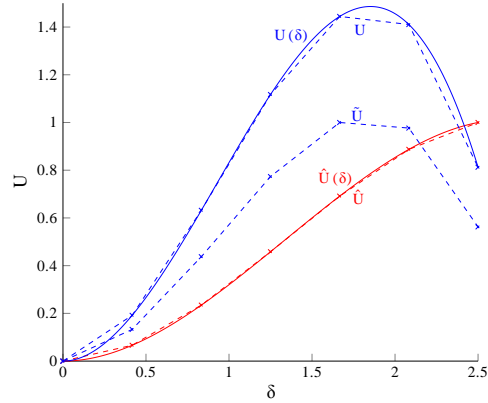
In the given context, a typical problem consists of obtaining an elastic system where a given force is provided along a given trajectory. Herein the terms force and trajectory can be used interchangeably with moments and rotations. Examples include constant force mechanisms [135], bi-stable and multi-stable mechanisms where the load-displacement response has multiple intersections with the zero-load line [113, 114], and static balancing [111] where the resulting load-displacement response neutralizes as much as possible an existing load-displacement response of the system to be balanced. In these examples obtaining a certain nonlinear load-displacement response is the goal of the design process.

Provided that the considered forces are conservative, the problem can be reformulated as obtaining a given potential energy along a given trajectory. The use of energy with respect to forces often proves to be convenient due to its scalar nature. The design challenge, here reformulated as a shape optimization problem, consists thus in finding a certain elastic system which, for a series of prescribed boundary

displacements and rotations, is compliant with a given potential energy-path.

A simple two-dimensional elastic beam is treated of which the shape is to be determined. Note that the method can in principle be extended to multiple beams and/or applied to other type of elements like shells or solids. In the example treated in Section 4.3 the beam is connected to the base hinge of a pendulum and the shape of the beam is optimized such that the moment characteristic balances the pendulum, see Fig. 4.4.

Figure 4.1: Illustration of energy-paths for objective function. $\hat{U}(\delta) \approx \hat{\mathbf{U}}$ is the target behavior, $U(\delta) \approx \mathbf{U}$ is the actual obtained behavior and $\tilde{\mathbf{U}}$ is the actual obtained behavior normalized for an amplitude-independent comparison.



In the current framework the given energy-path is described at a discrete number of steps m resulting in a vector of potential energy values, see Fig. 4.1,

$$\hat{U}(\delta) \approx \hat{\mathbf{U}} = [\hat{u}_1(\delta_1) \quad \hat{u}_2(\delta_2) \quad \dots \quad \hat{u}_m(\delta_m)], \quad (4.1)$$

where the hat ($\hat{}$) symbol refers to the target energy while the actual obtained energy-path is denoted by

$$U(\delta) \approx \mathbf{U} = [u_1(\delta_1) \quad u_2(\delta_2) \quad \dots \quad u_m(\delta_m)]. \quad (4.2)$$

In the previous equations the calligraphic \mathcal{U} denotes the potential energy of the system at a single configuration. δ is the imposed displacement value corresponding to the point of the trajectory.

In the case of load-displacement tailoring it is often useful to examine the shape of the energy-path without considering its amplitude. In a bending dominated problem the amplitude is scaled by sizing and material parameters through the Young's-modulus and cross-sectional properties, in the assumption that these parameters are constant over the length of the beam and that the Euler–Bernoulli assumptions hold (length \gg thickness). Therefore it is useful to do the optimization on the shape of the energy-path, and once the shape of the target energy-path is achieved, one can scale the amplitude by tuning the sizing and material parameters. In particular, the width of the beam can easily be adjusted to match the desired amplitude.

For this reason the target energy-path $\hat{\mathbf{U}}$ is required to be bounded between $[0, 1]$. The normalized obtained energy-path $\tilde{\mathbf{U}}$ is defined element-wise by

$$\tilde{u}_k = \frac{u_k - U_{min}}{U_{max} - U_{min}}, \quad (4.3)$$

where U_{min} and U_{max} are the minimum and maximum elements of the vector \mathbf{U} and the index $k = 1 \dots m$ represents the k th entry of the discrete energy vectors.

The proposed objective function is stated as

$$f_0 = \frac{(\tilde{\mathbf{U}} - \hat{\mathbf{U}})(\tilde{\mathbf{U}} - \hat{\mathbf{U}})^T}{\hat{\mathbf{U}}\hat{\mathbf{U}}^T}, \quad (4.4)$$

which can be interpreted as the normalized sum of squared residuals. As a consequence of the discretisation of the energy-path, the reader should be aware of the fact that the energy difference is minimized only at those discrete points. Fluctuations between the points can theoretically not be excluded. Increasing the resolution of the discretisation helps preventing this.

The given formulation of the objective function is convenient for the sensitivity analysis. Its derivative with respect to the design vector, containing the control point positions $\mathbf{x} = [P_{1x} P_{1y} \dots P_{nx} P_{ny}]^T$, can be derived as

$$\frac{df_0}{d\mathbf{x}} = 2 \frac{(\tilde{\mathbf{U}} - \hat{\mathbf{U}})}{\hat{\mathbf{U}}\hat{\mathbf{U}}^T} \frac{d\tilde{\mathbf{U}}}{d\mathbf{x}}, \quad (4.5)$$

where the derivative with respect to the normalized energy-path is

$$\begin{aligned} \frac{d\tilde{\mathbf{U}}}{d\mathbf{x}} &= \frac{(U_{max} - U_{min}) \left(\frac{d\mathbf{U}}{d\mathbf{x}} - \frac{d\mathbf{U}}{d\mathbf{x}} \Big|_{U=U_{min}} \right)}{(U_{max} - U_{min})^2} \\ &\quad - \frac{\left(\frac{d\mathbf{U}}{d\mathbf{x}} \Big|_{U=U_{max}} - \frac{d\mathbf{U}}{d\mathbf{x}} \Big|_{U=U_{min}} \right) (\mathbf{U} - U_{min})}{(U_{max} - U_{min})^2}, \end{aligned} \quad (4.6)$$

where $\frac{d\mathbf{U}}{d\mathbf{x}} \Big|_{U=U_{min}}$ and $\frac{d\mathbf{U}}{d\mathbf{x}} \Big|_{U=U_{max}}$ are the derivatives $\frac{d\mathbf{U}}{d\mathbf{x}}$ evaluated only for the minimum and maximum entries of \mathbf{U} . In the first term this vector, which would be one-dimensional, is replicated and tiled in order to match the dimensions of the vector $\frac{d\mathbf{U}}{d\mathbf{x}}$, from which it is subtracted. Also the U_{min} in the numerator of the second term is subtracted from all elements of the vector \mathbf{U} .

Since the potential energy \mathcal{U} at every configuration is a function of both design variables \mathbf{x} and the state variables (displacements) $\mathbf{u}(\mathbf{x})$,

$$\mathcal{U}(\mathbf{x}, \mathbf{u}(\mathbf{x})), \quad (4.7)$$

the total derivative of the potential energy is given by

$$\frac{d\mathcal{U}(\mathbf{x}, \mathbf{u})}{d\mathbf{x}} = \frac{\partial \mathcal{U}(\mathbf{x}, \tilde{\mathbf{u}})}{\partial \mathbf{x}} + \frac{\partial \mathcal{U}(\tilde{\mathbf{x}}, \mathbf{u})}{\partial \mathbf{u}} \frac{d\mathbf{u}}{d\mathbf{x}}. \quad (4.8)$$

The partial derivative of the energy function with respect to the displacement vector \mathbf{u} is by definition equal to the internal force vector \mathbf{F}_i , which will be used next,

but of which the derivation is omitted for the sake of conciseness. Substitution gives

$$\frac{d\mathcal{U}(\mathbf{x}, \mathbf{u})}{d\mathbf{x}} = \frac{\partial\mathcal{U}(\mathbf{x}, \tilde{\mathbf{u}})}{\partial\mathbf{x}} + \mathbf{F}_1 \frac{d\mathbf{u}}{d\mathbf{x}}. \quad (4.9)$$

The partial derivative with respect to the design vector \mathbf{x} is given in explicit form in Section 4.2.3, while the total derivatives of the displacement vector \mathbf{u} with respect to the design vector \mathbf{x} is elaborated in Section 4.2.4.

Note that Eq. (4.9) must be evaluated at every converged load step solution in order to feed $\frac{d\mathbf{u}}{d\mathbf{x}}$ as columns of the matrix $\frac{d\mathbf{U}}{d\mathbf{x}}$ in Eq. (4.6).

4.2.2. IGA introduction

Isogeometric analysis is a framework with growing popularity for a number of reasons that particularly hold for shape optimization. First, the fidelity between analyzed shape and designed shape. There is no approximation involved in the discretisation of the geometry as with meshing. Instead, a refinement of the parametric description of the geometry is performed, which increases the amount of parameters without altering the geometry itself.

Secondly, and related to the first argument, not needing a conversion step between the geometric description of the design to the analysis gives speed advantages, which are of major impact in optimization where this conversion happens many times.

Third, the availability of analytic derivative information can enhance an optimization procedure significantly.

Since a lot of literature can be found about IGA, just the needed formulas are given to understand the notation. For the notation [129] is followed. A B-spline, see Fig. 4.2, is defined as

$$\mathbf{r}(\xi) = \sum_{i=1}^n N_{i,p}(\xi) \mathbf{P}_i, \quad (4.10)$$

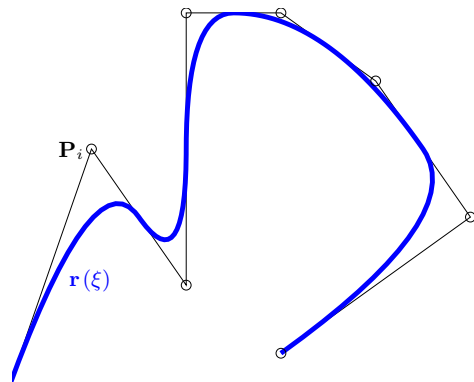


Figure 4.2: B-spline curve and control polygon.

where $\mathbf{P}_i \in \mathbb{R}^d$ is a control point, n is the number of control points and where the p th degree basis functions are constructed recursively starting with piecewise constants

$$N_{i,0}(\xi) = \begin{cases} 1 & \text{if } \xi_i \leq \xi < \xi_{i+1}, \\ 0 & \text{otherwise} \end{cases},$$

and for $p = 1, 2, 3, \dots$, they are defined by

$$N_{i,p}(\xi) = \frac{\xi - \xi_i}{\xi_{i+p} - \xi_i} N_{i,p-1}(\xi) + \frac{\xi_{i+p+1} - \xi}{\xi_{i+p+1} - \xi_{i+1}} N_{i+1,p-1}(\xi). \quad (4.11)$$

In the present work a geometrically nonlinear Euler–Bernoulli beam is used. The potential energy of the beam can be written as

$$\mathcal{U} = \frac{1}{2} \int (EA\epsilon^2 + EI\rho^2) dS, \quad (4.12)$$

where the integral is evaluated numerically following a Gaussian quadrature rule using

$$\mathcal{U} \approx \mathcal{U} = \frac{1}{2} \sum_{j=1}^{n+p} \sum_{k=1}^{n_{int}} (EA\epsilon_k^2 + EI\rho_k^2) J_k \bar{J}_j \bar{w}_k, \quad (4.13)$$

where E , A and I represent the Young's modulus, the cross-sectional area and the second moment of inertia, respectively, and are assumed constant over the length of the beam. Moreover J is the reference rod Jacobian, \bar{J} and \bar{w} are the Jacobian and the weight associated with the numerical integration, $n+p$ is the number of knot spans and n_{int} is the number of integration points per knot span.

The relative strain measures, i.e. the membrane strain ϵ and the bending strain ρ are given as defined in [136]

$$\epsilon = \frac{1}{2} \left(\left(\frac{ds}{dS} \right)^2 - 1 \right), \quad (4.14)$$

$$\rho = (\kappa - K) \frac{ds}{dS}. \quad (4.15)$$

The differential arch length and curvature of the line of centroids of the beam are denoted by the kinematic variables dS , ds , K and κ , where the capital symbols refer to the reference state $\mathbf{R}(S)$ and the minuscule symbols refer to the current state $\mathbf{r}(S)$. The definitions are

$$dS(\xi) = |\mathbf{r}^{(1)}| d\xi, \quad (4.16)$$

$$\kappa(\xi) = \frac{[\mathbf{r}^{(1)} \times \mathbf{r}^{(2)}]_3}{|\mathbf{r}^{(1)}|^3}, \quad (4.17)$$

where the subscript 3 refers to the third component of the vector in brackets and the superscript in parenthesis denote successive differentiation w.r.t. ξ , the variable of parametrization. The definition of dS and K is similar to Eq. (4.16) and (4.17), only replacing the curve of the current configuration $\mathbf{r}(S)$ by the one of the reference configuration $\mathbf{R}(S)$.

It is customary to define the geometry of a system by a relatively small set of control points which are used as optimization variables ($\mathbf{X} = \mathbf{P}^{design}$). A refinement step, preserving the exact shape of the curve itself, yields a larger amount of control points ($\mathbf{x} = \mathbf{P}^{analysis}$) that are used for the numerical analysis.

The discrete structural arrays, i.e. tangent stiffness matrix \mathbf{K}_t and the internal force vector \mathbf{F}_i , are derived from the energy functional of Eq. (4.12). The displacement of the control points of the analysis (\mathbf{x}) are the unknowns of the equilibrium equations indicated by the vector of state variables \mathbf{u} .

4.2.3. Energy derivative

Often in structural optimization the stored elastic energy, assumed equivalent to the structural compliance, is simply evaluated as $c = \frac{1}{2} \mathbf{F}_e^T \mathbf{u}$. While this is correct for a linear analysis, namely it represents the area under the force-displacement curve, this is not valid in general for nonlinear cases. Therefore we must go back to the definition of the strain energy given in Eq. (4.12) and its numerical approximation given in Eq. (4.13). The partial derivative of Eq. (4.13) with respect to the vector \mathbf{x} , where \mathbf{u} is kept constant, is given by

$$\begin{aligned} \frac{\partial U}{\partial \mathbf{x}} &= \frac{1}{2} \sum_{j=1}^{n+p} \sum_{k=1}^{n_{int}} \left((EA\epsilon_k^2 + EI\rho_k^2) \frac{\partial J_k}{\partial \mathbf{x}} \right. \\ &\quad \left. + \left(EA \frac{\partial (\epsilon_k^2)}{\partial \mathbf{x}} + EI \frac{\partial (\rho_k^2)}{\partial \mathbf{x}} \right) J_k \right) \overline{J_j w_k}. \end{aligned} \quad (4.18)$$

The partial derivatives of the squared strain measures read

$$\frac{\partial (\epsilon^2)}{\partial \mathbf{x}} = 2\epsilon \frac{\partial \epsilon}{\partial \mathbf{x}} = 2\epsilon \left[\frac{ds}{dS} \left(\frac{\partial ds}{\partial \mathbf{x}} dS - \frac{\partial dS}{\partial \mathbf{x}} ds \right) \right], \quad (4.19)$$

and

$$\frac{\partial (\rho^2)}{\partial \mathbf{x}} = 2\rho \frac{\partial \rho}{\partial \mathbf{x}} = 2\rho \left[\left(\frac{\partial \kappa}{\partial \mathbf{x}} - \frac{\partial K}{\partial \mathbf{x}} \right) \frac{ds}{dS} + (\kappa - K) \frac{\frac{\partial ds}{\partial \mathbf{x}}}{\frac{\partial dS}{\partial \mathbf{x}}} \right], \quad (4.20)$$

where

$$\frac{\partial ds}{\partial \mathbf{x}} = \frac{\mathbf{r}^{(1)} R_{i,p}^{(1)}}{|\mathbf{r}^{(1)}|} d\xi, \quad (4.21)$$

and

$$\frac{\partial \kappa}{\partial \mathbf{x}} = \frac{\frac{\partial}{\partial \mathbf{x}} \left([\mathbf{r}^{(1)} \times \mathbf{r}^{(2)}]_3 \right) \|\mathbf{r}^{(1)}\|^3 - [\mathbf{r}^{(1)} \times \mathbf{r}^{(2)}]_3 \frac{\partial}{\partial \mathbf{x}} (\|\mathbf{r}^{(1)}\|^3)}{\|\mathbf{r}^{(1)}\|^6}. \quad (4.22)$$

Similar equations hold for $\frac{\partial dS}{\partial \mathbf{x}}$ and $\frac{\partial K}{\partial \mathbf{x}}$, where again the reference curve is used instead of the current curve. Furthermore

$$\begin{aligned} \frac{\partial}{\partial \mathbf{x}} \left([\mathbf{r}^{(1)} \times \mathbf{r}^{(2)}]_3 \right) &= R_{i,p}^{(1)} (r_2^{(2)} - r_1^{(2)}) \\ &+ (r_1^{(1)} - r_2^{(1)}) R_{i,p}^{(2)}. \end{aligned} \quad (4.23)$$

The derivatives of the curves $\mathbf{r}^{(1)}$, $\mathbf{r}^{(2)}$ and their algorithmic implementations are readily available from e.g. [137].

4.2.4. State sensitivity

The more tedious parts of the derivation are not the partial derivatives but the total derivative of the state vector. Usually there is not an explicit relation between \mathbf{x} and \mathbf{u} , and thus the derivative cannot be found analytically. There are two common methods to compute them numerically. One is the direct method and the other one is the adjoint method. The direct method is used because of its simpler implementation and derivation. There is however no objection in using the adjoint method instead.

There are two aspects in the described situation that make the implementation not trivial. These two aspects have not been found combined in literature. The first aspect is that the set of equilibrium equations is nonlinear and thus requires an iterative, newton-like, procedure to solve it. The second aspect is the application of nonlinear constraint equations as Lagrange multipliers, which creates an augmented system of equations. Both aspects together lead to the following derivations. The formulation of the constraint equations in the present work will be illustrated in Section 4.2.5.

The equilibrium conditions to be solved can be formulated in terms of the tangent stiffness matrix \mathbf{K}_t , the internal and external force vectors \mathbf{F}_i and \mathbf{F}_e

$$\mathbf{K}_t(\mathbf{x}, \mathbf{u}) \Delta \mathbf{u} = \mathbf{F}_e(\mathbf{x}, \mathbf{u}) - \mathbf{F}_i(\mathbf{x}, \mathbf{u}), \quad (4.24)$$

which is solved for an increment of the displacement vector $\Delta \mathbf{u}$. While this is a good practice for the solution of the system itself, for the current derivation of the sensitivities it is more convenient to use the alternative formulation in terms of the secant stiffness matrix, where the internal force vector drops out

$$\mathbf{K}_s(\mathbf{x}, \mathbf{u}) \mathbf{u} - \mathbf{F}_e(\mathbf{x}, \mathbf{u}) = \mathbf{0}. \quad (4.25)$$

Contrary to the former formulation, here the total displacement vector \mathbf{u} is used. This is convenient because the constraint equations will be formulated in terms of the total displacements as well. The general set of constraint equations are noted as

$$\mathcal{F}_2 = \mathbf{A}(\mathbf{x}, \mathbf{u}) \mathbf{u} - \mathbf{b}(\mathbf{x}, \mathbf{u}) = \mathbf{0}, \quad (4.26)$$

and adding the constraints as Lagrange multiplier terms to the system in Eq. (4.25), see [118] for a concise explanation, gives

$$\mathcal{F}_1 = \mathbf{K}_s(\mathbf{x}, \mathbf{u})\mathbf{u} + \mathbf{A}(\mathbf{x}, \mathbf{u})^T \lambda - \mathbf{F}_e(\mathbf{x}, \mathbf{u}) = \mathbf{0}. \quad (4.27)$$

The set of equations in \mathcal{F}_1 and \mathcal{F}_2 collected into the so called augmented form

$$\begin{bmatrix} \mathbf{K}_s(\mathbf{x}, \mathbf{u}) & \mathbf{A}(\mathbf{x}, \mathbf{u})^T \\ \mathbf{A}(\mathbf{x}, \mathbf{u}) & \mathbf{0} \end{bmatrix} \begin{pmatrix} \mathbf{u} \\ \lambda \end{pmatrix} = \begin{pmatrix} \mathbf{F}_e(\mathbf{x}, \mathbf{u}) \\ \mathbf{b}(\mathbf{x}, \mathbf{u}) \end{pmatrix} \quad (4.28)$$

is normally solved simultaneously for both \mathbf{u} and the Lagrange multipliers λ which, pre-multiplied by the \mathbf{A} matrix, can be interpreted as the forces needed to impose the conditions.

Taking the total derivative of both vector equations \mathcal{F}_1 and \mathcal{F}_2 , applying the product rule and the chain rule and collecting $\frac{d\mathbf{u}}{d\mathbf{x}}$ and $\frac{d\lambda}{d\mathbf{x}}$ gives

$$\begin{aligned} \frac{d\mathcal{F}_1}{d\mathbf{x}} &= \left(\mathbf{K}_s(\mathbf{x}, \mathbf{u}) + \frac{\partial [\mathbf{K}_s(\mathbf{x}, \mathbf{u})\tilde{\mathbf{u}}]}{\mathbf{u}} - \frac{\partial \mathbf{F}_e(\mathbf{x}, \mathbf{u})}{\partial \mathbf{u}} \right) \frac{d\mathbf{u}}{d\mathbf{x}} \\ &+ \mathbf{A}(\mathbf{x}, \mathbf{u})^T \frac{d\lambda}{d\mathbf{x}} + \frac{[d\mathbf{K}_s(\mathbf{x}, \tilde{\mathbf{u}})\tilde{\mathbf{u}}]}{d\mathbf{x}} \\ &+ \frac{[d\mathbf{A}(\mathbf{x}, \mathbf{u})^T \tilde{\lambda}]}{d\mathbf{x}} - \frac{\partial \mathbf{F}_e(\mathbf{x}, \tilde{\mathbf{u}})}{\partial \mathbf{x}} = \mathbf{0}, \end{aligned} \quad (4.29)$$

and

$$\frac{d\mathcal{F}_2}{d\mathbf{x}} = \mathbf{A}(\mathbf{x}, \mathbf{u}) \frac{d\mathbf{u}}{d\mathbf{x}} + \frac{d[\mathbf{A}(\mathbf{x}, \mathbf{u})\tilde{\mathbf{u}}]}{d\mathbf{x}} - \frac{d\mathbf{b}(\mathbf{x}, \mathbf{u})}{d\mathbf{x}} = \mathbf{0}. \quad (4.30)$$

Here and in the following the tilde ($\tilde{\cdot}$) means that the variable is held constant during differentiation. Notice that for the terms containing $\mathbf{A}(\mathbf{x}, \mathbf{u})$ and $\mathbf{b}(\mathbf{x}, \mathbf{u})$ in the present work the total derivative is directly available as will be shown in Section 4.2.5, and thus the chain rule is not being applied to those terms. The following relations between secant and tangent stiffness matrices and between the secant matrix and the internal force vector are given in [138]

$$\mathbf{K}_t(\mathbf{x}, \mathbf{u}) = \mathbf{K}_s(\mathbf{x}, \mathbf{u}) + \frac{\partial [\mathbf{K}_s(\mathbf{x}, \mathbf{u})\tilde{\mathbf{u}}]}{\partial \mathbf{u}} \quad (4.31)$$

$$\frac{\partial [\mathbf{K}_s(\mathbf{x}, \tilde{\mathbf{u}})\tilde{\mathbf{u}}]}{\partial \mathbf{x}} = \frac{\partial \mathbf{F}_i(\mathbf{x}, \tilde{\mathbf{u}})}{\partial \mathbf{x}}. \quad (4.32)$$

Substituting Eq. (4.31) and (4.32) into Eq. (4.29) and (4.30) and rearranging them into matrix form gives

$$\begin{aligned} &\begin{bmatrix} \mathbf{K}_t - \frac{\partial \mathbf{F}_e(\mathbf{x}, \mathbf{u})}{\partial \mathbf{u}}(\mathbf{x}, \mathbf{u}) & \mathbf{A}(\mathbf{x}, \mathbf{u})^T \\ \mathbf{A}(\mathbf{x}, \mathbf{u}) & \mathbf{0} \end{bmatrix} \begin{pmatrix} \frac{d\mathbf{u}}{d\mathbf{x}} \\ \frac{d\lambda}{d\mathbf{x}} \end{pmatrix} = \\ &\begin{pmatrix} \frac{\partial \mathbf{F}_e(\mathbf{x}, \tilde{\mathbf{u}})}{\partial \mathbf{x}} - \frac{\partial \mathbf{F}_i(\mathbf{x}, \tilde{\mathbf{u}})}{\partial \mathbf{x}} - \frac{d[\mathbf{A}(\mathbf{x}, \mathbf{u})^T \tilde{\lambda}]}{d\mathbf{x}} \\ \frac{d\mathbf{b}(\mathbf{x}, \mathbf{u})}{d\mathbf{x}} - \frac{d[\mathbf{A}(\mathbf{x}, \mathbf{u})\tilde{\mathbf{u}}]}{d\mathbf{x}} \end{pmatrix}, \end{aligned} \quad (4.33)$$

which can be solved for $\frac{d\mathbf{u}}{d\mathbf{x}}$. Consider that in the case that the external forces are not depending on the displacements, e.g. no follower forces or pressure, the coefficient matrix on the left hand side is equal to the coefficient matrix used for the analysis steps, and is therefore already available in inverted form. This can save considerable computation time. The used constraint equations and its derivative terms are elaborated in Section 4.2.5.

4.2.5. Boundary constraint equations and derivatives

Constraint equations

In the current setting the system is loaded by applying displacements typically at the endpoints of the beam. Thereby the forces appear as reaction forces of the applied constraints instead of external forces. Once the displacement is applied, equilibrium can be found and the energy is derived. Displacements in this case can also mean rotations. In a typical example one would clamp one end of the beam, i.e. both translations and rotations zero, and apply a given motion on the other end, e.g. travelling along a curved line, or applying a rotation at a fixed point.

There is a complication that arises from the use of the isogeometric analysis method. From the rotation-less character of the control points, it follows that rotations cannot be directly applied. Instead, as described earlier in [134], a set of nonlinear constraints is applied that dictates the position of the second control point with respect to the first one. It is a given notion that the line connecting the first and the second control point is tangent to the beginning of the curve and, similarly, the line connecting the second-last to the last control point is tangent to the end of the curve. In the following only the beginning of the curve is considered, omitting the end of the curve. All the equations are similarly derivable replacing the subscripts 1 and 2 by $n-1$ and n .

In general there are two types of constraints that are applied to the beam. The first is a linear set $\mathbf{A}_l \mathbf{u} = \mathbf{b}_l$ prescribing the displacement on the endpoints as

$$\begin{bmatrix} 1 & 0 & 0 & 0 & \dots \\ 0 & 1 & 0 & 0 & \dots \end{bmatrix} \begin{pmatrix} u_{1x} \\ u_{1y} \\ \vdots \end{pmatrix} = \begin{pmatrix} b_{1x} \\ b_{1y} \end{pmatrix}, \quad (4.34)$$

where b_{1x} and b_{1y} are the applied x and y displacements. There are cases where the applied displacement is made dependent on the design vector \mathbf{x} . For instance in the design example given in Section 4.3, where the endpoint of the beam is prestressed by positioning the endpoint at the origin of the coordinate system. Here $b_{n_x} = -P_{n_x}$ and $b_{n_y} = -P_{n_y}$, and thus $\mathbf{b}_l = \mathbf{b}_l(\mathbf{x})$.

The second type of constraints concerns the rotations and is somewhat more involved. The inclination h of the tangent line at the beginning of the curve is defined as

$$h(\mathbf{x}, \mathbf{u}) = \tan(\theta_0(\mathbf{x}) + \Delta\theta(\mathbf{x}, \mathbf{u})), \quad (4.35)$$

where $\Delta\theta$ is the difference of the current angle θ_k from the an initial angle θ_0 . The initial angle depends on the design vector \mathbf{x} and the current angle θ_k on both the

design vector \mathbf{x} and the displacements vector \mathbf{u} . Therefore the inclination h is nonlinear in both \mathbf{x} and \mathbf{u} . The inclination h must equal the inclination of the line crossing the first two control points

$$h = \frac{(P_{2y} + u_{2y}) - (P_{1y} + u_{1y})}{(P_{2x} + u_{2x}) - (P_{1x} + u_{1x})}. \quad (4.36)$$

Rewriting and separating the displacements terms gives the nonlinear set of constraints $\mathbf{A}_{nl}(\mathbf{x}, \mathbf{u}) \mathbf{u} = \mathbf{b}_{nl}(\mathbf{x}, \mathbf{u})$ as

$$\begin{aligned} & \left[-h(\mathbf{x}, \mathbf{u}) \quad 1 \quad h(\mathbf{x}, \mathbf{u}) \quad -1 \quad \dots \right] \begin{pmatrix} u_{1x} \\ u_{1y} \\ u_{2x} \\ u_{2y} \\ \vdots \end{pmatrix} \\ & = \left[h(\mathbf{x}, \mathbf{u})P_{1x} - P_{1y} - h(\mathbf{x}, \mathbf{u})P_{2x} + P_{2y} \right]. \end{aligned} \quad (4.37)$$

The matrices \mathbf{A}_l and \mathbf{A}_{nl} and the vectors \mathbf{b}_l and \mathbf{b}_{nl} can be simply concatenated vertically to form a set of equations $\mathbf{A}\mathbf{u} = \mathbf{b}$ to be added to the system as Lagrange constraints, as described in Section 4.2.4.

Derivatives of constraint equations

The derivatives of the constraint equations, needed in Eq. (4.33), will be derived next.

For the linear part of the constraints only the case where \mathbf{b}_l is a function of \mathbf{x} , i.e. $\mathbf{b}_l = \mathbf{b}_l(\mathbf{x})$, is mentioned. This is the case when e.g. a prestress proportional to a design parameter is applied to the system. Typically, if \mathbf{b}_l is linear in \mathbf{x} , the total derivative $\frac{d\mathbf{b}_l(\mathbf{x})}{d\mathbf{x}}$ is a vector of constants.

The derivations for the nonlinear part of the constraints requires more attention. The following holds

$$\begin{aligned} \frac{d\mathbf{b}_{nl}(\mathbf{x}, \mathbf{u})}{d\mathbf{x}} \frac{dh}{d\mathbf{x}} &= \left((P_{1x} - P_{2x}) + h \left(\frac{dP_{1x}}{d\mathbf{x}} - \frac{dP_{2x}}{d\mathbf{x}} \right) \right. \\ & \left. = -\frac{dP_{1y}}{d\mathbf{x}} + \frac{dP_{2y}}{d\mathbf{x}} \right), \end{aligned} \quad (4.38)$$

$$\frac{d[\mathbf{A}_{nl}(\mathbf{x}, \mathbf{u})\tilde{\mathbf{u}}]}{d\mathbf{x}} = \left(\frac{dh}{d\mathbf{x}} (u_{2x} - u_{1x}) \right) \quad (4.39)$$

and

$$\frac{d[\mathbf{A}_{nl}(\mathbf{x}, \mathbf{u})^T \tilde{\boldsymbol{\lambda}}]}{d\mathbf{x}} = \begin{pmatrix} -\frac{dh}{d\mathbf{x}} \lambda \\ \cdot \\ \frac{dh}{d\mathbf{x}} \lambda \\ \cdot \\ \vdots \end{pmatrix}. \quad (4.40)$$

In these equations the derivative of h is calculated as

$$\begin{aligned} \frac{dh}{d\mathbf{x}} &= \frac{d}{d\mathbf{x}} (\tan(\theta_0 + \Delta\theta)) = \frac{d}{d\mathbf{x}} \left(\frac{h_0 + T_{\Delta\theta}}{1 - h_0 T_{\Delta\theta}} \right) = \\ &= \frac{\left(\frac{dh_0}{d\mathbf{x}} + \frac{dT_{\Delta\theta}}{d\mathbf{x}} \right) (1 - h_0 T_{\Delta\theta}) + (h_0 + T_{\Delta\theta}) \left(\frac{dh_0}{d\mathbf{x}} T_{\Delta\theta} + h_0 \frac{dT_{\Delta\theta}}{d\mathbf{x}} \right)}{(1 - h_0 T_{\Delta\theta})^2}, \end{aligned} \quad (4.41)$$

where $T_{\Delta\theta}$ is a shorthand notation for $\tan(\Delta\theta)$, h_0 is the initial inclination and their derivatives are given respectively by

$$\frac{dT_{\Delta\theta}}{d\mathbf{x}} = \sec(\Delta\theta) \frac{d\Delta\theta}{d\mathbf{x}}, \quad (4.42)$$

and

$$\frac{dh_0}{d\mathbf{x}} = \frac{d}{d\mathbf{x}} \left(\frac{P_{2y} - P_{1y}}{P_{2x} - P_{1x}} \right). \quad (4.43)$$

Now $\Delta\theta$, which is the difference between the current angle θ_k and the initial angle θ_0 , is split up in the angle of the converged solution of the last iterative step θ_{k-1} , the angle that is imposed in the current iteration θ_{step} , which is known and fixed, minus the reference angle θ_0 . This is a precaution measure. In fact, in the case that a rotation is applied from rest, $\Delta\theta$ is known and fixed. But in the case that the loading history is not fully known, e.g. a prestress is applied, than $\Delta\theta$ could contain a certain unknown rotation induced by a previous step. In order to avoid this type of error we define

$$\frac{d\Delta\theta}{d\mathbf{x}} = \frac{d}{d\mathbf{x}} (\theta_{k-1} + \theta_{step} - \theta_0) = \frac{d\theta_{k-1}}{d\mathbf{x}} - \frac{d\theta_0}{d\mathbf{x}}, \quad (4.44)$$

where

$$\frac{d\theta_0}{d\mathbf{x}} = \frac{d}{d\mathbf{x}} (\tan^{-1}(h_0)) = \frac{1}{1 + (h_0)^2} \frac{dh_0}{d\mathbf{x}} \quad (4.45)$$

is fairly simple to find, and where the following term is used which has been calculated at the end of the previous converged solution step, where the derivative of the state vector was already solved:

$$\frac{d\theta_{k-1}}{d\mathbf{x}} = \frac{\partial\theta_{k-1}}{\partial\mathbf{x}} + \frac{\partial\theta_{k-1}}{\partial\mathbf{u}} \frac{d\mathbf{u}}{d\mathbf{x}}. \quad (4.46)$$

The partial derivatives that are needed are

$$\frac{\partial\theta_{k-1}}{\partial\mathbf{x}} = \frac{\partial}{\partial\mathbf{x}} (\tan^{-1}(h_{k-1})) = \frac{1}{1 + (h_{k-1})^2} \frac{\partial h_{k-1}}{\partial\mathbf{x}} \quad (4.47)$$

and

$$\frac{\partial\theta_{k-1}}{\partial\mathbf{u}} = \frac{\partial}{\partial\mathbf{u}} (\tan^{-1}(h_{k-1})) = \frac{1}{1 + (h_{k-1})^2} \frac{\partial h_{k-1}}{\partial\mathbf{u}} \quad (4.48)$$

which turn out to be the same since

$$\frac{\partial h_{k-1}}{\partial \mathbf{x}} = \frac{\partial h_{k-1}}{\partial \mathbf{u}} = \begin{bmatrix} \frac{(P_{2y}+u_{2y})-(P_{1y}+u_{1y})}{((P_{2x}+u_{2x})-(P_{1x}+u_{1x}))^2} \\ -\frac{(P_{2x}+u_{2x})-(P_{1x}+u_{1x})}{((P_{2y}+u_{2y})-(P_{1y}+u_{1y}))^2} \\ \vdots \\ \frac{(P_{2x}+u_{2x})-(P_{1x}+u_{1x})}{((P_{2y}+u_{2y})-(P_{1y}+u_{1y}))^2} \end{bmatrix}^T. \quad (4.49)$$

At this point Eq. (4.38)–(4.40) are fully defined and can be used to find $\frac{d\mathbf{u}}{d\mathbf{x}}$ in Eq. (4.33).

4.2.6. Refinement term

In geometric design optimization it is a common use to define a geometry at a level with relatively few parameters which is refined to a more dense level at which the analysis is performed. Commonly this is done by meshing, while in isogeometric analysis there are so called refinement techniques, where the same spline curve is refined to a spline with more control points and/or higher order basis functions, but maintaining the exact original shape. It is not worth going much into detail here, given the amount and quality of literature on this topic, e.g. [124, 137].

The Jacobian of \mathbf{x} , the refined design vector, with respect to \mathbf{X} , the global design vector, is needed for the sensitivity of the objective with respect to the global design vector.

$$\frac{df_0}{d\mathbf{X}} = \frac{df_0}{d\mathbf{x}} \frac{d\mathbf{x}}{d\mathbf{X}} \quad (4.50)$$

The derivation of term $\frac{d\mathbf{x}}{d\mathbf{X}}$ is not within the scope of this work, but can be found e.g. in [139].

4.2.7. Variable transform

As a last (optional) step a transformation of variables on the global design vector \mathbf{X} to a generalized design vector \mathbf{q} has been adopted. The latter is a vector containing lengths l and relative angles θ of the lines connecting the control points B of the global design as if it were a linkage chain, see Fig. 4.3. This way it becomes easy, by imposing boundaries on the search space of the optimization, to avoid loops in the curve and avoid consecutive control points lying too close to each other. The first is done by bounding the angles avoiding too sharp corners in the control polygon, and the second is realized by limiting the minimum lengths of the links. In general this avoids awkward shapes that are undesired. The transformation is defined as

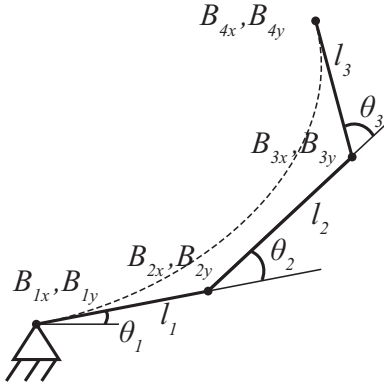


Figure 4.3: Transformation of coordinates of the control points in a set of generalized coordinates, described by the lengths and angles of the links of a linkage chain representing the control polygon.

$$\mathbf{x} = \begin{bmatrix} B_{1x} \\ B_{1y} \\ B_{2x} \\ B_{2y} \\ B_{3x} \\ B_{3y} \\ B_{4x} \\ B_{4y} \end{bmatrix} = \begin{bmatrix} q_1 \\ q_2 \\ q_1 + q_3 c(q_4) \\ q_2 + q_3 s(q_4) \\ q_1 + q_3 c(q_4) + q_5 c(q_4 + q_6) \\ q_2 + q_3 s(q_4) + q_5 s(q_4 + q_6) \\ q_1 + \dots + q_7 c(q_4 + q_6 + q_8) \\ q_2 + \dots + q_7 s(q_4 + q_6 + q_8) \end{bmatrix}, \quad (4.51)$$

where c and s are the shorthand notations for \cos and \sin , and \mathbf{q} defined as

$$\mathbf{q} = [B_{1x} \ B_{1y} \ l_1 \ \theta_1 \ l_2 \ \theta_2 \ l_3 \ \theta_3]. \quad (4.52)$$

Note that in a design with more control points \mathbf{q} can be longer than shown, in that case the expression would expand in a similar fashion. For the sensitivity of the objective with respect to the generalized variables $\frac{d\mathbf{x}}{d\mathbf{q}}$ is needed because

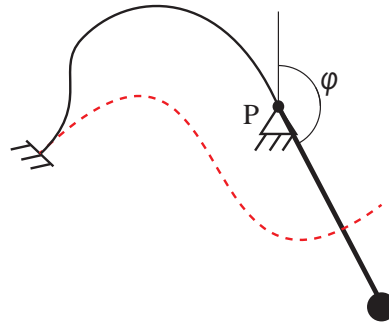
$$\frac{df_0}{d\mathbf{q}} = \frac{df_0}{d\mathbf{x}} \frac{d\mathbf{x}}{d\mathbf{q}}. \quad (4.53)$$

The full expression of $\frac{d\mathbf{x}}{d\mathbf{q}}$ is omitted for the sake of conciseness. Its derivation can however be considered straightforward. At this point all expressions for the sensitivity analysis are derived.

4.3. Design example

To assess the usefulness of the gradients in the given design problem several optimization runs are compared where one gradient-free algorithm and four gradient-based algorithms are used. The first type only needs Eq. (4.4) as an input, while the last four also use Eq. (4.53). The algorithms implemented in the *optimization toolbox* in Matlab[®] are used: Nelder–Mead Simplex (NMS), Trust-Region-Reflective (TRR), Interior-Point (IP), Active-Set (AS) and Sequential Quadratic Programming (SQP). See the [140] documentation for details on the algorithms.

Figure 4.4: Topology of the system: A leaf spring (red dashed) is prestressed (black) by connecting one endpoint with a rigid pendulum, while the other end of the spring is clamped.



Because of the high dependency with the starting point of the optimization, the runs are all performed starting at two different initial points, chosen such that the resulting behavior would be clearly distinct.

The case study is similar to the one found in [134]. The goal is to design a leaf spring able to statically balance a pendulum in the range from 0 to 180°, see Fig. 4.4. The objective is to make the reaction moment on the end of the beam follow a sinus-shaped characteristic with respect to the rotation of that point. Equivalently, knowing that the derivative of the energy with respect to the rotation equals the moment, the target energy-path $\hat{U}(\delta)$ is defined as a negative cosine function bounded in amplitude between 0 and 1, as prescribed for Eq. (4.3). Thus

$$\hat{U}(\varphi) = \frac{(1 - \cos(\varphi))}{2}, \quad (4.54)$$

where φ is the rotation of the endpoint P . Before this actual working range a prestress step is applied where one endpoint stays clamped, and the other end is brought to the origin of the coordinate system leaving the rotation free. This guarantees that the moment before the first actual step is zero, corresponding to the needed moment when the pendulum is upright.

Some details on relevant design choices are: cross-sectional width and height are 0.01 and 0.002 m, Young's modulus is 135 GPa. The design curve is a second order B-spline with four control points and uniform knot vector. The curve is refined for analysis with 20 additional knot evenly spread over the knot vector. The used bounds on the variables of optimizations: $q_1, q_2 : [-0.3, 0.3]$, $q_3, q_5, q_7 : [.1, 0.4]$ and $q_4, q_6, q_8 : [-2, 2]$.

Figure 4.5a and b show the progress of the objective function plotted against the iteration steps for the two initial points

$$\mathbf{q}_0 = [-0.2 \quad -0.2 \quad 0.2 \quad 1.5 \quad 0.2 \quad -1.5 \quad 0.2 \quad -1.5] \quad (4.55)$$

and

$$\mathbf{q}_0 = [-0.2 \quad -0.2 \quad 0.2 \quad 1.5 \quad 0.2 \quad -1.5 \quad 0.2 \quad 1.5]. \quad (4.56)$$

The corresponding initial shapes and the energy-paths are shown in Figs. 4.6a–4.9a. The shapes and energy-paths after optimization (the best result obtained)

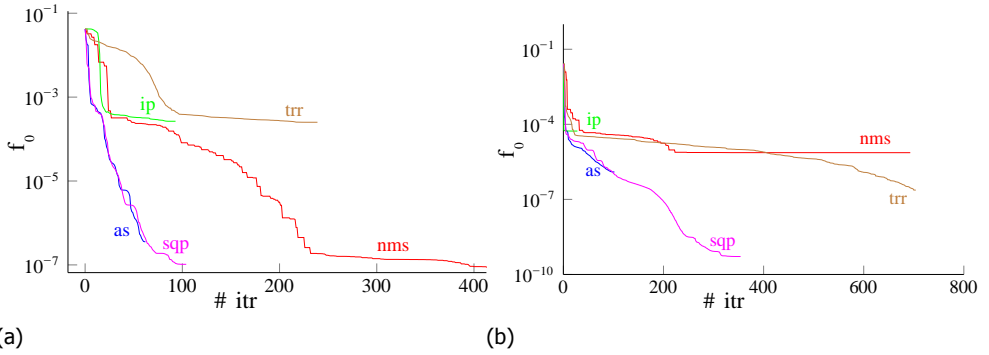


Figure 4.5: Objective function value vs iteration number for the algorithms Nelder-Mead Simplex (NMS), Trust-Region-Reflective (TRR), Interior-Point (IP), Active-Set (AS) and Sequential Quadratic Programming (SQP). (a) Example 1 and (b) Example 2.

are shown in Figs. 4.6b–4.9b. The thick red lines in the shape plots is the unloaded shape of the beam, while the thin blue lines represent the deformed states at the 15 load-steps. The red line in each energy plot is the target energy-path \hat{U} , while the blue crosses represent the actual normalized energy-path \tilde{U} . The optimized results have been evaluated at smaller increments of the displacement to verify sufficient smoothness between the original increment points. The energies at the smaller increments are shown as grey dots in Fig. 4.7b, 4.9b.

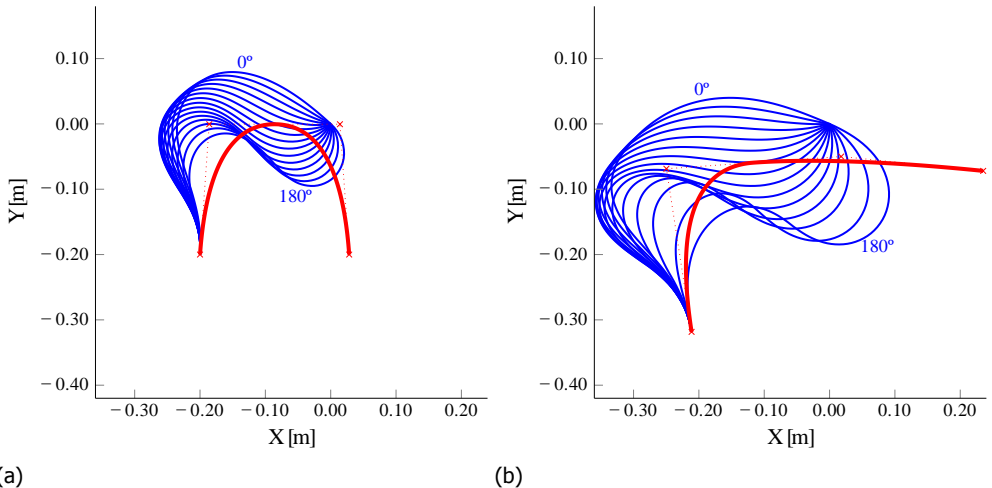


Figure 4.6: Example 1: Shape in neutral position (red) and at the 15 increments of applied rotation of the endpoint about the origin (blue). (a) Initial shape and (b) optimum shape.

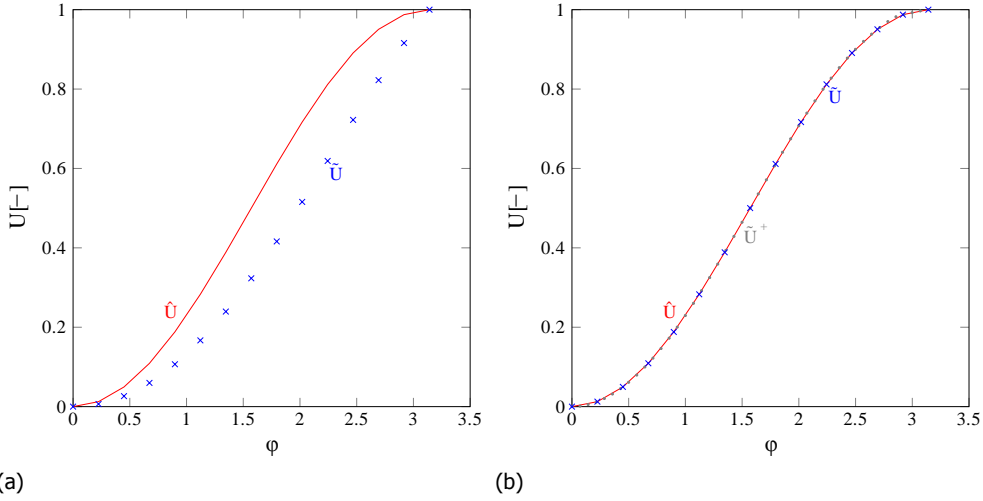


Figure 4.7: Example 1: target energy-path \hat{U} (red line), normalized actual energy-path \tilde{U} (blue crosses) and normalized actual energy path at smaller increments \tilde{U}^+ (grey dots). (a) Initial shape and (b) optimum shape.

4.4. Comparison with finite differences

This section is dedicated to a comparison of the result obtained in Section 4.2 with a numerical approximation of the sensitivity. The goal is twofold. One is to verify the validity of the derived equations and the other is to underline one advantage of the analytical sensitivity. Namely the independence between sensitivity and perturbation size.

In this analysis the gradient of the objective function with respect to the generalized coordinated $\frac{df_0}{d\mathbf{q}}$ is approximated by finite differences, using different perturbation sizes p ranging from 10^{-18} to 10^0 . The first is near or smaller than machine precision, while the latter is in this case obviously an overly large perturbation with respect to the physical dimensions of the system.

An error norm is defined to compare the analytical sensitivities with the finite difference sensitivities. The used norm is the normalized mean error e between the values of the analytical $\frac{df_0}{d\mathbf{q}}$, Eq. (4.55), and its numerical approximation $(\frac{df_0}{d\mathbf{q}})_{FD}$.

$$e = \frac{\text{mean}\left(\left|\left(\frac{df_0}{d\mathbf{q}}\right) - \left(\frac{df_0}{d\mathbf{q}}\right)_{FD}\right|\right)}{\text{mean}\left(\left|\left(\frac{df_0}{d\mathbf{q}}\right)\right|\right)}. \quad (4.57)$$

The analysis is performed at two different points. One is the first starting point of the optimization shown in Section 4.3. Another is near one of the found minima. The sensitivities at an optimum point are zero. The error e includes a division by

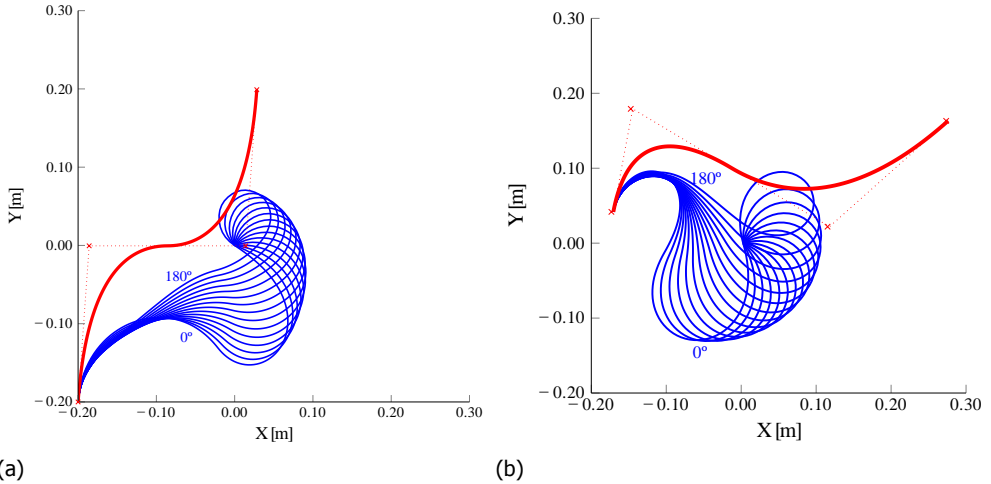


Figure 4.8: Example 2: Shape in neutral position (red) and at the 15 increments of applied rotation of the endpoint about the origin (blue). (a) Initial shape and (b) optimum shape.

zero in that case. Therefore this error is evaluated at a point near an optimum, and not at an optimum.

Figure 4.10 shows the error e for a range of perturbation sizes. The blue line (crosses) represents the error at the start point \mathbf{q}_0 and the red line (circles) represents the error at the point near the optimum.

4.5. Discussion

The optimization runs on the given example are considered successful in the sense that for both starting points, depending on the algorithm, a shape could be found that matches the given energy-path closely. Closely means that the significance of the remaining error is expected to be far beneath other types of errors expected in a physical realization of the concept. The optimized shapes have been analyzed again with smaller increments of the rotation. Minimal differences can be observed, meaning that the chosen amount of load steps was suitable for this example.

The objective function is non-convex, meaning that it cannot be guaranteed that the global minima are found in the examples. However, in the current scope it is not of practical relevance, as long as a 'good-enough' minimum is obtained. In fact the nature of the objective function, which cannot become negative, tells that if the solution is close enough to zero within relevant significance the goal has been achieved.

The use of sensitivity information on the illustrated example has shown its utility in Fig. 4.5a and b. It can be seen that with respect to the Nelder–Mead Simplex algorithm, especially with the Active-Set and the Sequential Quadratic Programming algorithms, either a quicker (more efficient) or deeper (more effective) descent is realized, and sometimes both. It is, however, not guaranteed that this is always

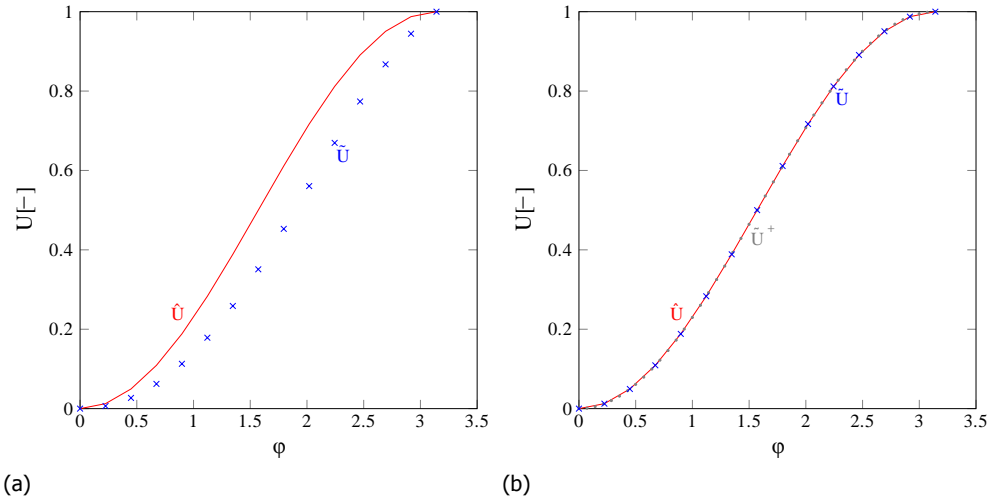


Figure 4.9: Example 2: target energy-path \hat{U} (red line), normalized actual energy-path \tilde{U} (blue crosses) and normalized actual energy path at smaller increments \tilde{U}^+ (grey dots). (a) Initial shape and (b) optimum shape.

the case.

It is also noticed that the Interior-Point and the Trust-Region Reflective algorithms fail to obtain either a lower minimum or a quicker descent. This emphasizes the importance of the choice of the algorithm. Investigation on the optimal algorithm has not been the scope of this work but is an important topic of further research. The optimal choice of the algorithm could be subject to factors like the number of design variables, boundary conditions and other constraints, and thus it may vary from case to case.

The comparison plots in Fig. 4.5a and b show the number of iterations on the horizontal axis. It must be noted however that for the Nelder–Mead Simplex the computation time of every iteration is shorter because it does not need to compute the sensitivity terms. The time saved at every iteration step highly depends on the performance of the code and the used hardware. To give an indication: Based on a Matlab code running on a Intel® Core™ i7 processor the additional computation cost for the sensitivity terms is about 60%. Nevertheless, the advantages of using sensitivity seem to hold.

The finite difference check is quite satisfying. It shows that there is a large range of perturbation sizes, from $p = 10^{-6}$ to $p = 10^{-11}$ where the difference between analytical and finite-difference sensitivities is small. On the one hand this tells that the calculations of the analytical sensitivities are correct. On the other hand it says that within this range the numerical sensitivities would give similar results, only less efficiently. However it still remains a risk that this range may vary from case to case, rising the chance to obtain imprecise or even useless numerical sensitivities.

The points where the comparison is performed are at one of the starting points

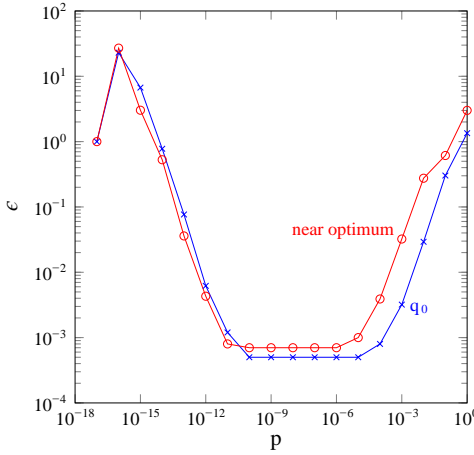


Figure 4.10: Error between finite-difference sensitivity and analytical sensitivities according to Eq. (4.57) at an initial configuration \mathbf{q}_0 and near one of the optimum configurations, plotted on a range of perturbation sizes.

of the optimization, and in the neighbourhood of the end of the optimization run. As discussed above, it would make little sense to compare the sensitivities at the end of an optimization run. Assuming this is an optimum, the sensitivities would be zero. At an optimum Eq. (4.57) would divide by zero giving an invalid error norm. It is therefore not surprising that the error norm near the optimum solution is higher than at a point far from an optimum. Similar tendencies as in Fig. 4.10 have been observed starting at various initial points.

In Section 4.2.5 a measure is taken to include the possibility to apply prestress on the system, thus inducing the system into a configuration where the angles of the endpoints are not known a priori. prestress is crucial in certain applications, especially those involving static balancing. However, if this is not required, then the procedure described in Section 4.2.5 will simplify significantly. Namely θ_{k-1} becomes fixed and thus its derivative zero. This reduces Eq. (4.44) to

$$\frac{d\Delta\theta}{d\mathbf{x}} = -\frac{d\theta_0}{d\mathbf{x}}, \quad (4.58)$$

and the part after that, Eq. (4.45)–(4.49), can be skipped.

In the definition of an amplitude invariant objective function the assumption was made that the sizing parameters would not affect the results. The Euler–Bernoulli conditions must be met in order for the numerical model to be valid in the first place. This means that shear terms are neglected and this is true for relatively long and slender beams. In the second place, also the stretch terms must be neglected in order for the thickness not to influence the energy-path. For a beam with the same shape but different thickness, namely, the stress condition is influenced by the stretch terms, and thus it affects the deformation and stored energy. It is verified that in the given example, multiplying the thickness by a factor of two yields a maximum amplitude deviation of 2.5%, and multiplying by a factor of ten yields a deviation of 4%. Care is thus needed in the choice of a suitable thickness when designing such system. The width of the spring seems in practice the most appropriate parameter to adjust after optimization without affecting the result.

4.6. Conclusion

This chapter presents the shape sensitivity analysis for the shape optimization of beams with prescribed load-displacement response. The work is based on an isogeometric framework. It has been shown that it is possible to derive the sensitivity parameters for this type of problem analytically.

A novel and general objective function is formulated for problems with prescribed load-displacement response. The objective function is based on the potential energy of the beam determined at discrete steps of the applied displacement path.

The travelled path is imposed by application of constraints on the endpoints of the beam, involving displacements but also rotations, which is more complex due to the rotation-less character of the degrees of freedom in isogeometric analysis.

The sensitivity of the state variables is determined through the direct method, with special attention to the complications brought by nonlinear equilibrium equations and the nonlinear constraints equations, applied as Lagrange multipliers.

The effect of the load history on the sensitivity analysis, e.g. by application of prestress in a previous load-step, is neutralized by making smart use of the sensitivities previously calculated for the previous load steps.

The optimization is performed on an example where the optimal shape of a beam is sought that is optimal for the static balancing of a pendulum. The influence of the use of sensitivity information is shown by comparison on different optimization algorithms, with and without the use of gradients. The optimization results in very satisfying balancing springs. The use of gradients is positively influencing the efficiency of the optimization, although determining the algorithm that performs best is still an open question.

The correctness of the derived sensitivity equations is verified by comparison with finite-difference gradients. It is shown that the numerical and the analytical gradients have a good match within a certain range of perturbation sizes.

5

A carbon fibre beam balancing a pendulum: experimental evaluation

This chapter presents the experimental evaluation of a carbon-fibre curved leaf spring used to balance a pendulum. The shape of the beam is found using shape optimization of a B-spline and the analysis is performed using an isogeometric analysis framework. The procedure is analogous to the one in Chapter 4. The result of the shape optimization has been constructed out of carbon fibre composite material, and its behavior is validated experimentally. The experimental results are in agreement with the simulation results, with an error of 3%.

This chapter is a short version of a paper published in the proceedings of the ASME IDETC 2014 38th Mechanisms and Robotics conference [134], recipient of the Best Paper Award. In this abstract the focus is on the experiment.

5.1. Introduction

The example provided in this chapter concerns a pendulum to be balanced from upright vertical to hanging vertical position, i.e. 180 degrees. To balance a pendulum over this range a counteracting moment-angle profile is required which follows a sinusoidal shape for an half period. Especially the strongly nonlinear stiffness behavior of this profile, i.e. initially positive-degressive and later even negative, makes it particular with respect to the more commonly encountered and easy to obtain progressive and positive stiffness characteristics. This moment profile has been selected because it is both very specific, but general enough to learn from it and apply to other examples. Other particularities of this example are the preloaded condition of the spring and the extremely large deformations.

The goal is to validate the results of a shape optimization procedure, similar to Chapter 4, experimentally. This is done by showing the constructed carbon-fiber reinforced spring and the measurements results.

5

5.2. Topology and characteristic

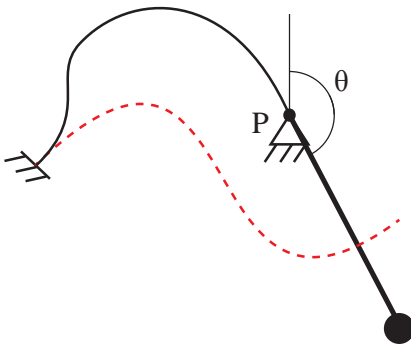


Figure 5.1: Topology of the system: A leaf spring (red) is prestressed (black) by connecting one end-point with a rigid pendulum, while the other end of the spring is clamped.

The topology of the system is a single beam element clamped at one end and pivoting with the other end around a fixed point P , see Fig. 5.1. Point P is not necessarily located at the free end of the undeformed beam. This makes it possible to apply prestress to the system. At the pivoting end of the beam a rigid pendulum is attached. The scope of this design is to find a single beam which by virtue of its shape can balance a pendulum by directly connecting it to the pendulum's base. The moment M_{ref} needed to keep the pendulum in equilibrium is zero at both upper and lower vertical positions, and reaches a maximum at the horizontal position. This maximum is equal to the pendulum's weight mg times the arm of

action l of the weight w.r.t. the base joint. The moment-angle characteristic within this range of motion equals the first half-period of a sine with amplitude $mg l$.

The reaction forces of the beam on the joint have no influence on the balance of the pendulum. It is required from the balancing unit to reach an instability point in order to balance the hanging pendulum which is stable. It is thus known a priori that the balancer should be a bi-stable beam, active in the range between the first stable equilibrium and the unstable equilibrium, without reaching the second stability point.

5.3. Optimization results

The moment-angle curve resulting from the optimization are given in Fig. 5.2a, which shows the reference sine curve (dotted red) and the obtained curve (blue). Figure 5.2b shows the difference between both. The initial shape and the deformed shapes are given in Fig. 5.3. The optimum value of the objective function is $1.857e-5$.

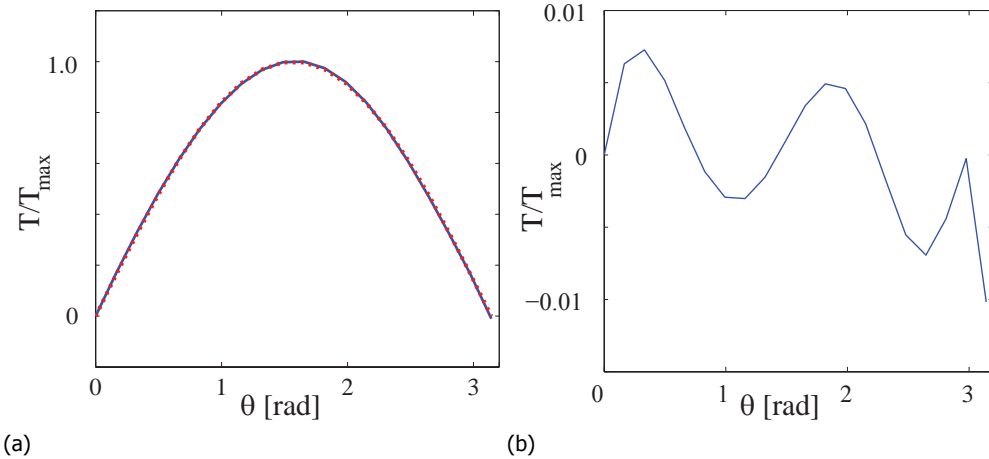
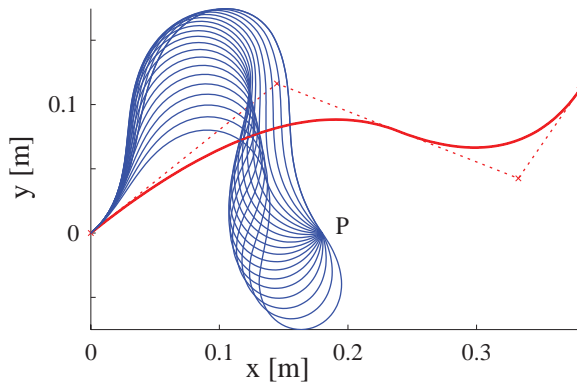


Figure 5.2: Optimization results. (a) The moment-angle curve of the obtained shape (blue) and the reference sine curve (dotted red). (b) Difference between obtained and reference curve.

Figure 5.3: The initial undeformed shape (red) is brought to a fixed turning point P where a rotation π is applied in 20 steps (blue). The undeformed spring is define by a B-spline with control points

$$\mathbf{B} = \begin{bmatrix} 0 & 0.145 & 0.333 & 0.380 \\ 0 & 0.116 & 0.043 & 0.111 \end{bmatrix}$$



5.4. Prototype design

A carbon fibre reinforced plastic is chosen as it is a convenient spring material. The ability to manufacture complex shapes, its high elastic strain energy density and the durability, i.e. resistance to creep and fatigue, are reasons to believe that carbon

fibre composites are a promising option for complex shaped springs. To increase the energy density of the system a high-tenacity carbon fibre type is used, which has increased ultimate tensile stress with respect to normal carbon fibres. These fibers have a Young's Modulus of 240 GPa, a tensile strength of 4300 MPa, and an elongation at break of 1.7%. Because of the high uncertainties of the production process (vacuum infusion) and the material combination with the epoxy resin, a safety factor has been used which sets the maximum elongation strain to 1%. The layup of the laminate has been designed such that the thickness is as close as possible to 0.75mm. This has been done with a laminate layup consisting of one layer of unidirectional fibers, a layer of a weave under 45 degrees, and another layer of unidirectional fibers ([UD 45/45 UD]). See in Fig. 5.4a a picture of the carbon leaf spring.

5



Figure 5.4: (a) Pictures of the carbon leaf spring. (b) Picture of the test setup. On the left hand side the potentiometer is connected with the rotation axis, while on the right hand side the torque-sensor is attached. The rotation is applied to the system by manually turning the outer ring of the torque-sensor. On the bottom the studs with the tensioning nuts are visible.

5.5. Testing

The moment profile of the leaf spring has been tested making use of a torque-sensor and a potentiometer. The leaf spring is thickened at the clamped edges by adding a MDF core. One edge is clamped with bolts at one side on a aluminum profile system. At the other side the edge of the spring is connected in line with two bearings, one at each side, see Fig. 5.4b. The bearings are fixed to the same aluminum profile system, where it is possible to adjust the location of the bearings in order to apply a pretension on the spring. The pretension is applied by turning the nuts on two long studs.

The potentiometer is connected at one of the bearings while the torque sensor

is fixed at the other side near the other bearing, rigidly connected to the spring. The system is driven manually by applying a rotation on the torque sensor. The data of both sensors is synchronized and read out digitally. The applied rotation/moment is manually controlled and therefore the angular velocity is not necessarily constant. But since the potentiometer is always matching the angle with the measured torque, this is a suitable setup for static or quasi-static measurements of the moment-angle characteristic. See Fig. 5.5 for the measurements results.

The blue line represents the measured data in a motion cycle, forming an hysteresis loop. The red line is the mean curve between onward and return line which, assuming that friction and other losses are equal in both directions and assuming negligible viscoelastic forces due to slow measurement speed, represents the moment profile that would remain in absence of friction. The black line represents the reference line, a sine, and finally the green line represents the error between mean curve and reference curve. The match with the sine shape is a measure for the balancing quality of the system if it would be connected with a pendulum. We quantify this match with the root-mean-square of the error (RMSE), the correlation coefficient ρ and the ratio R between work done by the error and the work done by the reference moment.

The resulting measures are $RMSE = 0.1046Nm$, $\rho = 0.9970$, and $R = 3.02\%$.

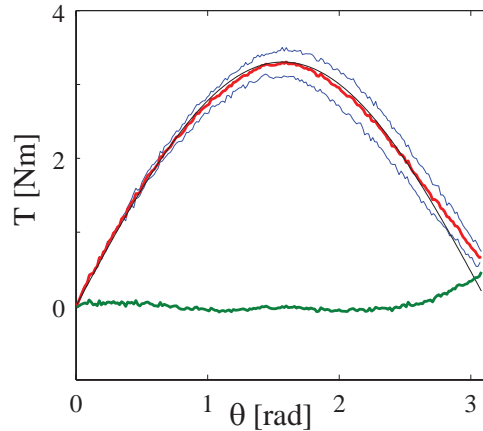


Figure 5.5: The mean of the measured moment-angle characteristic (red) is compared to the reference moment curve (black). The green line represents the error between both. Apart from the hysteresis, which is attributed mainly to the bearings, the match of the shapes is satisfying.

5.6. Conclusion

An example of a compliant balancer for a hinged pendulum has been developed, optimized, manufactured and tested.

The use of carbon fiber composites as basis material for large deflection systems and balancing springs is validated successfully, and the potentials and advantages of it are described. The main advantage of CF composites is the combination of high E-modulus and high ultimate strength, which imply a high elastic energy density. Moreover, the ability to manufacture complex shapes makes it a competitive alternative for conventional spring materials.

The carbon spring has been tested and its moment characteristic is compared to the goal function. A good match has been found that predicts good balancing qualities.

6

A monolithic compliant large-range gravity balancer

A new monolithic fully compliant gravity balancer is designed with help of a design approach based on shape optimization. The balancer consists of one single clamped-clamped complex-shaped beam on which a weight is attached. The beam is modelled as a planar isogeometric Bernoulli beam. The goal function of the optimization consists of an energy based evaluation of the load path of the beam which is compared with a desired response. The best result of the shape optimization has been constructed out of polycarbonate sheet and out of glass-fiber reinforced plastic laminate. Both have been tested on a compression test bench. The theoretical model has good resemblance with the experimental results.

This chapter has been published in Mechanism and Machine Theory (2016) [141], and in the conference proceedings of the 14th World Congress in Mechanism and Machine Science, Taipei (Taiwan), October 2015 [142].

6.1. Introduction

Compliant mechanisms, i.e. mechanisms that achieve their motion from the deflection of their members instead of from kinematic constraints [62], are more challenging to design due to their inherent coupling between kinetics and kinematics. Since forces and deflection in these mechanisms can never be considered separately because of the flexibility of the members, the design methods for conventional rigid-body mechanisms cannot be directly applied. Alternative design methods have been developed over the past decades, and a majority of designers have found their way to lumped parameter models like, e.g. pseudo-rigid-body models (PRBM) [79, 143, 144], in order to deal with these challenges, but compromising in terms of accuracy, freedom of shape, and moreover often basing their designs on equivalent rigid body mechanism designs.

Statically balanced compliant mechanisms (SBCM) [69, 145] are a subset of compliant mechanisms where undesired forces are counteracted by elastic forces generated by the deflection of the mechanism. These undesired forces can come from, e.g., an external payload [146] or stiffness, the self-weight of the system or an intrinsic stiffness [112, 147]. These forces are undesired since they either require more energy for actuation, they disturb a force signal to be transmitted, e.g., to provide haptic sense in surgical tools [68], or they result in higher stiffness and eigenfrequencies. Balancing these compliant mechanisms is thus an option to improve efficiency, force feedback fidelity, vibration isolation and energy harvesting properties.

In these and other types of mechanisms it is often desirable to follow a required force-displacement path with good accuracy in order to enhance the quality of balancing and thus its performance. Examples where following a force displacement path is relevant can be found in [4, 123, 148, 149].

Apart from balancing a weight, there are more applications of compliant constant force balancers. Examples include force regulation [7, 48], overload protection [48], constant force actuators [150] and adaptive robot end-effector operations [135].

Recently a design approach has been proposed by the authors [134] that enables the design of compliant mechanisms with prescribed load-paths with good accuracy and great flexibility of shape. The method is based on shape optimization of elastic structures undergoing large deflections modeled through the isogeometric analysis (IGA) framework [125]. This is an emerging framework allied to the finite element method (FEM), but with increased accuracy and efficiency especially due to the absence of a conversion step between CAD geometry and analysis geometry.

The goal of this chapter is to present a special design result. The design has been generated through the use of shape optimization and validated by the construction and measurements of physical models. The purpose of this design is to balance a weight, or constant force, over a fairly large vertical displacement without restricting the horizontal motion of the weight. The model consists of a fully distributed and monolithic compliant mechanism, that consists of a single branch prismatic beam.

The chapter also presents the measurement setup, where the challenge is to apply and to measure a vertical force while the motions in horizontal directions are not restrained.

Section 6.2 of this chapter shows the formulation of the design problem, the model and details of the optimization. In Section 6.3 the design resulting from the optimization is shown. Section 6.4 illustrates the design of the measurement setup and Section 6.5 shows the measurement results. Respectively, Section 6.6 and Section 6.7 contain the discussion and conclusion.

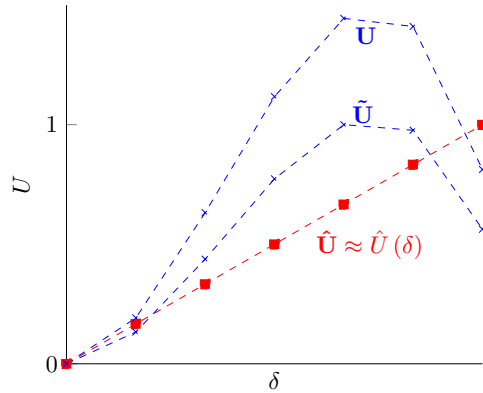
6.2. Method

The current section describes the formulation of the design problem and discusses some inputs for the design optimization.

6.2.1. Problem statement

The goal of the design procedure is to find a compliant mechanism of which a selected point L is displaced downwards resulting in a constant vertical force upward over a given range. Consequently, this constant force can be replaced by a weight obtaining a statically balanced system.

Figure 6.1: Linear reference energy $\hat{U} \approx \hat{U}(\delta)$, energy obtained by computational model \mathbf{U} and normalized obtained energy $\tilde{\mathbf{U}}$.



Considering a quasi-static and conservative mechanical system, a constant force mechanism is one that possesses a linearly increasing potential energy $\hat{U}(\delta)$ with respect to the vertical displacement δ at the point of application of the force and in its direction. This energy is evaluated at a discrete amount of displacements yielding the array $\hat{\mathbf{U}}$. This reference array is defined as a linearly increasing sequence from zero to one as

$$\hat{U}_k = \frac{k-1}{m-1} \quad \text{for } k = 1..m. \quad (6.1)$$

The array of potential energy obtained by the computational model \mathbf{U} is defined as

$$\mathbf{U} = [U_1(\delta_1) \quad U_2(\delta_2) \quad \dots \quad U_m(\delta_m)], \quad (6.2)$$

where U_k are the values of the potential energy of the system in an equilibrium situation corresponding to the applied displacement δ_k at step k . In this case δ_k , $k = 1..m$ is a discrete set of linearly spaced vertical displacements of the selected point.

Since the sizing (thickness, width, etc.,) of the resulting design has a direct relation to the magnitude of the constant force to be balanced, i.e. the payload, and less influence on the development of the force, the goal function will be made independent of the amplitude by normalization. This is done by normalizing the array of obtained energy values \mathbf{U} so that the minimum value corresponds to zero and the maximum value corresponds to one. The norm energy array is obtained by scaling every entry of \mathbf{U} according to

$$\tilde{U}_k = \frac{U_k - U_{min}}{U_{max} - U_{min}} \quad \text{for } k = 1..m. \quad (6.3)$$

As such, the goal function to be optimized is formulated as

$$f_0 = \frac{(\tilde{\mathbf{U}} - \hat{\mathbf{U}})(\tilde{\mathbf{U}} - \hat{\mathbf{U}})^T}{\hat{\mathbf{U}}\hat{\mathbf{U}}^T}, \quad (6.4)$$

which is the normalized sum of squared errors between reference energy array $\hat{\mathbf{U}}$ and the normalized obtained energy $\tilde{\mathbf{U}}$.

There is an initial build up of the vertical force expected since the system starts from rest and goes to a higher force level. This build up is desired to be short and steep, to keep the constant force region as large as possible. In terms of energy this means that the slope goes from initially zero to a certain slope which from that point on is desired to be kept constant. These initial steps of build-up influence the goal function negatively and are therefore omitted in above expressions. The precise amount of steps to be omitted is a design choice.

6.2.2. Model

The mechanical model that has been used is that of a single beam clamped at the two endpoints. The beam is modeled by an isogeometric, geometrically nonlinear Bernoulli beam [129], with a linear material constitutive law, of which the potential energy is evaluated at every imposed boundary condition. With the first material, polycarbonate (PC), that will be used in the experiments (section 6.4) a discrepancy is expected because of the material nonlinearity. For the second one, glass-fiber reinforced plastic (GFRP), this model is suitable because the majority of fibers are placed longitudinally with respect to the beam. It will be validated experimentally that a 1D planar beam model gives accurate enough results.

In the isogeometric formulation, a B-spline with relatively small amount of control points \mathbf{B}_i , with $i = 1..n$, describes the geometry of the beam, see Fig. 6.2. Consequently, for analysis, the shape is refined in a B-spline with a larger amount of control points \mathbf{P}_j , with $j = 1..r$ and $r \gg n$, where the displacements of the control points represent the degrees of freedom of the system.

The vertical displacement is applied at the central control point of the refined B-spline, point L . Strictly taken, this is not the same as applying a displacement on a point on the curve itself, since the B-spline is generally not interpolatory, i.e. the

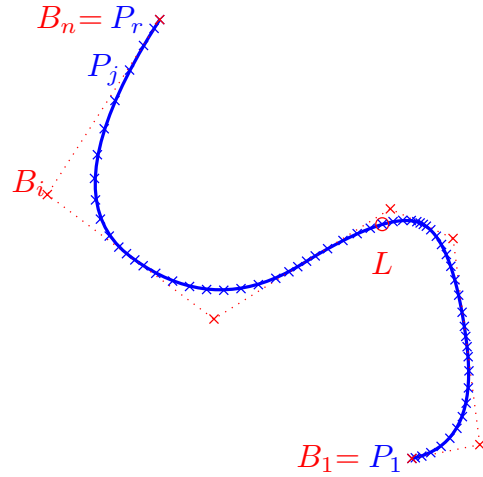


Figure 6.2: B-spline with original control points \mathbf{B}_i , with $i = 1..n$, refined control points \mathbf{P}_j , with $j = 1..r$, and point of displacement application L .

curve generally does not intersect the control points. However, the offset between control points and curve becomes smaller as the number of control points increases. In the presented analysis the shape is determined by $n = 7$ control points and is refined to $r = 50$ control points. The distance between the curve and point L is less than 0.1mm on a 300mm scale model. This is small compared with, e.g., fabrication and other errors.

Furthermore the curve is defined by the open, uniform knot vector

$$\Xi = [0 \ 0 \ 0 \ 0.2 \ 0.4 \ 0.6 \ 0.8 \ 1 \ 1 \ 1] .$$

6.2.3. Shape optimization

Optimization parameters

The set of control points \mathbf{B} are the parameters of the optimization. For convenience in the applications of bounds for the optimization and interpretation of the results, the positions of the control points are re-parameterized according to

$$\mathbf{B} = \begin{bmatrix} B_{1x} \\ B_{1y} \\ B_{2x} \\ B_{2y} \\ B_{3x} \\ B_{3y} \\ B_{4x} \\ B_{4y} \\ \vdots \end{bmatrix} = \begin{bmatrix} q_1 \\ q_2 \\ q_1 + q_3 c(q_4) \\ q_2 + q_3 s(q_4) \\ q_1 + q_3 c(q_4) + q_5 c(q_4 + q_6) \\ q_2 + q_3 s(q_4) + q_5 s(q_4 + q_6) \\ q_1 + \dots + q_7 c(q_4 + q_6 + q_8) \\ q_2 + \dots + q_7 s(q_4 + q_6 + q_8) \\ \vdots \end{bmatrix} \quad (6.5)$$

where c and s are the shorthand notations for \cos and \sin , and \mathbf{q} defined as

$$\mathbf{q} = [B_{1x} \ B_{1y} \ l_1 \ \theta_1 \ l_2 \ \theta_2 \ l_3 \ \theta_3 \ \dots] . \quad (6.6)$$

This transforms the parameters of optimization from an array of Cartesian coordinates to a sequence of lengths l_k and relative angles θ_k , i.e. it describes the control polygon of the spline as if it were a linkage chain, see Fig. 6.3. By this transformation it becomes easy to apply limits to the search space. For example, limiting the angles avoids sharp corners in the beam. Additionally giving a lower limit to the lengths also helps avoiding loops of the spline which in practice leads to unfeasible structures.

The applied optimization bounds on the lengths of the sides of the control polygon are $[0.05 \leq l \leq 0.15]$ and their relative angles $[-2 \leq \theta \leq 2]$. The total vertical applied displacement is 0.21 [m].

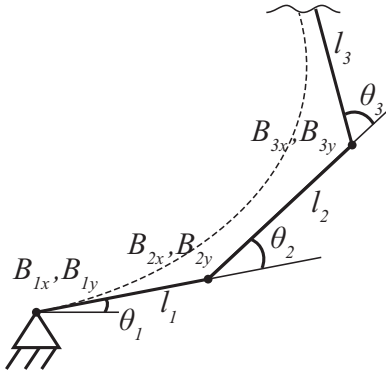


Figure 6.3: Transformation of coordinates of the control points in a set of generalized coordinates, described by the lengths and angles of the links of a linkage chain, representing the control polygon.

In the current optimization a control polygon of 7 control points is used. The first two parameters of vector \mathbf{q} , i.e. the position of the begin of the beam, are fixed to zero. In this particular case these parameters only determine the global position of the mechanism in space and have no influence on its behavior. This results in 12 optimization parameters of which 6 are the lengths of the control polygon sides and 6 are their relative angles.

Sizing parameters

The optimization is performed on the shape parameters only, while sizing parameters are kept out of consideration by normalizing for an undetermined payload, as discussed. As soon as the shape is found it is possible to change the sizing variables, i.e. the cross-section dimensions and the Young's modulus, to match a desired payload. As long as the Euler-Bernoulli conditions, i.e. $length \gg thickness$, are met, the sizing will not influence the balancing results significantly. Eventually, an additional optimization run can restore an altered behavior due to sizing changes.

The dimensions and properties used as starting point in current optimization run are given in Table 6.1, meant for a glass fiber reinforced plastic slender beam construction.

| parameter | value | unit |
|-----------|-------|-------|
| E | 25 | [GPa] |
| width | 0.15 | [m] |
| thickness | 0.002 | [m] |

Table 6.1: Material and sizing parameters

| par. | unit | \mathbf{q}_{end} |
|------------|-------|--------------------|
| B_{1x} | [mm] | 0.00 |
| B_{1y} | [mm] | 0.00 |
| l_1 | [mm] | 85.8 |
| θ_1 | [rad] | 1.23 |
| l_2 | [mm] | 10.8 |
| θ_2 | [rad] | 0.06 |
| l_3 | [mm] | 12.6 |
| θ_3 | [rad] | 1.54 |
| l_4 | [mm] | 05.1 |
| θ_4 | [rad] | 0.73 |
| l_5 | [mm] | 12.9 |
| θ_5 | [rad] | 1.24 |
| l_6 | [mm] | 11.9 |
| θ_6 | [rad] | 0.01 |

Table 6.2: Optimized design vector \mathbf{q}_{end}

Algorithm

The selected optimization algorithm is the Sequential Quadratic Programming (SQP) from the Matlab® *Optimization Toolbox*, started at 50 different starting points randomly distributed over the search space using the *MultiStart* option in the *Global Optimization Toolbox*.

6.3. Optimization results

Out of the 50 runs from different random starting points the best result has been selected. For this run the converged solution \mathbf{q}_{end} is shown in Table 6.2. The behavior of the optimized geometry is shown in Fig. 6.4, showing the undeformed geometry in red (thick line) and the deformed geometries corresponding to every displacement step in blue (thin lines). The red crosses are the control points of the design vector and the red circle is the point of application of the vertical displacement. Figure 6.5a shows the optimized energy graph (blue circled) compared to the reference energy (red crossed). Since the difference between the obtained and reference energy is hardly visible, the error between both is plotted in Fig. 6.5b. The final objective function, i.e. the normalized sum of squared errors, is $1.48e - 4$. The resulting reaction force in vertical direction due to the applied displacement is plotted in Fig. 6.6. Finally an overview of the strains is provided in Fig. 6.7. Here for every load step the strain is shown for the innermost material layer (green) and the outermost layer (blue). On the horizontal axis the parameter of the b-spline is ξ which ranges from 0 to 1 from the begin to the end of the curve.

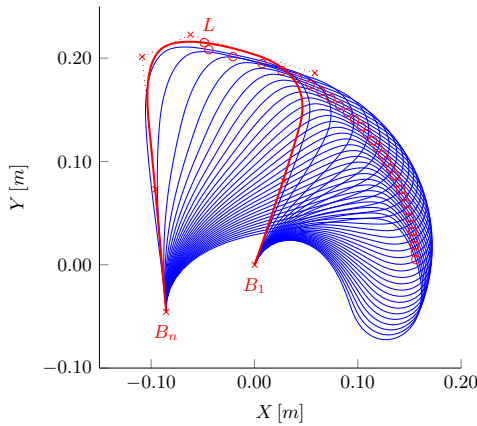


Figure 6.4: Undeformed geometry of the optimized shape (red) and deformed geometries corresponding to every displacement step (blue). The red dot indicates the point of application of the vertical displacement L .

6

6.4. Experimental evaluation

The construction of the physical model is shortly presented and the measurement setup explained.

6.4.1. Prototype construction

As a preliminary investigation before making a glass-fiber reinforced plastic (GFRP) version of the beam, as foreseen in the optimization material parameters, a polycarbonate version of the same beam is constructed. Polycarbonate is broadly available, cheap and has fairly good mechanical properties. Moreover the production process is fairly simple and leads quickly to acceptable results. Two beams have been constructed with different plate thicknesses: 1 mm and 2 mm . A one-sided mould is CNC-milled out of high-density foam material, see Fig. 6.8a. A polycarbonate plate is heated above its glass-transition temperature and then draped onto the mould. When the plastic reaches ambient temperature again, the beam is ready to be clamped onto the supporting structure, see Fig. 6.8b.

After, using the same type of mould, the same shape is fabricated out of glass-fiber reinforced plastic (GFRP), which is epoxy in this case. This is done using a vacuum infusion process. The dry fibers are placed onto the mould and sealed with a vacuum bag. Then the vacuum causes the liquid resin to infuse and spread through all fibers. The resin is then cured in an oven to get optimal strength. The resulting shapes are shown in Fig. 6.8c. Multiple layups have been constructed. The two presented in this work have the laminate layups $[0\ -45/45\ 0]$ and $[0\ -45/45\ 0\ -45/45\ 0]$, where the fibers in the 0-direction are unidirectional fibers (UD) of S2-type glass and the ones in $-45/45$ -directions are woven fibers of E-type glass. The UD S2-glass layers have a thickness of 0.2 mm , the woven E-glass have a thickness of 0.06 mm for each layer. The S2-type glass is selected because of the superior stiffness and strength properties. The woven E-glass fibers are applied to prevent easy crack propagation in longitudinal direction, but have a minor influence on the bending properties. This justifies the use of a 1D planar element, i.e. a beam element, with respect to a more complex orthotropic

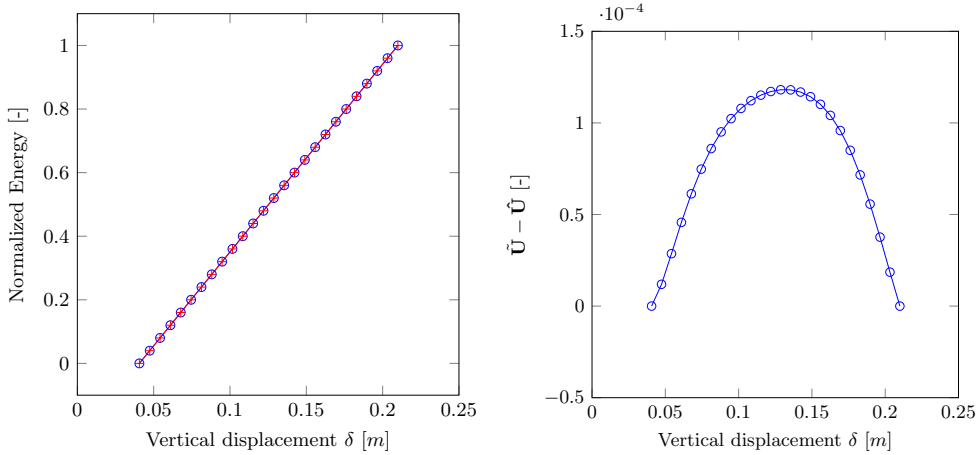


Figure 6.5: (a) Optimized energy graph \tilde{U} (blue circled) and reference energy graph \hat{U} (red crossed). (b) Error between optimized energy \tilde{U} and reference energy \hat{U} .

shell element.

6.4.2. Measurement setup

For the experimental evaluation the vertical reaction force is measured while a displacement is applied at the selected point. It is important that only a vertical displacement is applied, while the horizontal motion of that point is completely free. This is a challenge for conventional compression testing machines that travel along a straight line. To overcome this limitation, the base of the compliant mechanism is placed on a planar horizontal stage. This stage consists of three sets of orthogonally placed rollers that affect the planar translations with low friction. As shown in Fig. 6.9 two long steel rollers are placed in parallel with the direction of motion of the support of the beam. Other two rollers are placed in the perpendicular direction on top of the first set of rollers. Again other two rollers are placed in the direction of motion right underneath the support base of the beam. The roller configuration is chosen such that only point contacts are made between rolling parts and that the reaction force is always within the support polygon of these point contacts. The only motion in the horizontal plane that is restricted is the rotation. However, no such rotational motion is expected in this design, and no such tendency was observed during the measurements.

The interface between the beam and the load cell has been designed such that the applied displacement is evenly distributed along a line corresponding to the selected point in the planar representation of the beam. This has been achieved by a knife-edge bearing, created by a rectangular prismatic aluminum bar that makes contact with the beam only at one lower corner, see Fig. 6.10a. This contact is maintained during the whole range of motion. The position of the contact line on

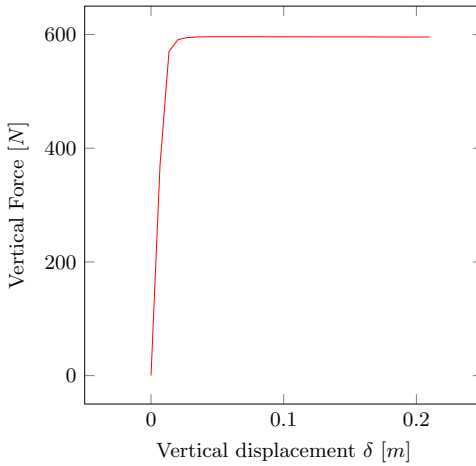


Figure 6.6: Optimized vertical force vs vertical displacement δ .

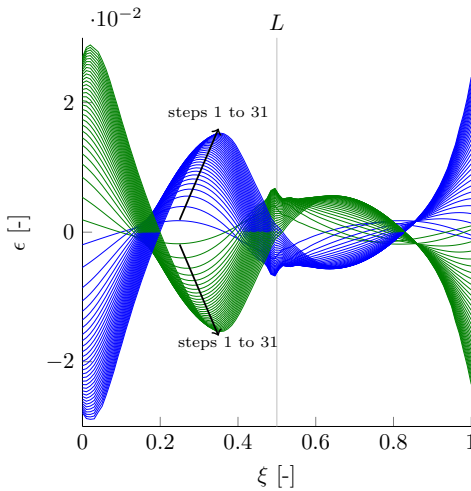


Figure 6.7: Material strains for a 2 mm thick plate. The lines represent the strain across the length of the beam, from curve parameter $\xi = 0$ to $\xi = 1$. The green lines represent the innermost material layer and the blue lines represent the outermost material layer. The lines are drawn for every load step from 1 to 31. Discontinuity can be observed at the position corresponding to point L , where the load is applied.

the beam is maintained by a double-sided adhesive tape that sticks to the beam on one side of the contact line and sticks to the bar at the other side of the line, see an impression in Fig. 6.10b. The tape is loaded in tension throughout the whole motion, therefore a fiber-reinforced tape is very suitable.

6.5. Measurement results

The results of the force measurements are shown in Fig. 6.11a for the polycarbonate version. The higher blue line is the force measured with the 2 mm plate in a forward and backward motion cycle. The lower blue line is the force measured on the 1 mm plate. Figure 6.11b shows the results from the GFRP version. The lower line represents the thinner laminate, which measures 0.7 mm on average, and the higher line represents the thicker laminate, which measures 0.9 mm on

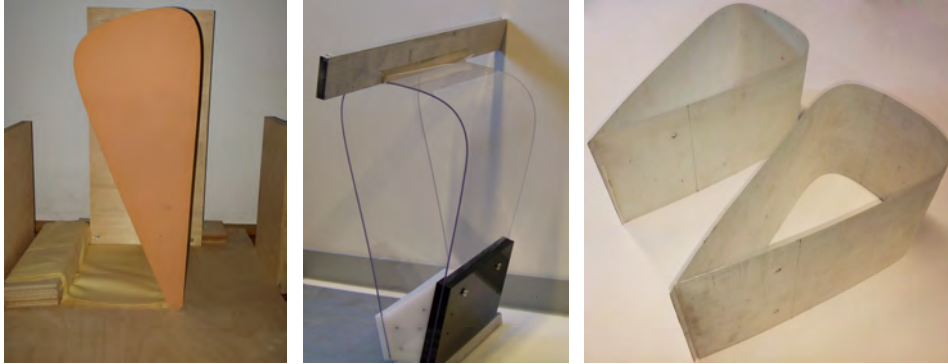


Figure 6.8: (a) One sided mould out of high-density foam material. (b) Polycarbonate beam clamped onto support structure. (c) Glass-fiber reinforced plastic springs, manufactured by a vacuum infusion process.



Figure 6.9: Rollers setup used as planar bearing underneath the beam support structure.

average. In red the theoretical forces from the computational model are plotted for comparison. The amplitude of these model forces are fitted onto the measured data because the exact cross-sectional properties are hard to predict, especially with the GFRP laminate. This circumvents the need to specifically tests these properties, which is out of the scope of this work and irrelevant for the outcome.

The fitting is done by using the thickness of the beam as a parameter and the coefficients of variation of the root mean squared error (CV(RMSE)) as a minimization criterion. The criterion is defined as

$$CV(RMSE) = \frac{RMSE}{\bar{y}}, \quad (6.7)$$

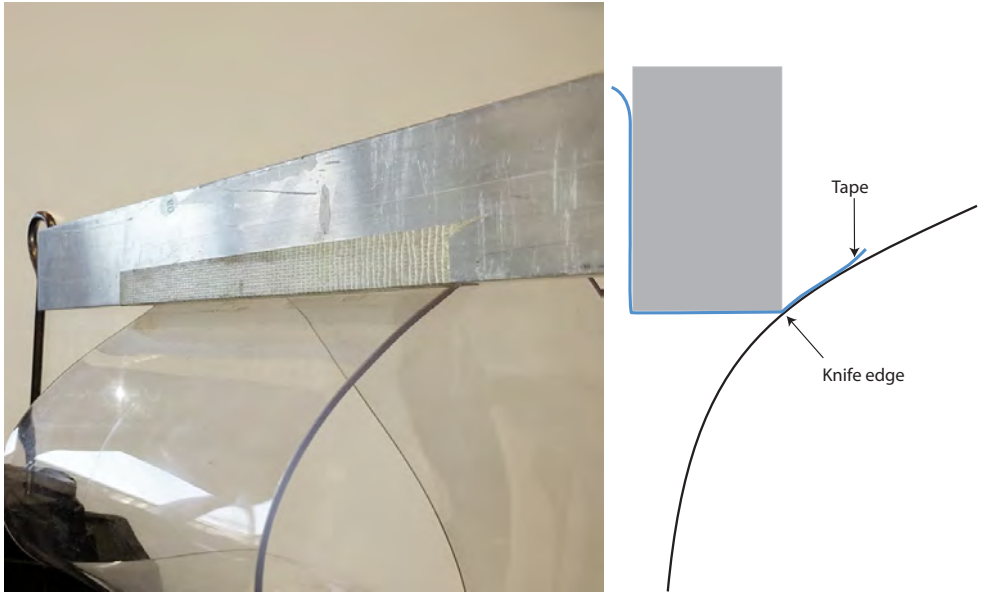


Figure 6.10: (a) Knife-edge bearing for the application of a vertical motion along a line of the surface. Double-sided adhesive tape holds the corner of the aluminum bar on its place. (b) Schematic of the adhesive tape holding the knife-edge bearing on its place on the surface of the beam.

| Sample | 1 mm PC | 2 mm PC | 0.7 mm GFRP | 0.9 mm GFRP |
|------------|---------|---------|-------------|-------------|
| $CV(RMSE)$ | 0.0287 | 0.0046 | 0.0087 | 0.0032 |

Table 6.3: Coefficients of variation of root mean squared error $CV(RMSE)$ values for all measured samples with respect to the modeled force.

where $RMSE$ is given by

$$RMSE = \sqrt{\frac{\sum_{t=1}^n (\hat{y}_t - y)^2}{n}}, \quad (6.8)$$

\bar{y} is the mean of the measured values y and \hat{y} represents the values predicted by the model. The range $t = 1..n$ for which this measure is calculated starts at the position for which the force is optimized, i.e. after the 6 steps of the ramp up. This corresponds to a displacement of 40 mm from the unloaded position.

Table 6.3 contains the $CV(RMSE)$ for the four measured samples. This measure is chosen to make the results comparable despite of the different amplitude of the forces. The values are given for the upper line of the hysteresis loop corresponding to the forward part of the motion cycle.

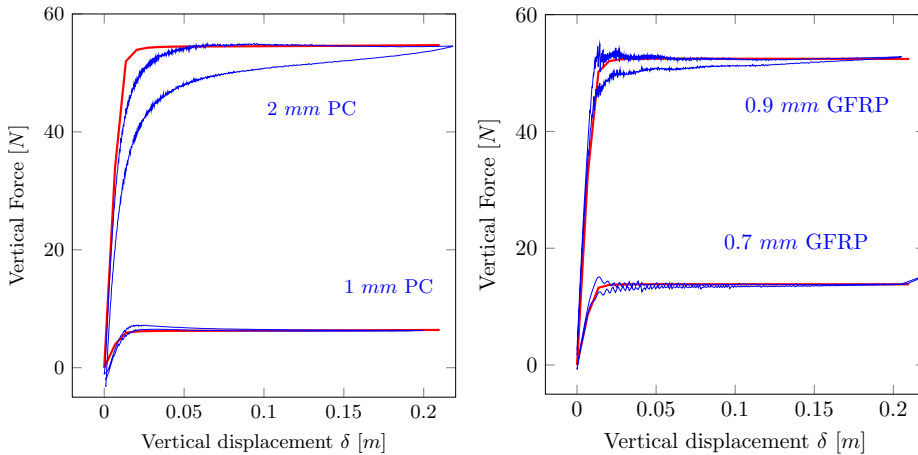


Figure 6.11: (a) Comparison of vertical force from the measurements and the model for the polycarbonate model, both 1 mm and 2 mm thickness, in forward (up) and backward (under) direction. (b) Comparison of vertical force from the measurements and the model for the GFRP model, both 0.7 mm and 0.9 mm thickness, in forward (up) and backward (under) direction.

6.6. Discussion

6.6.1. Modelling and optimization

The optimization works well as design-aid for some special types of compliant mechanisms. The designed load-path, the goal of the optimization, is well achieved by this approach. It is not trivial that by virtue of the shape of the beam alone, such a near-perfect constant force can be generated by this elastic system.

Interesting to point out is the self searching behavior of the point of application of the payload in horizontal direction. In fact this point does not need to be constrained over a particular path in order to achieve the desired behavior. The point moves vertically by imposing the displacement but at every vertical step it finds the horizontal position of minimal energy for the system.

Even though the goal function of the optimization is known to be non-convex, thus not guaranteeing convergence to a global optimum, by use of a multi-start method enough satisfying local minima have been found. It must be noted that for this situation it is not important to find the global minimum as long as the value of the local minimum is small enough in a practical sense. Since the goal function, by its definition, is lower-bounded at zero, finding the absolute zero is not better than finding a sufficiently small objective value. The threshold of good enough is of course a subjective matter and depends on the design requirements. Consider that the effect of a slightly higher goal function will in practice be overshadowed by imperfections of the physical system.

On the other hand it must be considered that due to the presence of many local optima, it always remains unclear which minima were *not* found by the optimization. Did it miss some interesting, better, more efficient solutions? One where with less

material a higher payload is balanced? Or one where the stresses in the material are distributed more evenly? These questions are subjects of investigation which may lead to improved designs and procedures in future.

One aspect of the modelling that is known to produce an error is the offset from the control point on which the displacement is applied, with respect to the beam surface. However, in the resulting geometry and with the applied refinement this offset is in the order of a tenth of a millimeter. This is considered insignificant especially compared to the more significant manufacturing errors.

A choice made in the modelling steps is to remove the first few load-steps, in this case the first 5 out of 31. This is a deliberate choice of the designer that may influence the result to a large extent. The authors have chosen for a minimal amount, such that the ramp-up would be as steep as possible. Choosing a larger amount presumably simply results in good balancing properties but with a slower ramp-up and a relatively smaller range of motion. A smaller amount of steps has the risk that the first few steps that are not removed will influence the goal function too much in a negative sense, thus bringing the algorithm further away from potentially good results.

6.6.2. Prototype

In the physical models out of polycarbonate, it must be taken into consideration that this thermoplastic has a strongly nonlinear stress-strain characteristic. In the model however, a linear constitutive law has been adopted. Therefore an error in the measurements is to be expected that derives from this simplification. It can be observed that the 1 *mm* prototype seems to have a better match with the model, while the 2 *mm* prototype has a more rounded transition between the ramped part of the force and the constant part. This difference with the model, where the transition is clearly sharper, is considered to be related with nonlinearity of the material: The 2 *mm* version achieves higher strains and thus reaches further into the nonlinear stress-strain curve, while the 1 *mm* stays in the region where the stress-strain curve can be considered linear.

Furthermore, inaccuracies deriving from this particular production method must be taken into account. When the material sheet is cooling down it shrinks. This can result in a transverse curvature that has a significant effect on the cross-section geometry. In fact, a strip with a transverse curvature, e.g. a tape measure, has totally different stiffness behavior than a flat strip.

The manufacturing of the GFRP yields quite some uncertainties. Although manufactured by a trustworthy and experienced company, it is still a challenge with this method to have an uniformly distributed thickness. In fact there were two more springs manufactured ranging up to a thickness of 2 *mm*, which is the thickness used in the optimization run. Unfortunately those springs broke due to imperfections in the laminate.

Despite the manufacturing errors, the results of the measurements are still impressive. The output force in both cases is following a nice straight line and small deviations from the model.

6.6.3. Measurement

The measurement setup is simple and effective. It contains, except for the test bench, no particularly complex or expensive components. The support on rollers provides low friction and high vertical stiffness of the support. Also the taped rectangular bar making the line-contact with the polycarbonate plate performs properly.

It can be noted from the measured data that there is a significantly higher noise in the beginning of the constant-force range. Even though the normal force, and thus the load on the rollers, is nearly constant, the horizontal velocity of the base is significantly higher there and goes back to zero at the end of the range. As visible in Fig. 6.4, the point of application of the displacements almost describes an arc: horizontal at the start and vertical at the end. Also there is a sudden acceleration sideways at the very beginning of the motion due to the buckling behavior of the structure. Both the oscillations of the structure and the imperfections in the rollers result in higher noise and oscillations under the described conditions of high acceleration and velocity.

Similar reasoning can explain the fact that the hysteresis in the measurement results is high in the beginning of the displacement and becomes smaller at the end of the range of motion, even though the vertical force does not change so much. At the begin the horizontal motion of the rollers is substantially larger than at the end where the rollers are almost standing still. Therefore there is more friction generated at the beginning and almost no friction generated at the end. The samples with higher normal force on the bearing setup (2 mm PC and 0.9 mm GFRP) have substantially higher friction losses, as expected.

6.7. Conclusion

This chapter presents a new monolithic, compliant, single branch and prismatic cross-section beam that balances a large weight over a large stroke with virtually perfect accuracy in the model. Moreover the system is self-searching in horizontal direction, i.e. the point of application of the weight does not have to be constrained over a certain path or line.

The previously presented design approach comprising a shape optimization procedure has been validated successfully by virtue of a non-trivial example. A rather complex shape was found that is able to exhibit a predefined complex behavior, i.e. large stroke with constant force. Such a design challenge is not easily achieved with existing methods for compliant mechanism design.

Physical models have been constructed for the validation of the results. A polycarbonate sheet has been thermoformed and draped onto a mould and GFRP laminate has been shaped onto the same mould.

The experimental validation of the numerical models shows a good resemblance between both. The observed errors can be explained by predictable causes. Especially the nonlinearity of the material, the imperfection of the shape and the rollers are the main sources of errors.

7

Design and Optimization of a General Planar Zero Free Length Spring

Arnoud A.T.M. Delissen, **Giuseppe Radaelli**, Just L. Herder

A zero free length (ZFL) spring is a spring with special properties, which is commonly used in static balancing. Existing methods to create ZFL springs all have their specific drawbacks, which rises to the need of a new method to create such a spring. In this research a methodology is proposed which enables the design of planar ZFL springs with specified stiffness and consisting of a single component. By curving a leaf spring its stiffness properties in different directions can be changed, exploiting its geometric nonlinearities. Using a numerical analysis in conjunction with an optimization algorithm the force profile is tailored to behave like a ZFL spring within a certain range. New type of ZFL springs can now be designed, which can not only be used in existing applications, but also enables the use of ZFL springs in micro mechanisms.

This chapter is a short version of a paper published in Mechanism and Machine Theory (2017) [151], with focus on the results.

7.1. Introduction

The spring is one of the most commonly used physical elements in engineering. A special sub-category in springs is the zero free length spring (ZFL spring), also null-length spring or ideal spring, which is - as the name implies - a spring with zero physical length when no forces are applied. This property results in a spring element which enables a range of special mechanisms to be realized, predominantly in the field of statical balancing. To mention a few: Slow wave seismometer [152, 153], Anglepoise suspension [102] which are basically balanced arms with a mass [154], zero stiffness mechanisms [155, 156], mobile arm support for humans [157, 158], camera stabilizer apparatus [43] and in (robotic) manipulators [46, 47].

A ZFL spring gets its unique properties from the sole fact that the unstretched (free) length of a linear spring is zero. Observing Fig. 7.1, a ZFL spring is shown on the left. The length being zero results in the spring's pivot and endpoint being coincident. The spring force is now directly proportional to the displacement vector, i.e. the force is in the same direction and its magnitude is proportional to the extension length of the spring ($\mathbf{F} = k\mathbf{u}$). This in contrast to a normal (non-zero free length linear) spring, where the force is not only dependent on the displacement, but also on the initial configuration of the spring ($\mathbf{F} = k(\mathbf{x}_0 + \mathbf{u})$). This is shown on the right in Fig. 7.1. In one dimension there is no difference between the two springs, as the reference (zero) point can be chosen freely. But in two or three dimensions the zero point will always be the pivot point on which the spring is fixed.

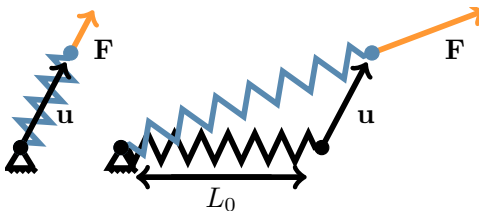


Figure 7.1: Comparison of a ZFL spring (left) and a 'normal' spring (right). In the ZFL spring $\mathbf{F} = k\mathbf{u}$, while in the normal spring $\mathbf{F} = k(\mathbf{x}_0 + \mathbf{u})$. The undeformed spring is shown in black, the deformed in blue.

Currently a general ZFL spring is not an existing product, although various methods exist to approach the behavior of a ZFL spring at least in a certain range, they all have their specific drawbacks. Furthermore it is not possible to create a spring on micro scale because fully three-dimensional structures, assembly methods and material choice are limited. The existing ZFL spring based on a compliant mechanism [123] is unable to obtain ZFL behavior close to zero and is limited to one direction.

The goal of this research is to provide the designer with a method to create their own ZFL spring, tailored for any chosen spring stiffness. The spring is realized by a beam which is formed into a yet unknown shape. When displacing one end of the beam over a predetermined area of operation, the beam shape inherently causes a linear force-displacement proportionality in all in-plane directions. This method is applied on three cases with different boundary conditions, each behaving differently and being suitable for different applications.

The method starts off with describing the numerical model which is used for simulation, followed by an explanation how of the desired and actual force profiles are translated to a mathematical objective function. Furthermore the optimization process is treated. The results section shows different designs and their performance, originating from various initial designs and desired stiffness values. Finally, the performance is analyzed and the optimization process, shape, possible applications and difficulties are discussed.

7.2. Method

In this section, a method is proposed which is able to obtain designs for ZFL springs. It is chosen to limit only to planar designs of curved flexures with constant thickness and height, the first step is to obtain a suitable numerical model. Then by numerically analyzing this model, the reaction forces can be calculated. An optimization problem is constructed, for which an objective function needs to be formulated from the reaction forces. Next some constraints on the shape are introduced and incorporated into the objective function, to make sure a valid design is reached. Finally, an optimization algorithm is used to obtain designs for the ZFL spring.

The numerical model of the springs is based on the isogeometric analysis, including the beam parameterisation and the sensitivity analysis as presented in Chapter 4. For different combinations of boundary conditions, distinct type of springs emerge. Three versions of a spring are identified as pinned-pinned, clamped-pinned and clamped-clamped, also seen in Fig. 7.2. There is a fundamental difference between these types of springs. Because of the rotational freedom of the pinned-pinned spring, the force is always aligned along the two pinned points, shown in Fig. 7.2a. This is comparable to a simple spring element as commonly used in engineering where the zero point or rotation point is at the base of the spring. The next type introduces a clamp on the base side, causing a reaction moment to be added. This allows for the direction of the force to be in any direction, as seen in Fig. 7.2b. The result of this is that there is no rotation point, but only a zero force point at the end of the spring. Begin and endpoint do not need to coincide to get zero free length properties. Another clamp on the displaced side also introduces a reaction moment at the displacement side in addition to the reaction force 7.2c. The force components for the clamped-pinned and clamped-clamped spring can be described as Cartesian (F_x and F_y) or as the axial and transverse force (F_A and F_T). The axial force is the component aligned with the displacement direction, while the transverse force is perpendicular to the displacement.

Last in the analysis phase is to displace the endpoint over a certain track and calculate the corresponding reaction forces at several sample points on this track. Starting with the pinned-pinned spring, it can already be deduced that due to its rotational freedom, the smallest spring will be the one that exploits this freedom. The force-displacement profile will thus be axial symmetric around the rotation point. Therefore the pinned-pinned spring will be displaced over a straight line in only one single direction. Because the spring's end-point is not always near the base point, the spring's end first is prestressed to the first sample point, close to the spring base joint. Then at a number (n_u) of sample points \mathbf{u}_i on this displacement

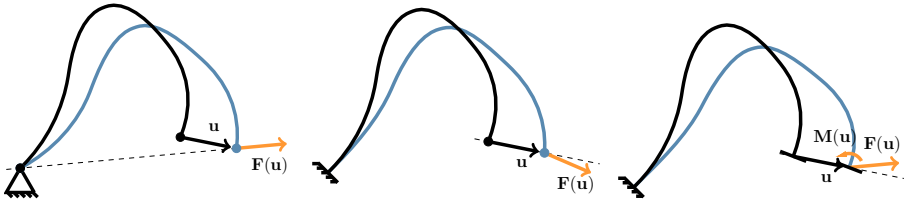


Figure 7.2: Different boundary conditions give springs with different behaviors. The undeformed spring (black) and arbitrarily deformed state (blue). (a) Pinned-pinned, (b) Clamped-pinned, (c) Clamped-clamped.

track the reaction loads are calculated.

The clamped springs don't have this rotational freedom, so being dependent on direction, multiple straight tracks are made in different directions from the initial end-point. A track is made in n_θ different directions, where on each line n_u sample points are taken. An example of multiple straight tracks can be seen in Fig. 7.3a. For the clamped-clamped spring, it is chosen that the endpoint additionally keeps the same orientation - always staying parallel to its original angle. In some applications this angle might be chosen differently, resulting in a different force profile.

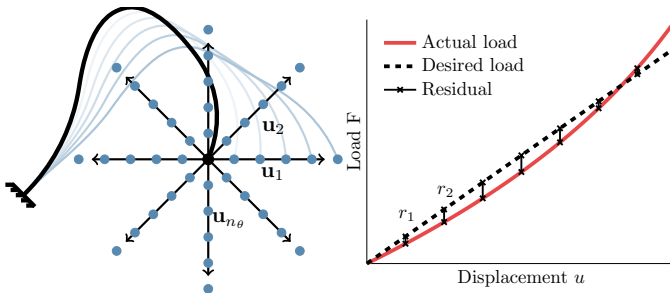


Figure 7.3: (a) A curved beam which is displaced over a straight line at discrete steps (sample points). At each of these locations the reaction loads are known. (b) An arbitrary force displacement plot. The indicated residuals should be minimized.

7.2.1. Objective Function

Now being able to calculate the reaction loads (\mathbf{F}_{ij} and M_{ij}) at the set of displacement sample points \mathbf{u}_{ij} , the next step will be to compare these values with a desired force value ($\tilde{\mathbf{F}}_{ij}$). In order to obtain a ZFL spring, the reaction force has to be linear proportional to the displacement, which means $\tilde{\mathbf{F}}_{ij} = k\mathbf{u}_{ij}$. These Cartesian forces are used during the optimization. For the pinned-pinned spring and the clamped-pinned spring only forces are acting on the endpoint. The clamped-clamped version also generates a torque at its endpoint. This moment is not taken into account during the optimization in this work. By taking the difference between the actual loads and the desired loads, residuals are formed illustrated in Fig. 7.3b. The objective

| | | | | | |
|--|----------|-----|------------|------|---------|
| Height h | 1.00 | mm | Design | PP | CP & CC |
| Width w | 10.0 | mm | u_{\min} | 5mm | 0mm |
| α_{\max} | 0.9π | rad | u_{\max} | 20mm | 20mm |
| l_{\min} | 0.1 | mm | n_u | 10 | 10 |
| l_{\max} | 200.0 | mm | n_θ | 1 | 8 |
| Young's modulus E | 113.8 | GPa | c | 10 | 10 |
| Yield strength σ_{yield} | 880.0 | MPa | | | |

Table 7.1: (a) Geometry, bound limits and material constants. (b) Design and optimization parameters. The desired stiffness values are chosen to be $k = 250, 375, 500, 625, 750\text{N/m}$.

function is defined as the sum of squares residuals, as

$$f_{\text{obj}}(\mathbf{q}) = \sum_{i=1}^{n_\theta} \sum_{j=1}^{n_u} \left((F_{x,ij}(\mathbf{q}) - \tilde{F}_{x,ij})^2 + (F_{y,ij}(\mathbf{q}) - \tilde{F}_{y,ij})^2 \right) \quad (7.1)$$

Since the displacements are taken constant during optimization, the loads are only dependent on the design \mathbf{q} . Only the spline geometry will thus be optimized.

7

7.2.2. Optimization Algorithm

The Matlab function for nonlinear least squares optimization `lsqnonlin` is used, since it is able to minimize nonlinear residual problems and makes use of the Jacobian sensitivity matrix. In this function the trust-region-reflective algorithm is used [159]. This optimization algorithm needs an initial design vector to start with.

Due to the possible existence of local minima, multiple different initial designs are used. These are randomly generated in the entire design space, as defined by the bounds, by using a latin hypercube [160]. This ensures the initial designs are spread randomly but evenly distributed over the design space (in terms of angles and lengths).

7.3. Results

In this section the resulting designs from optimizations of the different spring types will be shown and analyzed. Starting with the pinned-pinned designs for various stiffness values, their performances are quantified using an error measure to enable comparison. Followed by clamped-pinned and clamped-clamped designs which have to cope with extra parasitic loads (forces in transverse direction of the displacement, which should be zero) and had to be optimized for more than one direction. Finally, some general observations about the designs and their limitations are made.

For interpretation it is more intuitive to speak in terms of axial and transverse forces instead of the Cartesian forces. The desired axial and transverse force respectively are $F_{A,ij} = ku_{A,ij}$ and $F_{T,ij} = 0$, where the transverse force is called a parasitic force since it should be zero. The term k is the required stiffness and $u_{A,ij}$ the axial displacement.

The performances of the springs are quantified using two error measures. The first one giving information about the forces in axial direction - the maximum relative error ϵ_A - is introduced as the maximum error between the actual force in axial direction $F_{A,ij}$ and the desired force $\tilde{F}_{A,ij}$. This measure gives the error with respect to the desired axial force in percentages.

$$\epsilon_A = 100 \max \left(\left| \frac{F_{A,ij}}{\tilde{F}_{A,ij}} - 1 \right| \right) = 100 \max \left(\left| \frac{F_{A,ij}}{u_{A,ijk}} - 1 \right| \right). \quad (7.2)$$

Similarly, the performance of parasitic forces in transverse direction is quantified (if applicable). Since the desired transverse force is zero, the desired axial force will be used as a reference. This is now the error of the (parasitic) transverse force with respect to the desired axial force in percentages:

$$\epsilon_T = 100 \max \left(\left| \frac{F_{T,ij}}{u_{A,ijk}} \right| \right). \quad (7.3)$$

Note that in obtaining these performance parameters, the final design is re-evaluated with more sample points than used in the optimization phase (twice the steps in axial direction and thrice the number of directions). This is to prevent (possibly large) errors in between the sample points to go unnoticed.

All three type of springs were optimized using the same initial design vectors. The four initial designs used are shown in Fig. 7.4 and were generated using a latin hypercube as described in the method. The results from each of these initial designs is given to see the influence of differing initial design. For ease of indicating the various designs, they are indicated using a special notation. First of all is the spring type indicator - PP for pinned-pinned, CP for clamped-pinned and CC for clamped-clamped. Secondly comes the initial design number, and finally the stiffness it is designed for (separated with a dot). For instance, a clamped-pinned spring originating from the third initial design and optimized for a stiffness of 250N/m is indicated with CP3.250.

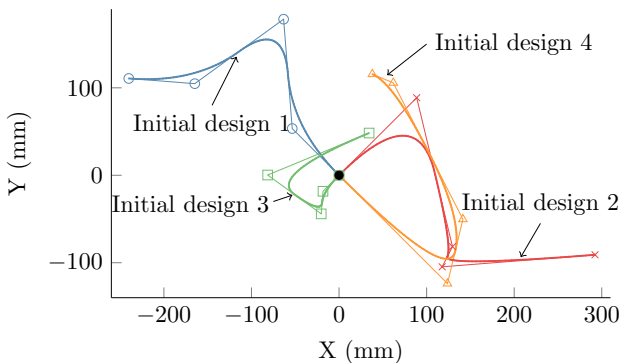
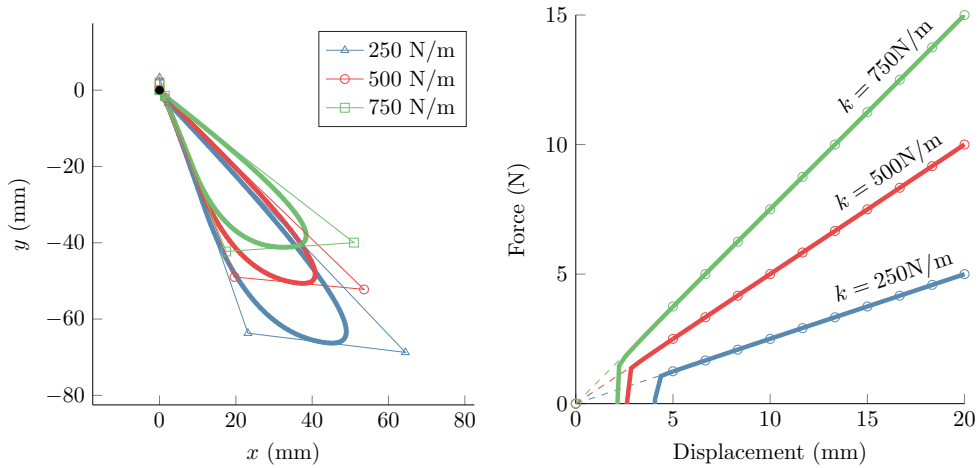


Figure 7.4: The four initial designs used during optimization, generated by random latin hypercube sampling.



(a) Best performing springs PP2.250, PP2.500 and PP2.750

(b) Force profiles of the best performing springs PP2.250, PP2.500 and PP2.750

Figure 7.5: Best pinned-pinned spring design results. The designs are rotated to align with each other. The relative axial error measures ϵ_A are 0.711, 0.157 and 0.279.

7

7.3.1. Pinned-Pinned Spring

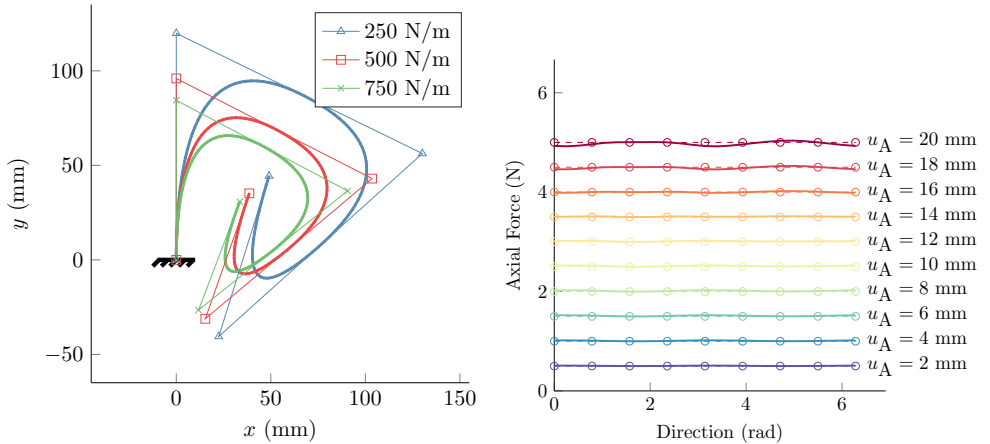
The pinned-pinned type of spring only had to be optimized for axial force as parasitic forces were absent. Optimizing for five different values of spring stiffness ($k = 250, \dots, 750 \text{ N/m}$) resulted in a range of designs - of which three will be shown every time, for overview in the figures. The designs from initial design 2, shown in Fig. 7.5a, generally perform best of all initial designs.

The resulting shapes tend to a drop-like shape, with the begin and end-point of the spring close together. For the different stiffness values the shapes resulting from the same initial design are comparable to each other. Only the size is different (Fig. 7.5a). The springs with lowest stiffness were the largest, while stiffer springs were smaller. The axial force-profiles of the best springs are shown in Fig. 7.5b. It can be seen that the best designs are seemingly spot on with the desired profile.

7.3.2. Clamped-Pinned Spring

Designing the clamped-pinned spring adds two new difficulties because of the added clamp. Paths in every direction had to be optimized and parasitic transverse forces were introduced. Again the optimization was run with 4 different initial designs and for 5 stiffness values of which the best designs are shown in respectively Fig. 7.6a. The results are (more or less) shaped like a spiral, with the pinned end-point at the center of the spiral. By increasing the required stiffness, the spring design becomes smaller.

Since the springs were optimized in 8 different track directions, it is interesting to see the force behavior at points in between the tracks. Therefore the axial force-



(a) Best performing springs CP3.250, CP3.500 and CP3.750

(b) The radial force profile of the best performing spring CP3.250

Figure 7.6: Best clamped-pinned spring design results. Designs are rotated to align with each other. The graphs represent force profile in circles around the zero point with constant radius for each level. The direction of displacement is shown on the horizontal axis. The relative axial and transverse errors ϵ_A and ϵ_T for the best spring are 1.817 and 0.957.

7

profile is shown for constant displacement length u_A . As if it were circling around the undeformed pinned end-point at a certain radius. These forces are shown for the best spring CP3.250 in Fig. 7.6b.

7.3.3. Clamped-Clamped Spring

The last new difficulty is introduced by also clamping the end-point of the spring, which introduces extra reaction moments at the tip. Once more the optimization was run for 4 different initial designs and the range of stiffness values, of which the best resulting designs are shown in Fig. 7.7a.

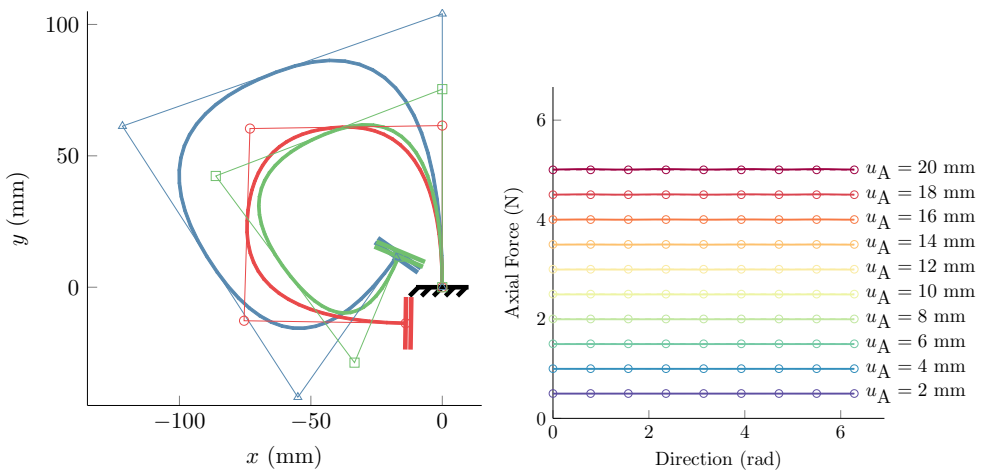
The resulting shapes either look like the shape of a horse-shoe (CC1.625), a spiral which is less spiraling than the clamped-pinned springs (CC1.250 and CC1.750) or an S-shape (CC2.250 and CC2.750). Also here the design becomes smaller as a higher stiffness is required.

7.4. Discussion

Following the structure of the Results section, the findings are discussed in order of the springs defined by the three different types of boundary conditions. The section is closed with some remarks about the general design of these springs.

7.4.1. Pinned-Pinned Spring

Because the pinned-pinned spring has a rotational freedom, the forces only need to be optimized over one track. Additionally the forces already always point to the point of rotation, making the transverse forces automatically zero. This makes it



(a) Best performing springs CC1.250, CC1.625 and CC1.750

(b) The radial force profile of the best spring CC1.250.

Figure 7.7: Best clamped-clamped spring design results. Designs are rotated to align with each other. The graphs represent force profile in circles around the zero point with constant axial radius for each level. The direction of displacement is shown on the horizontal axis. The relative axial and transverse errors ϵ_A and ϵ_T plus moments M of the best spring are 0.406, 0.102 and 0.211.

the spring with least residuals to optimize. When looking at the performance and comparing to the other spring types this appears to result in lower errors. It also results in a smaller spring compared to the others.

Not every initial design gives good zero free length springs. This means that the initial designs need to be chosen with care for this type of spring. A possible solution for this is to choose an already designed zero free length spring with another stiffness close to the new desired stiffness as initial design.

The general shape of the springs is a droplet shape, where begin and endpoint are close together. To get linearity and a low enough stiffness, the spring needs length, which it generates by making the droplet shape. The coinciding begin and endpoint are a direct result of the rotational freedom of the spring and extra enforced by the helping constraint of the distance between begin and endpoint (which speeds up the optimization considerably). The shape of the best performing springs in Fig. 7.5a has only three segments of considerable length, the first segment being very short (shorter than the width of the spring). This implies a redundancy in design variables, where the same spring shapes and performances might be obtained using less segments.

Possible applications for this spring are in the macro scale, where joints can be made, such as weight balancing [35, 161], robotics [46, 47], arm support [157, 158] and the like. Especially for systems with low stiffness in transverse direction or rotation this would be a good spring, since there are no parasitic transverse forces or torques which could cause errors in the movement of the system.

7.4.2. Clamped-Pinned Spring

For the clamped-pinned springs multiple track directions were added, furthermore a second type of error was introduced here. Initial design 1, 3 and 4 result in good springs for all chosen stiffness values, while initial design 2 only produces two well performing springs. Compared to the pinned-pinned springs the clamped-pinned are performing worse, which might be attributed to the added force requirements. On the other hand no convergence issues were encountered, since the newly introduced clamp prevents rigid-body motion.

Most of the designs found are around an error of 1-5%, but three have errors beyond 10%. In Fig. 7.6b can be seen that the forces in between the sample points do vary a little, however enough sample directions were used to capture the behavior in all directions as no strange peaks occur in between sample points.

The general spring shape can be characterized as being spiral shaped, see Fig. 7.6a. The low design stiffness gives need of generating enough flexure length. Combined with the fact that the stiffness needs to be equal in every direction, the material is distributed in an uniform shape with the same characteristics in every direction.

In practice this spring would also be used in macro applications due to the need of a joint like the pinned-pinned spring. In systems sensitive to transverse errors this spring type is less desirable. Still there are no parasitic torques possibly twisting the structure.

7.4.3. Clamped-Clamped Spring

The last spring type adds an extra clamp, introducing reaction moments. Surprisingly by the addition of this clamp, the found designs performed better in axial and transverse force in comparison to their clamped-pinned counterparts when comparing designs resulting from the same initial design and stiffness value. Here the resulting spring performances are more alike to each other in terms of performance.

It is difficult to say whether the reaction moments are big or small since there is no reference. If the connected structure is stiff in rotation direction this influence will of course be smaller than a very compliant structure in rotational direction. This causes the need of the spring to be designed in conjunction with the entire system it will be incorporated in. For instance a balancer with a mass on an arm [162] makes a rotation during operation. The designed spring was optimized for no rotations, so if a rotation were to be imposed, larger errors would occur. In such a case the (usually known) rotation would need to be used in the optimization procedure, possibly resulting in different designs than the ones presented in this work.

This kind of spring is very useful for applications where friction is a big issue as no joints are needed. This also results in application possibilities in systems on micro-scale.

7.4.4. General

Not in all applications a full circular range will be needed. Some systems only require one path or an oddly shaped area to have zero free length properties. Using this fact, application specific spring could be designed, behaving more precise in

the required area. This way for systems which are more critical with respect to transverse errors or reaction moments, a customized spring can be made.

7.5. Conclusion

From the research is proven that it is possible to design compliant zero free length springs, which have the desired force characteristics within a certain range. This is done for three different types which differ in boundary conditions; the pinned-pinned, clamped-pinned and clamped-clamped. For each type characteristic shapes are observed; for the pinned-pinned a droplet shape, clamped-pinned give a spiral and the clamped-clamped generally are shaped like a horse-shoe. In general the pinned-pinned spring has the lowest axial errors. The clamped-pinned spring has somewhat higher errors and additionally has an error in transverse direction. By using a clamped-clamped spring the axial and transverse error is reduced again, but a reaction moment is introduced. Not every initial design gives good springs, however using multiple initial designs it is possible to obtain at least one good working spring. It is proven that springs can be designed for different stiffness values. However the feasible values of stiffness are bounded by design area, minimum feature size and yield strength of the material. The lack of joints in the clamped-clamped spring enables a zero free length spring to be used in applications on micro scale.

8

Design and Characterization of a Linear Elastic Isotropic Meta-material with Zero Poisson's Ratio over Large Strains Using a Spring Lattice

Arnoud A.T.M. Delissen, **Giuseppe Radaelli**, Just L. Herder, Jonathan B. Hopkins

A lot of scientific effort is put into changing mechanical material properties by creating micro-structural architectures instead of chemical composition. This results in meta-materials, which are materials tuned to the needs of the user. To change the Poisson's ratio and Young's modulus, most current designs exploit mechanisms and hinges to obtain the desired behavior. However, this leads to nonlinear material properties and anisotropy, especially for large strains. In this work a method is proposed that makes use of specially curved leaf springs in a planar lattice. A material is designed with a isotropic Young's modulus and zero Poisson's ratio, both up to compressive and tensile strains of 0.1.

This chapter is a short version of a paper submitted for publication in Mechanism and Machine Theory [163], with focus on the results.

8.1. Introduction

In the field of mechanical meta-materials the goal is to change material properties not by altering chemical composition, but by changing the (micro)structure of the material.

Much research has been done on the subject of changing the Poisson's ratio. Especially materials with a negative Poisson's ratio (auxetic behavior) have been the interest for many researchers. Foam structures exhibited this behavior first [164] and later also more mechanism-like structures [165]. Mechanisms using hinge behavior have been exploited to create auxetic materials [166–168], but also incompressible ($\nu = 0.5$) pentamode materials [169, 170]. These mechanisms can also be recognized in material punctured with differently shaped holes to change the material properties, especially for compression [171–174]. The opposite of this idea is to make cuts into the material, which enables the material to be extended [175, 176]. Other Poisson's ratios have been achieved by making variations on the honeycomb [177–180], like a zero Poisson's ratio [181–183]. The natural material cork has a zero Poisson's ratio and also shows a micro structure resembling a honeycomb [184].

Others do not focus on the Poisson's ratio but on controlling the modulus of elasticity by different honeycomb structures [185], a composite material [186] or changing the dimensions of periodic structures [187]. A more complete overview of mechanical metamaterials can be found in [188, 189].

The work stated above is mainly valid for small deformations and problems occur for larger deformations. Isotropy might be lost and nonlinear material behavior occurs, which may not always be desirable. Some propose to introduce springs in order to create an isotropic structure [190, 191]. For small strains a planar material is isotropic when it contains hexagonal (6-fold) symmetry [192]. However, especially for large strains it often becomes difficult to keep isotropy since symmetries get lost and nonlinear effects occur.

Isotropy is hard to obtain with the current structures using straight members, favouring one direction over the other in terms of compliance. Additionally, the current research on zero Poisson's ratio materials is very limited. Therefore a new concept is introduced. Instead of using structures based on straight beams and hinges or honeycombs, a fully compliant (leaf) spring element is used in a lattice. Not just any compliant element will do, so the spring is especially optimized to show no favourable direction in its stiffness, i.e. the same stiffness in every direction. During this work we will limit ourselves to altering the (in-plane) Young's modulus (E) and Poisson's ratio (ν).

A theoretical background and methodology will be given to design a special spring and material structure with the desired properties. The goal is that by using this method the designer is able to synthesize a planar material structure, which is linear elastic and isotropic for large strains. The Young's modulus is directly controllable by the spring stiffness and automatically the Poisson's ratio is zero.

First the method (Section 8.2) describes spring design using approximate material properties derived from the structure using analytical spring elements. The results section (8.3) shows the resulting design and performance of the spring itself.

Also the properties numerically computed in a larger lattice are given in the results and are compared with the analytical solutions. Finally, the results are interpreted and difficulties are identified.

8.2. Method

In this abstract version only the essence of the steps of the method are explained. The reader is referred to [193] for a complete elaboration.

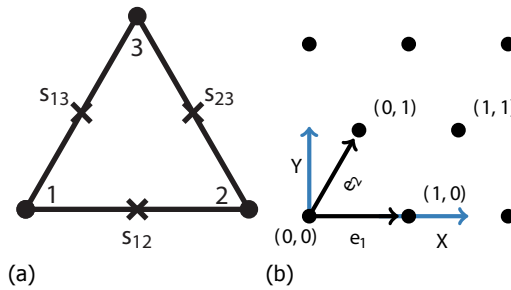


Figure 8.1: The architecture of the meta-material consists of a lattice of triangular unit cells. The structure exhibits 6-fold symmetry, thus ensuring isotropic properties in-plane at least for small strains [192]. a) The unit cell has one ideal spring on each edge (at \mathbf{s}_{12} , \mathbf{s}_{23} and \mathbf{s}_{13}), which deliver the stiffness of the material. b) The triangular cells form an hexagonal grid.

In the process of designing the material structure, first the architecture is chosen by defining the shape of the unit cell which is then placed into the lattice. The present material is based on a triangular unit cell, because it ensures isotropic properties, at least for small strains [192]. This unit cell has one ideal spring [35, 194] on each edge (at \mathbf{s}_{12} , \mathbf{s}_{23} and \mathbf{s}_{13}), which delivers the stiffness of the material, see Fig. 8.1a. At each corner of the triangle, a node (1, 2 and 3) exist which connects the triangle to the next cell in the grid.

Using the concept of Representative Volume Element (RVE), the relation between spring characteristics and the material properties is analytically derived. With this approximation, the suitable spring properties can be chosen and the specifics for the spring design are elaborated. Finally the design is validated with numerical simulations, which show the material performance.

Because discrete triangular unit cells are used, it is difficult to apply any uniaxial compression or extension conditions. These conditions needs to be applied in order to determine the homogeneous material properties and should be imposed on a rectangular area. To obtain this, the concept of the Representative Volume Element (RVE) is used [195]. This is a volume containing enough material to capture the bulk properties, while still being small enough for quick calculations.

From analytical relations between the strains of the RVE, the nodal forces and the nodal displacements (shown in Fig. 8.2), the material properties can be derived. In this derivations it is assumed that

1. The deformations of all unit cells are considered to be uniform. This implicates that knowing the deformation of one unit cell automatically results in knowing the

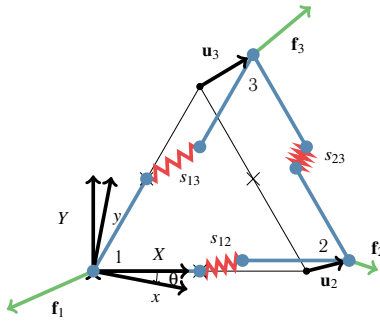


Figure 8.2: Triangular unit cell consisting of rigid segments connected by an ideal spring at the middle of each edge of the triangle. The forces and displacements are defined in the rotated x - y coordinated system.

deformation of the total RVE.

2. At the nodes no rotations are implemented. This removes torques and spring deformations due to rotations.

The Young's modulus is found to be equal to

$$E = \frac{\sigma_x}{\epsilon_x} = 2\sqrt{3}\kappa, \quad (8.1)$$

where κ is the spring stiffness per unit thickness of the material. Moreover, because of the isotropy of the ideal spring, it also results that an applied strain in x -direction results in no reaction force in y -direction, and thus no strain in y -direction. This causes the Poisson ratio to be zero regardless of the strain in x -direction

$$\nu = -\frac{\epsilon_y}{\epsilon_x} = 0. \quad (8.2)$$

Spring design

Until now the ideal spring has been treated as a mathematical element. To make a physical element from this, a curved leaf spring is used. The spring shape is obtained using an optimization algorithm as described in Chapter 7. For this specific application it is desirable to have a symmetrical structure to keep the symmetries in the triangular structure intact. Therefore the spring is symmetrical about the y -axis. This also reduces the optimization problem - half of the design variables are known and only half of the reaction forces needs evaluation¹. Also an additional constraint is introduced to improve the shape of the spring with respect to the triangular lattice. The spring is made to fit within the triangular subsection of the unit cell, as indicated in Fig. 8.3a, to prevent springs intersecting other springs. Points outside of the triangle are penalized.

Numerical evaluation

The next step is to incorporate the spring design into a lattice and perform a numerical analysis on the lattice. This way the effect of moments and errors in the spring

¹Due to the symmetry of the spring, the forces are mirrored about the x -axis. Thus only half of the directions have to be analyzed.

design can be analyzed. The clamped spring is rigidly connected to the nodes, having freedoms u_x , u_y and θ . By adding constraint equations with Lagrange multipliers the springs are connected (via translation and rotation of the nodes) into the lattice.

8.3. Results

Spring design

The result of the optimization is one single spring design, which is shown in Fig. 8.3a. The resulting shape fits well within the constrained area. The axial force, axial force error, transverse force are shown in respectively Fig. 8.4a, 8.4b and 8.4c.

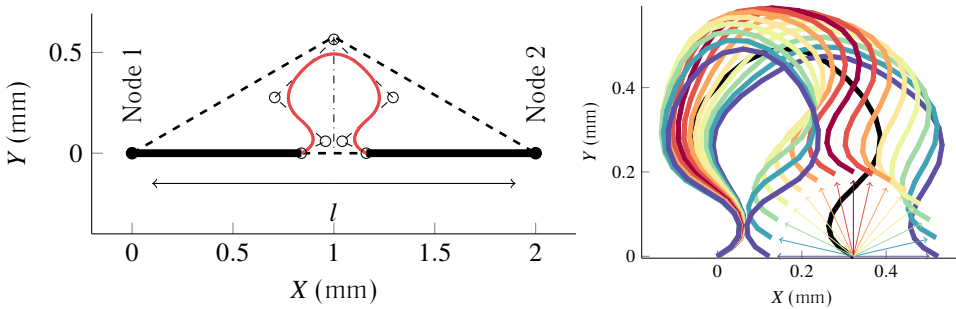


Figure 8.3: (a) The final spring design (red) within the design area (dashed). The unit cell length is l . Spring thickness is to scale. (b) The spring displaced to different orientations (colors), over a maximum displacement of u_{end} . Springs are to scale.

To quantify the performance of this spring the relative axial error ϵ_A and the relative transverse error ϵ_T are used [151]. These give the maximum error of respectively the realized axial force and the transverse force, with respect to the desired axial force (in percentages). The resulting values are $\epsilon_A = 2.103\%$ and $\epsilon_T = 0.104\%$.

Furthermore, the maximum reaction moment was found to be $9.6 \cdot 10^{-6}$ Nm.

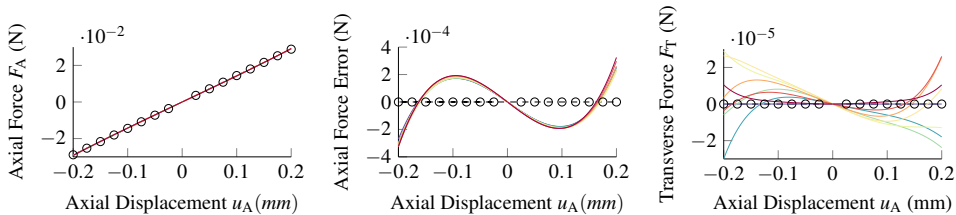


Figure 8.4: Spring characteristics in different displacement directions, indicated by the different colors, corresponding to those in Fig. 8.3b. The dashed line is the desired value and circles indicate locations of sample points used for optimization.

Numerical simulation results

A strain is applied in either extension or in compression. An example of a deformed lattice in extension compared to the undeformed is shown in Fig. 8.5. Information about the stress σ_x (Fig. 8.6a) and the strain ϵ_y (Fig. 8.6b) is extracted from the analysis results as function of the strain ϵ_x , which was applied in compression and extension. The strain is positive in extension. The rotation of the nodes were found to be identical to each other. Additionally being very small, with rotations not exceeding 10^{-4} rad within the range of 0.1 and not exceeding 10^{-3} rad for strains up to 0.2. Also in these simulations the unit cells deformed uniformly.

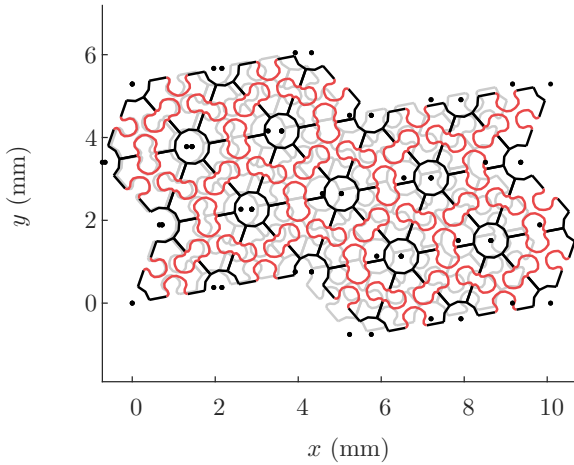


Figure 8.5: Example of numerical simulation on a Representative Volume Element (RVE). Application of a strain in x-direction ϵ_x results in transverse strain ϵ_y close to zero.

Material properties and performance

Finally the linearized material properties are calculated over the range of strains and for different material orientations. These can be seen in Fig. 8.7a for the modulus of elasticity and Fig. 8.7b for the Poisson's ratio. Within the range of $|\epsilon_x| \leq \epsilon_{\max} = 0.1$ the material properties can be summarized as:

$$E = 0.99 \pm 0.013 \text{ MPa} \quad \nu = (0.46 \pm 0.23) \cdot 10^{-3}. \quad (8.3)$$

8.4. Discussion

Spring Design

The optimization procedure results in a spring design (Fig. 8.3a) meeting the set requirements of force and design area. In this case it is a smooth harp-shaped spring.

To obtain the spring characteristic, the spring is optimized in different directions (Fig. 8.3b). Figure 8.4a shows the fit of the spring forces to the desired axial (linear) force profile. With a maximum relative error value of $\epsilon_A = 2.103\%$ it is considered good (comparing to springs in previous work [151]). Also in terms of transverse

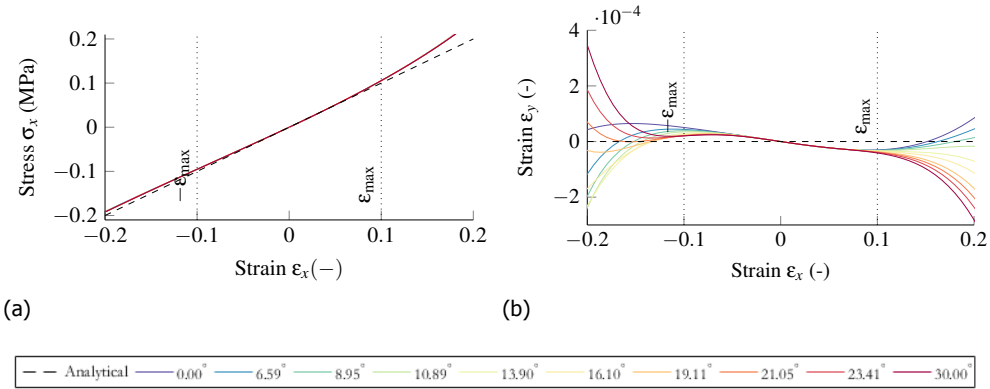


Figure 8.6: The responses in terms of (a) stress in x -direction σ_x and (b) transverse strain ϵ_y . The slope of the graphs determines the material properties respectively E and ν . The maximum and minimum strain limits are indicated, as is the analytical estimation. Different lattice orientations are indicated with different colors (refer to the online version).

force (Fig. 8.4c), the maximum relative error is small with a value of $\epsilon_T = 0.104\%$. The question is how these errors will transfer to the material properties.

Neglected so far are the reaction moments, with a maximum value of $9.6 \cdot 10^{-6}$ Nm. It is hard to indicate whether this is high or low since there is no reference.

Analytical vs. Numerical

The full RVE simulation was run for a number of material orientations. One of these is shown in Fig. 8.5. In this example the lattice is loaded in extension, but also simulations compressing the material were executed. During compression springs came just in contact with each other when the strain limit ϵ_{\max} was reached.

Two quantitative results can be distinguished from the fact that a strain was applied - first the stress (Fig. 8.6a) and secondly the transverse strain (Fig. 8.6b). In these figures the stress and strain are shown for different orientations and additionally compared to the analytical approximation. It can be seen that the stress-strain behavior is nicely linear between the strain limits, outside these limits it begins to deviate. Also the transverse strain ϵ_y , which analytically is supposed to be zero, keeps low values ($< 10^{-4}$) in between the strain limits. This suggests that the small errors don't have a significant influence on the material behavior.

It was also observed that the rotations were not exceeding 10^{-4} rad within the strain limits. This supports the assumption in the analytical derivation ignoring rotations. The size of these RVEs are still relatively small, but there is freedom in these simulations for the unit cells to deform non-uniformly. The unit cells were all found to deform with the same deformations, which supports the assumption of uniformity.

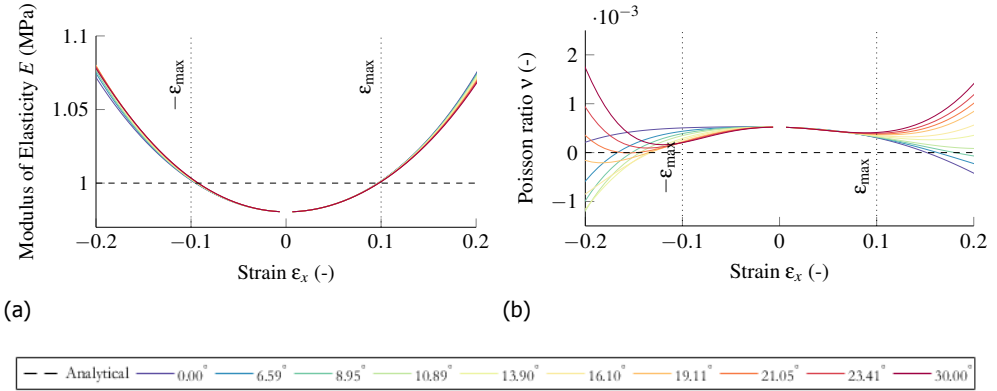


Figure 8.7: Over a strain range, the material properties are shown; (a) the modulus of elasticity E and (b) the Poisson's ratio ν . Different colors indicate the different lattice orientations. The maximum and minimum strain limits are indicated, as is the analytical approximations of the respective properties.

Material Properties and Performance

The material behavior is described by the modulus of elasticity (Fig. 8.7a) and the Poisson ratio (Fig. 8.7b). Within the strain limits the Young's modulus is very close to the desired elasticity with a value of $E = 0.99$ MPa, although there is a little offset downwards.

The Poisson ratio, with a value of $\nu = 0.46 \cdot 10^{-3}$, is constant within the strain limits compared to the values outside of the limit, which rapidly change (Fig. 8.7b). There is a slight offset above the zero level. This might be explained by the transverse force error (Fig. 8.4c) having in general a slightly downwards trend with respect to the displacement. Although a Poisson ratio value in the order of 10^{-3} might be negligible considering the classical limits of the Poisson's ratio are $-1 \leq \nu \leq 0.5$.

Besides isotropy for small strains, which are enforced by the material symmetries [192], it is also shown that isotropy is kept up to strains of $\epsilon_{\max} = \pm 0.1$. Up to a variation of the Young's modulus of ± 0.013 MPa at maximum strain, which is an error of 1.3%. The variation of the Poisson's ratio is $\pm 0.23 \cdot 10^{-3}$, which is negligible compared to the classical limits.

8.5. Conclusion

By placing ideal springs into a triangular lattice, a material approaching a zero Poisson's ratio and a controllable modulus of elasticity can be created. Using an analytical approximation, the desired Young's modulus can be related to a spring stiffness and is calculated as $E = 2\sqrt{3}\kappa$. The Young's modulus is thus directly proportional dependent on the distributed spring stiffness (spring stiffness per unit thickness in z -direction). Additionally, the analytical case proves in-plane linear elasticity, isotropy and a zero Poisson's ratio - under assumptions of a uniform deformation of all unit cells and ignoring rotations. These assumptions are supported by numerical simulations of larger lattices.

With the desired spring stiffness known, a fully compliant spring element is optimized. This results in a spring characterized with constant stiffness in every direction (up to a maximum relative error of 2.103%) and zero force perpendicular to this direction (with a maximum relative error of 0.104%).

Starting with a desired Young's modulus of $E = 1$ MPa, a material structure is created with $E = 0.99$ MPa. The Poisson's ratio is found to be $\nu = 0.46 \cdot 10^{-3}$. Both properties are isotropic within a strain range of $\epsilon \pm 0.1$, with only a variation of ± 0.013 MPa for the Young's modulus and $\pm 0.23 \cdot 10^{-3}$ for the Poisson's ratio.

9

Potential energy fields of systems with torsion stiffness

Static balance can be applied to improve the energy efficiency of mechanisms. In the field of static balancing, there is a lack of knowledge and design methods that are capable of dealing with torsional stiffness. This paper presents a design approach for statically balanced mechanisms, with the focus on mechanisms with torsional stiffness. The approach is graphical in nature and is based on the requirement of constant potential energy. The first achievements of this approach are presented as two conceptual designs of different types of mechanisms. One of them is developed further into a prototype and tested. The prototype has a correlation coefficient of 0.96 and a normalized mean squared error of 0.12 with respect to the mechanical model of the conceptual design.

This chapter is a short version of a paper published in the Journal of Mechanical Design (2011) [196], and in the in the proceedings of the ASME IDETC 2010 34th Mechanisms and Robotics conference, Montreal (Canada), August 2010 [94].

9.1. Introduction

In the context of statically balanced mechanisms where elasticity is involved, the use of extension springs is frequently investigated [35], while little work has been done that makes use of torsion springs. Torsional stiffness can be realized in many ways with the use of different types of springs, e.g., spiral springs, helical torsion springs, torsion bars, rectilinear springs in combination with pulleys, leaf springs etc. This consideration suggests that the ability to balance mechanisms with torsion stiffness can offer many opportunities in a diversity of designs. Also, other advantages appear with the employment of torsion springs like compact and safe designs because torsion springs do not elongate and can therefore be encased more easily. Moreover, compliant mechanisms are sometimes modeled as rigid bodies connected by torsion springs through the use of the Pseudo-Rigid Body Model (PRBM) [143]. Therefore, balancing general systems with torsional stiffness could lead to the balancing of compliant mechanisms.

The goal of this chapter is to present a novel, general, extensible and easy-to-use design approach to balance existing mechanisms and to create statically balanced mechanisms from scratch. Our approach is based on the requirement of constant potential energy, necessary for static balance. In this chapter, the focus lies in the use of linkages with torsional stiffnesses, but potentially the approach can be extended with different elements. Example results of this approach are presented as conceptual designs. Finally the design, construction, and testing of one concept is shown.

9.2. Method

9.2.1. Potential energy fields

A statically balanced mechanism is a mechanism in which the potential energy U , is constant over a certain range of motion [197]. Such a mechanism exhibits a neutral equilibrium along a given range of motion. From the relation between potential energy and the total external force vector \mathbf{f} applied on the system

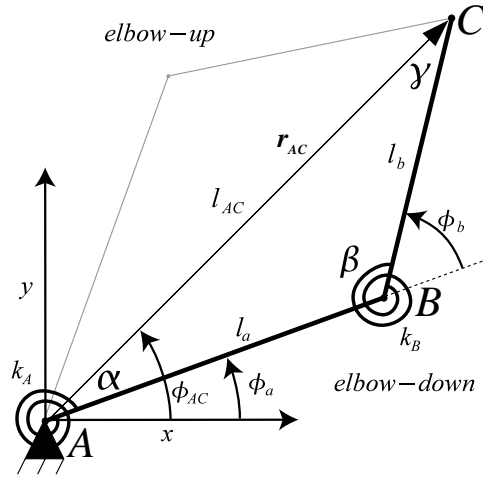
$$\nabla U = \mathbf{f}, \quad (9.1)$$

where ∇ defines the gradient of a function with respect to the chosen degrees of freedom and the entries of \mathbf{f} are related to the same degrees of freedom, it is recognized that the direction of the force is in the direction of steepest descent of the potential energy. This, on the other hand, implies that the force is zero in the perpendicular direction, which is tangent to the isopotential line (contour line) at that location. It follows that a system is in static equilibrium at every point if the motion is constrained along an isopotential energy line. A graphical representation of the potential energy field can aid the designer to conceive mechanisms that have a constant potential energy.

Energy derivation of linkages with torsion springs

Consider the model in Fig. 9.1. The model consists of two links with lengths l_a and l_b in series (called a dyad) with a torsion spring at point A acting between ground

Figure 9.1: A dyad element consists of two links and two torsion springs. For every location of point C there are two possible configurations: *elbow-down* and *elbow-up*.



and the first link, and a torsion spring at point B acting between the two links. The potential energy function to be obtained is the total potential energy of the system plotted at the location of the endpoint C .

Let the location of C with respect to the attachment point A be the vector \mathbf{r}_{AC} with length l_{AC} and angle ϕ_{AC} . α , β and γ are the internal angles of the triangle ABC . From the cosine rule we know that

$$\alpha = \arccos\left(\frac{l_b^2 - l_a^2 - l_{AC}^2}{-2l_a l_{AC}}\right) \quad \gamma = \arccos\left(\frac{l_a^2 - l_b^2 - l_{AC}^2}{-2l_b l_{AC}}\right). \quad (9.2)$$

Note that these relations are valid for both the *elbow-down* and the *elbow-up* solutions. The potential energy of the system is given by

$$U = \frac{1}{2}k_A (\phi_a - \phi_{a0})^2 + \frac{1}{2}k_B (\phi_b - \phi_{b0})^2, \quad (9.3)$$

where k_A and k_B are the spring stiffnesses, ϕ_a is the angle of the first link, ϕ_b is the relative angle between the two links, ϕ_{a0} and ϕ_{b0} are the neutral angles of the torsion springs. The angles ϕ_a and ϕ_b describe the current state of the system which depends on the endpoint location. They are found by

$$\phi_a = \phi_{AC} \mp \alpha \quad \phi_b = \pm (\alpha + \gamma), \quad (9.4)$$

which have different solutions for the *elbow-down* and the *elbow-up* conditions.

Substitution of Eq. (9.2) and Eq. (9.4) into Eq. (9.3) gives the potential energy as a function of the polar coordinates of the endpoint, l_{AC} and ϕ_{AC} . Transformation into the Cartesian coordinates x_{AC} and y_{AC} is useful for further manipulation. The function has two independent variables and can thus be plotted as a surface plot above the location of point C , see as an example Fig. 9.2c. Complex solutions of the equation indicates that the coordinate cannot be physically reached by the dyad.

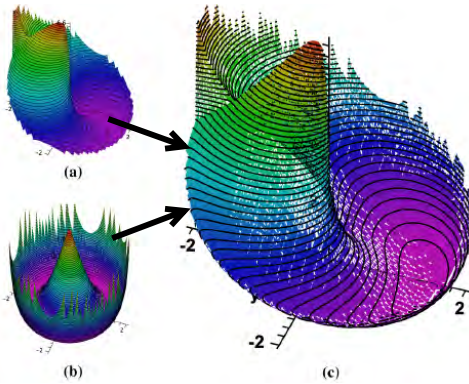


Figure 9.2: The potential energy of a dyad is a linear combination of the energy in both springs. (a) The contribution of the first spring, $k_B=0$, $\phi_a=-\frac{\pi}{4}$. (b) the contribution of the second spring, $k_A=0$, $\phi_b=\frac{\pi}{2}$. (c) Linear combination of two springs, elbow-down.

In order to understand the contribution from both the springs to the total energy, consider Fig. 9.2. The total energy function is a linear combination of the energy of both springs.

Combinations of systems

If mechanisms can be built out of multiple smaller components of which the energy functions are known, and particularly if the components are joined at the points for which the energy is calculated, the total energy function expressed at that particular point is the sum of the energy functions of the components.

Figure 9.3 shows some energy graphs of the combination of two dyads. Combining two components that have two solutions each, gives four solutions for the total system: two solutions with one *elbow-up* and one *elbow-down* configurations (9.3a and 9.3d), one with both *elbow-down* configurations (9.3b) and one with both *elbow-up* (9.3c). The latter two solutions normally result in asymmetric fields.

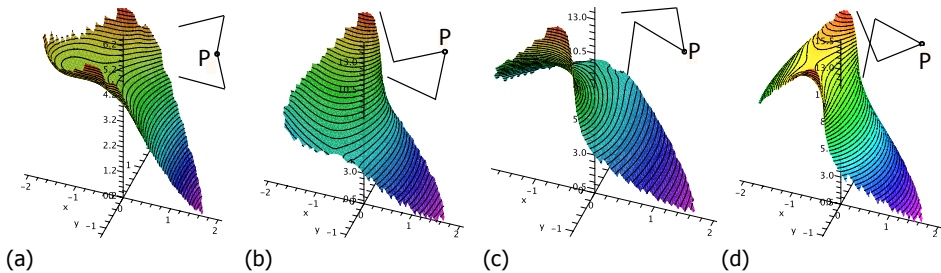


Figure 9.3: Potential energy of two dyads joined at point P . (a) One elbow-up and one elbow-down, (b) both elbow-down, (c) both elbow-up and (d) one elbow-down and one elbow-up.

Optimization

Designers can use the visual representation of the potential energy field to identify isopotential lines of interest. Constraining the system along such a line yields him a statically balancer mechanism. In this interactive part of the design process the aim

is to find approximate solutions, which can be refined in a subsequent optimization phase. In the optimization the design parameters are the spring stiffnesses and neutral angles, the link lengths and the ground coordinates of the dyads. The objective is to minimize the error between the energy and a constant value along a desired motion range. More details on the optimization procedure can be found in [196].

9.3. Examples

To illustrate the practical use and some first achievements of the presented design approach, this section presents some example mechanisms.

In the first example two dyads, mirrored w.r.t. the horizontal axis, are connected at point P . The point is constrained to move over a straight line by a linear guide, see Fig. 9.4a.

The second design example is composed of four dyads configured as two times the first example, mirrored with respect to the y -axis, see Fig. 9.5a. The resulting mechanism has the particularity that it moves with little effort over a straight line without being constrained over that line. The reason is that the potential energy field has canyon-like shape: a constant energy line on the bottom and a positive gradient perpendicular to that line, see Fig. 9.5b.

The third example consists of a mass connected to the endpoint P of a crank with length $r_{c,r}$, and a dyad connected at that same point, see Fig. 9.6a.

The fourth and last example consists of two dyads joined in P , constrained to move along a circle by a crank of length $r_{c,r}$, see Fig. 9.7a. The dyads are symmetric with respect to the x -axis.

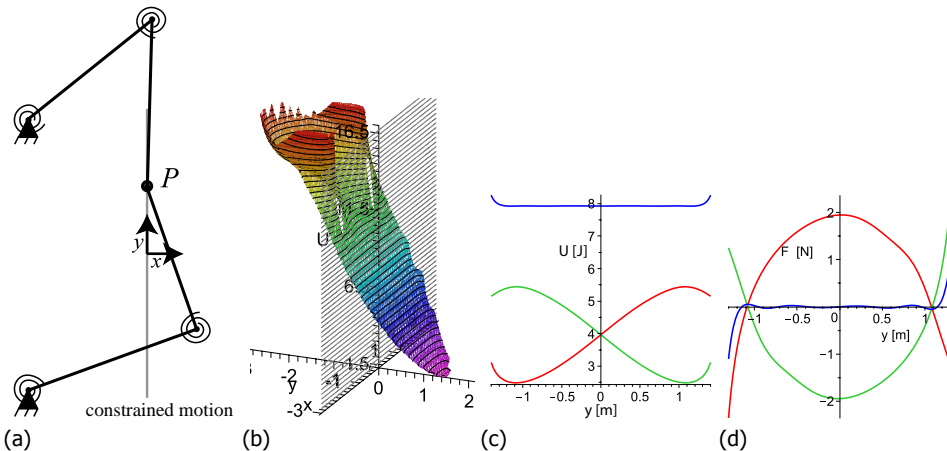


Figure 9.4: Example 1. (a) Two symmetric dyads are connected at point P and constrained to move along a vertical line. (b) Potential energy field. (c) Potential energy over constrained path. (d) Force in y -direction over constrained line. The red and green lines are the separate dyads and the continuous-blue line is the coupled system.

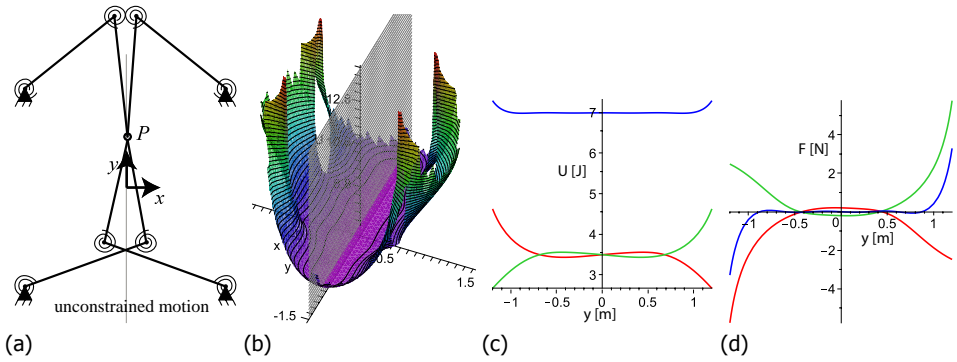


Figure 9.5: Example 2. (a) Four symmetric dyads are connected at point P and move unconstrained along a vertical line. (b) Potential energy field. (c) Potential energy along the bottom of the canyon-shaped field, where $x = 0$. (d) Force in y -direction along the same line of motion. The red and green lines are the contributions of separate dyads and the blue line is the coupled system.

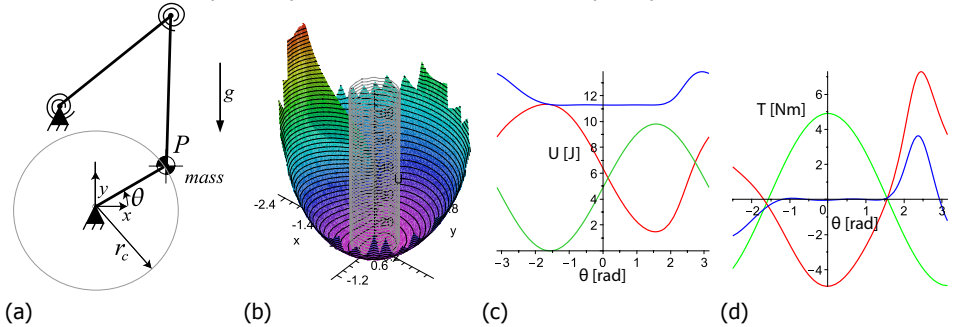


Figure 9.6: Example 3. (a) A crank with a mass balanced by a dyad. The mass is 1 kg. (b) Potential energy field of dyad and mass. (c) Potential energy along constrained circle. (d) Torque on the crank. Green lines are the unbalanced mass, red lines are the dyad and the blue lines are the combined systems.

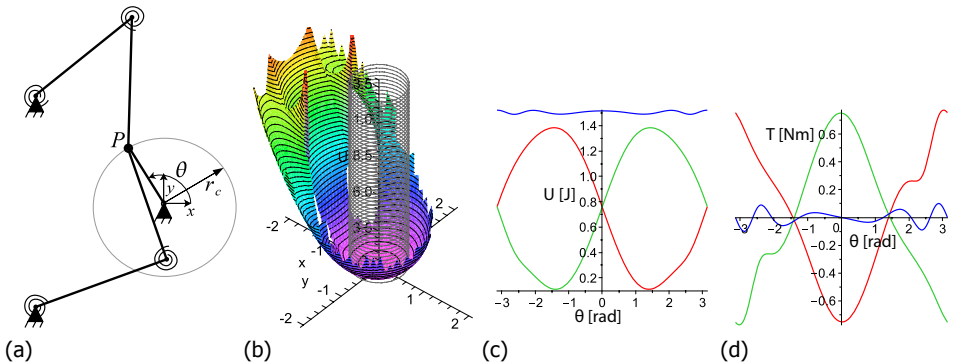


Figure 9.7: Example 4. (a) Two dyads coupled and constrained over a circle by a crank. (b) Potential energy field. (c) Potential energy along constrained circle. (d) Torque on the crank. Red and green lines are the separate dyads and blue lines are the coupled system.

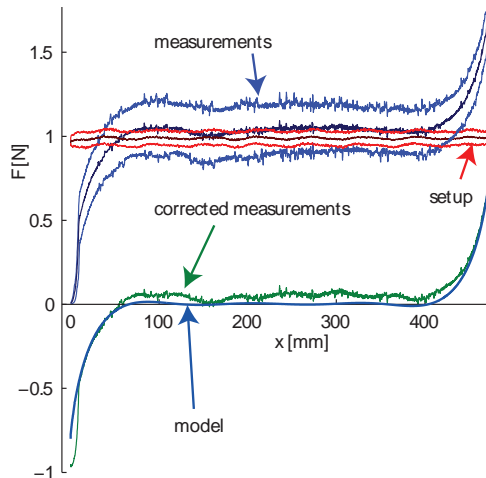
9.3.1. Measurements results

A design similar to example 1 but with different design parameters has been constructed and tested. The force along the direction of motion has been measured in two directions. The measurements are performed by connecting the mechanism through a cable to a vertical tensile test machine. The cable is kept in tension by a weight connected on the other side of the mechanism. Since the mechanism must move in the horizontal plane to avoid effects of gravity, the vertical motion is redirected by a set of pulleys. The results of the force measurements are plotted in Fig. 9.9. The figure shows the measured force in forward and backward direction for the whole mechanism including the test setup, i.e. mass and pulleys, and the mean of the hysteresis loop. Also, the hysteresis loop of the force measured with the setup only is shown, i.e. mass and pulleys, together with the mean of this hysteresis loop. From these previous measurements, the force coming from the mechanism only is obtained. This force is compared with the force predicted by the model.



Figure 9.8: (a) Picture of the prototype and (b) detail of a torsion spring at the connection of two links.

Figure 9.9: Measurement results. (a) For every set of three lines from top to bottom: Forward measurement, mean of forward and backward, backward measurement. Measurements are performed on the mechanism with the setup, and on the setup alone. Subtracting both gives the values for the mechanism alone. This force is compared to the force obtained by the model.



9.4. Conclusion

This chapter presents a novel approach for static balancing of mechanisms, focusing on systems with torsion springs. The approach is based on the fact that the total potential energy of a system is constant when statically balanced.

Graphical inspection of the potential energy fields and manipulation of the design parameters can lead to systems that are close to static balance.

A prototype was built that matches the model well with a correlation coefficient of 0.96 and a NMSE of 0.12 after filtering the effects of friction.

10

A lumped compliant statically balanced self-guiding straight-line mechanism

Emile J. Rosenberg, **Giuseppe Radaelli**, Just L. Herder

This chapter presents a lumped compliant version of the statically balanced self-guiding straight-line mechanism presented in Chapter 9. A preliminary design has been realized by translating the rigid-body model into a lumped compliant mechanism using the pseudo-rigid body model of short flexures. The errors introduced by the simplifications of the model are minimized through iterative adjustment of the design parameters. To this end a more accurate finite element model is used. The results have been validated experimentally. The prototype exhibits low resistance along the main line of motion, where it has three stable equilibrium positions.

This chapter is a short version of the paper published in the in the proceedings of the ASME IDETC 2010 34th Mechanisms and Robotics conference, Montreal (Canada), August 2010 [198], with focus on the result.

10.1. Introduction

Compliant mechanisms with so-called lumped compliance are mechanisms where the deformation of the structure occurs at certain concentrated areas while the rest of the mechanism is relatively rigid. In contrast, distributed compliant mechanisms derive their deformation from larger flexible areas smoothly integrated in the structure. As long as these flexible areas, also designated as flexure hinges, are relatively small, the kinematics of such mechanisms approximate the kinematics of rigid body mechanisms quite well. To model the kinematics and mechanics of such mechanisms the pseudo-rigid body model (PRBM) [143] can be applied, where the flexure hinges are replaced by pin joints with a torsion spring, see Fig. 10.1.

This work presents a preliminary evaluation of the conversion from a PRBM to a lumped compliant mechanism for a statically balanced, self-guiding straight-line mechanism.

10.2. PRBM design

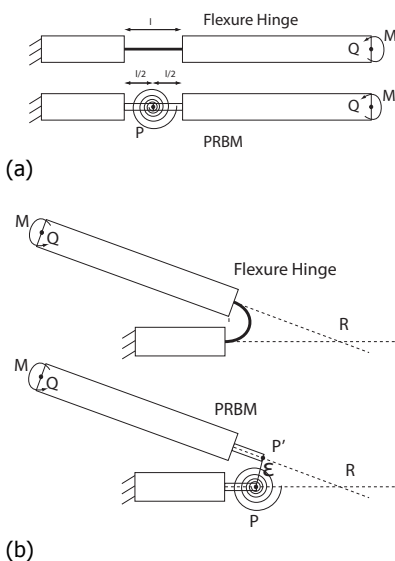


Figure 10.1: Flexure hinge and corresponding Pseudo-Rigid Body Model. (a) Straight. (b) Large angle: joint is pulled apart.

The stiffness of a flexure hinge is assumed to be constant when only a moment is applied in point Q . In a PRBM a flexure hinge is modelled as a pin joint with torsional stiffness connecting two rigid bodies. Some approximations are embodied in the conversion from PRBM to lumped compliancy which results in some inaccuracies. An inaccuracy arises when assuming rigid body kinematics equal to the kinematics of a lumped compliant mechanism. For relatively small angles [199] the pin joint is considered to have a fixed position with respect to the rigid links. For larger angles this approximation remains no longer valid. see Fig. 10.1b. Hence, an error ϵ is introduced which will initially be taken for granted and afterwards corrected for. Furthermore it is assumed that the largest contribution to the deformation comes from a moment load. Therefore, the force loads on the hinge will be disregarded. This introduces another source of inaccuracy in the PRBM.

The PRBM of the design considered in this work is a result of Chapter 9. Figure 10.2 shows the five stable equilibrium positions along a rectilinear motion of the middle point, the connection point of the four dyads. Figure 10.3 shows the force-displacement curve of the mechanism (red line). The curve has nine intersections with the x-axis, indicating nine equilibrium points. These equilibrium points are alternately stable and unstable, the first and last ones being stable.

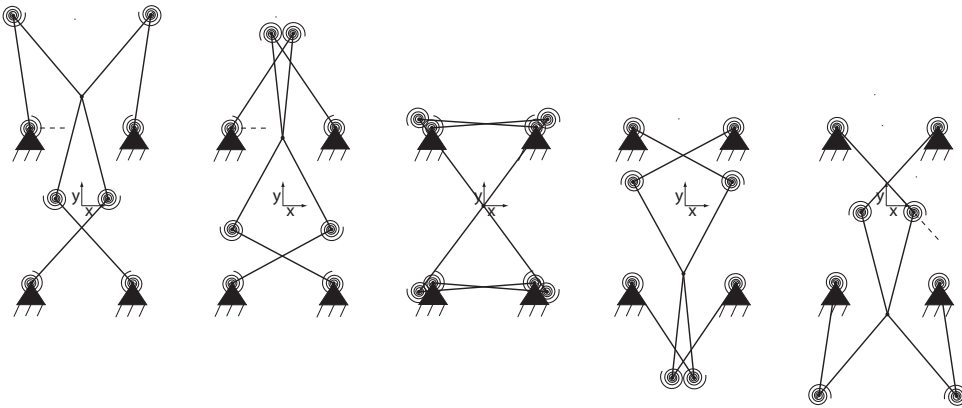


Figure 10.2: PRBM of self-guiding straight line mechanism in its five stable equilibrium configurations.

10.3. FEM evaluation and prototype

To verify the behavior of the model a finite element model of one lumped compliant dyad is set up. The mirrored dyads do not need to be modelled separately, since the forces can be mirrored and summed together afterwards. The model is made in ANSYS® and is built with planar BEAM3 elements. The thickness of the flexure hinges is 0.15mm , the rigid parts are 10m thick, and the width of the whole construction is 38mm . The material is steel with a modulus of elasticity of 210GPa . Both flexure hinges and the rigid parts consist of 30 elements each. The origin of the dyad is constrained in all directions, while the endpoint is moved 0.67m over the straight line.

The reaction force in the vertical direction is extracted for every point on the straight line. The force-displacement of the initial FEM model is shown in Fig. 10.3 (blue line). Due to the errors in the model only three stable equilibrium positions are obtained.

The FEM is tweaked manually in order to reduce the difference between the FEM and the PRBM, by adjusting the location of the clamping points. This yields an improved force-displacement characteristic, shown in Fig. 10.3 (green line). The corrected model has five stable equilibrium positions again.

A prototype has been constructed to evaluate the PRBM and the FEM model, see Fig. 10.4. The prototype exhibits three stable equilibrium positions, shown in Fig. 10.5

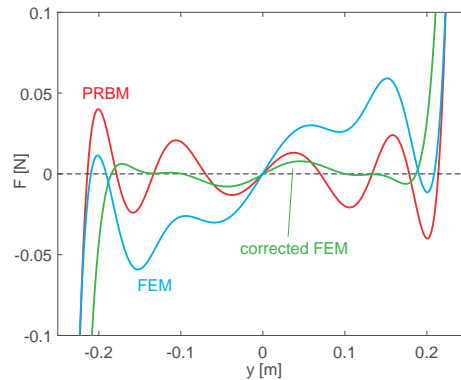


Figure 10.3: Force-displacement characteristic along the middle line for the pseudo-rigid body model (red), the initial FEM model (blue) and the corrected FEM model (green).

10.4. Discussion

The mechanism has been conceived starting from the assumption that a lumped compliant dyad has the same energy function as a rigid body dyad.

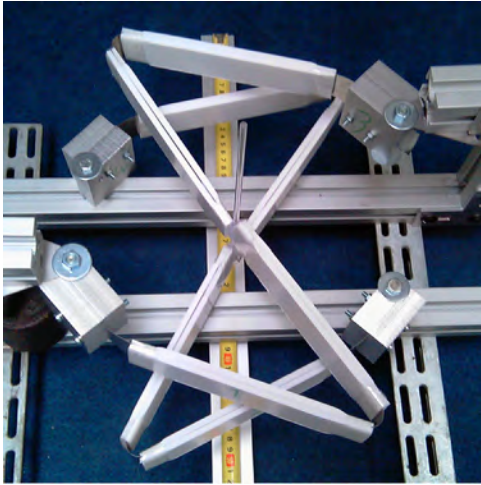


Figure 10.4: Picture of prototype

The error introduced by this rough assumption is the reason why the lumped compliant dyad is not yet readily implementable in the energy approach as a basic element. The iterative, error correcting approach used here gives a first feasibility indication, but it is rather time consuming and rough. The aim is to have a predictive synthesis method, rather than an error-correcting approach.

It is recommended to find an accurate energy description of a lumped compliant dyad. The dyad could be modelled including the length of the curved flexures, with the assumption that it bends with a constant curvature. Alternatively it may be possible to model the flexure with two pin joints

and two torsion springs. The kinematics of these two models would strongly improve the resemblance with the lumped compliant model. Ultimately, the aim is to have accurate energy descriptions of fully compliant segments to use as basic elements for the energy approach.

10.5. Conclusion

A lumped compliant version of the statically balanced self-guiding straight-line mechanism has been designed and constructed. The models reveal five stable equilibrium positions and nearly static balance throughout the range of motion. The physical construction shows up to three stable equilibria.

The error correcting approach to make the translation from rigid body to lumped compliance gives acceptable results. Developing energy descriptions of lumped compliant parts can improve the predictability of the approach for better and faster results.



Figure 10.5: Sequence of stable equilibrium positions.

11

A potential energy field (PEF) approach to the design of a compliant self-guiding statically-balanced straight-line mechanism

For the conception of compliant mechanisms various design aids have been proposed, including some graphical ones. In this work we propose to use the potential energy field of elastic systems to characterise their behavior over a large motion area. The system and its characterisation can be interactively adapted to obtain a behavior of interest. The behavior is fine-tuned by a shape optimization procedure. This approach is elaborated in this chapter for systems comprising curved planar beams. A design example is presented that can realize an unconstrained straight-line motion with a constant potential energy level, comprising four symmetrically arranged beams.

11.1. Introduction

Designing compliant mechanisms is not as straightforward as compared to conventional rigid body mechanisms. Methods that have been proposed for the conceptual and dimensional design of compliant mechanisms include the *pseudo-rigid-body model* (PRBM) [62, 201], the *freedom and constraints topologies* (FACT) [202], the *compliance and stiffness ellipsoids* [203], the *instant center approach* [204], and topology optimization.

One of the major challenges when designing compliant mechanisms derives from the fact that motions and forces are hard to treat in a decoupled fashion. Some of the methods, e.g. the PRBM, try to face this challenge by relating the compliant mechanism to an equivalent rigid linkage mechanism with integrated springs so that the kinematics can essentially be decoupled from the kinetics. An advantage is that to design a compliant mechanism the designer can rely on the vast collection of known conventional mechanisms [203, 205]. At the same time it might hamper the ability to come up with alternative designs.

FACT and other similar methods rely on the fact that certain compliant segments have a clearly distinct stiffness related to different load directions. For example living hinges and straight flexures have a very high resistance to tension and low resistance to bending, so that the directions of motion related to tension can be called constraint directions and the ones related to bending can be called freedom directions. As such, it becomes possible to successfully design compliant mechanisms with multiple degrees of freedom and high stiffness in the directions where motion is undesired. These methods are particularly suited for precision engineering applications. It is challenging, however, to apply them when dealing with large deflections, because freedom and constraint directions can change in a deformed configuration. Another challenge is to deal with complex shapes, where the distinction between freedom and constraint directions can become more blurred.

The building block approaches based on *compliance and stiffness ellipsoids* or on the *instant center* address the issue of the blurred distinction between constraint and freedom directions. The compliance ellipsoid gives a representation of the relation between the compliances in multiple directions. Also in this case, however, large deflections and nonlinearities are not well dealt with because the compliance and stiffness ellipsoids give an instantaneous representation. The behavior at a deformed configuration might very well be a lot different from the undeformed configuration.

Topology optimization is also frequently encountered in compliant mechanism synthesis. Examples can be found in [53, 116, 117, 121, 177, 206]. Topology optimization requires no a priori knowledge of the elementary components of a mechanism nor the understanding of their interaction. This makes it suitable for a broad range of applications and can be a valid source of new concepts. The drawbacks are mainly related to the sensitivity of the result w.r.t. the formulation of the objective function and w.r.t. the initial design choice. Also in topology optimization, dealing with large deflections is not straightforward.

In this work we propose the use of potential energy fields (PEFs) as synthesis aids for compliant mechanisms. The use of potential energy fields to characterise

the endpoint stiffness of a system has been shown by e.g. Hogan [207]. He uses the elliptical isopotential contours of the potential function to visualize the endpoint stiffness of multi-joint human limbs, e.g. the arm. English [208] uses this concept to mimic the stiffness properties of natural limbs in prosthetic limbs. He also compares the shape of the ellipses to the isopotential lines obtained when nonlinearities are taken into account. Moreover, he analyzes the effect of different stances of the two-link system and the effect of nonlinear spring functions at the joints on the shape of the isopotential lines at the endpoint. Herder [35] uses potential energy graphs of linear extension springs as graphical aid to the synthesis of statically balanced linkages. Analytical derivation of the potential energy of linear springs is straightforward and their isopotential lines are concentric circles. This facilitates the synthesis of systems with multiple springs. The concept applied as a synthesis tool is further extended by Radaelli [196] for systems comprising linkages with torsion springs. Rosenberg [198] makes a first attempt to use the potential energy of the rigid body linkage for the synthesis of a similar lumped compliant system. Here the torsion springs at the hinges were replaced by flexure hinges.

In this work the use of PEFs is extended and applied to continuous compliant curved beams. The potential energy function is generally not available analytically for such systems in combination with large displacements. Therefore, the surface function is evaluated numerically by means of finite element analysis. The principles of the synthesis method are similar to a building block approach where the behavior of multiple connected systems is visualized at one endpoint. In this case the energy of the system is visualized as function of the possible locations of an endpoint. Advantages include the easy assembly of parallel systems, representation of the whole large-range and nonlinear behavior, and the intuitive interpretation of the energy graphs. Moreover, the method is in principle suitable for any building block of which the potential energy can be derived, irrespectively of the type and shape.

The goal of this chapter is to present the PEF method, extended for continuous compliant beams. Furthermore the needed theoretical and practical aspects are elaborated and an example illustrates the use of the method. The example design is a parallel compliant mechanism, statically balanced in a preferred direction and compliant but stable in the other directions. This results in a straight line mechanism with soft behavior perpendicular to the line of motion.

The remainder of the chapter is structured as follows. Section 11.2 contains a review of the concept of PEFs for systems with linear and torsion springs. Furthermore, it provides the foundations for the extension of the method for continuous compliant beams and introduces the design example. In Section 11.3 the optimized design example is presented and a stability analysis is performed. Section 11.4 discusses the construction and testing of a physical demonstrator. Section 11.5 contains the discussion, and concluding remarks are given in Section 11.6.

11.2. Methods

11.2.1. Energy approach

A potential energy field as described in [35] and [196] can be defined as the collection of points in space for which an energy value is defined. The value of the energy at every spatial point corresponds to the total potential energy in the system when a chosen point of the system is displaced to that point. A PEF can in principle be determined for all forces that are conservative, e.g. elastic, gravity, magnetic etc. A brief review on the PEFs of linear springs and torsion-spring linkages is provided next as an introduction to the newly added continuous compliant beams.

11.2.2. Linear springs

In the example of a linear extension spring the PEF is calculated by taking the potential energy of the spring at every point in space where one chosen endpoint is positioned. Inevitably, to avoid rigid body motion and thus zero elastic potential energy change, the other end of the spring is pinned at a chosen location. The resulting energy field of a zero-free-length spring (ZFLS) in a plane is a paraboloid. Such springs have the property that the force is proportional to their length, not only to their elongation. The potential energy of a ZFLS is given by

$$U_{ZFLS} = \frac{1}{2}kl^2 \quad (11.1)$$

where k is the spring stiffness and l , the length of the spring, is given by

$$l = \sqrt{(x - x_0)^2 + (y - y_0)^2} \quad (11.2)$$

where x , y and x_0 , y_0 indicate the position of the moving end and the fixed end of the spring, respectively. Substitution in Eq.11.1 gives a paraboloid centred about the fixed end of the spring (x_0, y_0) . The energy field can be visualized by plotting the isopotential lines, as shown in Fig. 11.1a. Key property of paraboloids is that the sum of two paraboloids always yield another paraboloid. Thus, two connected ZFLS yield an equivalent ZFLS. In the case that the linear spring has a non-zero free length l_0 , the resulting field is similar but not equal to a paraboloid, see Fig. 11.1b, and given by

$$U_{LS} = \frac{1}{2}k(l - l_0)^2. \quad (11.3)$$

The summation property is not valid anymore in this case.

11.2.3. Torsion-spring linkage

The energy field of a double link with torsion springs at the hinges presented in [196] is given by

$$U = \frac{1}{2}k_A(\phi_a - \phi_{a0})^2 + \frac{1}{2}k_B(\phi_b - \phi_{b0})^2 \quad (11.4)$$

where k_A , k_B and ϕ_{a0} , ϕ_{b0} are the torsional stiffnesses and neutral angles of the two springs, respectively, and where ϕ_a and ϕ_b are the relative angles of the two links

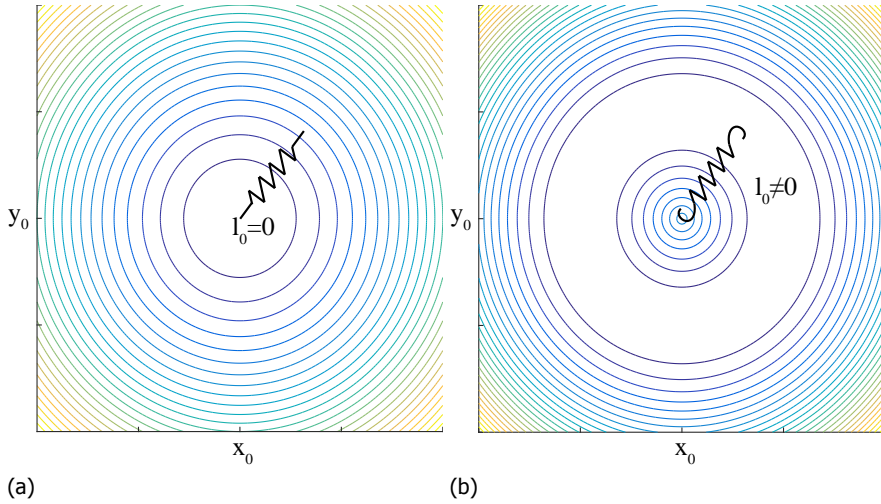


Figure 11.1: The PEF of linear springs has circular isopotential lines concentric with the fixed end of the spring. (a) A zero free-length spring has a parabolic (Eq. 11.1) PEF with minimum at the fixed end of the spring. (b) The PEF of a spring with finite free-length has a minimum valley with radius equal to the unloaded length.

given a certain endpoint location, which can be solved analytically using trigonometric relations. Every endpoint location corresponds to two possible configurations of the links, one with a positive and one with a negative relative angle ϕ_b between the links. An example of a double link with torsion springs and its PEF is given in Fig. 11.2.

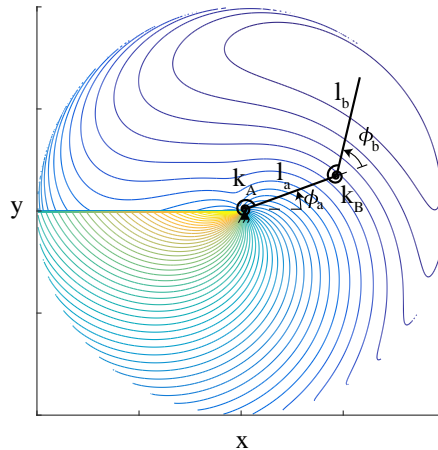


Figure 11.2: The PEF of a double link with torsion springs, given by Eq. 11.4, can be used as a rough estimation of the PEF of a continuous compliant beam.

With a number of links higher than two, the system has one redundant degree of freedom for every endpoint location. Obtaining the energy state is thus not possible

anymore by trigonometric relations alone. This implies that obtaining the potential energy of the linkage involves a minimization of the energy over the remaining degree of freedom. This corresponds to finding equilibrium of the linkage chain for a given endpoint location. Increasing the amount of links will increase the number of redundant degrees of freedom. The more degrees of freedom, the higher the computational effort becomes. With a large number of links the model essentially evolves into a finite element-like model of a continuous beam.

11.2.4. Continuous beams

Approximating a compliant mechanism with complex geometry or distributed compliance with a few links and torsional springs results in limited accuracy. Therefore, modelling a 1D continuum like a beam by any numerical mechanics technique is a logical next step for constructing useful potential energy graphs. In this work we make use of the isogeometric formulation for planar beams [127]. Note that any other numerical formulation suited for planar beams will give similar results, but comparison of alternatives goes beyond the scope of this chapter.

A geometrically nonlinear Bernoulli formulation is applied with a linear material constitutive law and with uniform cross-section and material properties along the length of the beam. The potential energy of the beam is defined as

$$U_{beam} = \frac{1}{2} \int (EA\epsilon^2 + EI\rho^2) dS, \quad (11.5)$$

where E , A and I represent Young's modulus, the cross-sectional area and the second moment of area, respectively. As defined in [127], the membrane strain ϵ and the bending strain ρ are given by

$$\epsilon = \frac{1}{2} \left(\left(\frac{ds}{dS} \right)^2 - 1 \right), \quad (11.6)$$

and

$$\rho = (\kappa - K) \frac{ds}{dS}. \quad (11.7)$$

The differential arch length (dS , ds) and the curvatures (K and κ) of the beam in undeformed state $\mathbf{R}(S)$ and deformed state $\mathbf{r}(S)$, respectively, are given by

$$ds(\xi) = \|\mathbf{r}^{(1)}\| d\xi, \quad (11.8)$$

$$\kappa(\xi) = \frac{[\mathbf{r}^{(1)} \times \mathbf{r}^{(2)}]_3}{\|\mathbf{r}^{(1)}\|^3}, \quad (11.9)$$

where the subscript 3 refers to the third component of the vector in brackets. The superscript in parenthesis denote successive differentiation w.r.t. ξ , the variable of parametrization of the curve. In a similar fashion, replacing $\mathbf{r}(S)$ by $\mathbf{R}(S)$ gives the definitions of dS and K .

Both the deformed $\mathbf{r}(S)$ and the undeformed curve $\mathbf{R}(S)$ are parametrized by a non-uniform rational basis spline (NURBS) [137]. A number n of control points (\mathbf{X}, \mathbf{x}) describe the curve in a non-interpolatory fashion. The displacements d of the control points are the degrees of freedom of the numerical model, similar to the displacement of the nodes in conventional finite element models (FEM). The reader interested in more details about the isogeometric analysis method is referred to [124], and to the vast collection of literature on the topic.

The PEF of a continuous beam is found by applying fixed boundary conditions at one endpoint and displacing the other endpoint in an ordered way over the area of interest and solving for equilibrium at every point. The boundary conditions at either points can be pinned or clamped, obtaining the variants p-p, p-c, c-p and c-c, where p stands for pinned and c stands for clamped. Figure 11.3 shows the PEF of a beam for the four clamping conditions. It can be observed that the p-p condition always yields a rotational symmetric PEF, similar to the finite free-length spring. This is indeed the case because every rotation of a pinned point about the other pinned point is a rigid body motion that does not change the energy state of the beam. The clamped endpoint conditions generally yield a higher stiffness, recognisable from the steeper energy profiles.

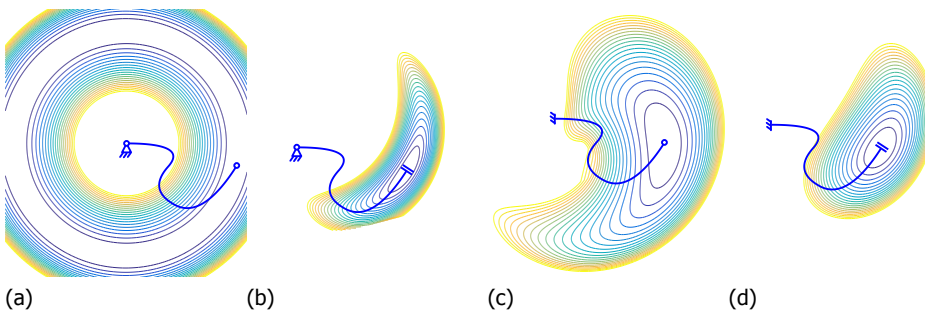


Figure 11.3: Different boundary conditions have a different impact on the PEF. The fixed endpoint is either pinned or clamped, the same holds for the moving endpoint which is either free to rotate or has a fixed inclination angle. The obtained variants are (a) p-p, (b) p-c, (c) c-p and (d) c-c

11.2.5. Energy field computation strategies

To have an efficient computation of the energy fields a sensible strategy must be adopted. Such a strategy consists in finding a workable order in which the points in the field are calculated, taking into account that for every point to be calculated it helps if an estimated solution is given as an input. Usually such an estimate comes from a previously calculated nearby solution. Therefore the sequence and parallelism in which calculations are performed has influence on the quality and smoothness of the resulting field.

The main issue is that for every endpoint location usually two classes of stable configurations can be found, i.e. mainly concave and mainly convex, and potentially even more if the curve has loops and/or self-intersections. It must be avoided that

two near points converge to a different configuration class and thus result in high discontinuities of the energy values. Another issue to be avoided is that starting from a given solution, the step to the next applied displacement is so large that the solver fails to converge. It is important that there are enough points in regions where the isolines in the PEF have large curvatures. Otherwise, when creating the surface plots the interpolation performed between the calculated points will not be smooth. Some exemplary strategies that have been experimented with are treated next.

rectangular grids

Following a rectangular grid is an obvious option. A variation to keep small step-sizes is to scan the surface in alternate directions, i.e. forward - step down - backward - step down etc., see Fig. 11.4a. Another alternative is to start with a vertical line and then take every point on that line as a starting point for a horizontal parallel scan, see Fig. 11.4b. However, it turns out that many of these strategies are prone to snapping from a configuration class to another, resulting in an irregular energy field.

reaction-force paths

A useful guidance for the scanning of the PEF is the direction of highest gradient. The direction of highest gradient of the potential energy is, by definition, the opposite direction of the resultant reaction force. It is possible to build up a collection of points by radially travelling away from the neutral position in many different directions, see Fig. 11.4c, possibly in a parallel computation. Following the path of the reaction forces rarely gives discontinuities in the potential energy. Also, by the magnitude of the reaction force, it is possible to estimate the step-size to match a desired energy increase. However, a drawback is that the density of points becomes smaller as you move further away from the neutral position. Moreover, the paths of reaction forces diverge if the equipotential lines are convex. Therefore, areas with more curvy equipotential lines are even more sparsely populated.

zero-force paths

Another type of strategy is to follow the lines of constant energy or, in other words, travelling in the direction perpendicular to the reaction force. In this direction the component of the reaction force is zero, see Fig. 11.4d. With a finite step-size and a non-zero curvature of the equipotential line a deviation from the equipotential line will occur. Although not necessarily, it is possible to apply some corrective steps in the direction of the reaction force to lead back to the original energy level. This correction step is similar to the one employed for tracing the nonlinear equilibrium path of systems in, e.g., arc length methods. Omitting this correction step saves computation time, but admits a drift away from the equipotential line. This does not need to be a problem, as long as the area of interest is evenly mapped. Once the equipotential line has formed a closed loop, the same procedure is followed at another energy level. The computation is independent for every level. As such, it is possible to compute the levels in parallel. One advantage of following the

equipotential lines is that by choosing an appropriate step-size you can ensure that there are enough points in the areas where the lines have large curvature.

The PEFs employed in this chapter are computed with the zero-force paths strategy. However, there could be situations where another strategy gives better results or where a combination of strategies can be beneficial.

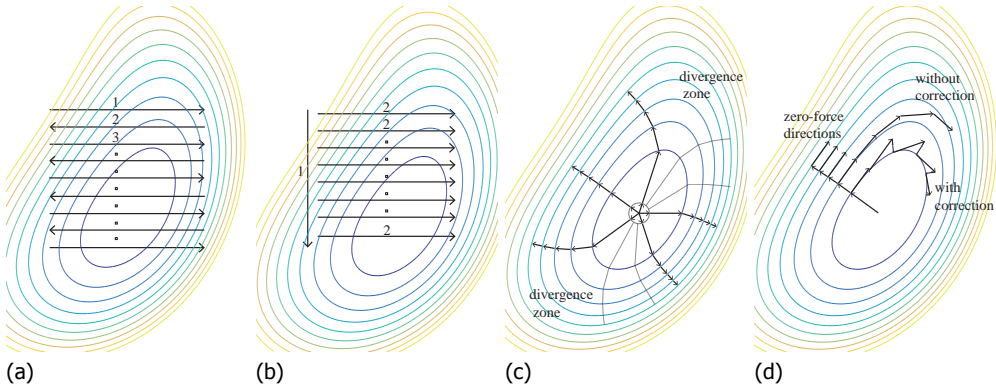


Figure 11.4: Various strategies can be adopted to efficiently compute the values of a PEF in a region of interest. (a) A rectangular grid is scanned in alternate directions. (b) A line of point is computed first, after which a rectangular grid is scanned in a parallel fashion. (c) The area is scanned in parallel tracks, where at every point a step is taken perpendicular to the isopotential line, i.e. in the direction opposed to the reaction force. (d) The area is scanned in parallel tracks following the isopotential line, i.e. zero force direction, in an approximate way or with additional correction steps.

11.2.6. Parallel connections

One of the main advantages in representing the behavior of mechanical systems in terms of their potential energy is the fact that when connecting multiple systems in parallel, the energy simply adds up. The potential energy of a system in a given state is the summation of the scalar values of potential energies of the subsystems. If the PEF of a beam is added to the PEF of a second beam, the resulting field describes the behavior of the coupled system, see Fig. 11.5a. If the neutral positions of the endpoints of the beams do not coincide, then the total energy field inherently includes the prestress action of bringing the two ends together, see Fig. 11.5b. In the shown figures, the visible part of the PEF is limited to the overlapping area of the computed areas of the subsystems. As the subsystems are placed further apart, the overlapping area becomes smaller. Theoretically, the area of the potential energy field is unlimited. In practice, however, the choice is made to confine the area for computational consideration, or for strength considerations. It is of little use to compute the energy of a beam in pure tension.

It is possible to integrate multiple types of systems by adding up the energy fields. For example, the energy field of a lumped mass is a flat plane with an inclination equal to the mass times the gravitational acceleration. The behavior of a beam with a lumped mass at its end is thus the sum of the beam's PEF and an

inclined plane.

It is also possible to derive the PEF of serial systems from those of the subsystems, but it is not as straightforward as with the parallel case. This subject is not treated in this work.

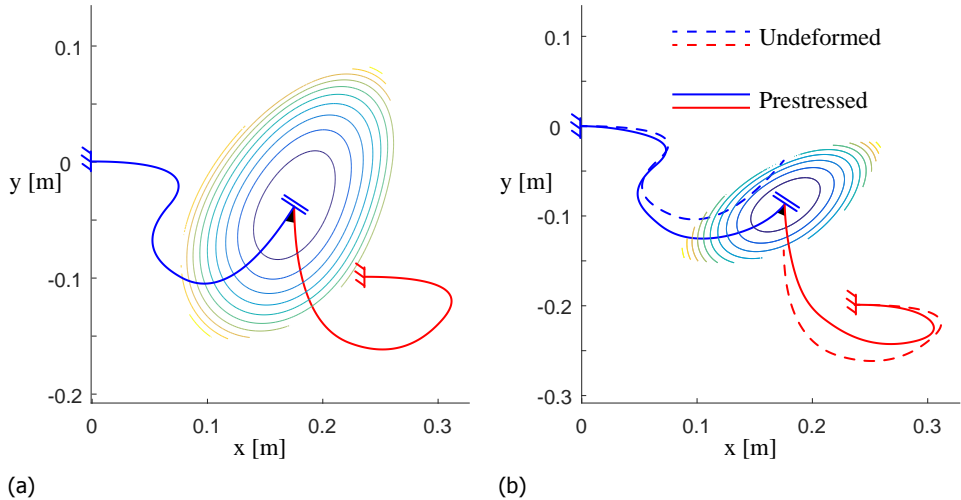


Figure 11.5: The PEF of a system of parallel coupled subsystems is simply the sum of the PEFs of the subsystems. (a) Two beams can thus be connected at their endpoints and the PEF of the coupled system is readily available. (b) If the endpoints of the beams in neutral state do not coincide, the PEF can still be calculated the same way. The system which is then represented is the coupled system with connected endpoints, i.e. prestress is inherently taken into account.

11.2.7. Interactive design

The power of the described method lies in the fact that the behavior of a conservative mechanical system at a selected point can be analyzed and interpreted by inspection of a single graph. This information is not restricted to small displacements and can combine many types of subsystems. If the energy fields of interesting systems are available, either by quick computation or in a database of pre-computed fields, it becomes useful as a synthesis method. By inspecting the behavior of connected subsystems repetitively, changing components, locations and other settings, a preliminary design can be obtained of which the behavior is tailored to the designer's needs.

Figure 11.6 shows a graphical user interface (GUI) that can be used to design systems that consist of multiple compliant beams. The GUI is shown as an example of how an interactive method based on PEFs can be implemented. The tool is used here to obtain a preliminary design for a compliant straight line mechanism, that will be refined using shape optimization in Section 11.2.8. In the GUI it is possible

to select two beam shapes of which the PEFs have been pre-computed following the methods described in Sections 11.2.4 and 11.2.5. It is possible to interactively manipulate the global position and orientation of the individual beams, as well as mirroring and scaling. Two types of scaling can be applied. In-plane scaling of the PEF is used to apply a geometrical scaling of the shape. Out-of-plane scaling has to do with the amplitude of the energy which is related to the cross-sectional and material properties of the beam.

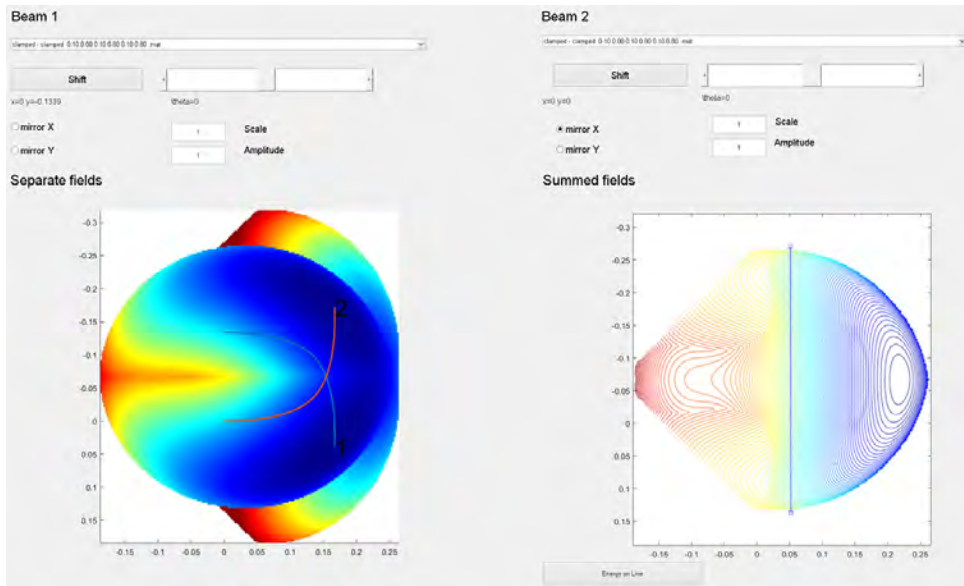


Figure 11.6: The presented method is implemented in an graphical user interface (GUI). Two compliant beams can be connected and the behaviors of the coupled system can be analyzed through its PEF. The shape, position, orientation and size of the beams can be interactively manipulated to search for a desired behavior. This tool can be used in the conceptual design phase of the design of compliant mechanisms.

It is possible to specify a line through the energy field on which the potential energy is further inspected. Along that line of interest, blue in the bottom right graph of the GUI, the energy of the two separate beams and the sum of both can be shown in a new plot. Figure 11.7 shows the contribution of the two beams to the total energy along the line of interest. It means that if the endpoints of both beams would be connected and moved along that line, the system would be tri-stable, according to U_{sum} .

Design example: Statically-balanced straight-line mechanism

The design method is illustrated by an example. The example is a statically-balanced straight-line mechanism. The chosen topology consists of four equal curved beams mirrored horizontally and vertically. The shape and location of one beam is sought and optimized such that the total system has a straight and constant valley of minimum energy. For this purpose the method is used to find an

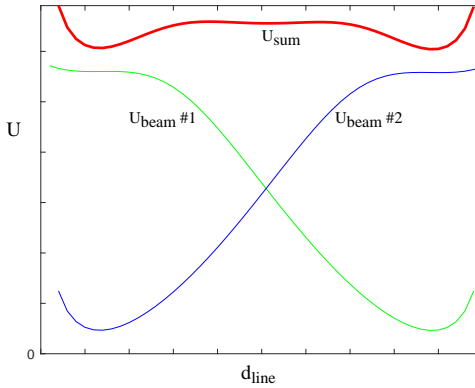


Figure 11.7: In the GUI shown in Fig. 11.6 a line can be selected on the PEF to further analyze the energy along that line of interest. The energy of the two individual beams (blue and green) is summed (red) to obtain the energy of the full system. The total energy is roughly constant. The design that is found can be used as a starting point to obtain a statically balanced system.

equipotential line that is as straight as possible. This is obtained by two mirrored beams with the same shape, both clamped at one end and rotationally fixed at the other end (c-c). The PEF is shown in Fig. 11.8b. Perpendicular to the line in question, the energy has a slope and a positive curvature (concave), indicating a reaction force and a positive stiffness. Thus, a guide is needed to constrain the system along that line. By doubling and mirroring the two-beams system about the line of interest, a four-beams system is obtained in which the perpendicular forces are balanced out. Also, the system stays stable in lateral direction obtaining a self-guiding statically-balanced straight-line, see Fig. 11.8c and 11.8d.

The result obtained in this conceptual design stage is a preliminary design, and the quality of balance is limited by the precision of the visual interpretation of the graphs and the interactive tuning of parameters. The obtained design is suitable as a starting point for the subsequent optimization step.

11.2.8. Optimization

To refine the result obtained with the graphical approach, a shape optimization step is performed. The variables of optimization \mathbf{q} are a sequence of distances l and relative angles α between subsequent control points of the NURBS that describes the shape of the beam, according to

$$\mathbf{x}_i = \begin{bmatrix} X_i \\ Y_i \end{bmatrix} = \mathbf{x}_0 + \sum_{p=1}^{n-1} l_p \begin{bmatrix} \cos \left(\sum_{q=1}^p \alpha_q \right) \\ \sin \left(\sum_{q=1}^p \alpha_q \right) \end{bmatrix} \quad (11.10)$$

and

$$\mathbf{q}_i = [X_0 \ Y_0 \ l_1 \ \alpha_1 \ \dots \ l_{n-1} \ \alpha_{n-1}]. \quad (11.11)$$

The location of the first beam-end determines the clamping location, and the location of the other end with respect to the line of interest determines the pre-stressing action needed when assembling the system of beams. Since the system has two lines of symmetry and the shape of the four beams is the same, it is sufficient to model one single beam.

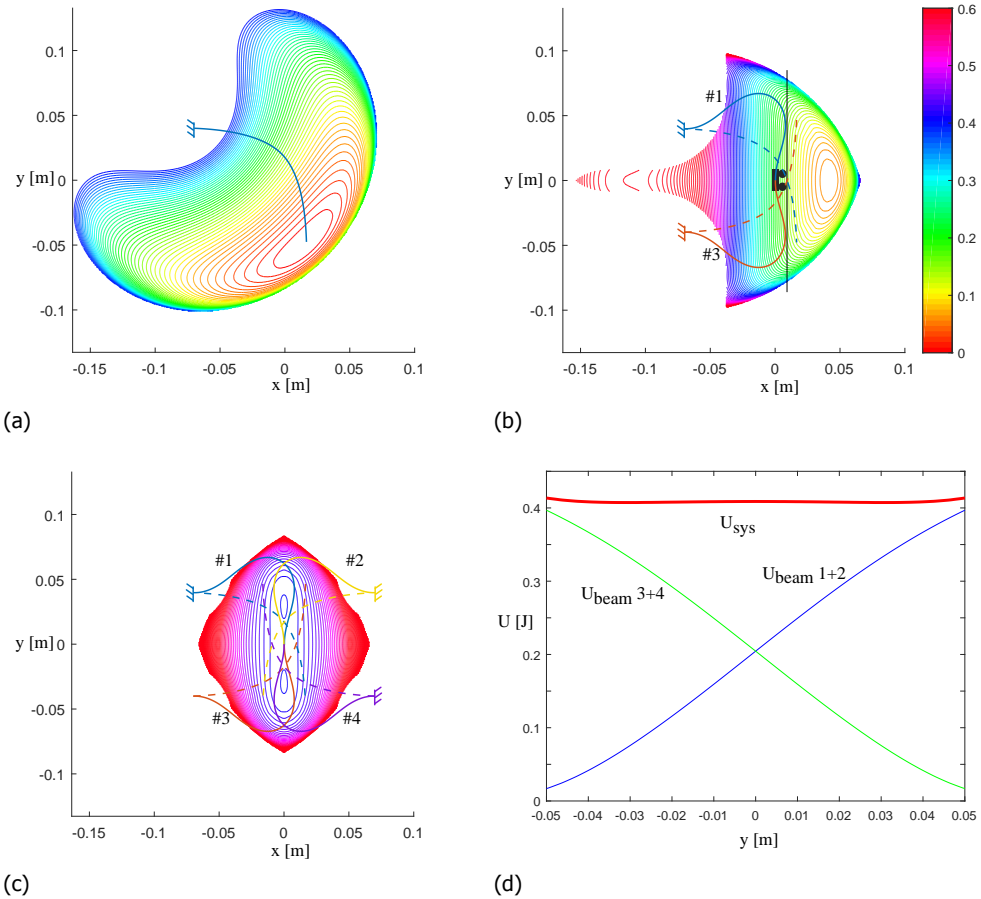


Figure 11.8: Design example part 1: A close to statically-balanced straight line mechanism is the result of the interactive phase of the method. The system consist of four equal beams mirrored twice and connected in the middle. (a) The PEF of a single beam. (b) The PEF of two connected beams, with horizontal line of symmetry. A straight line of constant energy can be identified, but the system must be kept on that line because of the horizontal gradient (lateral force). (c) The system is mirrored again, now with respect to the vertical line of interest, and results in a self guiding mechanism. The connection point is easy to move along the straight valley of almost constant energy. (d) The sum of the energy of the individual beams along the line of interest is nearly constant.

In the analysis, one end is clamped and the other end is first displaced horizontally until it reaches the $x = 0$ line, keeping the inclination fixed. Then the endpoint is displaced over a vertical line segment of $0.1m$ in downward direction, applied in 20 equal steps. The horizontal symmetry line must cut the line of interest in two equal parts. The energy of the beam at the 20 points on the line is written as

$$\mathbf{U}_{beam} = [U_1 \ U_2 \ \dots \ U_{20}]. \tag{11.12}$$

The energies of the left and the right beams are equal. The elements of Eq. 11.12 in reversed order give the energy of the lower beams. Therefore the energy of the total system on the line segment is twice the energy of a single beam plus twice the energy of the flipped beam, as in

$$\mathbf{U}_{sys} = 2 \cdot [U_1 \ U_2 \ \dots \ U_{20}] + 2 \cdot [U_{20} \ U_{19} \ \dots \ U_1]. \quad (11.13)$$

The objective function f_0 requires the level of energy to be as constant as possible, ensuring an optimized statically balanced condition. The objective is formulated as

$$f_0 = \left(\frac{\mathbf{U}_{sys}}{\bar{U}_{sys}} - \mathbf{1} \right) \cdot \left(\frac{\mathbf{U}_{sys}}{\bar{U}_{sys}} - \mathbf{1} \right)^T, \quad (11.14)$$

where \bar{U}_{sys} , the mean of vector \mathbf{U}_{sys} , is used to normalize. The optimization is unconstrained, thus the optimization comes down to

$$\underset{\mathbf{q}}{\text{minimize}} \quad f_0(\mathbf{q}). \quad (11.15)$$

11.3. Results

The result of the two-step design process, started with an interactive graphical step and refined with a shape optimization step, is shown in Fig. 11.9. The initial design vector \mathbf{q}_0 and the optimized design vector \mathbf{q}_{opt} are

$$\mathbf{q}_0 = [-0.07 \quad 0.04 \quad 0.05 \quad -pi + 3.10 \quad 0.05 \quad -0.75 \quad 0.05 \quad -0.70] \quad (11.16)$$

$$\mathbf{q}_{opt} = [-0.0434 \quad 0.0400 \quad 0.0678 \quad -0.0231 \quad 0.0376 \quad -0.7110 \quad 0.0632 \quad -0.7722] \quad (11.17)$$

To avoid contact between the beams they are connected by a rigid link to a remote point, such to create enough distance between them, see Fig. 11.10. The rigid link does not deform and thus stores no elastic energy. Therefore, with the same boundary conditions applied, the behavior of the system remains unchanged, except for the rotational stability of the midpoint, which has to be analyzed further.

11.3.1. Stability analysis

The optimization is performed on a planar beam model. Moreover the rotation of the endpoint remains fixed throughout the range of motion. Therefore, it is necessary to verify the stability in the out of plane displacements and rotations, and the in-plane rotation. For this purpose the stiffness at the rigid connection of the subsystems and of the total system, i.e. the sum of the individual beams, are calculated throughout the range of motion. The used design parameters are given in Table 11.1. In the stability analysis the additional rigid link has an influence because of the moment arm it creates between endpoint of the beam and the rigid

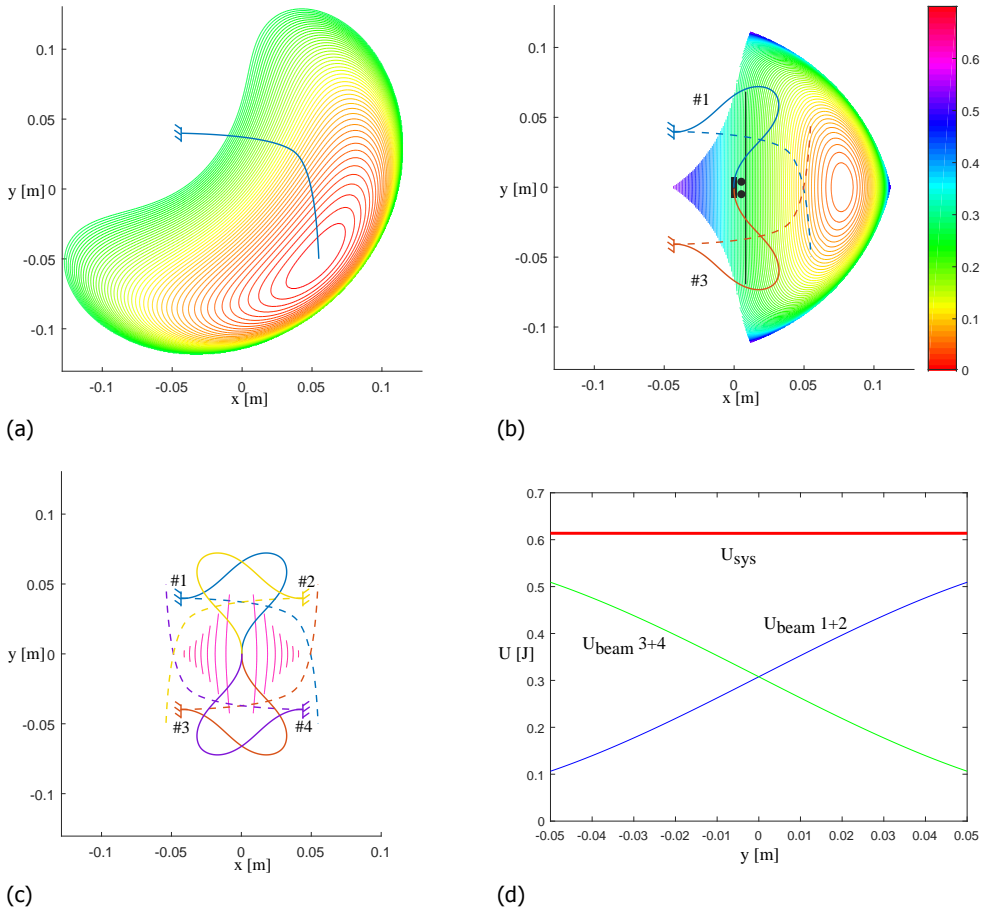


Figure 11.9: Design example part 2: After optimization the quality of balance is improved with respect to Fig. 11.8. (a) The PEF of a single beam. (b) The PEF of two connected beams, with horizontal line of symmetry. (c) The PEF of the full four-beams system. (d) The sum of the energy of the individual beams along the line of interest is virtually constant.

connection point. The results of the stability analysis are plotted in Fig. 11.11. It can be noted that the stiffness is very close to zero in the vertical in-plane direction (y), as designed. Moreover, all other directions have a positive stiffness, indicating stability.

11.4. Demonstrator

An experimental demonstrator is built and tested to demonstrate the design and to experience the practical challenges related to its realization.

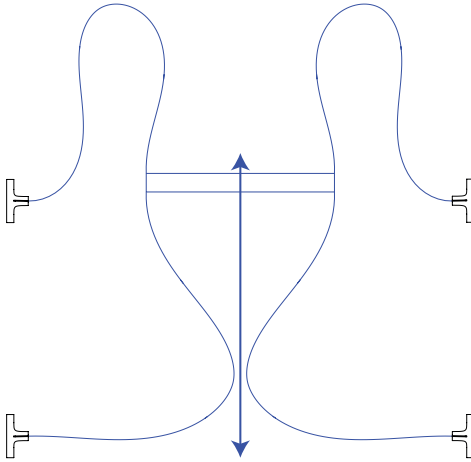


Figure 11.10: In the design an additional rigid body connects the four beams to avoid self-contact.

| parameter | numerical example | demonstrator |
|------------------|------------------------|---------------------|
| material | CFRP (quasi-isotropic) | CFRP random strands |
| flexural modulus | 70 GPa | ~10 GPa |
| shear modulus | 27 GPa | ~3.8 GPa |
| thickness | 0.3 mm | 0.3 mm |
| width | 20 mm | 19.6 mm |

Table 11.1: Design parameters of the design example. The values of the design examples are chosen, while for the demonstrator they are inferred from a linear fit on the experimental data.

11.4.1. Construction

The employed material is a carbon fibre reinforced plastic consisting of nonwoven mats of random continuous fibre strands in an epoxy matrix. A double sided poly-acetal (POM) mould is machined by cnc-milling, see Fig. 11.12a. Four layers of high tenacity (HT) carbon fibre mats are stacked and compressed obtaining a thickness of approximately 0.3 mm. For a better uniformity of thickness and other material properties across the four beams, a wide beam is fabricated in one single process and afterwards cut in four equally wide beams, see Fig. 11.12b.

The four beams are clamped in the right orientation by 3d-printed clamps which's position is adjustable in both vertical and horizontal direction on a multi-purpose profile system, see Fig. 12.9. The four beams are connected to each other trough a shuttle part with integrated clamps, also 3d-printed. This shuttle represents the rigid links that extend the beams in the simulations.

11.4.2. Test setup

The experiment consists in measuring the reaction force in two perpendicular directions while moving the midpoint of the mechanism along the line of interest, and along multiple adjacent parallel lines. The motion is applied by a belt driven linear actuator driven by a stepper motor (MOONS SSM 24Q-3RG). The forces are

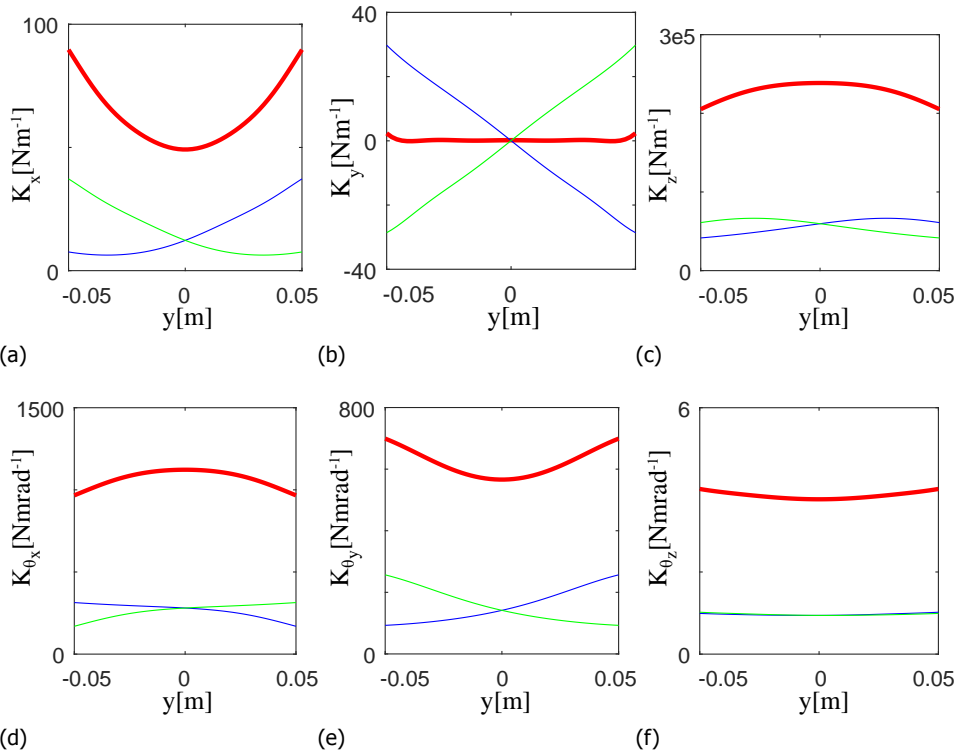


Figure 11.11: The stability of the system is analyzed by calculating the stiffness of the midpoint displaced along the line of interest. This is an additional validation to account for the out-of-plane dimension and for the additional rigid body added between the four compliant beams. The analysis shows a positive stiffness in all directions except for the motion direction, which fluctuates around zero, as expected.

retrieved from two perpendicular Futek S-beam Jr load cells (2 lb) connected in series and moving along with the actuator carriage, see Fig. 11.12c. A sideways displacement can be applied manually by a short-travel linear stage mounted between the sensors assembly and the actuator carriage.

The linear actuator moves from a position in the middle, up 60mm, down 120mm and back to the middle. The speed is set to 20mm s^{-1} . The position in the direction of motion is furthermore tracked by a laser interferometer. The sideways displacement is set discretely in steps of 1mm from -14mm to 14mm .

The measurements have been performed first on one single beam and then on the full system with four beams.

11.4.3. Test results

At every position there are two forces measured for each sensor, one corresponding to the forward motion and one corresponding to the backward motion. To filter the effect of hysteresis, these two forces are averaged. Furthermore, the resulting

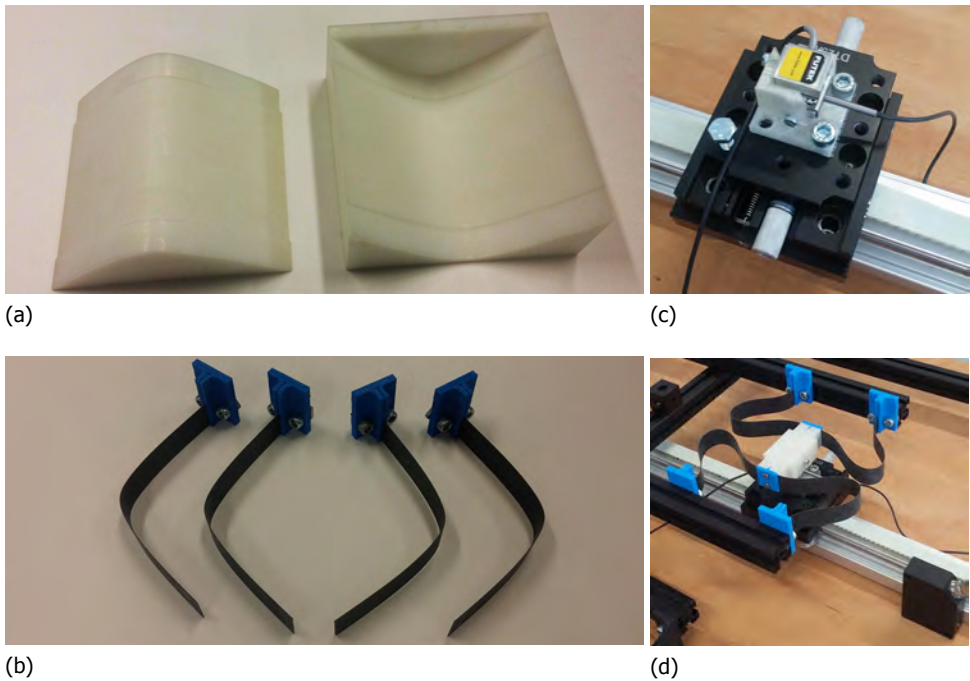


Figure 11.12: A demonstrator has been built and tested. (a,b) The beams are made by mats of random strands of carbon fibres on a double sided mould. (b,c) The measurement setup consists of a two perpendicular force sensors, a small-range planar stage for the lateral movement and a linear motor that applies the longitudinal motion.

signal is scaled in order to account for the unknown material and cross-section constants. It is time consuming to exactly determine the elastic properties of a composite beam, and since that goes beyond the scope of this research, they are inferred by this linear fit on the measurement data.

Figure 11.13a shows a quiver plot of the force field of the numerical model, for comparison. Figure 11.13b shows the quiver plot of the measurements of a single beam, mirrored artificially to resemble the full system. Figure 11.13c shows the quiver plot of the measurements done directly on the four-beams system.

11.5. Discussion

11.5.1. Method

We present a method that can be used for the conceptual design of compliant mechanisms. This method lends itself for applications where the elastic response is of primary importance, as is often the case in compliant mechanisms. It can be particularly helpful in cases where a kinematic approach alone would fail.

The method is an interactive visual aid that leaves a lot open for creativity and insight of the designer. As with many design methods or tools, it probably takes some time to get acquainted with the tool. As soon as the user makes a few basic

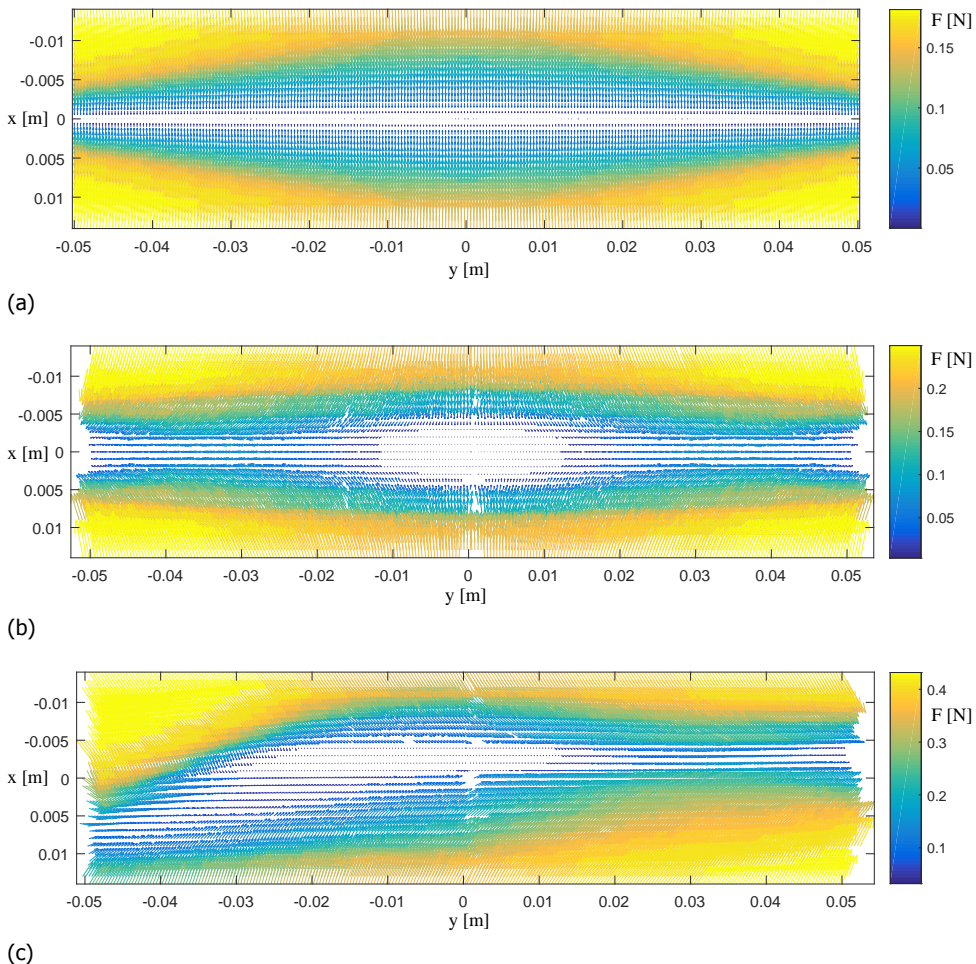


Figure 11.13: The quiver plots represent the forces of the system at the moving midpoint. (a) The forces predicted by the numerical model. (b) The forces measured on one single beam, and mirrored virtually to represent the full system in absence of manufacturing and alignment differences among the four beams. (c) The forces directly measured on the full four-beams system.

principles about the mechanical interpretation of the graphs his own, we believe the method can quickly show its benefits.

An example design has been shown to illustrate that uncommon designs can be produced by such method. Undoubtedly, the shown example is not a unique solution to the design problem. There are more solutions yielding the same balancing quality that may feature different footprint size, material efficiency, sensitivity w.r.t. fabrication errors, etc.

The interactive part of the method easily yields a solution which has near optimal balance. The optimization step is helped by the good initial estimate provided by the interactive part. The optimization accounts for the fine-tuning of the balancing

quality.

Little emphasis has been put on formulating the optimization problem. A drawback of the optimization as it is set up here, is that it only focusses on the balancing quality. It does not deal with tradeoffs that might be there with respect to, e.g., range of motion, footprint, and lateral stiffness, which depending on the application, might or might not be desired.

It is possible to use the method to design many other type of behaviors, including constant force mechanisms, multi-stable mechanisms, and other tailored load-responses.

The extension of the previously presented method [196] to compliant mechanisms was anticipated already in that paper. It was stated, in fact, that the two-link model is a rough approximation of a curved beam, as in a pseudo-rigid body model. In current work the PEF of a continuous and curved beam is obtained by a finer numerical analysis, which significantly improves the accuracy of the approximation w.r.t. the two-link model.

Conceptually, it is possible to extend the method even further to three dimensional systems, e.g., 3D beams and shells. However, the representation of the energy along more than three degrees of freedom becomes challenging. Moreover, the computation time for nonlinear calculations on shells quickly becomes prohibitive for a practical implementation of the method.

The explored endpoint conditions include pinning and clamping. In clamping we assume a constant endpoint angle. However, there are cases in which the endpoints of multiple systems are rigidly connected, but have an unknown and possibly varying angle. The PEF's evaluated with the clamped or pinned conditions are not suitable for those cases, except maybe for a rough initial estimate.

11.5.2. Experimental results

The experimental results reveal some clear similarities as well as some obvious discrepancies. The system with four connected beams is unable to trace a straight line without significant lateral forces. This is reflected by the non-straight tendency of zero-force regions in the field of Fig. 11.13c, especially on the left hand side. This asymmetric behavior can at least partially be explained by the differences in thickness and material of the four beams. A small difference in thickness, here in the order of 0.05mm , has a relatively large impact on the bending stiffness. It is challenging to produce beams with non-constant curvature and constant thickness, without resorting to high-end and expensive equipment and moulds. Another source of errors can be the alignment between the beams.

To eliminate the effects of the difference between the beams, the force field measured from a single beam is mirrored artificially according to the symmetry planes in the design. In Fig. 11.13b we observe a much better resemblance with the model of Fig. 11.13a. A slightly unstable equilibrium position in the middle and two stable equilibria at the sides (out of range) is as close to static balance as it got. No effort has been undertaken to optimize the measurements result by, e.g., tuning the clamping alignment and such.

11.6. Conclusion

This chapter presents a design method for compliant mechanisms based on the visualization of potential energy fields. This method is suitable for the conceptual design phase and can be complemented by a numerical optimization step, as shown in this work. The method is particularly appropriate for compliant mechanisms that have large deflections, complex shapes and complex behavior.

The illustrated method is adapted from an existing approach for the design of rigid-body spring mechanisms, particularly helpful for statically balanced mechanisms. The method is extended for continuous beam systems and its applicability is demonstrated.

A special mechanism is designed with help of the presented method in combination with a shape optimization procedure. The obtained design is a straight line mechanism with a constant potential energy along the principal line of motion. Deviations from that preferred line, including rotations, have a relatively low, positive stiffness. This means that the system is statically balanced along the main line of motion and compliant but stable in the other directions.

A physical demonstrator is constructed and tested as additional validation of the design method, the numerical method, and the mechanism's behavior. The measurement results show a rough behavioral similarity with respect to the numerical model. However, the manufacturing challenges to obtain a precise construction have a significant impact on the quality of the measurement result.

III

Compliant shell mechanisms

12

Gravity balanced compliant shell mechanisms

The research on compliant shell mechanisms is a new and promising expansion of the well established compliant mechanisms research area. Benefits of compliant shell mechanisms include being spatial and slender, having organic shapes and their high tailorability of the load-displacement response. This work focusses on the design of a shell with tailored force output at large deformations by means of a shape optimization procedure. The procedure is applied to create a statically balanced mechanism where the self-weight of the shell and an additional payload is balanced by the elastic forces of the deforming shell. The optimization is based on an isogeometric numerical simulation. A physical demonstrator is constructed by vacuum forming a PETG polymer sheet. The result of a force measurement on the prototype shows a good qualitative match, although quantitatively the discrepancies are substantial.

12.1. Introduction

Compliant mechanisms (CM) are increasingly popular in multiple fields of application. Designers become ever more familiar with their potential benefits, the most frequently mentioned being low friction, no wear, no need for lubrication, no backlash and easy assembly [62]. Other benefits include easy cleaning and possibly more appealing aesthetics. The last one is relevant in case the product is in close contact with the user and a mechanical look is undesired, e.g. in wearable structures (prostheses, orthoses and exoskeletons), consumer products, but also interactive architectural objects and interactive furniture pieces [210, 211].

To date by far most compliant mechanisms are conceived as planar mechanisms and, moreover, they are deduced from equivalent conventional (rigid body) mechanisms. The design process often consists in finding a compliant mechanism alternative to a given rigid body mechanism function [212]. Also, designers tend to subdivide systems in sub-functions and concatenate compliant sub-systems, which often results in relatively large and complex systems. Another observation is that, currently, many compliant systems are so called lumped-compliant. This means that the flexibility is concentrated at certain spots and that most of the material does not deform significantly. This is emphasized by the extensive use of flexures.

We foresee a growing attention for three-dimensional compliant mechanisms in the near future. This expansion makes sense from a technology point of view: planar CM are extensively being investigated thus the logical next step is towards spatial CM. But also from an application point of view it makes sense: Human-assistive devices and tools ought to act essentially spatially since human motion is often hard to approximate as planar.

For the application as human-assistive devices we focus on shell structures as constitutive elements of spatial compliant mechanisms. Shells are interesting from an application point of view because they can be shaped around a limb, for example. From a functional point of view shells are interesting and challenging at the same time, because of their nonlinear nature with respect to mechanical load bearing. Nonlinear load bearing is a risk if regarded as a failure mode, but a benefit when nonlinear load-displacement responses are intentionally produced by a mechanism. There are many examples where nonlinear load-displacements are a functional requirement. For this class of mechanisms we will use the term *nonlinear spring* from here on, following the definition given by Jutte [4]: "Nonlinear springs are a class of compliant mechanisms having a defined nonlinear load-displacement function measured at one point on the mechanism".

Seffen [37] defines compliant shell mechanisms as "open, thin-walled, discretely corrugated structures, with flat facets or curved regions of shell interconnected by folds or hinge lines", or elsewhere in the paper "discretely corrugated structures, capable of undergoing large, reversible displacements". It sometimes seems appropriate to broaden this definition by not excluding the more continuous case without corrugations, folds or hinge lines. In a more general definition, namely, a shell is a spatially curved, thin-walled structure, in accordance with Farshad's definition [72]. Therefore, if such a structure is compliant and employed as a mechanism, defined as "a mechanical device used to transfer or transform motion, force, or en-

ergy" [213, 214], we can call it a *compliant shell mechanism* .

Howell [62], Jutte [4], Leishmann [123] and Merriam [148] mention prosthetics, artificial implants, MEMS, electronic connectors, gripping devices and human interfaces as groups of possible applications of nonlinear springs. Specific nonlinear elastic response is often also at the basis of metamaterials with peculiar mechanical behavior like negative Poisson's ratio [215] and extreme elastic strain [216], just to name a few.

Another important class of mechanisms of which nonlinear springs are essential components are statically balanced compliant mechanisms (SBCM) [69, 145]. In statically balanced compliant mechanisms parasite forces are neutralized by elastic forces generated by the deflection of the mechanism. Parasite forces are called as such because they either require larger actuators or they result in higher stiffness and eigenfrequencies or they disturb a force signal to be transmitted, e.g., haptic sense in surgical tools [68]. The nature of these forces is usually elastic or gravitational. Examples of the first are the intrinsic stiffness of compliant mechanisms. Applications are found at both meso-scale [112] and micro-scale [115]. In the second case the parasite force is the self-weight or a fixed payload [146].

A special and frequently encountered type of nonlinear spring is a constant force spring. Although the name seems contradictory with the term "nonlinear", we do consider constant force springs as a class of nonlinear springs. The reason is that the constant force is always confined to a certain range. However, reaching that range from a neutral position (zero force) always involves a nonlinear transition. Constant force springs find their applications in gravity balancing, but also for force regulation [7, 48], overload protection [48], constant force actuation [150] and adaptive robot end-effector operations [135].

Buckling is another nonlinear behavior that designers use more and more to their advantage. In his long list of current and envisioned smart applications for buckling, Hu [217] mentions among others: energy production, energy harvesting, energy dissipation, actuators and micro-optical switching, self-deploying and self-locking. Some examples given in this review, e.g. [218–221], are three-dimensional, are elastic and have doubly curved zones and can thus in theory be classified as compliant shell mechanisms, or closely related.

We observe an increasing attention in other research fields that are related to compliant shell mechanisms. Lamina emergent mechanisms (LEMs) [222–224], a subset of orthoplanar mechanisms [225], are among the most relevant and fascinating attempts to make compliant mechanisms spatial. Herein designs that are initially fabricated from planar materials also exhibit motion that emerges out of that plane. In the state of the art, however, these mechanisms are mostly lumped-compliant. Moreover, partly due to their originally flat nature, they mostly consist of flat segments. That means that, even in the emerged configuration, single curved surfaces are scarce and double curved surfaces even more.

Origami mechanisms have drawn quite some attention in the past years as well [226–228]. Many inspiring designs have been realized that are clearly spatial in both the shape as the behavior. Seffen [37], Norman [73] and Schenk [229] describe extensively what they call *compliant shells* or *compliant shell mechanisms*.

The *hypars* shown by Seffen are examples where curvature is introduced in the shaping process. The facets of these special origami are developable surfaces, i.e. with zero Gaussian curvature, that can be shaped from a flat plate material. The *curved corrugated shells* on the other hand, also shown by Seffen, are examples where the surface is locally double curved.

Norman [73] goes in depth into the behavior of multistable corrugated shells that are mostly prestressed in the manufacturing process. Another example of a special shell that owes its behavior to prestress is the one shown by Seffen [230]. This shell has an infinite range of neutrally stable equilibrium configurations, or, in other words, it is statically balanced.

Pellegrino and his co-workers frequently employ the carpenter's tape as a way to create multi-stable deployable structures [29, 231, 232]. The carpenter's tape is also employed by Vehar [233] as a way to create linkages with variable length links. Here they make use of the fact that the longitudinal curvature of the tape in the bended region is constant, independently from the bending angle.

Most of the work found in literature has been focusing on shapes obtainable from flat sheets of material. The more general type of shape with double curved surfaces in the unstressed state is thus often excluded a priori. This fundamental choice has often been made due to the fabrication process. It is true that it is relatively easy to create a shape from a flat sheet of material, benefiting from the uniformity of the material properties and the availability of many common shaping techniques such as plate bending and rolling. On the other hand, there are manufacturing techniques that are becoming more and more accessible and reliable based on composites and polymers that enable shaping of complex double curved shells, e.g. press forming, automated fibre placement, 3d-printing and thermoforming in general.

From a functional perspective, it is expected that free-form shells of which the shape can be tailored will increase the ability to design specific nonlinear spring behaviors and more general compliant shell mechanism behavior. In previous work by the authors [141] it has been shown that the shape of a clamped-clamped planar prismatic beam has an important influence on its nonlinear load-displacement response. The ability to freely manipulate the shape of the undeformed beam by means of shape optimization made it possible to make a weight balancer out of one single piece. The overall shape change of the beam influences the global stiffness behavior, but at a cross-sectional level the bending and tension stiffness do not change. It is expected that giving a transverse curvature to such a beam, i.e. a thin curved cross-section, increases even more the possibilities of tailoring the nonlinear load-displacement response. This is due to the fact that such cross section shape may change during the changing load conditions.

The goal of this chapter is to investigate the applicability of a compliant free-form shell as a nonlinear spring of which the response is tailored by optimizing the shape. The work presented in this chapter focuses on the design of a constant force spring, as an example of a nonlinear spring. In this peculiar example the elastic forces of the shell, the weight of the shell and an external weight ought to be balanced over a broad range of motion. This balancing is accomplished intrinsically by specifying the function of the total mechanism (end-function) and not by

adding up the sub-functions of the sub-systems that counteract each other. Multiple shapes are presented that are obtained by the shape optimization procedure based on an isogeometric framework [124]. A selected shape was constructed by vacuum forming a PETG sheet and tested to verify the applicability of the results and understand the influences of the chosen production method.

The remainder of this chapter is structured as follows. The Methods (Section 12.2) contains a problem description, a description of the numerical model and the design optimization. Section 12.3 shows the results found by the optimization procedure and a convergence analysis on a selected result. Section 12.4 describes the physical realisation, the measurements setup and the test results. Section 12.5 contains the discussion and Section 12.6 ends the chapter with the conclusions.

12.2. Methods

This section illustrates the choices made about the topology of the system and the limitations imposed on the possible shapes. A physical justification of these choices is provided. Details on the numerical model, the parametrization and the optimization procedure are provided.

12.2.1. Problem description

Phenomenological expectation

Conceptually, the starting point for the gravity balancer to be designed is a clamped-free beam. Practically this is the simplest topology to start with. One single clamping point and one end effector point at the opposite side, i.e. the free end. This resembles roughly the basic structure of a serial robot with one base and one end-effector.

To obtain a constant force mechanism or gravity balancer it is required for a structure with an initial finite stiffness to exhibit a softening behavior in order to transition to a zero stiffness or constant force region.

In a planar beam configuration with constant cross-section, compression buckling is the most likely cause of softening behavior. That is, transitioning from an initial compression dominated load case to a bending dominated load case.

More generally, stiffness change can be caused by the change in alignment of the beam with the end-effector force. For example, if a beam segment is initially aligned with the end-force it primarily experiences either compression or tension, both relatively stiff configurations. If during deformation the orientation and position of this segment changes so that bending becomes dominant, the total stiffness is softening. The other way around, it is also possible that an initially unaligned segment becomes more aligned during deformation, thus causing a stiffening effect.

With a clamped-clamped planar beam with in-between end-effector another important local softening effect can occur. Namely that the two parts of the beam at the opposite side of the end-effector are initially at a certain distance. This distance can become smaller in the course of the deformation. This is illustrated in Fig. 12.1, modified from the results of [141]. For the illustration, regard the

cross-section indicated by the dashed line as a combined cross-section (CS1) of the system. In the deformed configuration the total cross-section (CS2) narrows down, thus resulting in a much lower bending stiffness. This effect is not expected in a single clamped free beam because the cross-section remains unchanged.

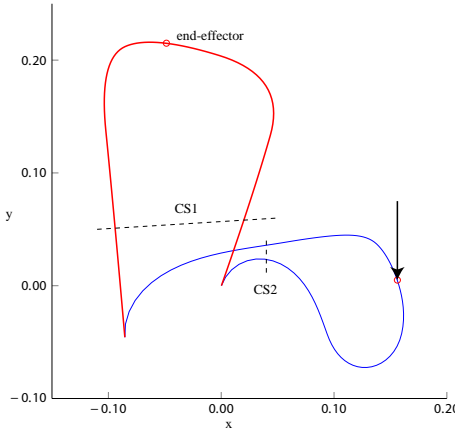


Figure 12.1: Clamped-clamped planar beam illustrating the softening effect caused by narrowing down of the effective cross-section from CS1 to CS2. Modified results from [141].

However, if the beam's cross-section itself can change shape during deformation, similar softening effects are expected. Think of a carpenter's tape measure. Initially the tension side and the compression side are relatively far apart causing a high second moment of inertia, see Fig. 12.2. As the bending load increases, a more favourable deformation state is adopted with small transverse curvature and small total thickness, thus with significantly smaller second moment of inertia. This effect is very localized. In the general case the cross-section is not necessarily constant throughout the length of the beam, as opposed to the carpenter's tape case. On a

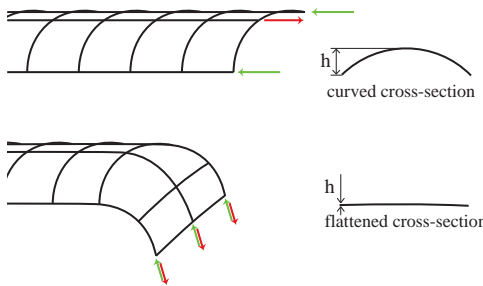


Figure 12.2: Bending of carpenter's tape measure. The total cross-sectional height h narrows down as the tape buckles to a flattened state. This results in a reduced bending stiffness.

global level the variation of the cross-section along the beam length is determinant. The stiffness at the end-effector is obtained by taking the inverse of the summed compliances of every infinitesimal beam part. That means that a more compliant segment, e.g. one with small curvature, is lower-bounding the total stiffness and as a consequence it is taking a relatively big part of the deformation. This is a self-amplifying effect, because the more a cross-section is deformed, the more it will tend to a flattened state, thus increasing even more its compliance. It is however

possible that the bending threshold at which the transverse curvature flattens is reached at multiple places. In that case the deformation will concentrate at multiple spots.

Another influence that will be taken in consideration in the given design example is the self-weight of the system. The shape of the beam has influence on the distribution of its weight. Since every segment of the beam moves differently, the effect of the shape on the deformation and on the balancing behavior is hard to predict without numerical modelling.

The effect of these local phenomena on the global behavior in combination with non-uniform shapes is hardly predictable by reasoning alone, or by analytical methods. Numerical simulations in combination with shape optimization are therefore applied to deal with those complexities and to be able to tailor the response of such structures.

Topology and choices

The chosen topology and parametrization (see 12.2.3) are formulated such that the above mentioned phenomena are exploited best: The ability to tailor the in-plane shape of the beam as well as its local transverse curvature.

A schematic representation of the topology is given in Fig. 12.3. The shell is defined on a rectangular domain. Two lateral edges are free (green). One transversal edge is clamped (red), and the other one is rigidly connected (blue) to a pilot point P . At the pilot point a vertical displacement D_z is imposed stepwise and the reaction force is retrieved at every step. The pilot point is free to move in the other directions and free to rotate in all directions. The geometry is symmetric in the xz -plane. Moreover the transverse curvature is either concave or convex for every cross-section, i.e. no inflection point, no corrugations.

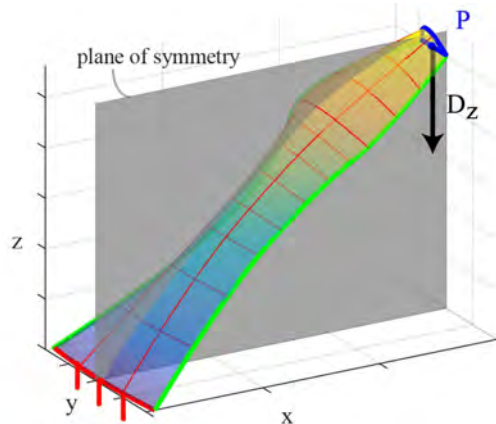


Figure 12.3: Topology of the compliant shell mechanism. A topologically rectangular patch with a clamped edge and with opposing edge driven by a vertical displacement D_z applied at a rigidly connected control point P . The shape is symmetric in the xz -plane.

12.2.2. Numerical model

The shell is modeled as a Kirchhoff-Love class Cosserat continuum. Herein a linear and isotropic material law is adopted that also takes the self-weight into account. Moreover a uniform thickness is assumed over the whole shell surface.

The numerical analysis is based on an isogeometric analysis [124] framework where the parametric descriptions of the geometry of both the design and the analysis are based on non-uniform rational basis splines (NURBS) [137]. The essence is that a relatively low number of control points of a NURBS surface are used as design variables, i.e. optimization variables, and an increased number of control points that describe the *same identical* geometry are employed as degrees of freedom of the numerical analysis. The burden, the time and the loss of continuity that accompanies meshing complex geometries in conventional FEA methods are overcome by the isogeometric discretization. In an optimization procedure where this is repeated a large amount of times, the advantage can be considerable.

B-splines, a uniform and non-rational subset of NURBS, are used in this work. A topologically rectangular set of control points $B_{i,j}$ with $i = 1, \dots, n + 1$ and $j = 1, \dots, m + 1$ controls the shape of the mid-surface of the shell. The surface is defined by the tensor product of two B-spline curves using two independent parameters u and v

$$Q(u, v) = \sum_{i=1}^{n+1} \sum_{j=1}^{m+1} N_{i,p}(u) N_{j,q}(v) B_{i,j}, \quad (12.1)$$

where the parameters u and v are defined within the range of the knot vectors, given by

$$U = [u_1, u_2, \dots, u_{p+(n+1)}], \quad (12.2)$$

and

$$V = [v_1, v_2, \dots, v_{q+(m+1)}], \quad (12.3)$$

and where $N_{i,p}$ and $N_{j,q}$, the basis functions of order p and q respectively, are defined recursively as

$$N_{i,0}(u) = \begin{cases} 1 & \text{if } u_i \leq u < u_{i+1}, \\ 0 & \text{otherwise.} \end{cases}, \quad (12.4)$$

and

$$N_{i,p}(u) = \frac{u - u_i}{u_{i+p} - u_i} N_{i,p-1}(u) + \frac{u_{i+p+1} - u}{u_{i+p+1} - u_{i+1}} N_{i+1,p-1}(u). \quad (12.5)$$

The basis functions for the v parameter are similar when replacing u, i, p by v, j, q respectively.

The nonlinear solution is found by a standard Newton-Rhapson scheme with position control.

The parametrization of the surface can be refined for the analysis phase by order elevation (p -refinement) and knot insertion (h -refinement) techniques [124]. Without going into detail in these refinement techniques, it is a peculiar fact that the geometry remains perfectly preserved when applying such refinement. This

makes it possible to conveniently use different levels of refinement in the subsequent stages of the optimization, incrementing the accuracy as the optimization progresses.

12.2.3. Optimization

The requirements for the parametrization of the shell model are related to an effective optimization, an accurate simulation and enough flexibility for a high influenceability of the response. For an effective and efficient optimization a low number of parameters is preferable and sensible bounds on the parameters must be possible to formulate. For this purpose a reparametrization of the rectangular set of control points is proposed, which is based on a central line of control points with branches to the sides.

Objective function

A stepwise displacement downwards is imposed on a pilot point P that rigidly transfers all rotations and translations to the upper edge of the shell. The reaction forces are retrieved at all load-steps. The optimization consists in finding the shape for which the force-displacement curve is most constant. The value of the constant force, i.e. the payload, is not considered relevant here. In fact, if the balancer would be able to balance just the self-weight of the shell plus a small payload to be able to fine-tune the behavior in real-life, this would be sufficient. Therefore the objective function is obtained by taking the sum of the absolute value of the deviation between the force F_k at all load-steps with respect to the mean value of this force \bar{F} .

Thus the optimization problem is defined as

$$\begin{aligned} & \underset{\mathbf{x}}{\text{minimize}} && f(\mathbf{x}) \\ & \text{subject to} && \mathbf{b}_l < \mathbf{x} < \mathbf{b}_u, \end{aligned} \quad (12.6)$$

where \mathbf{b}_l and \mathbf{b}_u are the lower and upper bound vectors, \mathbf{x} is the vector of parameters and f , the objective function, is given by

$$f = \sum_{k=r}^s |F_k - \bar{F}|, \quad (12.7)$$

with s the number of load-steps and r arbitrarily chosen. The steps smaller than r can be discarded because the force will rapidly change before reaching the desired constant force plateau.

Branch parametrization

The starting point for the proposed parametrization is a rectangular B-spline patch with a control net of $3 \times (m + 1)$ control points. The spatial position of the control points is redefined using a branching structure rather than using the Cartesian coordinates of the points in a grid. The branching consists of a middle longitudinal main branch, referred to as the spine, and symmetrical branches starting from the spine

in outward direction, referred to as the ribs, see Fig. 12.4. The spine, which connects the middle row of $m + 1$ control points, is constrained to the xz -plane due to symmetry of the shell in that plane. The position of the control points is described by using a sequence of lengths of the connecting lines L_j , with $j = 1, \dots, m$, and the relative angles between them θ_j . See [141], where a similar parametrization is applied to a planar beam.

At every control point of the spine two ribs are defined that connect to the corresponding control points on the two outer rows. Due to symmetry, the ribs have pairwise the same length, indicated by l_j with $j = 1, \dots, m + 1$, and opposite direction with respect to the xz -plane. As an additional constraint to reduce the amount of variables even further, the direction of the ribs is made perpendicular to the preceding line of the spine L_{j-1} . The direction of the ribs can now be described with a single angle α_j . These angles have a major influence on the local transverse curvature of the shell.

The advantages of this parametrization with respect to e.g. the Cartesian coordinates of all control points are a significant reduction of parameters due to symmetry and due to the elimination of less relevant direction parameters. In the Cartesian coordinates of the control points the parameter count amounts to $3 \times (3 \times (m + 1))$. In the proposed parametrization the number of parameters is $2 \times m + 2 \times (m + 1)$. If, e.g., $m = 4$, the number reduces from 45 to 18. Furthermore the parameters can be split in lengths and angles, where the lengths have more influence on the size of sections within the shell and the angles affect the local curvature the most. The spine angles θ_j affect the longitudinal curvature and the rib angles α_j affect the local transverse curvature most. This facilitation of the physical interpretation of the design variables has advantages when designing an initial guess and sensible bounds for an optimization run, and for the interpretation and comparison of results after optimization. Moreover, it is possible to add less impacting parameters, e.g. the lengths, in a later stage of the optimization, as will be discussed in Section 12.2.3.

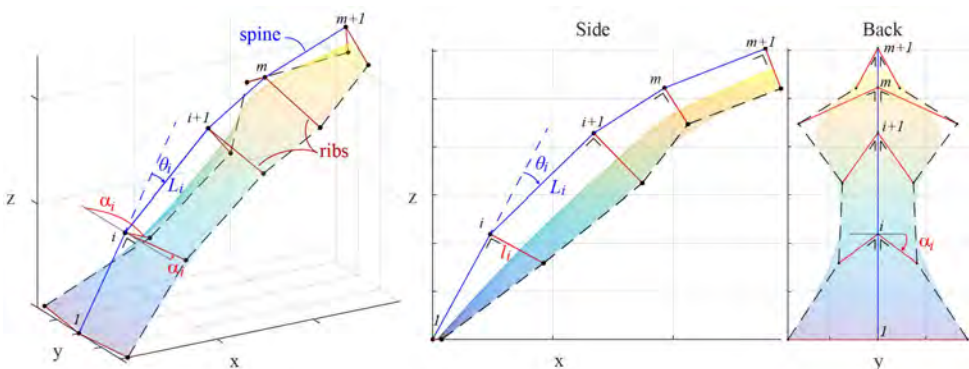


Figure 12.4: The reparametrization of the B-spline control net is defined by a middle main branch, referred to as the spine, and side branches, referred to as the ribs. The shape of the B-spline surface is defined by the lengths and the relative angles of the spine and ribs segments. This parametrization facilitates the physical interpretation of the design variables and the application of optimization bounds.

Stepwise optimization

Optimization of a shell shape including nonlinear behaviors can be a costly task. Moreover, if the problem is not convex, but in fact has many local optimum solutions, searching for a good solution is even harder.

A stepwise approach is adopted where an initially large population of initial guesses is optimized with a course refinement and a relatively low number of design parameters, i.e. some parameter values have been fixed. While the population size is reduced by selecting the best candidates, the level of refinement and the number of parameters is increased. This stepwise process is illustrated in Table 12.1.

At the first step a large set of design vectors is randomly distributed over the bounded search space and evaluated once. A selection of best performing candidates continues the procedure using an unbounded Nelder-Mead Simplex algorithm (Matlab® `fminsearch`). This is a gradient free algorithm that handles discontinuities and bumpyness of the objective function decently. In the subsequent steps the optimization is continued by adding the segment lengths to the list of parameters, increasing the number of degrees of freedom and orders of the basis functions. At each step the population size is reduced by selecting the best candidates from the previous step.

No additional optimization constraints were employed to prevent excessive stress levels. However, between the steps it is possible to check the stress levels in the selected candidates, and in case of excessive stresses the thickness of the shell can be adapted. The subsequent optimization step is likely to correct the resulting change in objective function value. This is only a feasible strategy since the magnitude of the resulting force does not matter, i.e. the important thing is that static balance results.

| step | pop. | des. params. | order p and q | DoFs |
|------|------|--------------------------------|-------------------|------|
| 1 | 5000 | θ_j, α_j | 3 3 | 300 |
| 2 | 50 | θ_j, α_j | 3 3 | 300 |
| 3 | 25 | $\theta_j, \alpha_j, L_j, l_j$ | 3 3 | 300 |
| 4 | 12 | $\theta_j, \alpha_j, L_j, l_j$ | 4 4 | 483 |
| 5 | 3 | $\theta_j, \alpha_j, L_j, l_j$ | 4 4 | 2040 |

Table 12.1: Stepwise optimization: In five subsequent phases the initial population is reduced from 5000 candidates to 3 best solutions. In the process the number of degrees of freedom, the number of parameters and the order of the basis function are gradually increased.

12.3. Results

The best three results of an optimization run are presented in this section. The results are based on the following input details. The knot vectors of the bivariate B-splines describing the surface geometry are uniform vectors, given by

$$U = [0 \ 0 \ 0 \ 1 \ 1 \ 1] \quad (12.8)$$

and

$$\boldsymbol{v} = [0 \quad 0 \quad 0 \quad 1/3 \quad 2/3 \quad 1 \quad 1 \quad 1]. \quad (12.9)$$

The full vector of design parameters is given by

$$\boldsymbol{x} = [\theta_1 \cdots \theta_4 \quad \alpha_1 \cdots \alpha_5 \quad L_1 \cdots L_4 \quad l_1 \cdots l_5]. \quad (12.10)$$

The lower and upper bounds on the vector of design parameters are imposed only during the first step of the stepwise optimization. Here the optimized variables are only the angles θ and α and are all bounded between -1 rad and 1 rad. The lengths of the spine segments en ribs, L_j and l_j , are all set to 0.1 m and 0.05 m respectively. This yields shells with length to width relation of about 4:1. This is done to resemble roughly the thin walled slender beam with varying curvature, following the rationale of Section 12.2.1. After the first step, i.e. the random search, all bounds are released and the lengths are set as free variables.

The analyzes are performed by applying a downward displacement of 0.4 m in 50 load-steps. The simulated material is PETG (Polyethylene terephthalate glycol-modified) with a Young's modulus of 2.35 MPa, Poisson's ratio of 0.38 and a density of 1300 kg/m³. The chosen thickness is 0.9 mm. This is a rough estimate of the shrinking of a 1 mm sheet in the vacuum forming production process.

The best three results of the optimization are presented in figures 12.5, 12.6 and 12.7. The plots on the left hand side show the vertical forces at the base and at the top of the shell versus the applied displacement. On the right hand side the undeformed shape and the maximally deformed shape are shown. The von Mises strains are shown as colors on the deformed shape.

Furthermore the design vector and the objective value of the three results are given in Table 12.2.

12.3.1. Convergence analysis

The analysis is repeated with increasing refinement by knot insertion (h-refinement). This is done by inserting equally distributed knots within every non-zero knot span. In the u direction the additional knots are inserted in multiples of six, while in the v direction the knots are inserted in multiples of twenty for every non-zero knot span. The convergence is performed in ten steps for both the 3th order model as for the 4th order model. The details are shown in Table 12.3 where also the resulting number of DoFs is indicated and the relative error with respect to the last result in each series. The error is defined as the root mean square of the normalized error between the force values of the current analysis with respect to the most refined analysis, i.e. step 10. This gives

$$error = \sqrt{\frac{1}{s-r} \sum_{k=r}^s \left(\frac{F_{k,step} - F_{k,10}}{F_{k,10}} \right)^2}, \quad (12.11)$$

where $step$ is the step in the convergence analysis corresponding to Table 12.3. Figure 12.8 shows the resulting force-displacement results of the analyzes before and after the convergence analysis.

| # 1 | # 2 | # 3 |
|----------------------------|---------|---------|
| Objective f | | |
| 0.0330 | 0.0969 | 0.0422 |
| Design vector \mathbf{x} | | |
| -0.1011 | -0.6814 | -0.6472 |
| 0.1173 | 0.0461 | 0.0579 |
| -0.1114 | 0.7841 | 0.9505 |
| -0.2505 | -0.1044 | -0.2717 |
| -0.1202 | 0.0870 | -0.1219 |
| 1.1895 | 1.0836 | 0.6269 |
| -0.1741 | -0.4877 | -0.3797 |
| -1.2974 | 0.0795 | 0.5297 |
| 1.3033 | 0.9035 | -0.2627 |
| 0.1266 | 0.0978 | 0.0920 |
| 0.0740 | 0.1351 | 0.1463 |
| 0.1801 | 0.1551 | 0.2126 |
| 0.1452 | 0.1590 | 0.1720 |
| 0.0199 | 0.0675 | 0.0304 |
| 0.0427 | 0.0481 | 0.0336 |
| 0.0497 | 0.0518 | 0.0468 |
| 0.0530 | 0.0502 | 0.0202 |
| 0.0911 | 0.0449 | 0.0462 |

Table 12.2: Objective function value f and design vector \mathbf{x} of results #1, #2 and #3 corresponding to figures 12.5, 12.6 and 12.7.

Observe that control points in this IGA formulation have three degrees of freedom, i.e no rotations. The number of DoFs is thus the number of control points in both direction times three.

12.4. Physical model

A physical model was constructed out of PETG thermoplastic sheet material. The shell was made by vacuum-forming the sheet over a high-density foam CNC-milled mold. This is an accessible, quick and cheap manufacturing method. The sheet was trimmed manually at the edges of the shell. The designed shell shape is extended at its bottom edge in order to be able to clamp it to a ground structure, see Fig. 12.9a. The ground structure consists of an aluminum clamping unit that presses two 3d-printed jaws of which the clamping surfaces fit the shell shape. Two cylindrical rods are fastened to the bottom of the clamping unit in order to increase the support polygon of the ground structure. These rods also serve another purpose related to the measurement setup described in Section 12.4.1. At the opposite side of the

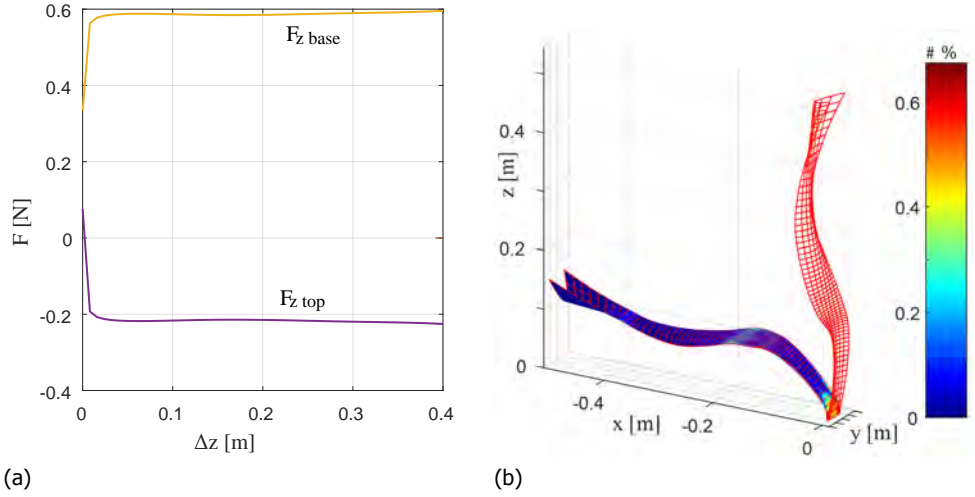


Figure 12.5: Result#1 (a) Vertical forces at base and top (b) Undeformed shape (wireframe) and von Mises strains on the maximally deformed shape

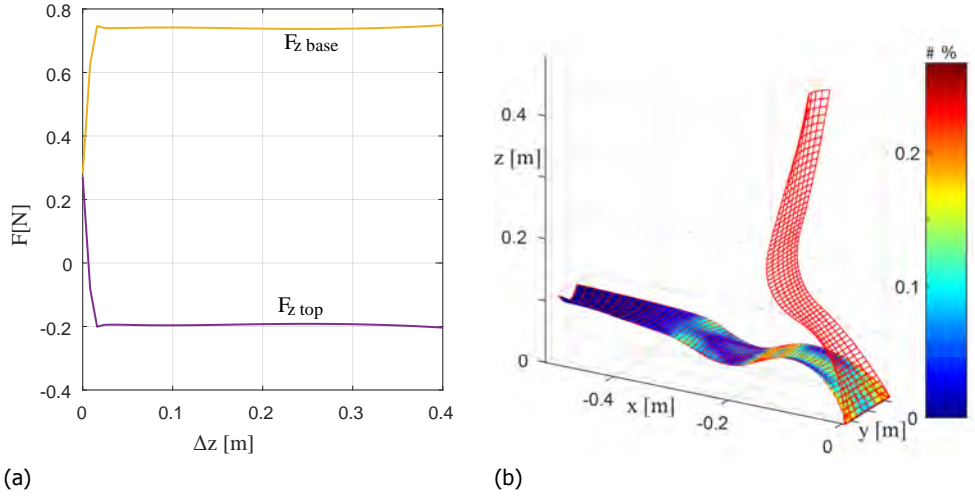


Figure 12.6: Result#2 (a) Vertical forces at base and top (b) Undeformed shape (wireframe) and von Mises strains on the maximally deformed shape

shell the edge is trimmed such to include the position of the pilot point P , where the payload can be fixed and where the displacement is applied. Figures 12.9b and 12.9c show the clamped shell in the two extreme positions, with and without payload, respectively.

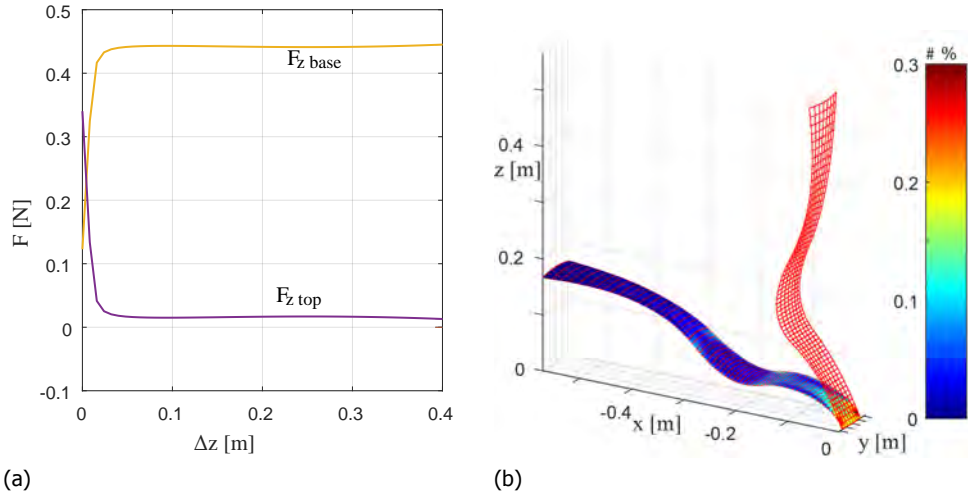
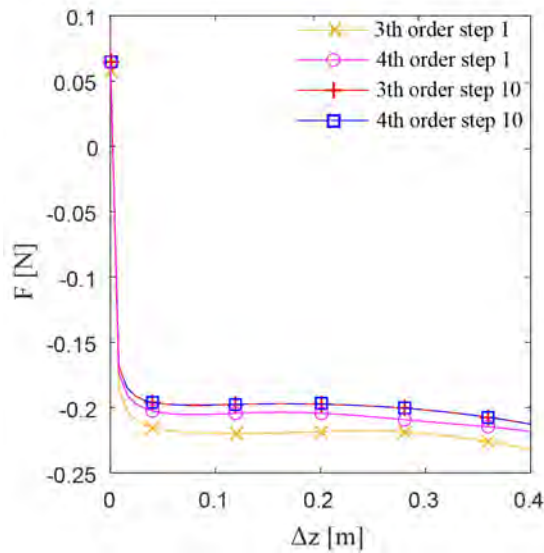


Figure 12.7: Result#3 (a) Vertical forces at base and top (b) Undeformed shape (wireframe) and von Mises strains on the maximally deformed shape

Figure 12.8: Comparison of force-displacement responses of the numerical results at beginning and end of the convergence analysis.



12.4.1. Measurement setup

For the measurement of the vertical reaction force it is important to apply only a vertical displacement while not restraining any motion in the horizontal plane. Since conventional compression benches apply a vertical displacement but do constrain the motion in the horizontal directions, it is possible to position the ground structure on a low-resistance planar stage. This is accomplished here by positioning the base

| step | knot ins./span | | 3th order | | | | 4th order | | | |
|------|----------------|-----|-----------|-----|--------|-----------|-----------|-----|--------|-----------|
| | u | v | u | v | DoFs | error [%] | u | v | DoFs | error [%] |
| 1 | 6 | 20 | 9 | 65 | 1755 | 3.54 | 10 | 68 | 2040 | 1.307 |
| 2 | 12 | 40 | 15 | 125 | 5625 | 0.602 | 16 | 128 | 6144 | 0.128 |
| 3 | 18 | 60 | 21 | 185 | 11655 | 0.279 | 22 | 188 | 12408 | 0.063 |
| 4 | 24 | 80 | 27 | 245 | 19845 | 0.164 | 28 | 248 | 20832 | 0.043 |
| 5 | 30 | 100 | 33 | 305 | 30195 | 0.106 | 34 | 308 | 31416 | 0.032 |
| 6 | 36 | 120 | 39 | 365 | 42705 | 0.071 | 40 | 368 | 44160 | 0.024 |
| 7 | 42 | 140 | 45 | 425 | 57375 | 0.047 | 46 | 428 | 59064 | 0.017 |
| 8 | 48 | 160 | 51 | 485 | 74205 | 0.028 | 52 | 488 | 76128 | 0.011 |
| 9 | 54 | 180 | 57 | 545 | 93195 | 0.013 | 58 | 548 | 95352 | 0.005 |
| 10 | 60 | 200 | 63 | 605 | 114345 | 0 | 64 | 608 | 116736 | 0 |

Table 12.3: Details of the convergence analysis. The analysis is repeated in ten steps for both the 3th and 4th order basis functions. The refinement is done by inserting equally distributed knots in every non-zero knot span. The insertion is done in multiples of six for the u direction and in multiples of twenty for the v direction.

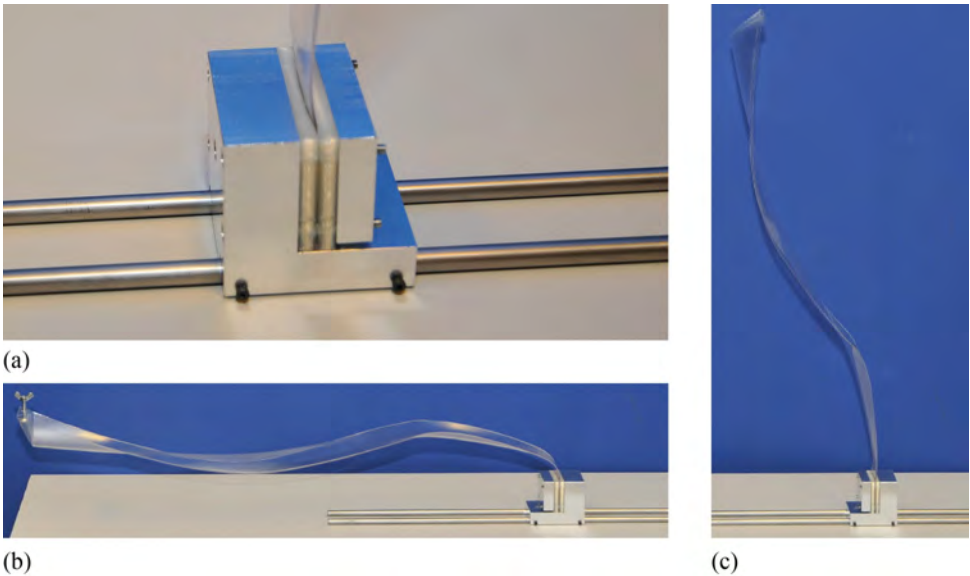


Figure 12.9: Pictures of the physical realization of shape #1: (a) Detail of ground structure, (b) loaded shell in maximum deformation, (c) unloaded shell.

on three pairs of cylindrical rods configured pairwise perpendicular to each other so that they can roll over each other in the two orthogonal directions with no more than the rolling resistance of hardened steel in point contact, i.e. very low. Figure 12.10 illustrates that pair of rollers number 2 facilitates rolling in the x -direction, which is the main direction of motion. Pair number 1 is fixed to the aluminum clamp and is used to extend the range of motion of the other rods and to assure a Hertzian point contact. Roller pair number 3 facilitates the motion in y -direction, i.e. perpendicular

to the main direction of motion. Although from the numerical models and because of symmetry this component of motion is not expected, in a physical realization with all types of possible errors in fabrication, alignment and material unknowns, such motion cannot be excluded a priori and must therefore be allowed. A last degree of freedom in the horizontal plane that should not be restricted is the rotation. As can be observed in Fig. 12.11a the interface between the force sensor and the shell is equipped with a loose vertical screw and a magnet. Rotations in the horizontal plane are easily accommodated. Moreover a small split tube is clamped onto the shell at the position of the pilot point. This ensures that the force sensor which applies the displacement does not restrict the rotation in the direction of the y-axis, at that point.

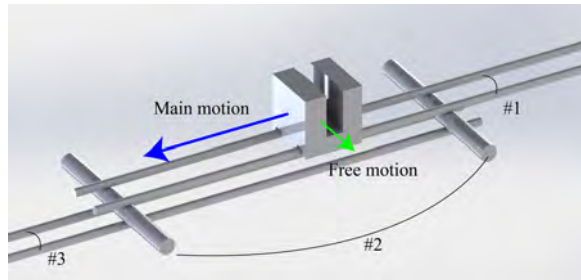


Figure 12.10: Schematic of the ground structure resting on a planar stage based on three pairs of perpendicular rollers permitting motion in x and y direction.



(a)



(b)

Figure 12.11: Detail pictures of measurement setup. (a) The application of the vertical displacement from the test bench goes through a magnet and a rolling tube, allowing for both rotations about the x and z axis. (b) Ground structure resting on the planar stage based on perpendicular rollers.

The displacement is applied by a compression test bench (Testometric M250-2.5CT) with an accuracy of 0.001 mm. The force is measured with a Futek 9N load cell (JR S-Beam Load Cell FSH00092). The travel speed was varied to assess the influence of dynamic effects on the results. The shown results are obtained with 100 mm/min travel speed, at a sampling frequency of 1000 Hz.

The production process has an effect on the thickness of the product that is difficult to predict. This is caused by the stretching of the sheet when formed over the mold. As the sheet stretches out the thickness reduces. The thickness of the shells is measured at multiple sampling points using a digital thickness caliper.

12.4.2. Measurements results

Figure 12.12 shows the results of the force measurements. Two identically fabricated shells were tested under the same conditions. The signal from the load cell is filtered with a moving average filter (function *smooth* in MATLAB). Both the unfiltered as the filtered results are shown in transparent and opaque lines respectively. The blue lines represent the force for sample 1 in both downward and upward motion direction. The green line shows the same for the sample 2. The force from the optimization result is plotted for reference in red.

Figures 12.13a and 12.13b show the thickness distribution of both samples at selected locations on the shell. The thickness is given in hundreds of a millimeter.

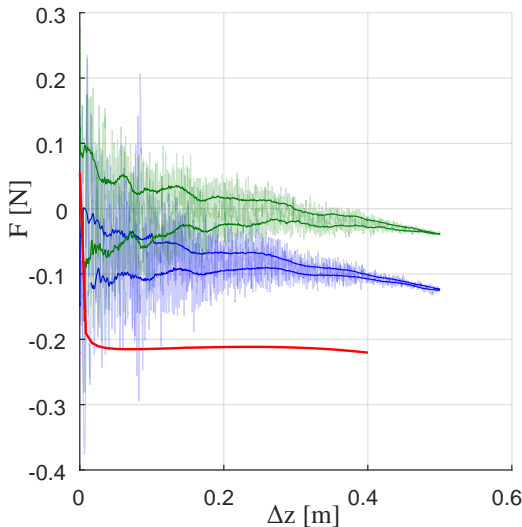
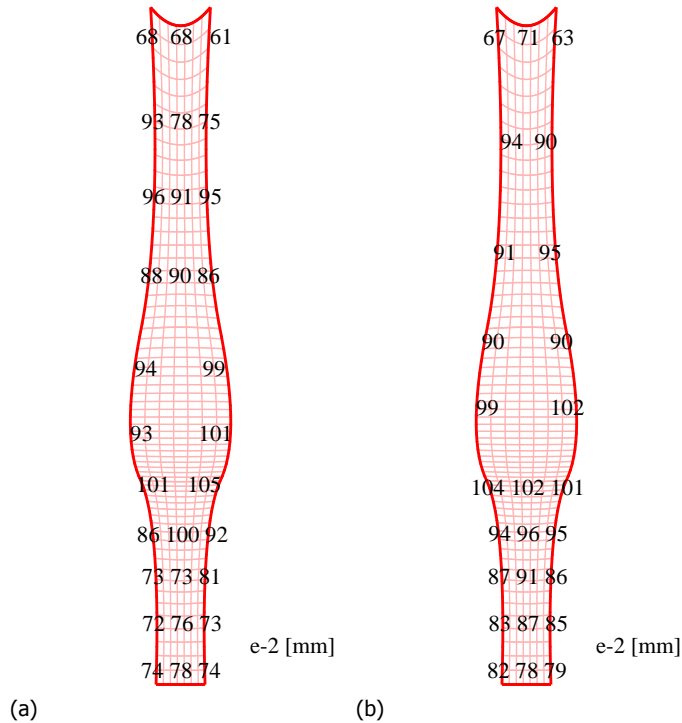


Figure 12.12: Measurements result. The vertical force at the top of the shell is plotted for the two samples, green and blue, and both unfiltered and filtered, transparent and opaque respectively. The red line shows the result of the optimization, for reference.

12.5. Discussion

This section is subdivided in categories discussing first the opportunities for generalization of the obtained results, the numerical analysis and optimization, the results and finally the physical model.

Figure 12.13: The thickness of the physical model is measured locally at multiple spots to show the influence of the production method on the output of the physical model. (a) and (b) show the thickness values for the two samples at the corresponding locations.



12.5.1. General

It is a general trend to make use of nonlinear effects such as buckling in designing resilient structures. The presented approach and results illustrate the potential of shape optimization to obtain tailored responses. The presented work shows a case study where a constant force is obtained as a result of the double curved complex shape of the shell. This illustrates the potential of shells as integrated nonlinear force generators. We have no reasons to assume that other behaviors, including negative stiffness, can not be accomplished by this approach.

Beyond the application of shells as nonlinear force generators, i.e. springs, it is expected that shells with a properly designed and optimized shape can serve more general purposes as mechanisms. While a spring can be defined as a mechanism of which the input and output are at the same location, as suggested by Vejar [4], a general mechanism can be defined as a system transforming motion, energy and/or force, with an input and an output, not necessarily at the same location. A compliant shell mechanism can be employed as a mechanism, taking advantage of the possibility to tailor the elastic response even further with respect to planar compliant mechanisms.

In current work we have considered only symmetric geometries and loading conditions. Even though the motions out of the symmetry plane were not constrained (only vertical displacements were applied), no measures were taken to stimulate

the optimizer to seek such behavior. Allowing asymmetric shapes could result in interesting constructions with the same type of objective but with asymmetric motions. Asymmetry could be achieved by simply adding a noise on the location of the control points, adding no additional design variables, or by allowing truly asymmetric shapes by increasing the number of design variables. That way also effects as lateral and torsional buckling can be exploited beneficially.

12.5.2. Numerical model and optimization

The use of isogeometrical analysis for the shape optimization has lead to satisfactory results. The results are smooth and the convergence is good. The refinement level used during the optimization already gives a reasonable prediction of the response. After two refinement steps the error already drops under the 0.1%. Knowing the location of stress concentrations it is advisable to apply the refinement only locally, where needed most. In this case that would be near the base of the shell mechanism. This can drastically reduce the number of degrees of freedom and thus the computational time. This has not been done here in order to make the comparison within the steps and within the different orders more clear.

It must be stressed that the choice of the isogeometric formulation is not a necessary condition for the proposed design process. Although the method has some clear advantages when applied to shape optimization, mainly related to shape fidelity, no need for repeated meshing, and computational cost efficiency (see e.g. [234]), it is possible to base the optimization on other available software packages like Ansys or Abacus.

The reparametrization of the cartesian coordinates of the B-spline into a branch topology turned out beneficial. It makes it easy to apply bounds intuitively, makes results easier to compare and to interpret. Specifically it helps distinguishing parameters that influence the curvature in both longitudinal and transverse direction, and parameters that influence the width and length of portions of the shell.

The numerical model is based on a linear material law. It is generally known that most polymers, including PETG, have a nonlinear stress-strain relation. Because in this work the strain regime is relatively small ($<1\%$) a linear model was employed. Applying a nonlinear constitutive law should yield improved representation of the physics. However, in that case the trade-off with the additional computational expenses must be taken into consideration.

12.5.3. Results

The results of the optimization are very satisfactory in terms of achievement of the objective. The three shown examples have all very good constant force output.

In terms of the distribution of stress over the available material the results are less satisfactory. As anticipated in Section 12.2.1 the soft parts of the shell tend to attract most deformation. As these portions deform they become flatter and thus softer, therefore amplifying this effect. The result is a lumped deformation even though the shell thickness is not narrowed down at specific regions as is done in conventional lumped compliant mechanisms. It is expected that by introducing an additional cost function to the optimization this negative effect can be mitigated.

Such cost function could include a penalty for stress concentrations and reward designs where the stresses are more evenly distributed.

A benefit of the illustrated approach is that it provides intrinsic end-function realization. There is no need to build it up from multiple subsystems with sub-functions. In the obtained results it is hardly possible to attribute various sub-functions to various parts of the shell. For example, it is not easy to point out a load-carrying positive stiffness part vs a compensator part with negative stiffness, as is the case in many other compliant constant force generators [115, 146].

12.5.4. Physical model

The physical model was constructed for a qualitative and quantitative evaluation of the system. The measurements show that the behavior of the shell is as predicted, i.e. a constant force. Quantitatively, however, a large discrepancy between measured and predicted force is observed. Main cause of this discrepancy is assumed to be in the production process. Due to the uneven stretching of the material during the vacuum-forming process, and possibly also the anisotropy that is introduced, the thickness of the shell is non-uniform and significantly different with respect to the modelled shell, as can be verified in Fig. 12.13. Therefore this experiment cannot be used for validation of the numerical model, but rather only for a qualitative, conceptual validation of the design.

For a successful realization of a shell mechanism it is crucial to obtain a better match between numerical and physical model, taking into account the effects of the production process. It is therefore recommended to invest in the ability to obtain uniform thickness shells, or to integrate the production related effects into the numerical model and accommodate for variable thickness and eventual anisotropy.

The roughness and the hysteresis of the measured force express the difficulty to measure such small forces on such a large travel range, and in particular to measure only the vertical force without influencing the other loading directions. Part of the noise in the results is due to dynamic vibrations of the shell which were observed during the measurements. Another cause of noise and hysteresis is the resistance of the planar stage. Although the resistance is low, it does introduce some small stick-slip disturbances which in turn induce the dynamic vibration. It can be noticed that the noise and the hysteresis is significantly bigger at the begin of the range of motion with respect to the end of the range. That is because initially a small vertical displacement results in a large horizontal displacement of the base, while at the end the vertical displacement results in almost no horizontal displacement. This brings the hysteresis and vibration in relation to the imperfections and friction caused by the rollers.

12.6. Conclusion

The design of a gravity balancing compliant shell mechanism with help of shape optimization lead to multiple results with good balancing quality. To the authors' knowledge, the shown results are first of a kind in the design of an irregular shell shape that exhibits a tailored force-displacement response.

The results give confidence that more general mechanism functions can be achieved by spatial, doubly curved structures with large deformations, i.e. compliant shell mechanisms.

Shape optimization as a design tool provides results with intrinsic end-function realisation. Instead of realizing a desired output from the connection of subsystems with dedicated sub-functions, the desired output is tailored at once in the optimization procedure.

A selected design was validated with a convergence analysis. Furthermore two physical models were built and tested. The physical models show qualitatively comparable behavior, but the measurements reveal substantial quantitative discrepancies. The discrepancies, however, can at least partially be explained by the manufacturing uncertainties of the vacuum-forming process and the side effects of the measurement method. As a consequence of the built-in static balancing, both the physical models can be operated with very little effort.

13

Pseudo Rigid Body Modeling of a single vertex compliant-facet origami mechanism (SV-COFOM)

Jelle Rommers, **Giuseppe Radaelli**, Just L. Herder

Recently, there has been an increased interest in origami art from a mechanism design perspective. The deployable nature and the planar fabrication method inherent to origami provide potential for space and cost efficient mechanisms. In this paper, a novel type of origami mechanisms is proposed in which the compliance of the facets is used to incorporate spring behavior: Compliant Facet Origami Mechanisms (COFOMs). A simple model that computes the moment characteristic of a Single Vertex COFOM has been proposed, using a semi-spatial version of the Pseudo-Rigid Body (PRB) theory to model bending of the facets. The PRB model has been evaluated numerically and experimentally, showing good performance. The PRB model is a potential starting point for a design tool which would provide an intuitive way of designing this type of mechanisms including their spring behavior, with very low computational cost.

This chapter is a short version of a paper published in the Journal of Mechanisms and Robotics (2017) [235], and in the proceedings of the ASME IDETC 2016 40th Mechanisms and Robotics conference, Charlotte (USA), August 2016 [236], recipient of the Compliant Mechanism Award. In this abstract the focus is on the results.

13.1. Introduction

Origami, the art of paper folding, has inspired the engineering community for decades. Applications range from solutions in packaging, to stiff sandwich panels with an origami inspired core. Recently there has been an increased interest in origami from a mechanism design perspective. In this view, the paper is replaced by plate material and the creases by hinges. These hinges are usually constructed by introducing a flexible material, categorizing the origami mechanisms as *compliant mechanisms*. We will refer to these surrogate creases as *hinge lines*. The plate material between those hinge lines will be referred to as *facets*. Mainly *action origami* patterns are of interest, which are designed to exhibit motion in the deployed state. Existing origami patterns have been converted to mechanical designs, like a solar array that can be stowed in a square satellite and deployed in space [237] or a stent that can be deployed in the desired place in an artery [238]. Advantages of origami mechanisms are the deployable nature and the 2D fabrication method which produces 3D mechanisms.

Literature in which the facets in origami mechanisms are considered as compliant instead of rigid, is scarce. Schenk and Guest [239] investigated the macro-scale deformation modes of *Folded Textured Sheets*, incorporating the bending of facets by introducing virtual hinge lines with torsional stiffness. Tachi [240] addressed the same topic with emphasis on design. Saito et al. [241] presented a theoretical design of a self-deployable rigid origami tessellated sheet which uses strain energy from one compliant facet. Silverberg et al. [242] analyzed an origami mechanism based on the square-twist pattern, which shows a bi-stable behavior due to bending deformations of the facets.

In current research the flexibility of the facets is primarily seen as an unwanted side-effect, whilst this property can be used to the designers advantage. Compliant facets can function as springs, adding a fundamental attribute to origami mechanisms. The scarce literature on origami with compliant facets primarily deals with small deformations and macro-scale behavior of lattices, instead of origami from a mechanism perspective.

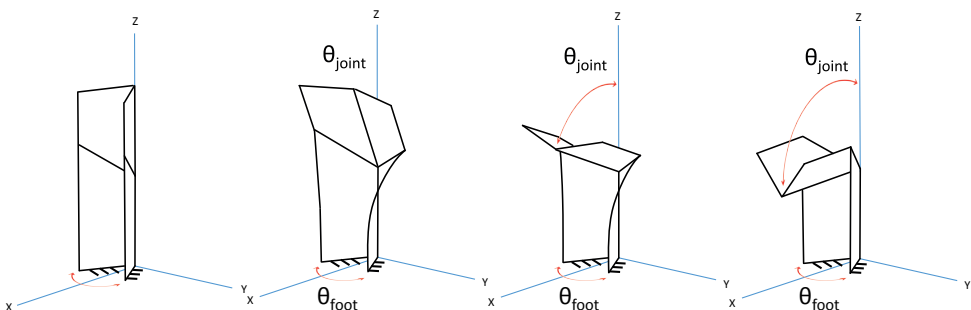


Figure 13.1: The SV-COFOM clamped at the bottom at an angle θ_{foot} . The bottom facets are forced to bend during movement, acting as springs and causing a bi-stable behavior. The mechanism can be viewed as a joint with angle θ_{joint} with a nonlinear torsional stiffness.

The subject of this chapter is the basic origami mechanism which is shown in Fig. 13.1. The mechanism belongs to the *Single* class according to the categorization by Bowen et al. [227]. The term *Single* refers to the single intersection point of the hinge lines, commonly called a *vertex*. 36% of the 130 action origami patterns that Bowen et al. investigated belong to this category. The hinge lines in the mechanism are assumed to have a negligible torsional stiffness. When the mechanism is clamped at the bottom and the facets would be considered as rigid, the mechanism would have exactly zero degrees of freedom (DOF). But bending of the bottom facets provides additional degrees of freedom, allowing movement of the top facets. This results in a bi-stable behavior in which the mechanism snaps to the first or last position in the figure. The mechanism can be viewed as a joint with angle θ_{joint} and a nonlinear torsional stiffness.

The mechanism in Fig. 13.1 is an example of a novel type of origami mechanism where the flexibility of the facets is used to incorporate spring behavior. We will call these *Compliant-Facet Origami Mechanisms*, abbreviated as *COFOMs*. Analog to the categorization of Bowen et al. we will categorize the mechanism of interest as a *Single Vertex COFOM*, or *SV-COFOM*.

The goal of this chapter is to propose and validate a simple yet accurate model that computes the moment curve of the mechanism in Fig. 13.1 as a function of the indicated θ_{joint} . The main challenge is to describe the spring behavior of the bending facets. Such a simple model could be the starting point for a design tool which would provide an intuitive and insightful way of designing with low computational cost.

13.2. Methods

The approach to construct the model which computes the moment curve of the SV-COFOM is analog to the Pseudo-Rigid Body (PRB) model theory from L.L. Howell [62]. Applying this theory leads to a parametric formula with two unknowns, the *model parameters*. These are used to fit the formula on data from a Finite Element (FE) model for a defined *standard design* of the mechanism. With the two obtained model parameters, the model is tested by comparing it to a FE model for altered designs of the mechanism. The FE model is validated experimentally.

PRB model

The Pseudo-Rigid Body model is normally used as a simple model to describe the large deflection of beams. A beam is approximated by two rigid beams connected by a torsion spring. The location and stiffness of this torsion spring are unknown and are used to fit the PRB model on existing force and deflection data.

Figure 13.2 shows how PRB theory can be applied to the bending of the bottom facets of the SV-COFOM. The left figure shows the mechanism in unfolded state. Bending of the facets is approximated by introducing virtual hinge lines (dashed) with virtual torsion springs. The modeled mechanism now exists out of six rigid facets. The angular rotation of the virtual springs is denoted by τ_B . This angle is defined to be zero when the bottom facets align, corresponding to the unbent facets in the real model. The clamped PRB model has two DOF. A constraint is

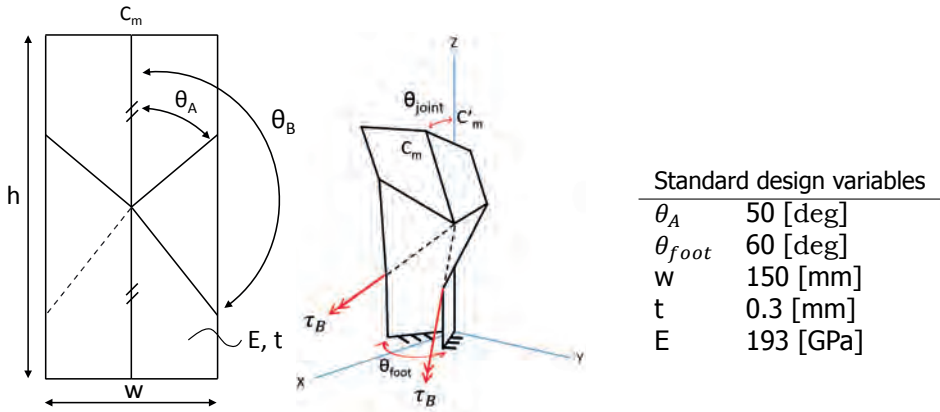


Figure 13.2: Pseudo-Rigid Body (PRB) model of the clamped SV-COFOM. Bending of the bottom facets is modeled by introducing virtual hinge lines (dashed lines) with a torsion spring, dividing both compliant facets in two rigid ones. Point C_m is constrained to lie in the XZ-plane, creating a 1 DOF mechanism. By writing the angular rotation of the torsional springs τ_B as a function of θ_{joint} , the moment curve of the mechanism can be constructed.

added by constraining point C_m to be in the XZ-plane. Because of symmetry, only the right half of the SV-COFOM needs to be modeled. The resulting moment curve is multiplied by two afterwards.

Parametric formula

The torsional stiffness in the real hinge lines is assumed to be zero and gravity is neglected, making the virtual torsion springs the only attribute capable of storing strain energy. To construct the parametric formula from the PRB representation in Fig. 13.2, we need to find the relation between the angular rotation of the virtual hinge lines τ_B and the joint angle θ_{joint} . Once we have found this relation, the moment curve can be constructed by first computing the strain energy in one spring:

$$V_{spring}(\theta_{joint}) = \frac{1}{2} \kappa_{virtual} \tau_B(\theta_{joint})^2, \quad (13.1)$$

where $\kappa_{virtual}$ denotes the torsion stiffness of the virtual hinge line. Secondly, by taking the derivative of the energy of the two springs with respect to θ_{joint} , the moment curve is obtained:

$$M_{PRB}(\theta_{joint}) = 2 \frac{\partial V_{spring}(\theta_{joint})}{\partial \theta_{joint}}. \quad (13.2)$$

Note that the energy is multiplied by two because two virtual springs exist in the mechanism.

Model parameters

The torsion stiffness of the virtual hinge line is defined as

$$\kappa_{virtual} = \xi_1 Et^3 \frac{w}{2 \sin(\theta_B)}, \quad (13.3)$$

where ξ_1 is the first model parameter and the last term is the length of the hinge line. The angle of the virtual hinge line θ_B is defined to be half way between θ_A and the bottom vertical hinge line in Fig. 13.2, plus the second model parameter ξ_2 :

$$\theta_B = \frac{\pi + \theta_A}{2} + \xi_2. \quad (13.4)$$

These model parameters are unknown and are obtained by fitting the PRB model on data from a FE model for a defined *standard design* of the SV-COFOM.

The kinematic relation between τ_B and θ_{joint} is found by representing the model as a spherical mechanism. The full derivation of this relation can be found in [235], but is omitted here for conciseness.

Fitting and comparison

The two model parameters ξ_1 and ξ_2 are obtained by fitting the moment curve of the PRB model on data from a FE model for a defined *standard design*, see Fig. 13.2, of the SV-COFOM. Fitting is done by minimizing the Root Mean Squared Error (RMSE) between the two models.

Next, the prediction performance of the PRB model with the obtained model parameters are evaluated. This is done by comparing the PRB model to the FE model for deviating designs of the SV-COFOM. The deviating designs are constructed by varying one of the standard design variables at a time to minus and plus a third of the original value (the values of the angles θ_A are rounded to 30 deg and 70 deg). Changing the E-modulus will not be tested because this only effects the moment curve by multiplication, in both the PRB and FE model. The performance of the PRB model is quantified by the RMSE between the PRB and the FE model data.

Note that the earlier obtained model parameters ξ_1 and ξ_2 will not be refitted on the new design variable sets. The SV-COFOM is modeled in the Finite Element software package Ansys. The facets of the mechanism are modeled as slender plates composed of *Shell63* elements with the nonlinear geometry option enabled. The elements are based on Kirchoff-Love theory and have four nodes with 6 DOF. The FE model is runned for the *standard design* using 121, 288, 1006 and 4020 elements. The model with 1006 elements is assumed to be 'valid' and this number of elements is used throughout the chapter to fit and test the PRB model. This validity assumption is tested by comparing to empirical data. The models with the other numbers of elements are used to test if the model with 1006 elements can be considered to be converged. Also, they serve as benchmarks to compare the performance of the PRB model.

The results of the FE model for the standard design of the SV-COFOM are validated experimentally. The mechanism is fabricated using spring steel AISI 304

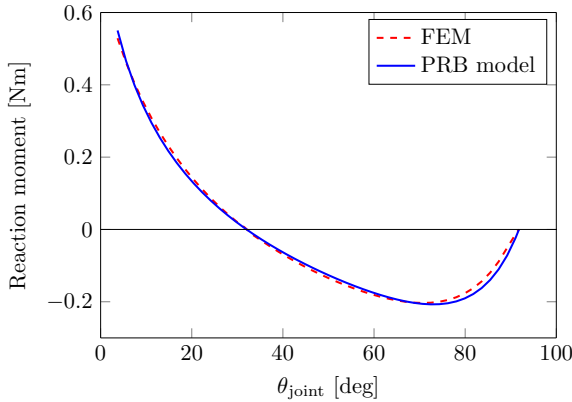


Figure 13.3: Reaction moment curve of the standard design of the SV-COFOM. The PRB model is fitted on the FEM data, resulting in model parameter values $\xi_1 = 0.994 \text{ m}^{-1}$ and $\xi_2 = 16.9 \text{ deg}$, RMSE = 1.0 e-2 Nm .

plates as facets. Hinge lines are introduced by applying Mylar[®] tape with pressure sensitive adhesive in an alternating pattern. The experimental is shown in Fig. 13.5a.

13.3. Results

Figure 13.3 shows the moment curve of the SV-COFOM with the standard design variables set. The PRB model (blue solid line) is fitted on the FE model by varying the model parameters. The optimized model parameters are $\xi_1 = 0.994 \text{ m}^{-1}$ and $\xi_2 = 16.9 \text{ deg}$. This gives a RMSE of 1.0 e-2 Nm between the two models.

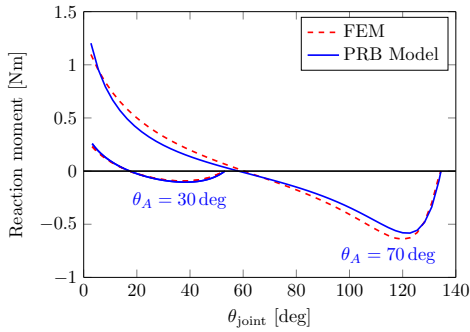
The prediction performance of the PRB model with the obtained model parameters $\xi_1 = 0.994 \text{ m}^{-1}$ and $\xi_2 = 16.9 \text{ deg}$ is shown in Fig. 13.4. The PRB model is compared to the FE model for designs of the SV-COFOM that deviate from the standard design.

Figure 13.5b shows the empirical validation of the FE model. The RMSE is 4.5 e-2 Nm .

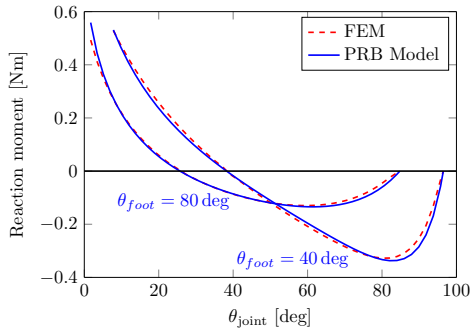
13.4. Discussion

Figure 13.3 shows that the PRB model can be fitted well on the standard design of the SV-COFOM. The prediction tests of the PRB model in Fig. 13.4 also show good results. Note the large scaling differences in the y-axes of the graphs, showing that the test cases cover a broad range. The test cases do not include a simultaneous change of parameters. However, because the tests are separated from the fitting procedure, the results are considered to indicate that the model produces useful output.

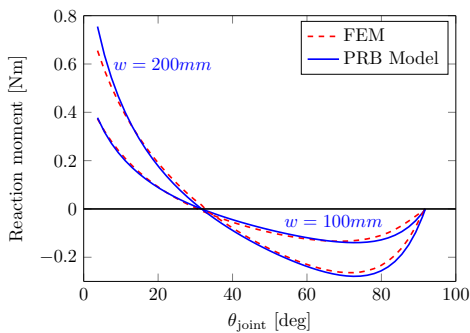
The prediction performance of the PRB model in the executed tests is comparable to a FE model with 121 elements. The RMSE between the output of the FE model with 121 elements and the converged FE model with 1006 elements (which is considered valid) modeling the standard design is 2.9 e-2 Nm . The average RMSE between the output of the PRB model and the converged FE model when modeling



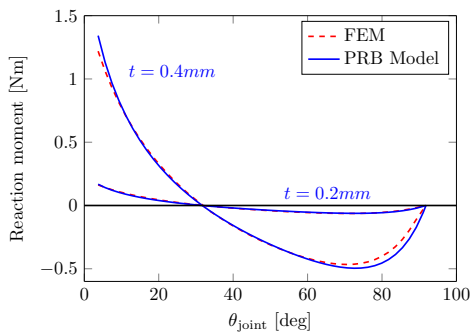
(a) Varying θ_A . RMSE = 0.9 - 5.8 e-2 Nm.



(b) Varying θ_{foot} . RMSE = 1.7 - 1.0 e-2 Nm.



(c) Varying w . RMSE = 1.2 - 1.8 e-2 Nm.



(d) Varying t . RMSE = 0.4 - 2.9 e-2 Nm.

Figure 13.4: Prediction performance of the PRB model with the earlier obtained model parameters.

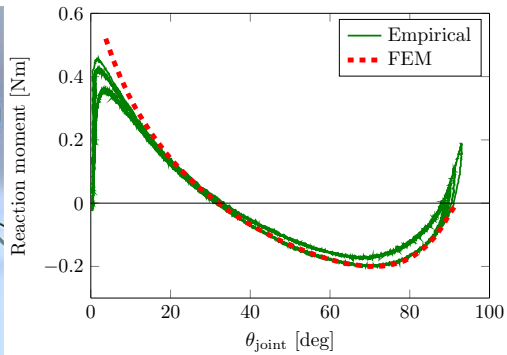
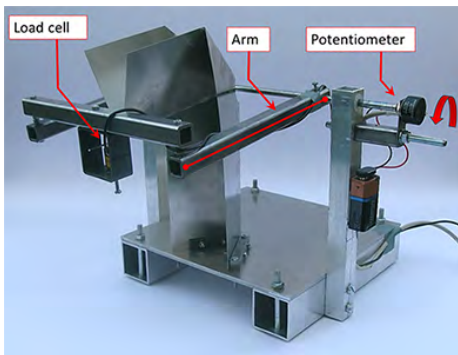


Figure 13.5: (a) Experimental setup. The moment curve of the clamped SV-COFOM is recorded using a load cell and a potentiometer. (b) Empirical validation of the FE model for the standard design of the SV-COFOM. The RMSE is 4.5 e-2 Nm.

the varied design test cases is 1.8×10^{-2} Nm. Note that an exception is the case where θ_A is varied to 70 deg, with an RMSE of 5.8×10^{-2} Nm. However, if the RMSE values would be normalized by the reaction moment values, the PRB model would also in this case score equal to better than the FE model with 121 elements.

The PRB model could be used in the early design stages of origami mechanisms with compliant facets providing an easy, insightful way of designing with very low computational cost. The computational cost of the model is orders of magnitude lower compared to the FE model because it is a closed-form expression. This makes it feasible to use optimization algorithms to search for the right design variables to approach a desired moment curve.

Figure 13.5b shows good correspondence of the FE model with the measurements. The empirical data around the buckling point $\theta_{joint} = 0$ shows lower values than the FE data. This is probably due to imperfections, as normally the case when buckling is measured empirically. The empirical data curve shows some hysteresis. This is probably due to energy dissipation due to strain in the Mylar[®] tape, or play in the hinge lines or attachment to the load cell.

13.5. Conclusion

A new type of origami mechanisms has been proposed in which compliance of the facets is used to incorporate spring behavior: Compliant Facet Origami Mechanisms (COFOMs).

A simple and accurate 1 DOF model which computes the moment curve of a Single Vertex COFOM is proposed, using a semi-spatial version of Pseudo-Rigid Body theory to model bending of the facets. The performance of the model has been evaluated numerically and experimentally. The model showed an average RMSE of 1.8×10^{-2} Nm (on a magnitude in the order of 0.45 Nm) which is comparable to a Finite Element model with 122 elements. The PRB model is a potential starting point for a design tool which would provide an intuitive way of designing this type of mechanisms including their spring behavior, with very low computational cost.

The FE data shows good correspondence with an experimental test, with a RMSE of 4.5×10^{-2} Nm on an order of magnitude of 0.45 Nm.

14

A design tool for a single vertex compliant-facet origami mechanism (SV-COFOM) including torsional hinge lines

Jelle Rommers, **Giuseppe Radaelli**, Just L. Herder

A large part of the application driven research of origami-like mechanisms focuses on devices where the creases (hinge lines) are actuated and the facets are constructed as stiff elements. In this chapter, a design tool is proposed in which hinge lines with torsional stiffness and flexible facets are used to design passive, instead of active mechanisms. The design tool is an extension of a model of a Single Vertex Compliant Facet Origami Mechanism (SV-COFOM) and is used to approximate a desired moment curve by optimizing the design variables of the mechanism. Three example designs are presented: a Constant Moment Joint, a Gravity Compensating Joint and a Zero Moment Joint. The Constant Moment Joint design has been evaluated experimentally, resulting in a RMSE of $6.4 \cdot 10^{-2}$ Nm on a constant moment value of 0.39 Nm.

This chapter is a short version of a paper published in the Journal of Mechanisms and Robotics (2017) [243], with focus on the results.

14.1. Introduction

A large part of the recent application driven origami mechanisms research focuses on self-folding robots and structures. In this field, the hinge lines are actuated so that the device can fold itself, starting from a printed flat sheet [226, 244, 245]. The vast majority of this research is based on the premise of rigid facets. In Chapter 13 Compliant Facet Origami Mechanisms (COFOMs) are introduced in which flexible facets act like springs [235]. The presented mechanism can be viewed as a joint with a nonlinear spring. A PRBM model is proposed which computes the moment curve resulting from bending of the facets. The model is developed on the assumption of zero torsional stiffness in the hinge lines. Aside from the fact that this assumption is never fully valid in reality, this torsional stiffness could be used to design mechanisms with interesting moment-rotation curves. The SV-COFOM could be used as a building block, a joint, of which the stiffness curve can be manipulated.

The goal of this chapter is to propose and validate a design tool for the presented SV-COFOM. This is done by first extending the model to include torsional stiffness in the hinge lines. Second, an optimization algorithm is used to find the design variables that give the closest approximation of a desired moment curve.

14.2. Method

Incorporating stiffness of the hinge lines

The model in [235] is extended by introducing the torsional stiffnesses κ_A and κ_C in the real hinge lines τ_A and τ_C , see Fig. 14.1. In order to construct the moment curve, the relation between the rotation of the hinge lines and θ_{joint} must be found. This is done based on a spherical mechanism representation, but is omitted here for conciseness. Once this is done, the potential energy in the SV-COFOM can be calculated as (gravity is neglected):

$$V(\theta_{joint}) = \frac{1}{2}(2\kappa_A\tau_A^2 + 2\kappa_{virtual}\tau_B^2 + \kappa_C\tau_C^2). \quad (14.1)$$

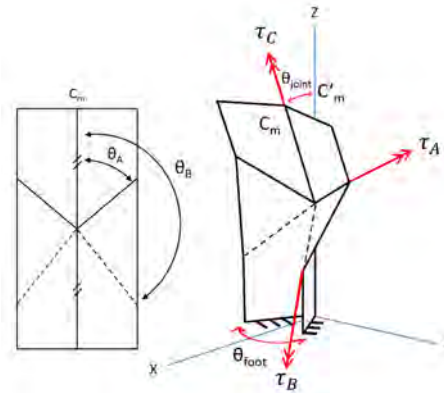
Note that κ_A and $\kappa_{virtual}$ are multiplied by two because these hinge lines appear twice in the SV-COFOM. The derivative of this energy with respect to θ_{joint} gives the moment curve of the mechanism:

$$M(\theta_{joint}) = \frac{\partial V(\theta_{joint})}{\partial \theta_{joint}}. \quad (14.2)$$

Optimization

A gridsearch with iterative local refinement of the grid is applied. The grid search approach strongly reduces the possibility of finding a local optimum, as in other optimization tools. The low computational power used by the design tool makes the use of the grid search approach possible. The design variables of the SV-COFOM are depicted in Figs. 13.2 and 14.1: the torsional stiffness of the hinge lines κ_A and κ_C , the position angle of the hinge lines θ_A , the foot angle θ_{foot} and the width, thickness and E-modulus. The last three variables all have the same effect on the

Figure 14.1: The Pseudo-Rigid Body (PRB) model of the SV-COFOM is modified by adding the torsional stiffness τ_A and τ_C .



moment curve (a multiplication), so only the width is varied. The E-modulus and thickness are fixed at 193 Gpa (AISI 304 spring steel) and 0.3 mm respectively.

Example designs

Three example designs are worked out. In each example, the design of the SV-COFOM is optimized to approach a certain desired moment curve.

The first example design is a Constant Moment Joint (CMJ). The objective is to construct a moment curve which has a constant value for a range as large as possible. A constant range is defined as the range for which the moment values are within boundaries of 3% of the average of these values. The result is shown in Fig. 14.2.

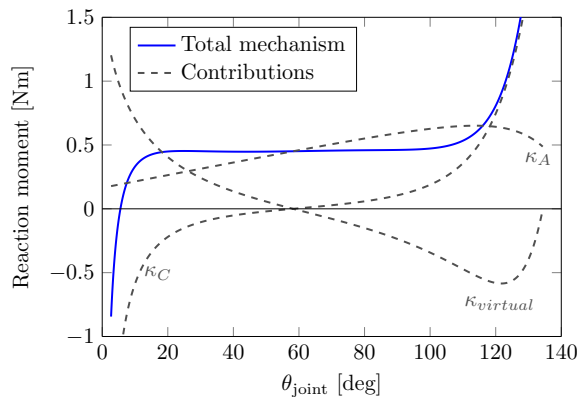


Figure 14.2: Design 1: Constant Moment Joint and separate contributions of the hinge lines. The range is 77 deg with a maximum 3% error from its mean constant value of 0.45 Nm.

The second example is a Gravity Compensating Joint. In this design, a virtual mass of 0.4 Kg is attached at the top of the SV-COFOM (point C_m in Fig. 14.1). The goal is to counteract the gravity forces on the mass, i.e. to get a reaction moment curve of zero of the mechanism including the mass. The objective function determines the range in which the reaction moment curve is between $\pm 3\%$ of the maximum exerted moment of the mass. One extra design variable is added: a tilt

of the mechanism, measured from the vertical in the positive y-direction. The result is shown in Fig. 14.3.

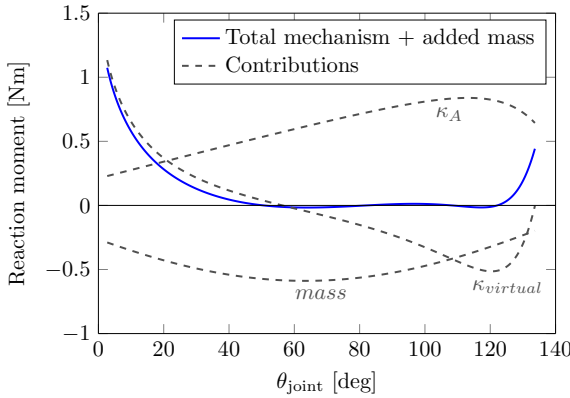


Figure 14.3: Design 2: Gravity Compensating Joint. Range of 80 deg with a maximum deviation of 3% of the maximum moment of the mass (0.4 Kg). The mechanism is tilted forward 27 deg (in the positive Y-direction in Fig. 13.1).

The third example is a Zero Moment Joint. The design is optimized to obtain a moment curve that stays within boundaries around zero for a range as large as possible. The boundaries are defined as $\pm 3\%$ of the absolute value of the minimum moment of the contribution from the virtual hinge lines. The result is shown in Fig. 14.4.

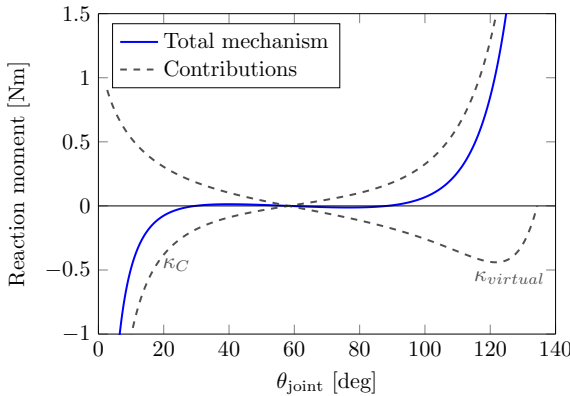


Figure 14.4: Design 3: Zero Moment Joint. Range of 66 deg within 3% error of the minimum value of the $\kappa_{virtual}$ curve.

14.3. Experiments

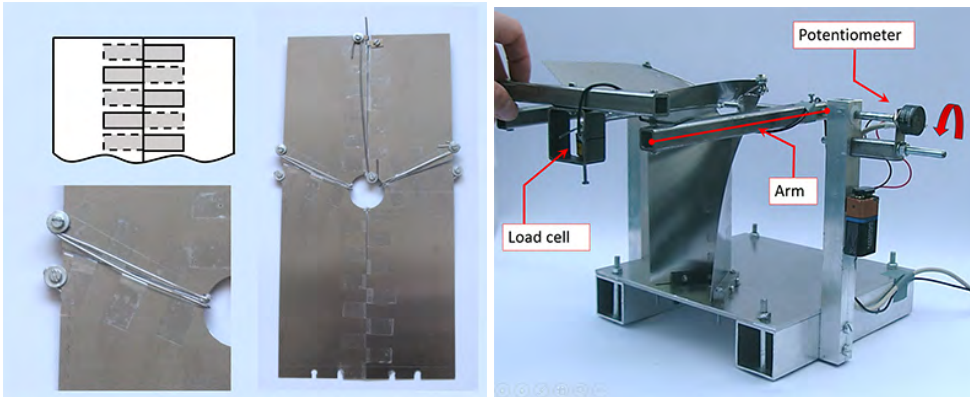
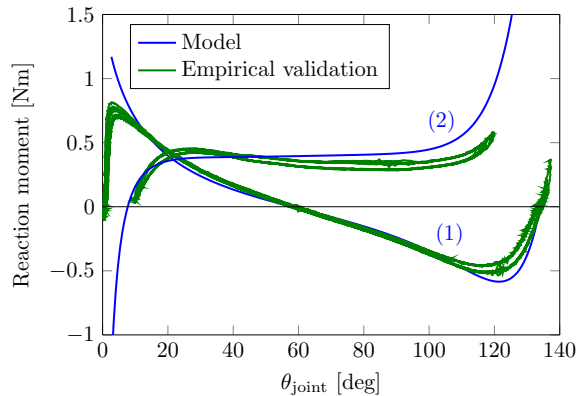


Figure 14.5: (a) Fabrication of the Constant Moment Joint (CMJ) design. Hinge lines are created by applying Mylar[®] tape between two spring steel plates in an alternating pattern. Torsional stiffness is added by clamping spring steel wire (torsion bars) at both sides of the hinge lines. (b) Experimental setup used to record the moment curve of the Constant Moment Joint design.

Figure 14.6: Empirical validation of the Constant Moment Joint design. (1) is the mechanism with $\kappa_A = \kappa_C = 0$. (2) is the complete mechanism with added torsional stiffness $\kappa_A = 0.1250\text{Nm/rad}$ and $\kappa_C = 0.3204\text{Nm/rad}$. The RMSE between model and empirical data for the original constant range of the CMJ is 6.4×10^{-2} Nm.



14.4. Conclusion

A design tool which optimizes the design variables of a clamped SV-COFOM to approach a desired moment curve is proposed. This is done by extending a model in earlier work of the authors [235] to include torsional stiffness in the hinge lines and by using an optimization algorithm.

Three example designs have been presented: a Constant Moment Joint, a Gravity Compensating Joint and a Zero Moment Joint. The design examples showed that the moment curve of the SV-COFOM can be manipulated to a large extend.

The Constant Moment Joint design has been evaluated experimentally. The

RMSE between the model output and the experimental data for the constant range showed to be 6.4×10^{-2} Nm, on constant moment value of 0.39 Nm. This indicates that the design tool is suitable for a course estimation of the moment curve of the SV-COFOM in early stages of a design process.

15

Study on the large-displacement behavior of a spiral spring with variations of cross-section, orthotropy and prestress

This work is dedicated to the study of the large-displacement behavior of a spiral spring. Parameters that influence the local torsion stiffness of the beam that constitutes the spiral are varied and their effect is studied. Cross-sectional shape, orthotropic material orientation and prestress are the three classes of parameters that are varied. The effect that the local change in torsional stiffness has on the overall behavior is illustrated in a linearized way by comparing in-plane and out-of-plane stiffnesses, and nonlinearly by inspecting three-dimensional potential energy field (PEF) of the system. Several embodiments composed of multiple spirals are showed to illustrate how the understanding of the nonlinear behavior could be exploited in conceptual design of compliant mechanisms.

15.1. Introduction

In the process of designing compliant mechanisms an important step is often the tailoring of the nonlinear stiffness behavior. Compliant mechanisms often work in a displacement range where their members undergo large deflections. In most cases the load response and the stiffness properties are not uniform across the motion range. It is thus challenging to thoroughly understand and exploit these properties. As such, innovative ideas that require this understanding may remain unexplored.

English [208] shows the use of isopotential energy lines to visualize the end-point stiffness of a 2-DoF robotic manipulator. The isopotential lines show that the commonly used stiffness ellipses give an insufficient representation for systems that are nonlinear. Herder [35] employed the potential energy field (here PEF) of linear springs for the synthesis of mechanisms, especially statically balanced ones. Radaelli [196] employs potential energy fields for the synthesis of linkages with torsion springs, and later on for the synthesis of compliant mechanisms [200]. The use of PEFs as visual aids enhances the understanding of the elastic behavior of systems with large deflections. This visualization gives the designer information on the size and direction of forces, stiffnesses, and on the (multi-)stability in the whole motion range, not just at a single configuration as is the case with e.g. the FACT method [202], or with the use of compliance and stiffness ellipsoids [203]. It is possible to extend the PEF representation to 3D motion by using colors for the 4th dimension, i.e. the energy scalar, and with isopotential surfaces instead of isopotential lines. No examples hereof have been found in literature.

To tailor the behavior of a curvilinear beam-based spring, it is worthwhile considering both the global shape of the curve and the local properties at cross-section level. Examples of compliant mechanisms where the global shape has been optimized for specific load responses can be found in [4, 134, 141]. In these examples the effect of the curved shape of the beam is clearly demonstrated. However, the examples are planar and the cross-sections are uniform and simple, i.e. rectangular or circular. In [71, 246, 247] we find examples where in addition to the shape, also the cross-section is varied through the length of beam segments. Varying the shape and the cross-section is done as an additional step after obtaining a topology by means of topology optimization, in order to improve the performance in terms of stress concentration and strength. Nevertheless, the considered geometries are planar and have solid cross-section. Thin and open cross-sections, for instance, are left out of consideration.

Another means to tailor the global behavior is by changing the structure at a local level. Merriam [248] reduced the bending stiffness of flexures by changing the blade flexures into lattice flexures. He shows an increase of the torsional-to-bending stiffness ratio of up to 1.7 times higher than an equal aspect-ratio blade flexure, and an up to 6.5 times higher transversal-to-principal bending stiffness ratio. Integrated into a cross-axis flexural pivot joint he obtains a substantial stiffness reduction in the motion direction with respect to all other directions.

Lachenal [249] makes use of an I-beam of which the open cross-section results in a low torsion and high bending stiffness, to tailor the nonlinear twist of a morphing wing. The carbon fibres that constitute the flanges are mostly placed in the

longitudinal direction of the beam, pronouncing even further the contrast between the low torsion and high bending stiffness. By applying prestress on the flanges they even obtain a bi-stable twist behavior.

The open tube or split-tube concept can be found in different works, where the very low torsion-to-bending stiffness ratio is cleverly exploited. Goldfarb [250, 251] proposes a well-behaved revolute flexure joint and applies it in various embodiments. Well-behaved refers particularly to a fixed axis of rotation and high off-axis stiffnesses, properties that are non-typical in compliant mechanisms. Vos [252] employs the open tube geometry to twist a morphing wing. Moreover he controls the warping, and thus the twist, by actuating the relative position of the opposing sides of the slit. The CR joint introduced by Trease [253] has a cruciform cross-section. Also this open profile has a comparatively low torsion-to-bending stiffness ratio. These examples show that the cross-section shape, the material orientation and the application of prestress are ways to selectively increase compliance in certain directions in despite of other directions. It can be noticed, however, that in the given examples the goal is limited to a rotational motion about an axis, as fixed as possible.

It is worthwhile exploring alternative global shapes and combine them with various cross-sections, material orientation and prestress conditions. It becomes then possible to have combinations of selective compliance between other directions, including translational motions. This opens up the possibility to design, for instance, prismatic joints, cylindrical joints and other type of path following mechanisms.

Current work presents the results of an exploratory study on the effects of cross-sectional shape, material orientation and prestress on the large deflection elastic behavior of a given complex beam geometry. A spiral is chosen as global geometry because of the evident coupling between torsional deformation mode on a local level with the out-of-plane translational motion of the endpoint. A linearized stiffness measure is used to compare the out-of-plane stiffness with the in-plane stiffness. To analyze the behavior with large deflections the graphical representations of the PEF are used, which have been extended to 3D for the occasion. It is the first time that such PEF representations are used for spatial mechanisms.

The remainder of the chapter is structured as follows. Section 15.2 describes the concept of the spiral spring and the coupling between local and global deformation in further detail. Furthermore, the proposed variations in cross-section shape, material orientation and prestress are discussed. Section 15.3 contains the small displacement and large displacement analyzes. Section 15.4 gives some illustrative embodiments of multi-spring arrangements. The results are discussed in Section 15.5 and the conclusions are given in Section 15.6.

15.2. Concept

The investigated concept consists of a spiral-shaped elastic body. The outer end of the spiral is fixed to ground. The inner end of the spiral is rigidly connected to a point that in undeformed configuration coincides with the origin (hereinafter *endpoint*),

see Fig. 15.1. This point is treated as the end-effector throughout the remainder of the chapter. The spiral is defined in the yz -plane, (hereinafter *main plane*). In this concept it is interesting to analyze the effect of the global displacement of the endpoint on the local load-mode at cross-sectional level. If the endpoint of the spiral is loaded in the main plane the prevalent load-mode of the cross-section is bending. If the endpoint is loaded out of the plane instead, the prevalent load-mode of the cross-section is torsion. In this study we analyze the effect of altering the torsion stiffness in relation to the bending stiffness and its effect on the global behavior of the spiral. The torsional stiffness is altered through variations in the cross-section shape, orthotropic material orientation and prestress. It is expected that by lowering the torsional stiffness at the cross-section level, the global stiffness out-of-plane is reduced as well. Particular attention is given to the behavior at large displacements which is not obvious.

The spiral curve is defined as

$$r(t) = ((r_{in} - r_{out})t + r_{out}) \begin{pmatrix} 0 \\ \cos(n2\pi t) \\ \sin(n2\pi t) \end{pmatrix} \quad 0 < t < 1, \quad (15.1)$$

where n is the number of revolutions, r_{in} and r_{out} are the distance from the origin to the inner and the outer endpoint, respectively, see Fig. 15.1. The chosen parameter values are $n = 3$, $r_{in} = 10\text{mm}$ and $r_{out} = 100\text{mm}$.

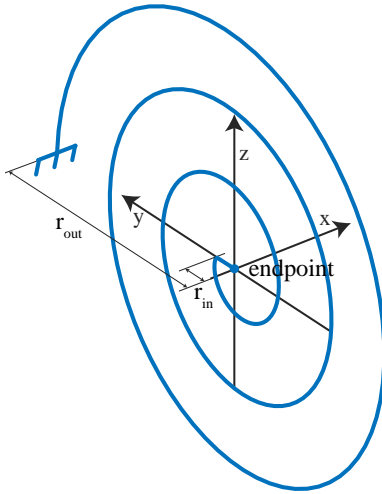


Figure 15.1: Basic shape of a spiral turning inward from radius r_{out} to r_{in} in three full revolutions. The curve defining the spiral is defined in the yz -plane. The inner end of the spiral is rigidly connected to the *end-point*, considered the end-effector of the spring.

15.2.1. Variations

Cross-section shape

The first variation to be analyzed is related to the cross-sectional shape. In thin-walled open cross-sections it is quite easy to increase the bending stiffness, which is related to the material's distance to the centroidal axis of the shape. The torsional stiffness, on the other hand, is mainly related to the section wall length. For

example, if a thin rectangular shape is bent into a curved section, the bending stiffness increases substantially while the torsional stiffness remains unaltered. There are many open thin-walled sections that would yield the sought behavior (I , T , L , Z , composed sections, etc.). To limit the number of variations and for a fair comparison this study is focussed on rectangular and curved sections that consist of a single branch with uniform thickness and length.

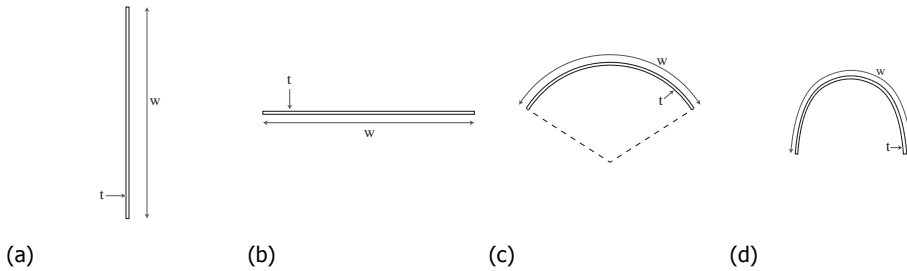


Figure 15.2: The four cross-sectional shapes that are considered are (a) a flat vertical in-plane strip, (b) a flat horizontal out-of-plane strip, (c) an arc and (d) a curved U-section. All shapes have the same thickness $t = 1\text{mm}$ and length $w = 10\text{mm}$.

The four shapes that are considered are: a vertically oriented thin rectangle (flat in-plane), a horizontally oriented thin rectangle (flat out-of-plane), an arc with two radians arc-length and a curved U-section, see Fig. 15.2. The curve-length of all sections is kept constant, so that the amount of material is kept approximately constant between variants. The curve length w and the thickness t are set to 10mm and 1mm , respectively. The four geometries are shown in Fig. 15.3.

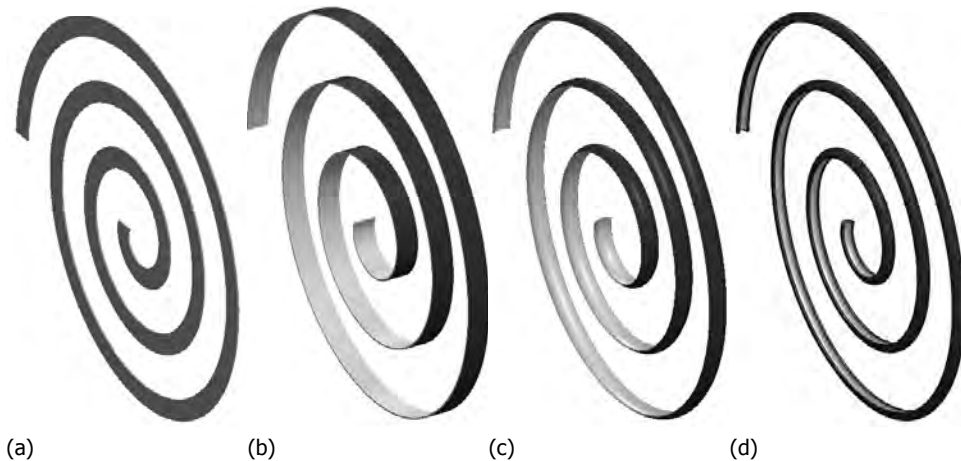


Figure 15.3: The four distinct cross-section shapes are swept uniformly over the spiral basic curve giving the spatial geometries of the springs.

Material orthotropy

An orthotropic material configuration also leads to differences of the stiffness ratio between bending and torsion. For example, a fibre reinforced material with the fibres mainly in diagonal (e.g. $\pm 45^\circ$) direction creates additional resistance to torsion and diminished resistance to bending. On the contrary a composite with all fibres placed in the length direction of the beam has a relatively low resistance to torsion and high resistance to bending. The cases that are considered here are: quasi-isotropic $[0^\circ 90^\circ 45^\circ -45^\circ]_s$, diagonal $[\pm 45^\circ]_s$ and longitudinal $[0^\circ]$, where the angle is measured with respect to the longitudinal direction of the spiral curve. The material properties used in the model are those of a standard unidirectional (UD) carbon fibre and epoxy resin combination, cured at 120°C with a fibre volume fraction of 60%. The used values for Young's modulus, the shear modulus, and Poisson's ratio are: $E_1 = 135\text{GPa}$, $E_2 = 10\text{GPa}$, $G_{12} = 5\text{GPa}$ and $\nu_{12} = 0.3$.

Prestress

Prestress is another source of changes in the stiffness behavior of elastic systems. There are many ways to apply prestress, with different advantages and effects. We will consider a way that seems most viable in this practical embodiment. The prestress is introduced by applying a rotation θ at the endpoint in the positive x -direction. The angle is then hold constant throughout the rest of the analysis. This type of prestress causes a bending load at a local level that brings the structure towards or into lateral buckling. The result is a lowered or even negative out-of-plane stiffness.

15.3. Analysis and results

The variations on the concepts are analyzed and compared using two aids: a linearized stiffness measure at the undeformed configuration and the potential energy field (PEF). The first is favourable because it gives an easy to compare numeric value for each concept variation. The drawback is that it provides only insight at small displacements around the undeformed configuration. The second analysis aid is a visual representation of the potential energy on an finite space of possible displacements of the endpoint from its undeformed configuration. It is therefore much more appropriate to get understanding of the behavior at large displacements. The drawback is that the comparison among design alternatives is more open for interpretation.

15.3.1. Linearized stiffness

The linearized stiffness measure κ is defined as the fraction of the out-of-plane stiffness over the minimum in-plane stiffness, as in

$$\kappa = \frac{\lambda_1}{\min(\lambda_2, \lambda_3)}, \quad (15.2)$$

where λ_1 is the stiffness out-of-plane and $\lambda_{2,3}$ are the principal stiffnesses in the main plane. The three values are obtained by determining the eigenvalues of the

stiffness matrix at the endpoint. In other words, they represent the length of the principal axes of the stiffness ellipsoid. Table 15.1 shows the values of κ for the concept variants of shape and material orientation without prestress.








| |  |  |  |
|---|---|---|---|
|  | 0.0072 | 0.0430 | 0.0014 |
|  | 0.2611 | 1.8459 | 0.0590 |
|  | 0.1217 | 0.5765 | 0.0209 |
|  | 0.0699 | 0.2977 | 0.0121 |

Table 15.1: The linearized stiffness measure κ at the endpoint in the undeformed state is given for the four shape variants and the three material orientation variants. A low value indicates a low out-of-plane stiffness as compared to the in-plane stiffnesses.

The effect of prestress on the linearized measure is indicated in Table 15.2 by the angle for which the stiffness measure becomes negative, the critical angle θ_c . It is clear that the angle at which the stiffness measure becomes negative is very much dependent on the other variables of geometry and material. This is comparable to the lateral buckling load of a beam loaded by a bending moment. For instance, the flat in-plane beam is very prone to lateral buckling, while the flat out-of-plane beam is not. No value (-) is assigned for the variant (flat out-of-plane, +/- 45°) since a negative κ value is not reached within eight full revolutions (4π).








| |  |  |  |
|---|--|--|--|
|  | 0.054 | 0.119 | 0.031 |
|  | 7.255 | - | 1.458 |
|  | 1.216 | 12.85 | 0.453 |
|  | 0.637 | 5.721 | 0.268 |

Table 15.2: To quantify the impact of the prestress rotation on the stiffness measure κ , the critical angle θ_c at which κ becomes negative is provided in this table. The critical angle is given for the four shape variants and the three material orientation variants. No value (-) is assigned to the variant where a negative κ is not reached within eight full revolutions.

15.3.2. Potential energy fields

Visualisation of the potential energy field (PEF) is used for a broader comprehension of the elastic behavior. A PEF, namely, represents the potential energy of the whole system as a function of the endpoint location, also at large displacements. The val-

ues of the energy are visualised as color-mapped isopotential surfaces. That means that the endpoint of the structure can be positioned at all points on an isopotential surface without changing its potential energy. As a consequence the direction of the reaction force is at all times perpendicular to such isopotential surface and zero in any tangent direction. With this understanding a PEF gives an immediate insight on the global behavior of the system which is normally not achieved by other local methods. The PEFs are constructed by computing the elastic energy of the system

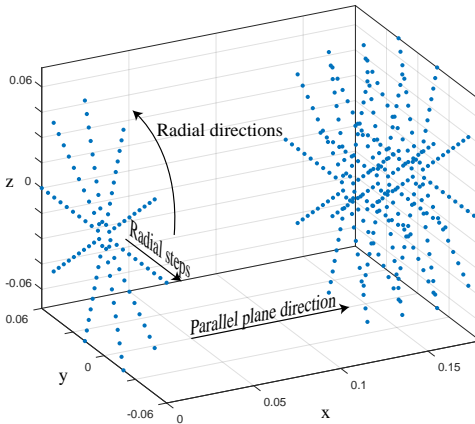


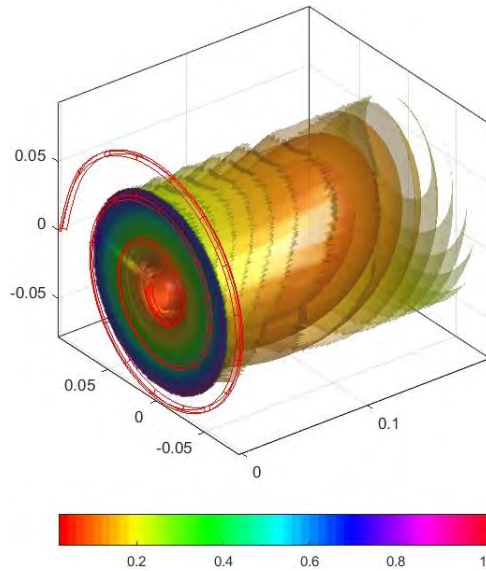
Figure 15.4: The potential energy of the whole system is evaluated for a multitude of endpoint displacement locations. The set of points is ordered in a radial grid of 70 radial steps along 36 radial directions. This is repeated for a set of 100 equally spaced planes parallel to the yz-plane.

for a set of endpoint displacements. This set of displacements is ordered in a radial grid in a series of planes parallel to the main plane, see Fig. 15.4. In the shown PEFs the grid consists of 70 steps on 36 radial directions on 100 planes, for a total number of 252000 evaluated points. Finally, for plotting purposes, the points are interpolated linearly on a Cartesian grid of 100x100x100 points. Figure 15.5 shows an example of an obtained PEF. Note that displacements are applied only in the positive x-direction. Because the construction is symmetric in the yz-plane, the whole PEF can be mirrored in that plane. In applying the endpoint displacements, the orientation is kept fixed. This choice is motivated by the possibility to easily connect systems that are, for example, mirrored or with an x-offset, and have a common intermediate body. The assumption is that the moment of one spiral is cancelled by the moment of the opposing spiral(s). The stability of these equilibrating moments must then still be checked. In addition, the assumption of no rotation facilitates the calculations of the PEF of a spring with a rigid (intermediate) body at the endpoint. The PEF in that case, namely, shifts by the dimensions of the rigid link.

The analysis is performed with a finite element tool based on thin shell elements, including geometrical nonlinearity and with a linear orthotropic material constitutive law. No contact model is implemented, meaning that the structure can freely intersect itself without affecting the behavior. This will oftentimes result in unrealistic situations. In a real implementation of this concept it must be checked if contact occurs in the desired range of motion.

Figure 15.6 shows the PEFs of all variants of shape and material with no pre-

Figure 15.5: The energy values obtained at the points on the grid are interpolated to create isopotential surfaces. The isopotential surfaces are visualised with colors corresponding to the energy value. Since the system is symmetric in the yz-plane, the PEF at the side of the negative x-axis (not shown) is the mirrored replica of the shown PEF.



stress. The plots are sectioned at the xz-plane for a better view of the inner isopotential surfaces.

Figures 15.7 and 15.8 show the PEFs with a progression of prestress rotations on two chosen variants.. The variants where the effect of prestress is most pronounced are chosen.

15.4. Embodiments

In this section we illustrate the possibility to combine and manipulate PEFs to obtain a desired behavior. A PEF can be manipulated (rotated, mirrored and translated) according to the rigid body motion of the element that it represents. Furthermore, the PEFs of multiple elements can be summed if the elements are rigidly connected in parallel. The connection consists of a rigid link between the ends of multiple spirals at a finite distance. This can be done in order to avoid physical contact between multiple elements.

Figure 15.9 shows the possibility to eliminate the asymmetric behavior of a single spiral by connecting mirrored replica of the same spiral. Namely, as will be discussed later, the preferred out-of-plane motion of many variants drifts away from the x-axis. The assembly consists of the chosen variant (U-section, quasi isotropic, no prestress) replicated three times by mirroring in the xy and the xz planes. Figure 15.9a shows an impression of how such system with connected spirals could look like. In a practical embodiment there would be an x-offset between the spirals to avoid physical contact. The effect of the offset on the rotational stability of the shuttle is neglected here. In an assembly with more replicas the moments can be balanced out. The obtained PEF is given in Fig. 15.9b. It can be noticed that the preferred out-of-plane motion is now following the x-axis.

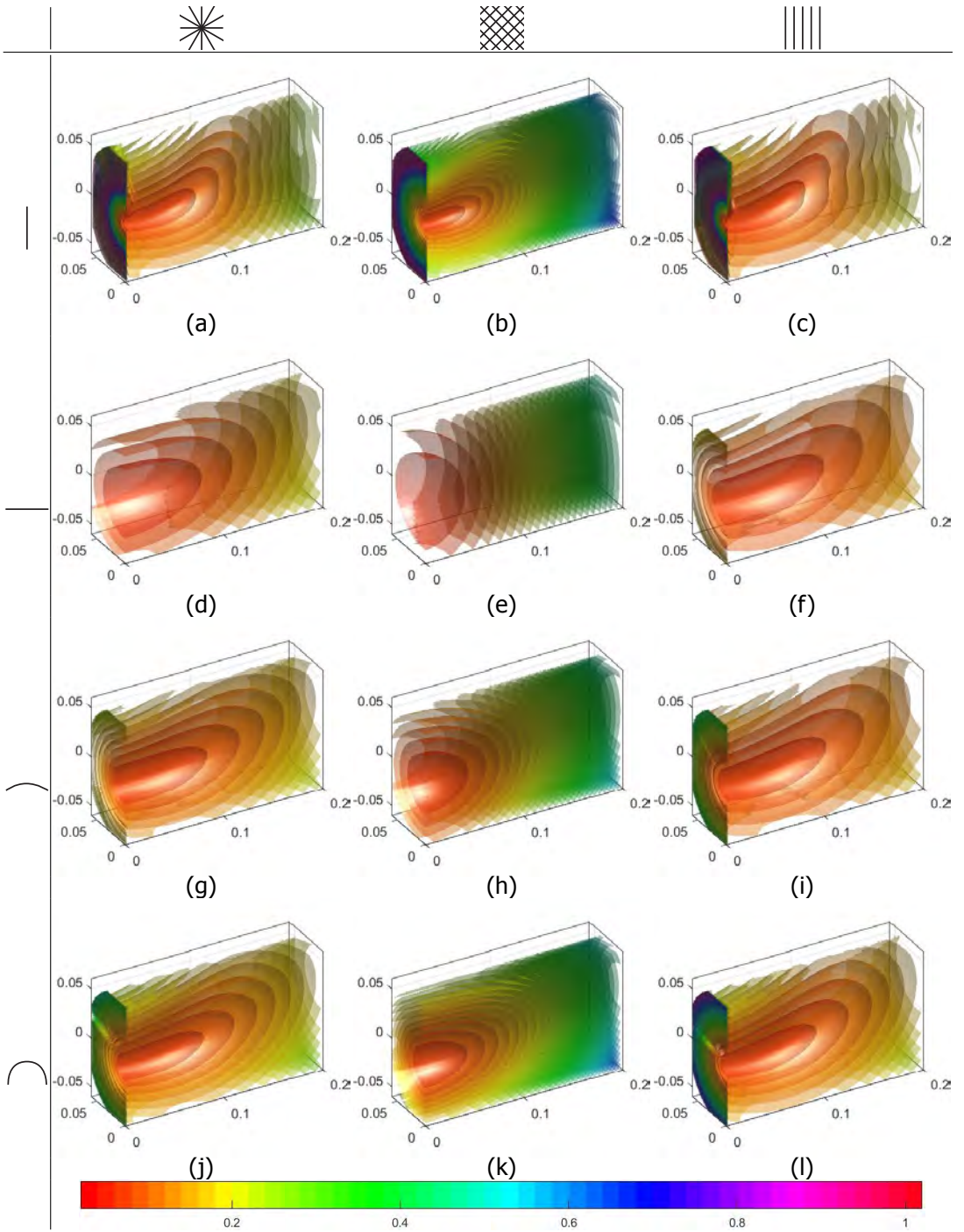


Figure 15.6: The PEFs of the variants of shape (flat in-plane, flat out-of-plane, arc, and U) and the variants of material orientation (quasi-isotropic, $\pm 45^\circ$, and 0°) are given. No prestress rotation is applied. The PEFs are sectioned at the xz-plane in order to improve the visibility of the isopotential surfaces.

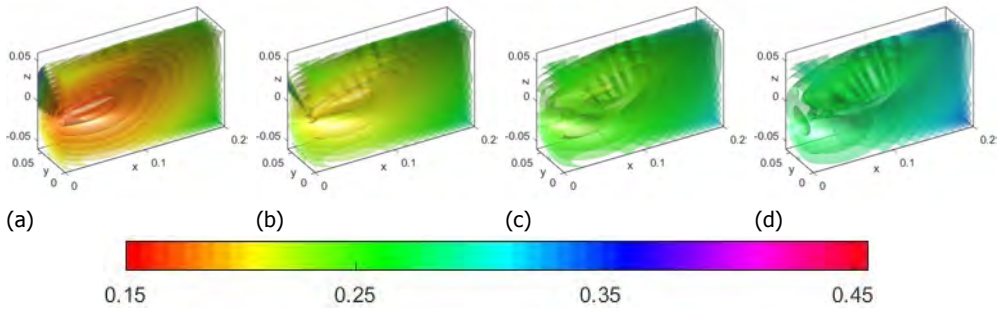


Figure 15.7: The PEFs of the variant arc-section and quasi-isotropic material, with a progressive prestress angle show that the lowest energy “bubble” drifts away from the main plane. The applied angle is (a) $1\theta_{cr}$, (b) $1.1\theta_{cr}$, (c) $1.2\theta_{cr}$, and (d) $1.3\theta_{cr}$. The critical angle in present variant is $\theta_c = 1.216rad$, as can be found in Table 15.2.

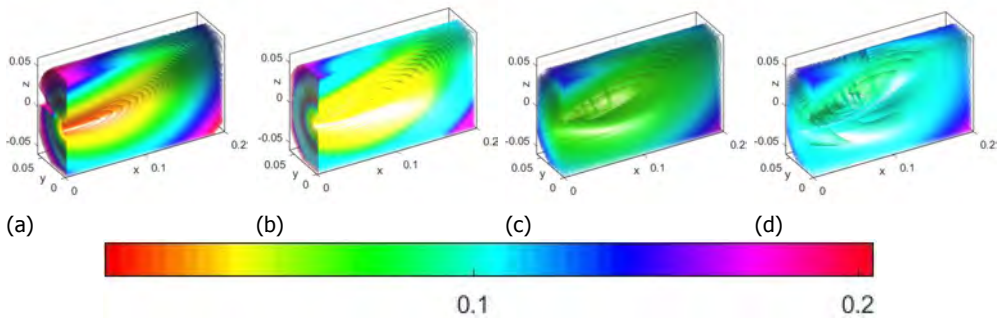


Figure 15.8: The PEFs of the variant U-section and 0° material orientation, with a progressive prestress angle show that the lowest energy “bubble” drifts away from the main plane. The applied angle is (a) 0 , (b) θ_{cr} , (c) $1.5\theta_{cr}$, and (d) $2\theta_c$. The critical angle in present variant is $\theta_c = 0.268rad$, as can be found in Table 15.2.

Figure 15.10 shows that two mirrored uni-stable spirals (flat in-plane section, 0° material orientation, no prestress rotation) connected at the endpoint and subsequently preloaded can exhibit a bi-stable behavior. The spirals are mirrored in the horizontal xy -plane. Then the clamped outer-end of the original spiral is displaced downwards in z -direction by 20mm down, and that of the replica by 20mm upward. The result is that the “bubble” of lowest energy drifts away from the main plane and separates into two local minima, one in the positive x -direction (shown) and one in the negative x -direction (not shown). Again, the effect of the offset on the rotational stability is neglected in this illustrative embodiment.

An extreme case is shown in Fig. 15.11 where an octo-stable configuration is shown with the corresponding PEFs. A spiral that is bi-stable because of the applied rotation at the endpoint (arc-section, quasi-isotropic material, $1.3\theta_c$ prestress) is connected to its three mirrored replicas, where the mirror planes are the xy and xz

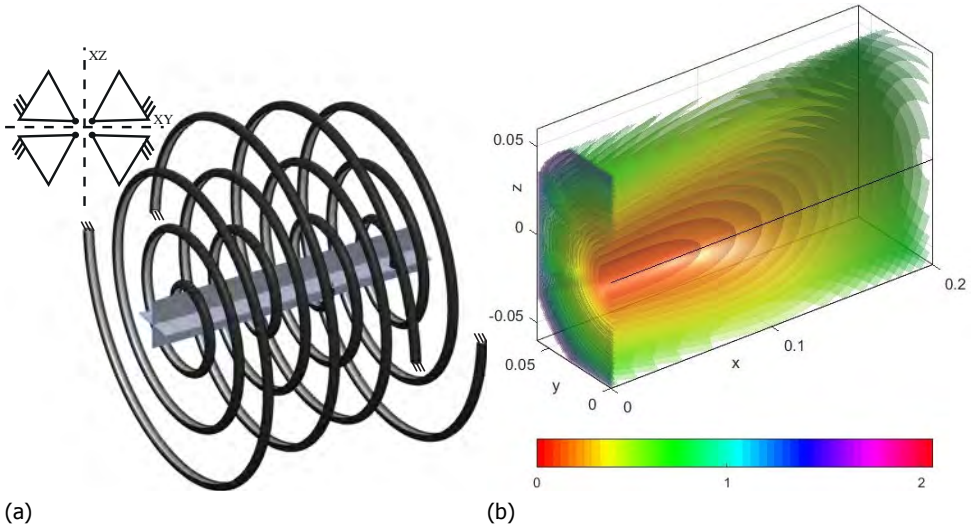


Figure 15.9: (a) A spiral with U-section and quasi-isotropic material is replicated four times by mirroring about the xy and xz planes. The endpoints are connected through a central shuttle. The spirals have an offset in the x direction to avoid contact. (b) The sum of the PEFs of the components gives the PEF of the whole system. The preferred out-of-plane motion direction exhibited a drift away from the x -axis in the separate components, but is corrected in the assembled system.

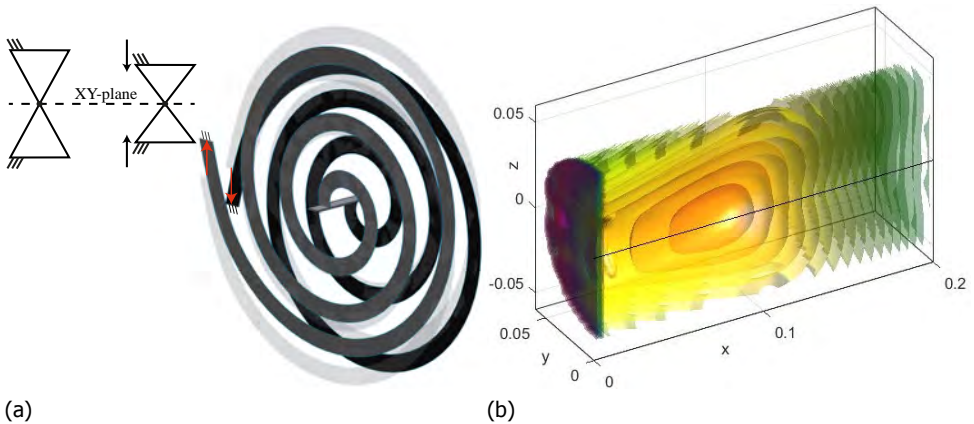


Figure 15.10: (a) Two mirrored flat in-plane spirals with 0° material orientation are connected at their endpoints through a shuttle. Subsequently, the clamped outer ends of the spiral are moved apart by 20mm each in the z -direction. (b) In the PEF of the obtained system the “bubble” of lowest energy drifts away from the main plane. Considering symmetry about the main plane, a bi-stable system is obtained.

planes. Additionally, the outer clamps are displaced down by 5mm for the upper two replica and 5 mm up for the other two, as shown in Fig. 15.11a. The result is a separation of the minimum energy “bubble” into four. Accounting for the symmetry

about the main plane of the spiral (yz) there are other four stable equilibria in the negative x -direction (not shown) resulting in an octo-stable system. As before, the offset and its effect on the stability is neglected.

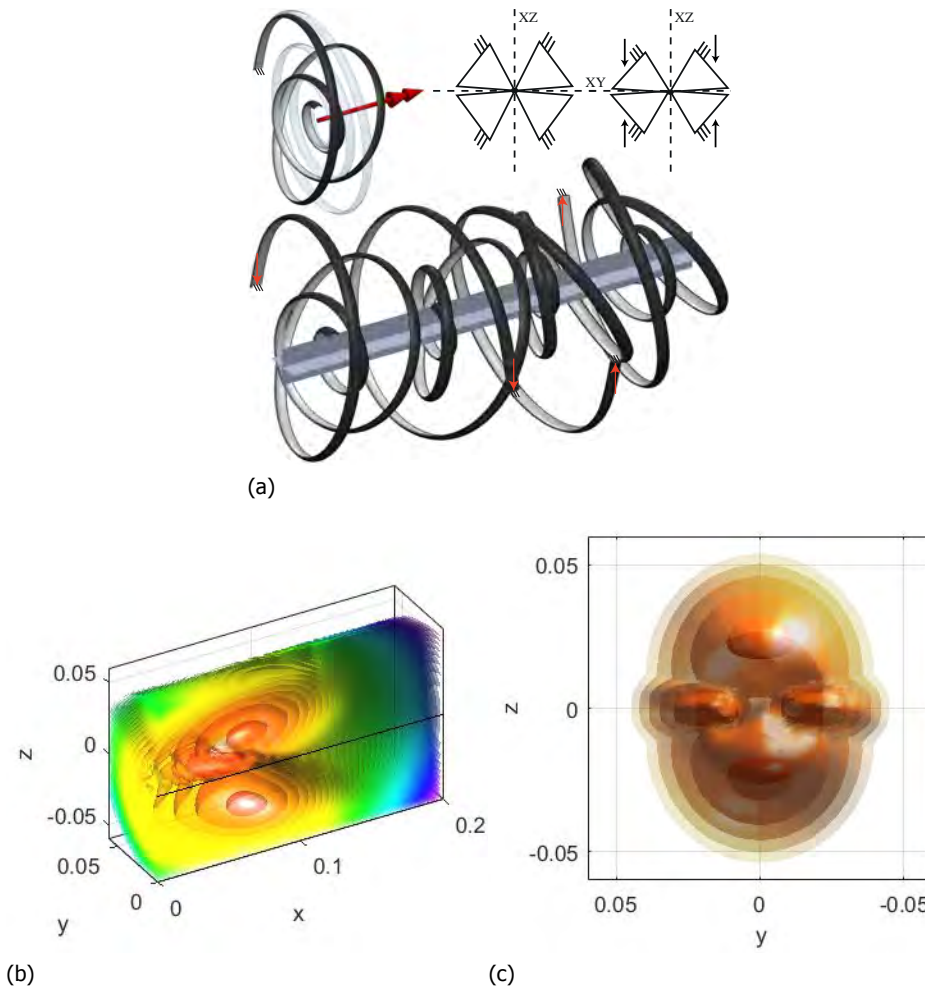


Figure 15.11: An octo-stable system is obtained by connecting four mirrored spirals (arc-section, quasi-isotropic material, $1.3\theta_c$ prestress) to a central shuttle and by displacing the clamped outer ends. (a) An illustrative embodiment is shown. (b), (c) Four distinct energy minima are visible in the PEF of the total system that including their counterparts in the negative x -direction reveal an octo-stable system.

15.5. Discussion

We present a study on the effect of different types of parameters on the elastic behavior of a spiral shaped spring. In this section the results are discussed and compared. Also, some limitations and side-notes to this study and the results are

discussed. The section ends with some thoughts on generalization and applicability of the study.

15.5.1. Observations

It was anticipated that a reduction in torsional stiffness with respect to the bending stiffness of the beam at a local level would result in a lowered out-of-plane to in-plane stiffness ratio of the endpoint of the spiral. This is indeed confirmed by the linearized stiffness measure κ (Table 15.1), and by the PEF graphs (Fig. 15.6). The longitudinal (0°) material orientation, where the contribution to the torsional stiffness is minimal, always gives a lower stiffness measure and an elongated energy field shape with respect to the quasi-isotropic cases. On the other hand, the diagonal ($\pm 45^\circ$) material orientation gives the opposite effect, i.e. higher stiffness measure and a shortened energy profile.

Looking at the cross-sectional shape it appears that the flat out-of-plane profile has in-plane and out-of-plane stiffnesses of the same order of magnitude. The out-of-plane stiffness is reduced in the arc section, and even more in the U-shaped section. The lowest ratio of stiffnesses is obtained with the in-plane flat strip. This is as expected, because every in-plane motion tends to bend the beam in its stiffest bending direction.

Some of the PEFs in Fig. 15.6 (namely 15.6a, 15.6b, 15.6c and 15.6l) show a discontinuity of the energy near the main plane (yz). This is a result of the fact that the analysis is based on a geometry without imperfections. An applied displacement in the plane of symmetry of the geometry will not cause any point of the geometry to deviate from that plane. In reality, a small imperfection in the construction or in the application of the load can cause deviations from that plane, i.e. buckling can occur. Any displacement out of the main plane is in fact an asymmetric load-case and thus the deformed shape is a buckled one. Correspondingly, the energy value is normally much lower. Figure 15.12 shows a flat in-plane spiral on which an in-plane displacement is applied (Fig. 15.12a). Consecutively, a small out-of-plane displacement is applied (Fig. 15.12b) resulting in a buckled shape with relatively low energy level. This can be compared to the simple column buckling, where an analysis without imperfections will result in a straight compression of the beam with corresponding high energy values. A slight imperfection causes the column to bend asymmetrically, usually with lower energy values.

Since in reality a system without imperfections does not exist, the high energy gradients in the plane could be disregarded. However, they indicate another phenomenon. Namely, that crossing from one side of the main plane to the other side will most likely be accompanied by a snap-back, unless crossing through the channel of lowest energy. In the assembly of Fig. 15.10 it can be noted that due to the preload, the discontinuity forms a closed barrier. This means that crossing the main plane is accompanied by a snap-back. The spring variation was selected purposely to illustrate this effect. For a smoother transition through the main plane another variant (e.g. arc-section, 0° material orientation) can be selected.

Another conclusion related to this discontinuity can be drawn regarding the us-

ability of a linearized stiffness based analysis. Namely that the stiffness between neighbouring points can sometimes change substantially. This compromises the validity of a linear analysis on a single point.

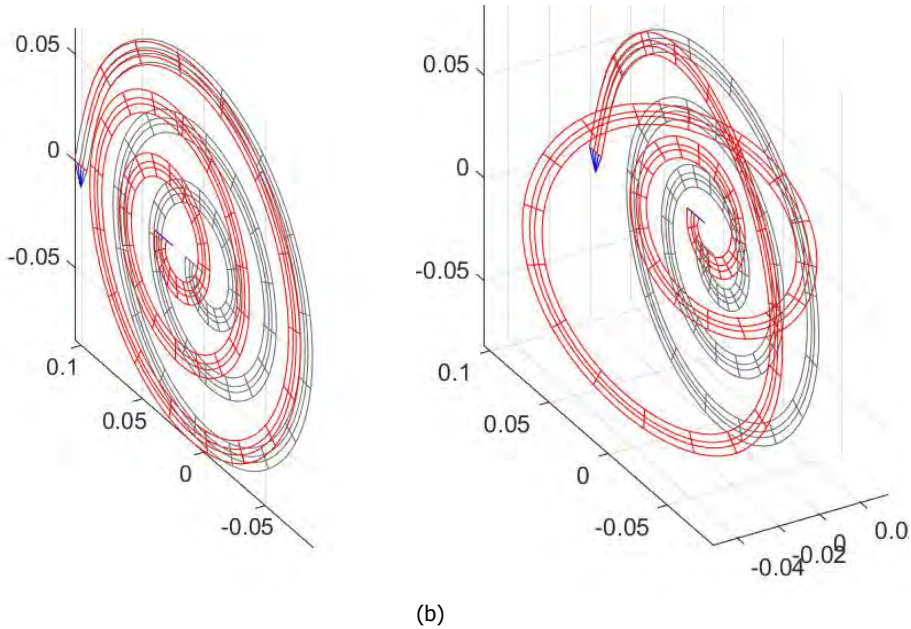


Figure 15.12: (a) An in-plane displacement is applied to a flat spiral. (b) An additional small out-of plane displacement brings the spiral in a post-buckling state.

Figures 15.7 and 15.8 reveal that prestress, applied as a midpoint rotation, often causes a drift of the stable equilibrium out of the plane, giving rise to bi-stability. As further demonstrated in Table 15.2, the sensitivity of the cross-section and material variants to the critical angle is quite high. If the stiffness is to be adjusted by this prestress angle a compromise must be made between sensitivity and a practical angle range.

It is also shown that in an embodiment like the one of Fig. 15.11, all kind of multi-stability can be created. The other option shown to create multi-stability is by applying a displacement at the clamped outer-ends of the spirals. The prestress angle and the position of the clamped outer-ends can also be used to tune the positions of the equilibria.

From the PEFS in Fig. 15.6 it can be noticed that although initially the preferred out-of-plane direction is perpendicular to the main plane, further on the isopotential surfaces reveal a drift away from the x-axis. This drift is caused by the moments induced by fixing the orientations of the endpoints and the moment arm that separates both endpoints.

The drift is mainly in the positive y and z-directions. Presumably this has to do with the fact that the first quarter turn of the spiral is in that quadrant. This portion of the spiral is the one with largest distance to the endpoint. Therefore, because of the large moment arm, it feels the highest torsion. As a consequence the system tends to hinge about that portion of the spiral, causing the drift to be towards that quadrant.

An option to correct this drift is shown in the embodiment of Fig. 15.9. The straightening effect of this solution is quite obvious and clearly visible. A less obvious effect is that the isopotential surfaces of comparable width become shorter. This means that the achieved compliance out-of-plane is reduced on the long strokes. It can be explained as follows: All four component spirals are forced by symmetry to stay on the x-axis, while that is the preferred path to none of them. As a result they force each other on a relatively high energy state, thus increasing the resistance. An alternative solution to the drift can come from optimizing the basic shape of the spiral. The assumption, not unlikely, is that there exists a shape where this drift is self-correcting.

15.5.2. Notes

In this study the orientation of the inner endpoint is fixed. The practical assumption is that multiple springs are employed with an offset in x-direction to restrict the rotations about y and z. Using mirroring in either xy or xz plane further restrict the rotation in x direction. Enough replica of springs in the x-direction stabilizes the orientation of the shuttle. The resulting system could be a tubular straight-line mechanism with low stiffness in the direction of motion and with low friction. If miniaturised it could be suitable for e.g. laparoscopic tools, or as a substitute of high friction transmissions like bowden cables.

This fixed endpoint orientation condition may not be the most appropriate if the interest goes to, e.g., the free vibration of the spring. In such case constructing the PEFs with free endpoint condition would give a more appropriate representation.

The present study is limited by a specific set of choices to make the treatise compact and comprehensible. Certainly, every design choice has its influence on the resulting behavior. In design practice, specific behavior can be tuned and optimized according to the design requirements. The geometrical dimensions and material variants have been chosen such that the effects treated here are clearly visible such to convey the message. No effort has been undertaken to take the effects to extrema, such as to obtain, e.g., a minimum κ value.

An auxiliary goal of this work is to promote the use of PEFs for the analysis and synthesis of compliant mechanism. In this work it is shown that PEFs are a powerful tool, especially when dealing with very large deflections. It must be stressed that the visibility and thus the usability of a PEF (especially in 3-D) is very much compromised in a paper version. The full significance of this visualization method can be appreciated only in a virtual environment that allows for selective transparency of the isopotential surfaces, and for manipulation, reorientation and summation of the PEFs.

15.5.3. Outlook

The choice of the spiral as a basic shape for this study was motivated by the observation that a pure twist of the beam results in an out-of-plane displacement of the inner endpoint. There are many more shapes that would be worth investigating. One of them is the helix. By applying the same type of variations as in this study one could obtain helical springs with reduced resistance to compression and tension, especially compared to the torsion. Such spring could be used as a compliant replacement for a prismatic joint.

A smaller portion of the spiral could be more convenient in a practical embodiment. For example, multiple arcs configured with rotational symmetry, can result in a linear motion spring, similar to the one shown by Parise [225]. The variations proposed in this study could enhance the out-of-plane compliance of such spring.

In general, by tailoring the global shape of the curve together with the local properties, e.g. reducing torsion stiffness, a multitude of preference path can be created. Thus it becomes possible to design a spatial curve which by allowing torsion and impeding bending traces a predefined trajectory. In such a case, a PEF representation would be a helpful instrument to analyze the behavior on the defined track and away from it.

15.6. Conclusion

This work describes an exploratory study on the elastic behavior of a spiral shaped spring and the effect of varying the cross-sectional shape, the material orientation and the prestress. It is shown that by lowering the torsion stiffness of the beam that constitutes the spiral with respect to its bending stiffness results in a reduced out-of-plane to in-plane stiffness ratio of the endpoint. By applying prestress as a rotation at the endpoint it becomes even possible to achieve a negative out-of-plane stiffness.

A measure for the linearized stiffness around the undeformed configuration is provided and gives a comprehensible overview of the behavior of the concept variations. Because the information is limited to a very confined working range, the graphic representation of the PEF is employed for a more complete understanding of the large deflection behavior. In the PEFs it is possible to grasp information about stability, equilibria, direction and magnitude of forces at every position of the displaced endpoint.

A few exemplary embodiments of multiple connected spirals are presented and their PEF is shown. The embodiments show a straightened out-of-plane preference path, a bistable, and a octo-stable behavior.

The study explores a new strategy to the design of compliant mechanisms with preference directions and/or paths. The resulting mechanism would typically be a slender spatial curvilinear beam with optimized local properties and global shape that follows a specific endpoint path.

IV

Application examples

16

Application examples

Authors Section 1:

Giuseppe Radaelli, Werner W.P.J. van de Sande, Awaz Ali

Authors Section 2:

Hoessein Alkisaie, **Giuseppe Radaelli**, Just L. Herder, Henriette H. Bier, Bert J. Sluys

This chapter presents two examples of application ideas. In Section 16.1 a tip of a heart ablation catheter is designed to provide a constant force in order to maintain contact with the heart wall without risk of puncturing it. The constant force is realized over a self-constrained linear motion by a small scale compliant shell mechanism. In Section 16.2 a large scale compliant shell mechanism is employed as a collapsible wall. As an example, the case is explored of a sound barrier along train tracks that could disappear out of sight when there are no trains passing.

In these preliminary investigations the conceptual and dimensional design and some preliminary simulations are performed to assess the potential of the concepts in these real scenarios.

Section 16.2 of this chapter is an abstract based on the M.Sc. thesis of Hoessein Alkisaie [254], focussing on some of the results.

16.1. Constant force catheter tip

16.1.1. Introduction

People suffering from cardiac arrhythmia, irregular heartbeat, can be helped by undergoing a heart ablation procedure. In this kind of procedure the abnormal electrical pathways that cause the irregular contractions of the heart are interrupted by forming scar tissue. Usually, either radiofrequency ablation or cryoablation is used to scar affected areas. A heart ablation procedure is a relatively long procedure (>4h) where a flexible catheter is fed through a vein inside the heart. The catheter tip approaches the inner side of the heart wall, see Fig. 16.1. Ideally, a path of scarred tissue is created such that a continuous barrier interrupts the faulty electrical pathways. In practice this is done by applying multiple adjacent scar dots. It is of paramount importance that the contact force between the catheter tip and the heart is kept underneath a safety value. Exceeding this force could cause puncturing of the heart wall causing serious complications. On the other hand, if during the time that the ablation instrument is activated (a few seconds) the contact force is too low or the contact separates, the procedure can become ineffective. Considering the cardiac and respiratory motions during the procedure, keeping the force between the limits is not trivial at all.

The electrophysiologist that performs the procedure can monitor the contact force which is measured at the catheter tip and displayed on a screen. However, the control that he has over the position and force of the tip is limited because of the long flexible tube between the tip and the handle. Following the heart movements at the speed of the heartbeat is practically impossible. This combination of challenges and risks makes this procedure a lengthy and technically very challenging intervention.

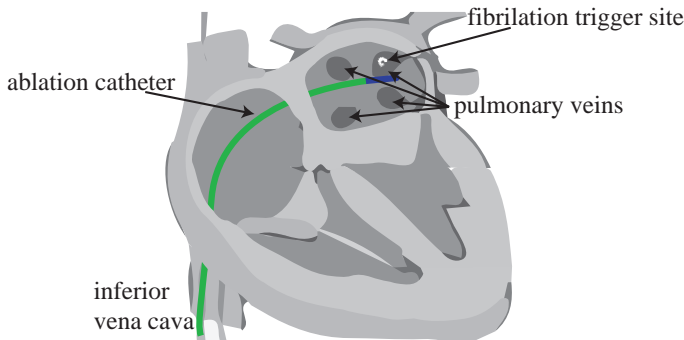
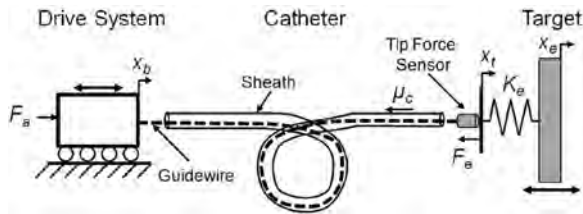


Figure 16.1: The catheter sheath is fed through the inferior vena cava to the heart. The ablation catheter tip forms scar tissue to impede faulty electrical pathways coming from the pulmonary veins to the heart.

In recent developments researchers have tried to track the fast moving cardiac tissue by implementing motion compensation [255, 256] and force control [257, 258] on a flexible robotic catheter. In Fig. 16.2 the active approach used by Gelman [258] is illustrated. They realize significant improvements in following the motion and maintaining a constant force level in their experimental setups. However, it is challenging to control the non-collocated system, i.e. actuators at the handle and sensors at the tip, because the force transmission is overclouded by

the friction and elastic losses throughout the flexible tube. This approach thus results in complex systems that are failure prone, expensive, and that are difficult to miniaturize to the dimensions required for real implementation.

Figure 16.2: Gelman et al. (2016) [258] use an actively controlled system to provide a constant force at the catheter tip. It is challenging to control this system due to the frictional and elastic losses throughout the long catheter sheath between the sensor at the tip and the actuation at the handle of the catheter.



16.1.2. Conceptual solution

We propose a conceptual solution of a passive constant force catheter tip, capable to apply a constant force throughout a desired range of motion at high speeds. Such a system could be applied, e.g., for the ablation of moving heart tissue without puncturing it nor losing contact. A clear advantage of a passive solution is that within the range of motion with constant force it is not needed to move the tip by an external actuation nor to transfer the sensor information through the whole length of the catheter.

The proposed concept is based on a compliant shell mechanism with constant curvature and tapered width. This concept is related to the tape-loop [233, 259], illustrated in Fig. 16.3, which can make a rolling movement while maintaining a constant radius of curvature at the two bends. Therefore the potential energy of the system is constant and the moving side of the loop maintains a constant distance to the base side. To convert the zero-force behavior in a finite constant force behavior a cross-sectional parameter can be varied throughout the length of the tape. A convenient one to use is the transversal arc length, because it appears as a linear factor in the energy term and it is practical for manufacturing. Similar constant force mechanisms, or mechanisms with different force-displacement characteristics, are obtained by varying the effective width of leaf springs. Usually, such systems require something that constrains the motion. In the example of Fig. 16.5 this is achieved by a symmetric embodiment that forces the motion along the symmetry line. The constrained width forces the flexure to bend with a given curvature. English [260] uses bands with varying width and also cut-outs to synthesise a desired force output, see Fig. 16.4. The band is forced to bend over the surface of a rolling joint and the rollers are constrained between two guide walls. In the proposed solution the motion is already self-constrained due to the constant transversal curvature that, like in the tape-loop, maintains the radius of curvature of the folds. Figure 16.6 shows the design of the constant force two-fold tapered tape-loop.

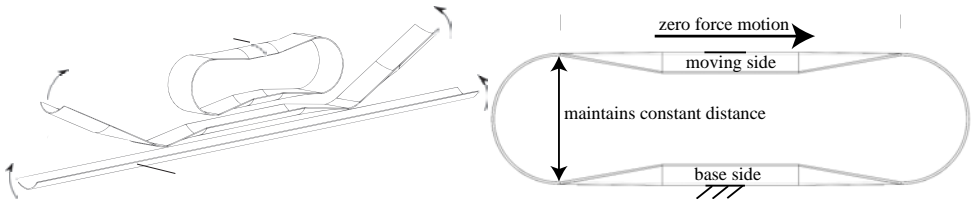


Figure 16.3: A tape-loop is obtained by connecting two ends of a tape spring. In the obtained closed loop the distance between the straight segments is constant and rolling can be done without changing the potential energy of the system thus requiring zero elastic force. Pictures modified from [259].

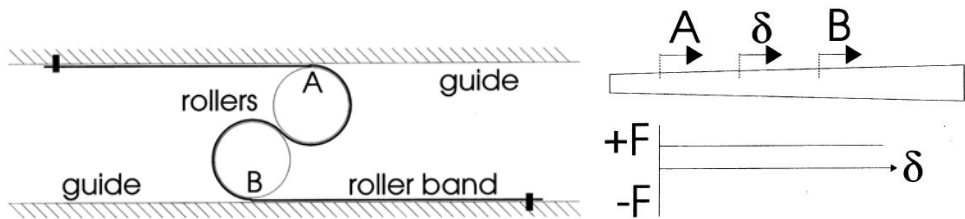


Figure 16.4: English [260] obtains various force profiles, among which a constant force, by varying the effective width of a roller band. The potential energy of the system changes according to the width of the band that is bent over the rollers.

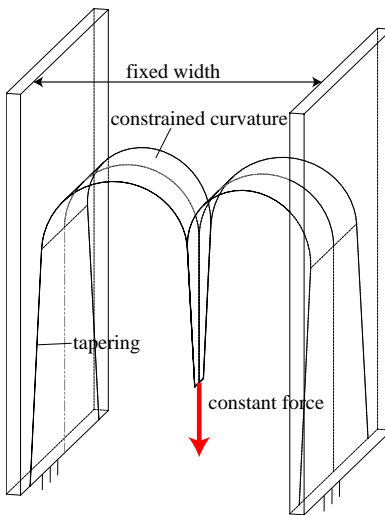


Figure 16.5: Two tapered leaf springs are folded between two constraining walls. The tapering can be used to control the output force, for instance to produce a constant force.

16.1.3. Numerical analysis

A FEM analysis performed on half of the system, i.e. a single fold, validates the constant force output, see Fig. 16.7. The system fits within a diameter of 3mm and moves over a range of motion of 30mm with an approximate constant force of 0.25N . The modelled material is a sheet of spring steel with a thickness of 0.07mm

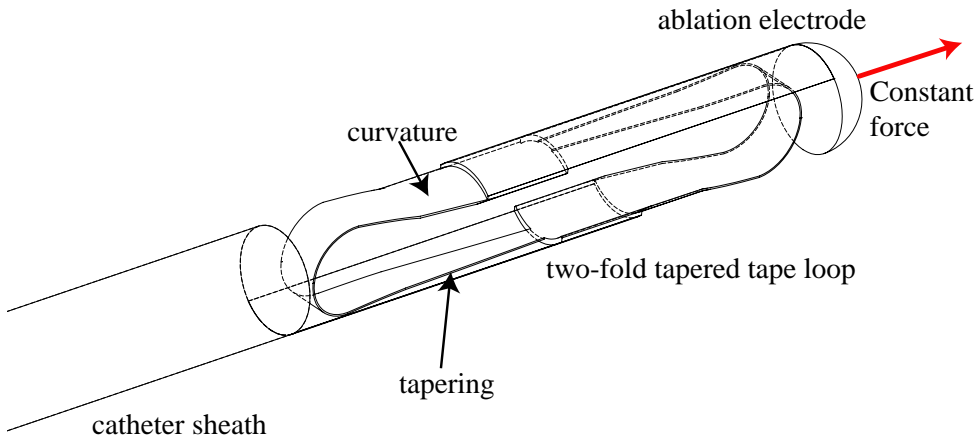
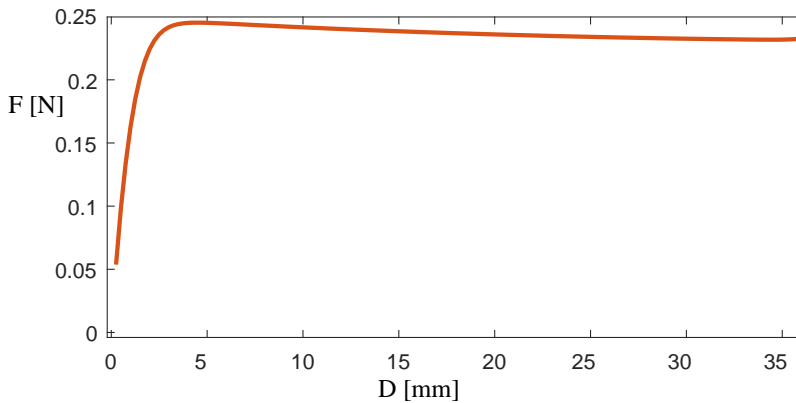


Figure 16.6: The proposed solution consists of a two-fold tapered tape-loop. The tapering of the effective width of the spring is responsible for the constant force. The transverse curvature of the tape makes it possible to maintain the radius of curvature constant without additional constraints.

and 30mm length. The endpoint of the tapered shell is pulled downwards while the initially applied rotation of 180° is kept throughout the range of motion, see Fig. 16.8. It is assumed that the counteracting moment of the antagonistic system keeps the fixed rotation.

Figure 16.7: From the FEM analysis an approximately constant force results throughout the range of motion.



16.1.4. Discussion

In the numerical results a lateral drift can be observed, i.e. the distance between the straight segments is not constant as was assumed. Moreover, the force level is also not perfectly constant but slightly diminishing. These two effects seem to be affected among others by the plate thickness and the transversal arc length. It must therefore be validated whether the conditions are met for which the radius of the folds equals the radius of the transversal curvature. In practice, however, neither the small deviation of the distance, nor the slightly diminishing force is a

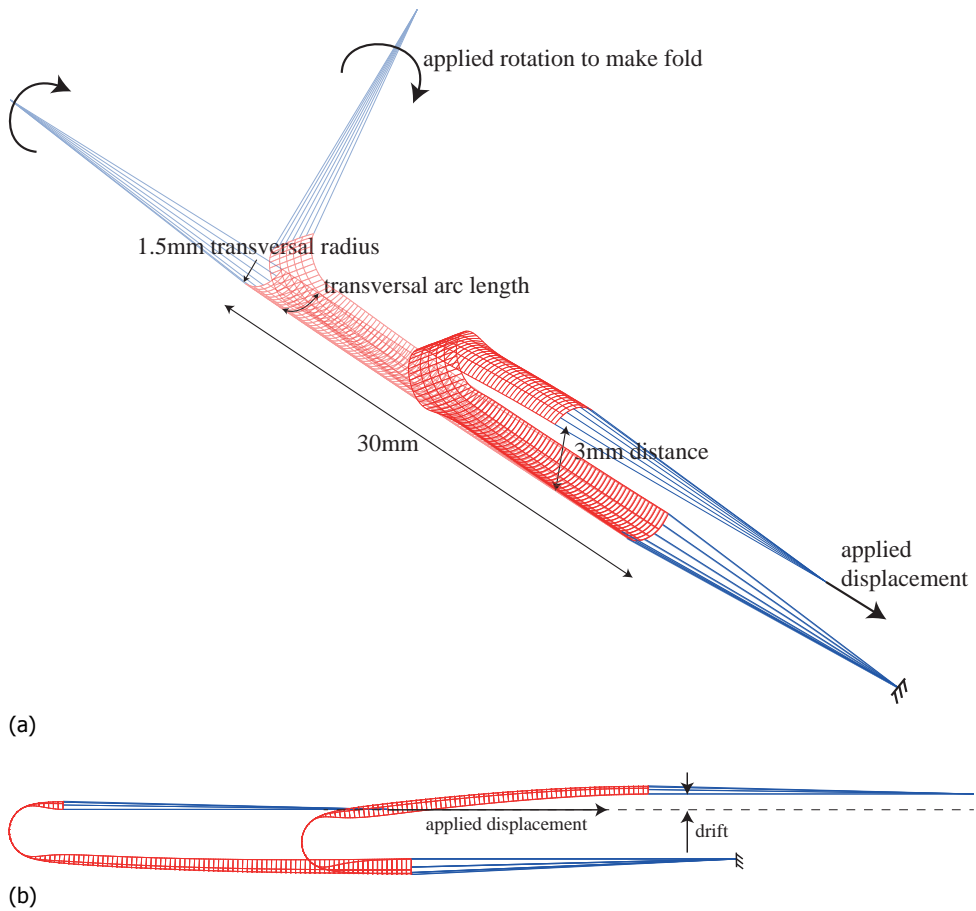


Figure 16.8: FEM simulation of tapered tape. (a) Initially the tape is folded by applying a 180° rotation. After, a displacement is applied in the longitudinal direction, while the rotation is maintained. (b) A small drift perpendicular to the applied displacement is observed.

real problem. For the force it is only important that it stays between some given upper and lower threshold values. Exact values for these thresholds are not easily assessed, but the obtained result is promising when compared to the force fluctuations observed in current clinical practice and in the cited literature. The varying distance does also not need to be a problem, as long as it is small compared to the applied displacement.

16.1.5. Conclusion

A conceptual design for a constant force catheter tip is presented. A constant force on a catheter tip can be beneficial in interventions like heart ablation procedures, where a too high force gives the risk of puncturing and a too low force gives the risk of losing contact, with an ineffective procedure as a result. The main strengths of

the proposed concept are the fact that it is passive and simple. Simulations reveal a satisfying behavior. Manufacturing challenges and other practical implementation aspects must be faced in future research.

16.2. Collapsible walls

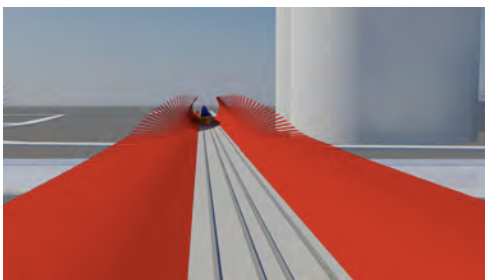
The second example regards a feasibility study on the application of a statically balanced shell mechanism as a large-scale collapsible wall.

16.2.1. Introduction

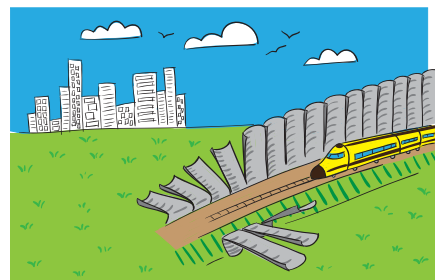
In modern architecture there is an increasing interest in moving structures that provide flexible adaptation to the constantly changing needs and desires of people or environmental conditions. However, the implementation of novel architectural concepts into real constructions is often hampered by many technical challenges.

At the scale of civil engineering and architectural constructions self-weight plays such an important role that moving constructions with large deformations is extremely challenging. Powered motion of heavy objects against gravity is often prohibitive for the size of the bearings, the size of the actuators and the consumed energy. There are of course examples where counterweights are employed to reduce the required actuation power, think of drawbridges and the like. But in many other cases the increased complexity and additional weight does not outweigh the benefits of an adaptable construction.

Some of the proposed novel architectural concepts might benefit from the techniques presented in this dissertation. Monolithic statically balanced structures could resolve the problem of structures with significant weight that must exhibit large motions. Oosterhuis et al. [261] proposed the Barrier in Motion (BiM) in which sound barriers along train tracks are flattened to the ground when no trains are passing by. As soon as trains enter the area the BiM is triggered to erect, so that the noise is blocked effectively. This way, there is only a barrier when there is sound, and the landscape is preserved the rest of the time. See Fig. 16.9 for an impression of the idea.



(a)



(b)

Figure 16.9: (a) An impression of the *Barrier in motion* along a train track, from [262]. (b) An impression of a gravity balanced compliant shell mechanism applied as a collapsible sound barrier, copyright © 2016 H. Alkisaiei.

16.2.2. Concept and results

In this section we explore the applicability of the monolithic compliant shell balancer presented in Chapter 12 at the scale of an architectural construction, for instance a sound barrier. The procedure described in Chapter 12 is repeated for a 5m tall, 0.02m thick PETG shell. The resulting optimized shape is shown in Fig. 16.10 in the fully erected and the fully flattened state. The vertical force required to move from one state to the other is shown in Fig. 16.11.

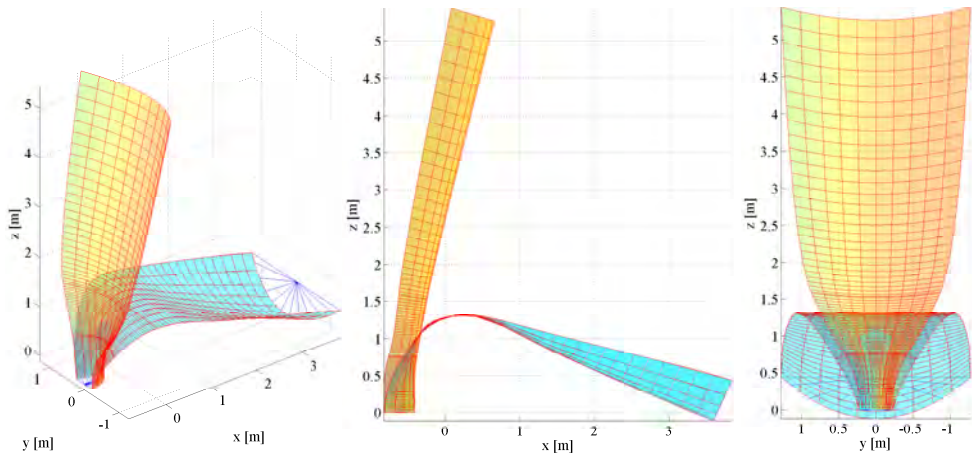


Figure 16.10: The gravity balanced shell in upright and flat state. Moving from one state to the other requires very little force because the gravity and the elastic forces are in balance throughout its range of motion.

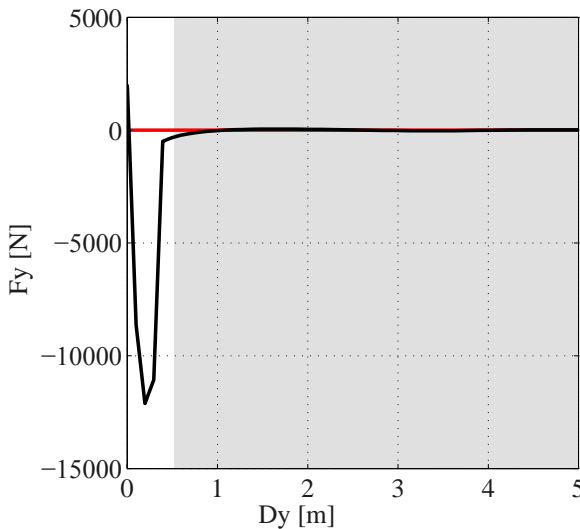


Figure 16.11: The force required to move the barrier from upright to flattened state is minimal, compared to the gravity forces involved in such a large construction. The initial negative peak is due to the application of the self-weight that brings the structure in a post-buckling condition. This is a numerical artefact, because in reality gravity will always be present and the barrier will move only within the optimized range of motion (shaded area).

16.2.3. Discussion and conclusion

The conceptual design and the numerical analysis of a functionally collapsible barrier are shown. The behavior is obtained by an inherently statically balanced large-scale shell.

Much can be said about the difficulties regarding the real implementation of this concept, which might be still far away from now. Dealing with wind loads, the real acoustic isolation performance, manufacturing challenges, material durability, etc., are all issues that have been dealt with only minimally. The work is not presented as a finished design achievement, but it is rather proposed as a disruptive view on dealing with moving architecture in general.

V

Conclusion

17

Conclusion

In this chapter the contributions of this thesis are highlighted and some directions of future research are sketched.

17.1. Contributions

This thesis consists of a collection of scientific articles, each of which presents a novel concept, method to design or evaluate it, and/or its physical realisation. The concepts represent different ways and principles by which nonlinearity is synthesised according to a desired specified behavior. In particular, these concepts address the challenges of obtaining softening, constant stiffness and negative stiffness characteristics. The obtained characteristics are defined on relatively large ranges of motion, normally in the order of magnitude of the largest dimension of the mechanism.

Torsion is an efficient energy storage deformation mode in terms of material volume and occupied volume. Two concepts to balance a pendulum by using torsion bars are presented. In both, the linear characteristic of torsion bars is transformed into the required sinusoidal characteristic. Both remarkable concepts have the benefit that the mechanism occupies a fixed and compact space along the hinge line of the pendulum. Therefore they represent suitable solutions for an accurate balance of pendulums with long hinge lines, e.g., collapsible walls and doors, without occupying the free space around.

The use of shape optimization of planar beams has led to unconventional solutions to challenging design objectives. These solutions could not have been found using combinations of elementary shapes. Using only elementary beam shapes restricts the variety of achievable behaviors. Instead, freely shaping the components of a compliant mechanism increases the design freedom which broadens the set of solutions. There is a high chance that within the broadened set, better solutions can be found. Because of the infinite options, the design freedom also results in a more intricate design process. The design strategy that was followed in the shown

examples has led to unique designs with good attainment of the desired functions. The strategy consisted of 1) choosing a topology, as simple as possible, 2) finding an approximate solution using a priori characterisation of basic shapes (e.g. PEFs) or random initial estimates, 3) defining a parametrization based on a low number of parameters but enough flexibility to describe complex shapes (to this end, B-Splines and a linkage parametrization of the control polygon were employed, see e.g. Chapter 4), and 4) local shape optimization based on an accurate numerical model of the mechanics (here isogeometric analysis was employed). We were able to apply optimized free-form beams to the balancing of a pendulum, to obtain a constant force, in a statically balanced large-range straight-line mechanism, to emulate a zero free-length spring and as building blocks for a meta-material with zero Poisson's ratio. These examples emphasize the potential of this approach to obtain desired equilibrium paths.

A monolithic weight balancer of remarkable simplicity was realized with a free-shape doubly curved shell. The distributed compliance and distributed weight of the system are in balance throughout a large range vertical displacement, while unconstrained in other directions.

The monolithic nature of most of the presented designs makes them suitable for downscaling and upscaling. These monolithic designs lend themselves well for scaling to large scale constructions where self-weight plays an important role. We demonstrated this with the design of monolithic sound walls as an example application.

The expansion of the concept of potential energy fields as characterisation method for complex compliant mechanisms has shown to be beneficial for the intuitive understanding of their large range elastic behavior. In this thesis we introduced this concept for torsion-linkages, free-shape planar compliant mechanisms and spatial compliant shell mechanisms. Compared to known alternative characterisation methods, e.g., the compliance ellipsoids, the main advantage is that it represents the behavior in a range of deformed configurations, and not only at one instantaneous configuration.

We investigated the effects of variations of cross-section, material anisotropy and prestress on the spatial behavior of a simple basic geometry for which a spiral was selected. It is shown that these parameters can be used to influence the anisotropic stiffness of the endpoint, such to obtain, e.g., a very low out-of-plane stiffness as compared to the in-plane stiffness. Applying these learnings to other shapes seems to be a promising way to create spatial path-following mechanisms with strong anisotropy, i.e. with a strong preference to move along that path although not constrained to it.

For almost all the explored concepts and examples a physical demonstrator was built and experimentally evaluated. It demonstrates the feasibility of realising the aimed equilibrium paths with relatively simple constructions. Manufacturing and detailed design was not a main objective in this work. Furthermore, measuring small forces and moments accurately, often in combination with large ranges of motion, turned out to be a major challenge in the design of the measurements setups. Also, trying to measure a single degree of freedom without influencing the

others appears challenging without introducing cross-talk and other disturbances on the measurements, as e.g., friction and vibrations in the measurement setup. Further emphasis and effort on these aspects is expected to improve the evaluation results and thus the convincingness of the concepts.

17.2. Future directions

17.2.1. From springs to mechanisms

Present work was limited to springs, i.e. mechanisms where the input and the output points coincide. The introduced concepts, however, might be useful for mechanisms more in general, i.e. with distinct and possibly multiple input and output points, for example transmissions. Also, the work was focussed on obtaining desired equilibrium paths in a given load direction, not considering much the kinematics, i.e. the resulting motion. This is the case in, e.g., the two monolithic weight balancers of Chapters 6 and 12. In general, kinematics play role of paramount importance in mechanism design. In distributed compliant mechanisms, however, kinematics cannot be considered the same way as in rigid body mechanisms. In rigid body mechanisms there is a strict distinction between degrees of freedom and constraints. This is not the case in compliant mechanisms. The presented methods to enhance stiffness anisotropy (3d-shaping, material anisotropy, creases) and the tools to analyze it (PEFs), can be used in future research efforts for more comprehensive design assignments. Thus, both the desired kinematic and the desired load response can be achieved simultaneously.

17.2.2. Actuation

Present work focusses on passive structures, leaving actuation and sensing out of consideration. This is often sufficiently relevant and, even more, the absence of actuators is a pre in many applications. In body support devices, for example, if the function can be realized by a solely passive system it is preferable over an active system where issues related to control, power supply, weight, and safety come into play. Nevertheless, for a broader application of the achievements of this work, it is a logical next step to investigate the possibilities to integrate actuation and sensing. Following the paradigm of distributed compliance and weight, it would make sense to distribute the actuation and the sensing as well. This would be particularly beneficial in shell mechanisms, where large surfaces are available, and where locally induced deformations almost always lead to global displacement of the end-effector. Another recommendable strategy is to use distributed actuation to apply changes to the passive structure instead of directly actuating the motion. Motion is then indirectly obtained by a change in, e.g., stiffness, equilibrium position, or constant-force level.

17.2.3. Material

In the presented designs spring-steel was used for off-the-shelf components, e.g., spiral torsion springs, torsion bars, etc. For custom made complex shaped parts mostly engineering plastics or fibre reinforced polymers were used. These mate-

rials are good candidates because of the freedom of shaping. In addition to that, especially in the case of fibre reinforced polymers, they have good spring qualities such as high elastic strains and elastic energy absorption, in combination with high stiffness. Many opportunities accompany the use of fibre reinforced polymers that are not much exploited in this thesis. Their local anisotropic material constants (stiffness, strength, thermal expansion) provide additional design variables to the optimization problems. Thus, optimizing the stack layup and orientation can enhance the performance of the designs and lead to, e.g., higher force densities, better distribution of stresses and deformations. For instance, by determining the optimal stack sequence and fibre orientation due to draping, the shell-balancer of Chapter 12 could be designed to carry higher loads and with the deformations less concentrated near the base. As done in a preliminary way in Chapter 15, the direction of the fibres also serves to enhance the anisotropic stiffness of the end-effector of a compliant shell mechanism. This can lead to elegant ways to design for desired kinematics (directions and motion paths with low stiffness) in combination with desired equilibrium paths. Coupling effects due to asymmetric layups can instead of being avoided, as is usually done, be used to influence the nonlinearity of the load response and the stiffness anisotropy at the end-effector. Another opportunity that is worthwhile exploring is the effect that residual fabrication stresses can have on the stiffness of composite structures. Due to different thermal expansion coefficients of the constituting materials, stresses are introduced when cooling down after the curing process. In the direction of the fibres the contraction is small as compared to the perpendicular direction. Usually, this effect is mitigated through the (almost mandatory) use of symmetric layups. In an asymmetric layup this prestress is not neutralized and can be used to alter the stiffness of the structure. It is even possible to obtain zero and negative stiffnesses in certain directions, while keeping high stiffnesses in other directions.

17.2.4. Characterisation methods for compliant mechanisms

Due to the fact that in compliant mechanisms kinetics and kinematics are inseparable, the availability of useful elastokinematic characterisation methods is of paramount importance. Most available methods are only valid for selected types of elements and/or for small deformation ranges. The advocated use of potential energy fields (PEFs) has clear advantages in these respects, but is far from being a turnkey solution for the compliant mechanism designer. Points of attention for coming research efforts should include

- ways to speed up the calculations in order to enhance interactivity between a design tool and the designer. Preferably, a designer should immediately see the effects of his proposed design changes in order to make quick design iterations.
- improvements in the visualization of three dimensions.
- an intuitive way to display rotational degrees of freedom in the displacement field.

- a comprehensible way to combine more relevant quantities such as force and stiffness in the field representations.

17.2.5. Applications

It is becoming common practice to equip mechanical devices with as many actuators and control systems as may possibly be needed. This tendency is comprehensible because of the increasing availability of hardware and software that allows to design that way. Also, it results in systems that can be used more flexibly because of the redundant freedom to control the system the way you like. It is indeed easier to apply changes to the software that controls a machine, then changing its hardware.

But there are cases where this approach reaches its limit. Applications where requirements on compactness, weight, energetic efficiency and autonomy, etc., play an essential role are not necessarily well served by a fully actuated and controlled system. In these cases spending more effort in a solid passive basis can lead to systems that require less controlled degrees of freedom and lower operating forces, thus saving on weight of the motors, consumed energy, space occupied by the motors, shielding of the electrical circuits, etc. In this respect shape morphing structures, deployable structures, and statically balanced mechanisms attract much attention because their function is often fulfilled as much passively as possible. It is therefore useful to be able to design the nonlinear equilibrium path such that most of the required forces are provided passively.

A category where the above named requirements are pushed to the limits is wearable devices. Obviously, a wearable device should be lightweight, compact, and portable. In many current exemplars much of the energy provided by the actuators is used to keep up the weight of the body or parts of it. Since the potential energy of the weight is substantially preserved, much of the introduced energy is spilled. Also, a substantial part of the motions sustained by wearable devices is repetitive, for instance in tasks related to locomotion, bending forward, reaching upwards, and handling objects with the hands. We observe an emerging trend in the design of wearables that appropriately addresses the named challenges. This approach results in (semi-)passive devices where most of the forces are provided passively, and actuation is only marginally employed to alter the passive behavior. Vanguard examples of this trend are the Laevo [263], Lockheed Martin's Foritis [264], Walsh's quasi-passive leg exoskeleton [265], the A-gear [45], and the like. Designing proper elastic behavior in these systems is essential. Advancements of the ideas proposed in this thesis can More function integration, compactness and slenderness, more specific equilibrium paths, etc., are things that can be pursued by advancing the ideas of this thesis.

Another category that can benefit from the proposed developments is interactive furniture and architecture. Moving, adapting, and responsive systems are increasingly popular at the large scale of architecture and civil engineering, as well as at a relatively small scale of household objects and furniture. The practical limitation that often impedes a successful implementation is the way it is dealt with energy and forces. It is tempting to actively control every degree of freedom. But this again results in a superabundance of actuators, sensors and control systems, that

make the systems complex, vulnerable and heavy. Again, being most of the forces conservative, namely self-weight, and the movements repetitive, such constructions can highly benefit from the implementation of static balancing and multi-stability principles. But conventional approaches with normal springs and linkages likely yield to bulky and aesthetically unacceptable solutions. We believe that the sleek torsion-spring systems that can be integrated in the hinges, the curved compliant (shell) mechanisms, the origami structures with inherent spring function, etc., can contribute to elegant and functional solutions in this field. The presented concept of the collapsible sound-barrier walls represent a first exploration in this direction, but the application field is much more vast: sun-, wind-, and sound shields, multi-position sitting furniture, deployable furniture for easy storage, responsive and adaptable buildings, reconfigurable living spaces, etc.

There are many more application areas that can benefit from features as light-weight, simple and integrated designs, scalability, and the other common advantages of compliant mechanisms. Think, e.g., of aerospace, unmanned aerial vehicles, collaborative robotics, legged robotic locomotion, miniature robotics and meta-materials.

Acknowledgements

This work is part of the research programme HTSM-2012 with project number 12814 (ShelMech: Shell-based mechanisms out of composite materials), which is (partly) financed by the Netherlands Organisation for Scientific Research (NWO).



Nederlandse Organisatie voor Wetenschappelijk Onderzoek

Parts of this dissertation are also made possible by the following research programmes:

- SPISTA: Combinations of spiral springs and torsion bars, SenterNovem kenniswerkersregeling, KWR09086
- ElastiCom: Compliant mechanisms for gravity balancers, SenterNovem kenniswerkersregeling, KWR09084
- X-arm: An exoskeleton to reduce back injuries, RVO Agentschap NL



References

References

- [1] K. D. Hjelmstad, *Fundamentals of structural mechanics*, 2nd ed. (Springer, New York, 2005).
- [2] B. J. Schwarz and M. H. Richardson, *Linear Superposition and Modal Participation*, De Clerck J. (eds) *Topics in Modal Analysis I*, Volume 7. Conference Proceedings of the Society for Experimental Mechanics Series. Springer, Cham , 161 (2014).
- [3] K.-J. Bathe and E. L. Wilson, *Solution methods for eigenvalue problems in structural mechanics*, *International Journal for Numerical Methods in Engineering* **6**, 213 (1973).
- [4] C. Vehar-Jutte, *Generalized Synthesis Methodology of Nonlinear Springs for Prescribed Load-Displacement Functions*, *PhD Thesis*, The University of Michigan, Michigan, USA (2008).
- [5] C. A. Felippa, *A tour of nonlinear analysis*, in *Nonlinear Finite Element Methods (ASEN 6107)*, Vol. Chapter 2 (Department of Aerospace Engineering Sciences, University of Colorado at Boulder, U.S.A., 2016).
- [6] W. B. Fraser and B. Budiansky, *The Buckling of a Column With Random Initial Deflections*, *Journal of Applied Mechanics* **36**, 233 (1969).
- [7] D. R. Nahar and T. Sugar, *Compliant constant-force mechanism with a variable output for micro/macro applications*, in *Proceedings of the IEEE International Conference on Robotics and Automation (ICRA), 2003*, Vol. 1 (2003) pp. 318–323.
- [8] Y.-H. Chen and C.-C. Lan, *An Adjustable Constant-Force Mechanism for Adaptive End-Effector Operations*, *Journal of Mechanical Design* **134**, 031005 (2012).
- [9] Kazuo Haiya, S. Komada, and J. Hirai, *Control of tendon-driven robotic mechanisms by non-linear springs with hysteresis characteristics*, in *Proceedings of IEEE International Conference on Mechatronics, Malaga, 2009* (IEEE, 2009) pp. 1–6.
- [10] M. Kilic, Y. Yazicioglu, and D. F. Kurtulus, *Synthesis of a torsional spring mechanism with mechanically adjustable stiffness using wrapping cams*, *Mechanism and Machine Theory* **57**, 27 (2012).

- [11] M. I. Friswell, E. S. Flores, and Y. Xia, *Vibration isolation using nonlinear springs*, in *Proceedings of ISMA-USD* (2012) pp. 2333–2342.
- [12] Q. Boehler, M. Vedrines, S. Abdelaziz, P. Poinet, and P. Renaud, *Parallel Singularities for the Design of Softening Springs Using Compliant Mechanisms*, in *Proceedings ASME IDETC/CIE 2015* (ASME, 2015) p. V05AT08A019.
- [13] A. Carrella, M. Brennan, T. Waters, and V. Lopes, *Force and displacement transmissibility of a nonlinear isolator with high-static-low-dynamic-stiffness*, *International Journal of Mechanical Sciences* **55**, 22 (2012).
- [14] A. M. Elshurafa, K. Khirallah, H. H. Tawfik, A. Emira, A. K. S. Abdel Aziz, and S. M. Sedky, *Nonlinear Dynamics of Spring Softening and Hardening in Folded-MEMS Comb Drive Resonators*, *Journal of Microelectromechanical Systems* **20**, 943 (2011).
- [15] C. Goll, W. Bacher, B. Büstgens, D. Maas, W. Menz, and W. K. Schomburg, *Microvalves with bistable buckled polymer diaphragms*, *Journal of Micromechanics and Microengineering* **6**, 77 (1996).
- [16] R. Luharuka and P. J. Hesketh, *A bistable electromagnetically actuated rotary gate microvalve*, *Journal of Micromechanics and Microengineering* **18**, 035015 (2008).
- [17] J. Sutanto, P. J. Hesketh, and Y. H. Berthelot, *Design, microfabrication and testing of a CMOS compatible bistable electromagnetic microvalve with latching/unlatching mechanism on a single wafer*, *Journal of Micromechanics and Microengineering* **16**, 266 (2006).
- [18] B. Yang, B. Wang, and W. K. Schomburg, *A thermopneumatically actuated bistable microvalve*, *Journal of Micromechanics and Microengineering* **20**, 095024 (2010).
- [19] T. Lisec, M. Kreutzer, and B. Wagner, *A bistable pneumatic microswitch for driving fluidic components*, *Sensors and Actuators A: Physical* **54**, 746 (1996).
- [20] S. Mao, H. Wang, Y. Wu, J. Tang, and G. Ding, *A latching bistable microswitch using dual-beam electrothermal actuation*, in *Proceedings of 2010 IEEE 5th International Conference on Nano/Micro Engineered and Molecular Systems* (2010) pp. 732–735.
- [21] B. D. Jensen, M. B. Parkinson, K. Kurabayashi, L. L. Howell, and M. S. Baker, *Design optimization of a fully-compliant bistable micro-mechanism*, in *Proceedings of ASME International Mechanical Engineering Congress and Exposition 2001*, Vol. 3 (2001) pp. 357–363.
- [22] J. Casals-Terre, A. Fargas-Marques, and A. Shkel, *Snap-Action Bistable Micromechanisms Actuated by Nonlinear Resonance*, *Journal of Microelectromechanical Systems* **17**, 1082 (2008).

- [23] J. Barth, B. Krevet, and M. Kohl, *A bistable shape memory microswitch with high energy density*, *Smart Materials and Structures* **19**, 094004 (2010).
- [24] P. Meneroud, G. Magnac, G. Patient, and F. Claeysen, *Bistable micro actuator for energy saving*, in *Proceedings of 10th International Conference on New Actuators, 14 – 16 June 2006, Bremen, Germany* (2006) p. P076.
- [25] B. Halg, *On a micro-electro-mechanical nonvolatile memory cell*, *IEEE Transactions on Electron Devices* **37**, 2230 (1990).
- [26] B. Charlot, W. Sun, K. Yamashita, H. Fujita, and H. Toshiyoshi, *Bistable nanowire for micromechanical memory*, *Journal of Micromechanics and Microengineering* **18**, 045005 (2008).
- [27] B. Ando, S. Baglio, G. L'Episcopo, and C. Trigona, *Investigation on Mechanically Bistable MEMS Devices for Energy Harvesting From Vibrations*, *Journal of Microelectromechanical Systems* **21**, 779 (2012).
- [28] S. P. Pellegrini, N. Tolou, M. Schenk, and J. L. Herder, *Bistable vibration energy harvesters: A review*, *Journal of Intelligent Material Systems and Structures* **24**, 1303 (2013).
- [29] M. Santer and S. Pellegrino, *Compliant multistable structural elements*, *International Journal of Solids and Structures* **45**, 6190 (2008).
- [30] J. Wu, J. Li, and S. Yan, *Design of deployable bistable structures for morphing skin and its structural optimization*, *Engineering Optimization* **46**, 745 (2014).
- [31] K. Iqbal and S. Pellegrino, *Bi-stable composite shells*, in *Proceedings of 41st Structures, Structural Dynamics, and Materials Conference and Exhibit* (2000) p. 1385.
- [32] P. A. Besselink, *Bistable spring construction for a stent and other medical apparatus*, U.S. Patent 6488702, Dec, (2002).
- [33] G. Cella, V. Sannibale, R. DeSalvo, S. Márka, and A. Takamori, *Monolithic geometric anti-spring blades*, *Nuclear Instruments and Methods in Physics Research Section A: Accelerators, Spectrometers, Detectors and Associated Equipment* **540**, 502 (2005).
- [34] M. Schenk and S. D. Guest, *On zero stiffness*, *Proceedings of the Institution of Mechanical Engineers, Part C: Journal of Mechanical Engineering Science* **228**, 1701 (2014).
- [35] J. L. Herder, *Energy-free systems: theory, conception, and design of statically balanced spring mechanisms*, *PhD Dissertation*, University of Technology Delft, Delft, the Netherlands (2001).
- [36] S. Guest, E. Kebabze, and S. Pellegrino, *A zero-stiffness elastic shell structure*, *Journal of Mechanics of Materials and Structures* **6**, 203 (2011).

- [37] K. A. Seffen, *Compliant shell mechanisms*, *Philosophical Transactions of the Royal Society of London A: Mathematical, Physical and Engineering Sciences* **370**, 2010 (2012).
- [38] E. Lamacchia, A. Pirrera, I. V. Chenchiah, and P. M. Weaver, *Non-axisymmetric bending of thin annular plates due to circumferentially distributed moments*, *International Journal of Solids and Structures* **51**, 622 (2014).
- [39] M. J. French and M. B. Widden, *The spring-and-lever balancing mechanism, George Carwardine and the Anglepoise lamp*, *Proceedings of the Institution of Mechanical Engineers, Part C: Journal of Mechanical Engineering Science* **214**, 501 (2000).
- [40] *BalanceBox*, <http://www.balancebox.eu/> (), accessed: 2017-04-25.
- [41] *Mobilescreen*, <http://www.mobilescreen.nl/pdfs/msis.pdf> (), accessed: 2017-04-24.
- [42] *The 4fold Foldable Container saves up to 25% on empty repositioning*, <http://hcinnoventions.nl/> (), accessed: 2017-04-25.
- [43] G. Brown and A. O. DiGuilio, *Support apparatus*, U.S. Patent 4208028, June, (1980).
- [44] S. K. Banala, S. K. Agrawal, A. Fattah, V. Krishnamoorthy, W.-L. Hsu, J. Scholz, and K. Rudolph, *Gravity-Balancing Leg Orthosis and Its Performance Evaluation*, *IEEE Transactions on Robotics* **22**, 1228 (2006).
- [45] P. N. Kooren, A. G. Dunning, M. M. H. P. Janssen, J. Lobo-Prat, B. F. J. M. Koopman, M. I. Paalman, I. J. M. de Groot, and J. L. Herder, *Design and pilot validation of A-gear: a novel wearable dynamic arm support*, *Journal of NeuroEngineering and Rehabilitation* **12**, 83 (2015).
- [46] M. Vermeulen and M. Wisse, *Intrinsically Safe Robot Arm: Adjustable Static Balancing and Low Power Actuation*, *International Journal of Social Robotics* **2**, 275 (2010).
- [47] C. M. Gosselin and J. Wang, *Static balancing of spatial six-degree-of-freedom parallel mechanisms with revolute actuators*, *Journal of Robotic Systems* **17**, 159 (2000).
- [48] H.-T. Pham and D.-A. Wang, *A constant-force bistable mechanism for force regulation and overload protection*, *Mechanism and Machine Theory* **46**, 899 (2011).
- [49] J.-Y. Wang and C.-C. Lan, *A Constant-Force Compliant Gripper for Handling Objects of Various Sizes*, *Journal of Mechanical Design* **136**, 071008 (2014).

- [50] L. Howell, A. Midha, and M. Murphy, *Dimensional Synthesis of Compliant Constant-Force Slider Mechanisms*, American Society of Mechanical Design, Design Engineering Division (1994).
- [51] C. Boyle, L. L. Howell, S. P. Magleby, and M. S. Evans, *Dynamic modeling of compliant constant-force compression mechanisms*, *Mechanism and machine theory* **38**, 1469 (2003).
- [52] Y.-H. Chen and C.-C. Lan, *Design of a constant-force snap-fit mechanism for minimal mating uncertainty*, *Mechanism and Machine Theory* **55**, 34 (2012).
- [53] A. Saxena and G. K. Ananthasuresh, *Topology Synthesis of Compliant Mechanisms for Nonlinear Force-Deflection and Curved Path Specifications*, *Journal of Mechanical Design* **123**, 33 (1999).
- [54] C. V. Jutte and S. Kota, *Design of Single, Multiple, and Scaled Nonlinear Springs for Prescribed Nonlinear Responses*, *Journal of Mechanical Design* **132**, 011003 (2010).
- [55] C. B. Pedersen, N. A. Fleck, and G. K. Ananthasuresh, *Design of a Compliant Mechanism to Modify an Actuator Characteristic to Deliver a Constant Output Force*, *Journal of Mechanical Design* **128**, 1101 (2005).
- [56] G. Krishnan, R. Rank, J. Rokosz, P. Carvey, and S. Kota, *A Strength Based Approach for the Synthesis of a Compliant Nonlinear Spring for an Orthotic Knee Brace*, in *Proceedings of ASME DETC 2013* (2013) p. V06AT07A033.
- [57] A. Gopalswamy, P. Gupta, and M. Vidyasagar, *A new parallelogram linkage configuration for gravity compensation using torsional springs*, in *Proceedings of IEEE International Conference on Robotics and Automation* (1992) pp. 664–669 vol.1.
- [58] B. Trease and E. Dede, *Statically-Balanced Compliant Four-Bar Mechanism for Gravity Compensation*, *Ann Arbor* **1001**, 48109 (2004).
- [59] E. J. Eshelman, *Multi-rate torsion bar independent suspension spring*, U.S. Patent 20030201591, Okt 30, (2003).
- [60] P. Castrilli, *Nonlinear torsion spring*, U.S. Patent 4884790, Dec 5, (1989).
- [61] F. J. C. Osch, *Design of an adjustable gravity equilibrator using torsion bars*, *MSc Thesis*, Delft University of Technology, Delft, The Netherlands (2011).
- [62] L. L. Howell, *Compliant Mechanisms* (John Wiley and Sons Inc., New York,US, 2001).
- [63] D. Petković, N. D. Pavlović, S. Shamshirband, and N. Badrul Anuar, *Development of a new type of passively adaptive compliant gripper*, *Industrial Robot: An International Journal* **40**, 610 (2013).

- [64] T. M. Allred, *Compliant Mechanism Suspensions*, MSc thesis, Brigham Young University, Provo, Utah (2006).
- [65] S. Kota, K.-J. Lu, Z. Kreiner, B. Trease, J. Arenas, and J. Geiger, *Design and Application of Compliant Mechanisms for Surgical Tools*, *Journal of Biomechanical Engineering* **127**, 981 (2005).
- [66] W. Crooks, G. Vukasin, M. O'Sullivan, W. Messner, and C. Rogers, *Fin Ray® Effect Inspired Soft Robotic Gripper: From the RoboSoft Grand Challenge toward Optimization*, *Frontiers in Robotics and AI* **3** (2016), 10.3389/frobt.2016.00070.
- [67] L. Kölle and O. Schwarz, *Bionic forceps for the handling of sensitive tissue*, *Current Directions in Biomedical Engineering* **2** (2016), 10.1515/cdbme-2016-0023.
- [68] A. Stapel and J. L. Herder, *Feasibility Study of a Fully Compliant Statically Balanced Laparoscopic Grasper*, in *Proceedings of ASME DETC 2004*, Vol. 2 (2004) pp. 635–643.
- [69] J. L. Herder and F. P. A. van den Berg, *Statically balanced compliant mechanisms (SBCM's), an example and prospects*, in *Proceedings ASME DETC 26th Biennial Mechanisms and Robotics Conference* (2000).
- [70] A. Rai, A. Saxena, N. D. Mankame, and C. S. Upadhyay, *On Optimal Design of Compliant Mechanisms for Specified Nonlinear Path Using Curved Frame Elements and Genetic Algorithm*, in *Proceedings of ASME DETC 2006* (2006) pp. 91–100.
- [71] H. Zhou and K.-L. Ting, *Shape and Size Synthesis of Compliant Mechanisms Using Wide Curve Theory*, *Journal of Mechanical Design* **128**, 551 (2005).
- [72] M. Farshad, *Design and Analysis of Shell Structures*, (Springer Netherlands, Dordrecht, 1992).
- [73] A. D. Norman, *Multistable and morphing corrugated shell structures*, Phd thesis, University of Cambridge, Cambridge, UK (2009).
- [74] G. Radaelli, R. Buskermolen, R. Barents, and J. L. Herder, *Static balancing of an inverted pendulum with prestressed torsion bars*, *Mechanism and Machine Theory* **108**, 14 (2017).
- [75] G. Radaelli, J. L. Herder, R. Buskermolen, and R. Barents, *Static balancing of an inverted pendulum with pre-stressed torsion bars*, in *Proceedings 13th World Congress in Mechanism and Machine Science* (2011).
- [76] V. Hayward, P. Gregorio, O. Astley, S. Greenish, M. Doyon, L. Lessard, J. McDougall, I. Sinclair, S. Boelen, X. Chen, and others, *Freedom-7: A high fidelity seven axis haptic device with application to surgical training*, in *Experimental Robotics V* (Springer, 1998) pp. 443–456.

- [77] R. Fan, C. Zhao, and H. Zhao, *Improvement of dynamic transparency of haptic devices by using spring balance*, in *Proceedings of IEEE International Conference on Robotics and Biomimetics (ROBIO) 2012* (2012) pp. 1075–1080.
- [78] T. Rahman, R. Ramanathan, R. Seliktar, and W. Harwin, *A Simple Technique to Passively Gravity-Balance Articulated Mechanisms*, *Journal of Mechanical Design* **117**, 655 (1995).
- [79] J. Wang and C. M. Gosselin, *Static balancing of spatial three-degree-of-freedom parallel mechanisms*, *Mechanism and Machine Theory* **34**, 437 (1999).
- [80] I. Simionescu and L. Ciupitu, *The static balancing of the industrial robot arms: Part I: Discrete balancing*, *Mechanism and Machine Theory* **35**, 1287 (2000).
- [81] I. Simionescu and L. Ciupitu, *The static balancing of the industrial robot arms: Part II: Continuous balancing*, *Mechanism and Machine Theory* **35**, 1299 (2000).
- [82] L. Kang, S.-M. Oh, W. Kim, and B.-J. Yi, *Design of a new gravity balanced parallel mechanism with Schönflies motion*, *Proceedings of the Institution of Mechanical Engineers, Part C: Journal of Mechanical Engineering Science* **230**, 3111 (2015).
- [83] A. Agrawal and S. K. Agrawal, *Design of gravity balancing leg orthosis using non-zero free length springs*, *Mechanism and Machine Theory* **40**, 693 (2005).
- [84] A. G. Dunning and J. L. Herder, *A review of assistive devices for arm balancing*, in *Proceedings of IEEE International Conference on Rehabilitation Robotics (ICORR), 2013* (2013) pp. 1–6.
- [85] B. Lenzo, M. Fontana, S. Marcheschi, F. Salsedo, A. Frisoli, and M. Bergamasco, *Trackhold: A Novel Passive Arm-Support Device*, *Journal of Mechanisms and Robotics* **8**, 021007 (2015).
- [86] H. Hilpert, *Weight balancing of precision mechanical instruments*, *Journal of Mechanisms* **3**, 289 (1968).
- [87] J. M. Herve, *Device for counter-balancing the forces due to gravity in a robot arm*, U.S. Patent 4620829, Nov, (1986).
- [88] D. A. Streit and B. J. Gilmore, *'Perfect' Spring Equilibrators for Rotatable Bodies*, *Journal of Mechanisms, Transmissions, and Automation in Design* **111**, 451 (1989).
- [89] N. Ulrich and V. Kumar, *Passive mechanical gravity compensation for robot manipulators*, in *Proceedings of IEEE International Conference on Robotics and Automation* (1991) pp. 1536–1541 vol.2.

- [90] F. L. S. te Riele, E. E. G. Hekman, and J. L. Herder, *Planar and Spatial Gravity Balancing With Normal Springs*, in *Proceedings of ASME DETC 2004* (ASME, 2004) pp. 415–424.
- [91] G. Kusuma and J. Herder, *Foldable container*, E.P. Patent 2036835, Mar 18, (Google Patents, 2009).
- [92] K. Koser, *A cam mechanism for gravity-balancing*, *Mechanics Research Communications* **36**, 523 (2009).
- [93] W.-B. Shieh and B.-S. Chou, *A Novel Spring Balancing Device on the Basis of a Scotch Yoke Mechanism*, in *Proceedings of the 14th IFToMM World Congress* (nov, 2015) pp. 206–212.
- [94] G. Radaelli, J. A. Gallego, and J. L. Herder, *An energy approach to static balancing of systems with torsion stiffness*, in *Proceedings of the ASME IDETC/CIE 2010* (2010).
- [95] J. Fader, M. Clements, C. Keeney, S. Yollick, and J. Hawkins, *Torsion bar with multiple arm adjusters for a vehicle suspension system*, U.S. Patent 6425594, Jul 30, (2002).
- [96] M. R. Claus, *Gravity balancing using configurations of torsion bars; with application to the HCI foldable container*, MSc Thesis, Delft University of Technology, Delft, The Netherlands (2008).
- [97] J. C. Cool, *Werktuigkundige systemen*, 3rd ed. (VSSD, Delft, The Netherlands, 2005).
- [98] B. G. Bijlsma, G. Radaelli, and J. L. Herder, *Design of a Compact Gravity Equilibrator With an Unlimited Range of Motion*, *ASME Journal of Mechanism and Robotics* (2017), 10.1115/1.4037616.
- [99] B. G. Bijlsma, G. Radaelli, and J. L. Herder, *Design of a Compact Gravity Equilibrator With an Unlimited Range of Motion*, in *Proceedings of ASME IDETC/CIE 2016* (2016) p. V05AT07A065.
- [100] W. D. van Dorsser, R. Barents, B. M. Wisse, M. Schenk, and J. L. Herder, *Energy-free adjustment of gravity equilibrators by adjusting the spring stiffness*, *Journal of Mechanical Engineering Science* **222**, 1839 (2008).
- [101] K. Kobayashi, *Comparison Between Spring Balancer and Gravity Balancer in Inertia Force and Performance*, *Journal of Mechanical Design* **123**, 549 (2001).
- [102] G. Carwardine, *Improvements in elastic equipoising mechanisms*, G.B. Patent 404615, Jan, (1934).
- [103] F. L. Litvin, A. Fuentes-Aznar, I. Gonzalez-Perez, and K. Hayasaka, *Noncircular Gears, design and generation* (Cambridge University Press, New York, 2009).

- [104] C. Fetvaci and E. Imrak, *Mathematical Model of a Spur Gear with Asymmetric Involute Teeth and Its Cutting Simulation*, *Mechanics Based Design of Structures and Machines* **36**, 34 (2008).
- [105] F. L. Litvin and A. Fuentes, *Gear geometry and applied theory* (Cambridge University Press, New York, 2004).
- [106] A. Boresi and R. Schmidt, *Advanced mechanics of materials, sixth edition* (John Wiley & sons, inc, United States of America, 2003).
- [107] *Torsion bars*, <http://www.mitcalc.com>, accessed: 2012-01-21.
- [108] *Method to generate 3 dimensional complex shapes*, <http://www.materialise.com>, accessed: 2017-04-24.
- [109] G. Radaelli and J. L. Herder, *Shape optimization and sensitivity of compliant beams for prescribed load-displacement response*, *Mechanical Sciences* **7**, 219 (2016).
- [110] K. M. Powell and M. I. Frecker, *Method for Optimization of a Nonlinear Static Balance Mechanism With Application to Ophthalmic Surgical Forceps*, in *Proceedings ASME IDETC/CIE 2005* (2005).
- [111] G. Chen and S. Zhang, *Fully-compliant statically-balanced mechanisms without prestressing assembly: concepts and case studies*, *Mechanical Sciences* **2**, 169 (2011).
- [112] K. Hoetmer, G. Woo, C. Kim, and J. Herder, *Negative Stiffness Building Blocks for Statically Balanced Compliant Mechanisms: Design and Testing*, *Journal of Mechanisms and Robotics* **2**, 041007 (2010).
- [113] M. A. Pucheta and A. Cardona, *Design of bistable compliant mechanisms using precision–position and rigid-body replacement methods*, *Mechanism and Machine Theory* **45**, 304 (2010).
- [114] Y. Oh, *Synthesis of Multistable Equilibrium Compliant Mechanisms*, PhD Thesis, The University of Michigan, Michigan, USA (2008).
- [115] N. Tolou, *Statically Balanced Compliant Mechanisms for MEMS and Precision Engineering*, PhD Thesis, Delft University of Technology, Delft, The Netherlands (2012).
- [116] O. Sigmund, *On the Design of Compliant Mechanisms Using Topology Optimization**, *Mechanics of Structures and Machines* **25**, 493 (1997).
- [117] Y. Du and L. Chen, *Topology optimization for large-displacement compliant mechanisms using element free galerkin method*, *International Journal of CAD/CAM* **8** (2009).
- [118] A. Eriksson, *Constraint paths in non-linear structural optimization*, *Computers & Structures* **140**, 39 (2014).

- [119] R. T. Haftka, *Simultaneous analysis and design*, *AIAA Journal* **23**, 1099 (1985).
- [120] U. T. Ringertz, *Optimization of Structures with Nonlinear Response*, *Engineering Optimization* **14**, 179 (1989).
- [121] T. E. Bruns and D. A. Tortorelli, *Topology optimization of non-linear elastic structures and compliant mechanisms*, *Computer Methods in Applied Mechanics and Engineering* **190**, 3443 (2001).
- [122] J. Joo, S. Kota, and N. Kikuchi, *Large deformation behavior of compliant mechanisms*, in *Proceedings of the ASME Design Engineering Technical Conference*, Vol. 2 (2001) pp. 709–714.
- [123] L. C. Leishman and M. B. Colton, *A Pseudo-Rigid-Body Model Approach for the Design of Compliant Mechanism Springs for Prescribed Force-Deflections*, in *Proceedings of ASME IDETC/CIE 2011* (2011) pp. 93–102.
- [124] J. A. Cottrell, T. J. R. Hughes, and Y. Bazilevs, *Isogeometric Analysis: Toward Integration of CAD and FEA* (John Wiley & Sons, Ltd, Chichester, 2009).
- [125] T. J. R. Hughes, J. A. Cottrell, and Y. Bazilevs, *Isogeometric analysis: CAD, finite elements, NURBS, exact geometry and mesh refinement*, *Computer Methods in Applied Mechanics and Engineering* **194**, 4135 (2005).
- [126] S. Cho and S.-H. Ha, *Isogeometric shape design optimization: exact geometry and enhanced sensitivity*, *Structural and Multidisciplinary Optimization* **38**, 53 (2009).
- [127] A. P. Nagy, M. M. Abdalla, and Z. Gürdal, *Isogeometric sizing and shape optimisation of beam structures*, *Computer Methods in Applied Mechanics and Engineering* **199**, 1216 (2010).
- [128] B. Koo, S.-H. Ha, H.-S. Kim, and S. Cho, *Isogeometric Shape Design Optimization of Geometrically Nonlinear Structures*, *Mechanics Based Design of Structures and Machines* **41**, 337 (2013).
- [129] A. P. Nagy, *Isogeometric Design optimisation*, *PhD Dissertation*, Delft University of Technology, Delft, the netherlands (2011).
- [130] W. A. Wall, M. A. Frenzel, and C. Cyron, *Isogeometric structural shape optimization*, *Computer Methods in Applied Mechanics and Engineering* **197**, 2976 (2008).
- [131] J. M. Kiendl, *Isogeometric Analysis and Shape Optimal Design of Shell Structures*, *PhD Thesis*, Munich University of Technology, Munich, Germany (2011).
- [132] Y.-L. Hsu, *A review of structural shape optimization*, *Computers in Industry* **25**, 3 (1994).

- [133] Y. Ding, *Shape optimization of structures a literal survey*, *Computers & Structures* **24**, 985 (1986).
- [134] G. Radaelli and J. L. Herder, *Isogeometric Shape Optimization for Compliant Mechanisms With Prescribed Load Paths*, in *Proceedings of IDETC/CIE 2014* (Buffalo, New York, USA, 2014).
- [135] C.-C. Lan, J.-H. Wang, and Y.-H. Chen, *A compliant constant-force mechanism for adaptive robot end-effector operations*, in *Proceedings of IEEE International Conference on Robotics and Automation (ICRA), 2010* (2010) pp. 2131–2136.
- [136] J. Simo, *A finite strain beam formulation. The three-dimensional dynamic problem. Part I*, *Computer Methods in Applied Mechanics and Engineering* **49**, 55 (1985).
- [137] L. Piegl and W. Tiller, *The NURBS Book (2Nd Ed.)* (Springer-Verlag New York, Inc., New York, NY, USA, 1997).
- [138] Y. S. Ryu, M. Haririan, C. C. Wu, and J. S. Arora, *Structural design sensitivity analysis of nonlinear response*, *Computers & Structures* **21**, 245 (1985).
- [139] X. Qian, *Full analytical sensitivities in NURBS based isogeometric shape optimization*, *Computer Methods in Applied Mechanics and Engineering* **199**, 2059 (2010).
- [140] Matlab, *MATLAB and Optimization Toolbox Release R2014a* (The MathWorks, Inc., Natick, Massachusetts, United States, 2014).
- [141] G. Radaelli and J. L. Herder, *A monolithic compliant large-range gravity balancer*, *Mechanism and Machine Theory* **102**, 55 (2016).
- [142] G. Radaelli and J. L. Herder, *A Monolithic Compliant Large-Range Gravity Balancer*, *Proceedings of the 14th IFToMM World Congress*, 132 (2015).
- [143] L. L. Howell and A. Midha, *A Method for the Design of Compliant Mechanisms With Small-Length Flexural Pivots*, *Journal of Mechanical Design* **116**, 280 (1994).
- [144] D. Bandopadhyaya, B. Bhattacharya, and A. Dutta, *Pseudo-rigid Body Modeling of IPMC for a Partially Compliant Four-bar Mechanism for Work Volume Generation*, *Journal of Intelligent Material Systems and Structures* **20**, 51 (2009).
- [145] S. Deepak R, *Static balancing of rigid-body linkages and compliant mechanisms*, *PhD Thesis*, Indian Institute of Science, Bangalore, India (2012).
- [146] A. G. Dunning, N. Tolou, and J. L. Herder, *A compact low-stiffness six degrees of freedom compliant precision stage*, *Precision Engineering* **37**, 380 (2013).

- [147] N. Tolou, V. A. Henneken, and J. L. Herder, *Statically Balanced Compliant Micro Mechanisms (SB-MEMS): Concepts and Simulation*, in *Proceedings of the ASME IDETC/CIE 2010* (2010).
- [148] E. G. Merriam, S. Magleby, M. Colton, and L. L. Howell, *The Design of a Fully Compliant Statically Balanced Mechanism*, in *Proceedings of ASME IDETC/CIE 2013* (2013).
- [149] Ü. Sönmez and C. C. Tutum, *A Compliant Bistable Mechanism Design Incorporating Elastica Buckling Beam Theory and Pseudo-Rigid-Body Model*, *J. Mech. Des.* **130**, 042304 (2008).
- [150] G. Berselli, R. Vertechy, G. Vassura, and V. P. Castelli, *Design of a Single-Acting Constant-Force Actuator Based on Dielectric Elastomers*, *Journal of Mechanisms and Robotics* **1**, 031007 (2009).
- [151] A. A. T. M. Delissen, G. Radaelli, and J. L. Herder, *Design and optimization of a general planar zero free length spring*, *Mechanism and Machine Theory* **117C**, 56 (2017).
- [152] L. J. B. LaCoste, *A New Type Long Period Vertical Seismograph*, *Journal of Applied Physics* **5**, 178 (1934).
- [153] L. J. B. LaCoste and A. Romberg, *Force measuring device*, U.S. Patent 3717036, Apr 6, (1970).
- [154] D. A. Streit and E. Shin, *Equilibrators for Planar Linkages*, *Journal of Mechanical Design* **115**, 604 (1993).
- [155] J. L. Herder, *Design of spring force compensation systems*, *Mechanism and Machine Theory* **33**, 151 (1998).
- [156] M. Schenk, S. Guest, and J. Herder, *Zero stiffness tensegrity structures*, *International Journal of Solids and Structures* **44**, 6569 (2007).
- [157] B. Mastenbroek, E. de Haan, M. van den Berg, and J. L. Herder, *Development of a Mobile Arm Support (Armon): Design Evolution and Preliminary User Experience*, in *Proceedings of IEEE 10th International Conference on Rehabilitation Robotics 2007* (IEEE, 2007) pp. 1114–1120.
- [158] A. G. Dunning, *Slender spring systems*, *PhD Dissertation*, Delft University of Technology, Delft, the netherlands (2016).
- [159] MathWorks, *Least-Squares (Model Fitting) Algorithms* (2016).
- [160] K.-T. Fang, R. Li, and A. Susjianto, *Design and Modeling for Computer Experiments* (Taylor & Francis Group, LLC, Boca Raton, 2006).
- [161] S. R. Deepak and G. K. Ananthasuresh, *Perfect Static Balance of Linkages by Addition of Springs But Not Auxiliary Bodies*, *Journal of Mechanisms and Robotics* **4**, 021014 (2012).

- [162] J. L. Herder, R. Barents, B. M. Wisse, and W. D. van Dorsser, *Efficiently variable zero stiffness mechanisms*, in *4th International Workshop on Human-Friendly Robotics* (2011) pp. 2–3.
- [163] A. A. T. M. Delissen, G. Radaelli, J. L. Herder, and J. B. Hopkins, *Design and characterization of a linear elastic isotropic meta-material with zero poisson's ratio over large strains using a spring lattice*, To be submitted to *Advanced Functional Materials* .
- [164] R. S. Lakes, *Foam structures with a negative Poisson's ratio*, *Science* **235**, 1038 (1987).
- [165] G. W. Milton and A. V. Cherkaev, *Which Elasticity Tensors are Realizable?* *Journal of Engineering Materials and Technology* **117**, 483 (1995).
- [166] J. N. Grima and K. E. Evans, *Auxetic Behavior from Rotating Squares*, *Journal of Materials Science Letters* **19**, 1563 (2000).
- [167] G. W. Milton, *Complete characterization of the macroscopic deformations of periodic unimode metamaterials of rigid bars and pivots*, *Journal of the Mechanics and Physics of Solids* **61**, 1543 (2013).
- [168] T. Bückmann, R. Schittny, M. Thiel, M. Kadic, G. W. Milton, and M. Wegener, *On three-dimensional dilational elastic metamaterials*, *New Journal of Physics* **16**, 033032 (2014).
- [169] M. Kadic, T. Bückmann, N. Stenger, M. Thiel, and M. Wegener, *On the feasibility of pentamode mechanical metamaterials*, *Applied Physics Letters* **100**, 191901 (2012).
- [170] M. Kadic, T. Bückmann, N. Stenger, M. Thiel, and M. Wegener, *On the practicability of pentamode mechanical metamaterials*, *Applied Physics Letters* **100**, 191901 (2012).
- [171] K. Bertoldi, P. M. Reis, S. Willshaw, and T. Mullin, *Negative Poisson's Ratio Behavior Induced by an Elastic Instability*, *Advanced Materials* **22**, 361 (2010).
- [172] J. T. B. Overvelde, S. Shan, and K. Bertoldi, *Compaction Through Buckling in 2d Periodic, Soft and Porous Structures: Effect of Pore Shape*, *Advanced Materials* **24**, 2337 (2012).
- [173] B. Florijn, C. Coulais, and M. van Hecke, *Programmable Mechanical Meta-materials*, *Physical Review Letters* **113**, 175503 (2014).
- [174] S. Shan, S. H. Kang, P. Wang, C. Qu, S. Shian, E. R. Chen, and K. Bertoldi, *Harnessing Multiple Folding Mechanisms in Soft Periodic Structures for Tunable Control of Elastic Waves*, *Advanced Functional Materials* **24**, 4935 (2014).

- [175] S. Shan, S. H. Kang, Z. Zhao, L. Fang, and K. Bertoldi, *Design of planar isotropic negative Poisson's ratio structures*, [Extreme Mechanics Letters](#) **4**, 96 (2015).
- [176] J. N. Grima, L. Mizzi, K. M. Azzopardi, and R. Gatt, *Auxetic Perforated Mechanical Metamaterials with Randomly Oriented Cuts*, [Advanced Materials](#) **28**, 385 (2016).
- [177] U. Larsen, O. Sigmund, and S. Bouwstra, *Design and fabrication of compliant micromechanisms and structures with negative Poisson's ratio*, in [Proceedings of Ninth International Workshop on Micro Electromechanical Systems](#), Vol. 6 (IEEE, 1996) pp. 365–371.
- [178] C. Lira, F. Scarpa, M. Olszewska, and M. Celuch, *The SILICOMB cellular structure: Mechanical and dielectric properties*, [physica status solidi \(b\)](#) **246**, 2055 (2009).
- [179] J. N. Grima, R. Caruana-Gauci, D. Attard, and R. Gatt, *Three-dimensional cellular structures with negative Poisson's ratio and negative compressibility properties*, [Proceedings of the Royal Society A](#) **468**, 3121 (2012).
- [180] T. Bückmann, N. Stenger, M. Kadic, J. Kaschke, A. Frölich, T. Kennerknecht, C. Eberl, M. Thiel, and M. Wegener, *Tailored 3d Mechanical Metamaterials Made by Dip-in Direct-Laser-Writing Optical Lithography*, [Advanced Materials](#) **24**, 2710 (2012).
- [181] J. N. Grima, L. Oliveri, D. Attard, B. Ellul, R. Gatt, G. Cicala, and G. Recca, *Hexagonal Honeycombs with Zero Poisson's Ratios and Enhanced Stiffness*, [Advanced Engineering Materials](#) **12**, 855 (2010).
- [182] K. R. Olympio and F. Gandhi, *Zero Poisson's Ratio Cellular Honeycombs for Flex Skins Undergoing One-Dimensional Morphing*, [Journal of Intelligent Material Systems and Structures](#) **21**, 1737 (2010).
- [183] P. Soman, D. Y. Fozdar, J. W. Lee, A. Phadke, S. Varghese, and S. Chen, *A three-dimensional polymer scaffolding material exhibiting a zero Poisson's ratio*, [Soft Matter](#) **8**, 4946 (2012).
- [184] S. P. Silva, M. a. Sabino, E. M. Fernandes, V. M. Correlo, L. F. Boesel, and R. L. Reis, *Cork: properties, capabilities and applications*, [International Materials Reviews](#) **50**, 345 (2005).
- [185] A.-J. Wang and D. L. McDowell, *In-Plane Stiffness and Yield Strength of Periodic Metal Honeycombs*, [Journal of Engineering Materials and Technology](#) **126**, 137 (2004).
- [186] H. X. Zhu, T. X. Fan, and D. Zhang, *Composite materials with enhanced dimensionless Young's modulus and desired Poisson's ratio*, [Scientific Reports](#) **5**, 14103 (2015).

- [187] W. Lee, D.-Y. Kang, J. Song, J. H. Moon, and D. Kim, *Controlled Unusual Stiffness of Mechanical Metamaterials*, *Scientific Reports* **6**, 20312 (2016).
- [188] J.-H. Lee, J. P. Singer, and E. L. Thomas, *Micro-/Nanostructured Mechanical Metamaterials*, *Advanced Materials* **24**, 4782 (2012).
- [189] A. A. Zadpoor, *Mechanical meta-materials*, *Materials Horizons* **3**, 371 (2016).
- [190] R. F. Almgren, *An isotropic three-dimensional structure with Poisson's ratio = -1*, *Journal of Elasticity* **15**, 427 (1985).
- [191] L. Cabras and M. Brun, *Auxetic two-dimensional lattices with Poisson's ratio arbitrarily close to -1*, *Proceedings of the Royal Society A* **470**, 20140538 (2014).
- [192] R. M. Christensen, *Sufficient Symmetry Conditions for Isotropy of the Elastic Moduli Tensor*, *Journal of Applied Mechanics* **54**, 772 (1987).
- [193] A. A. T. M. Delissen, *Meta-material based on an Ideal Spring Lattice: A Linear Elastic Isotropic Material with Zero Poisson's Ratio over Large Strains*, *MSc thesis*, Delft University of Technology, Delft, The Netherlands (2016).
- [194] E. A. Jagla and D. A. Dalvit, *Null length springs: some curious properties*, Vol. 59 (1991) p. 434.
- [195] R. Hill, *Elastic Properties of Reinforced Solids: Some Theoretical Principles*, Vol. 11 (1963) pp. 357–372.
- [196] G. Radaelli, J. A. Gallego, and J. L. Herder, *An Energy Approach to Static Balancing of Systems With Torsion Stiffness*, *Journal of Mechanical Design* **133**, 091006 (2011).
- [197] J. A. Gallego and J. L. Herder, *Criteria for the Static Balancing of Compliant Mechanisms*, in *Proceedings of ASME IDETC/CIE 2010*, Vol. 2010 (2010) pp. 465–473.
- [198] E. J. Rosenberg, G. Radaelli, and J. L. Herder, *An Energy Approach to a 2dof Compliant Parallel Mechanism With Self-Guiding Statically-Balanced Straight-Line Behavior*, in *Proceedings of ASME IDETC/CIE 2010* (ASME, 2010) pp. 455–464.
- [199] L. L. Howell, A. Midha, and T. W. Norton, *Evaluation of equivalent spring stiffness for use in pseudo-rigid-body model of large-deflection compliant mechanisms*, *ASME Journal of Mechanical Design* **118**, 126 (1996).
- [200] G. Radaelli and J. L. Herder, *A potential energy field (PEF) approach to the design of a compliant self-guiding statically-balanced straight-line mechanism*, *Mechanism and Machine Theory* **114**, 141 (2017).

- [201] A. Saxena and S. N. Kramer, *A Simple and Accurate Method for Determining Large Deflections in Compliant Mechanisms Subjected to End Forces and Moments*, *Journal of Mechanical Design* **120**, 392 (1998).
- [202] J. B. Hopkins and M. L. Culpepper, *Synthesis of multi-degree of freedom, parallel flexure system concepts via Freedom and Constraint Topology (FACT) – Part I: Principles*, *Precision Engineering* **34**, 259 (2010).
- [203] C. J. Kim, Y.-M. Moon, and S. Kota, *A Building Block Approach to the Conceptual Synthesis of Compliant Mechanisms Utilizing Compliance and Stiffness Ellipsoids*, *Journal of Mechanical Design* **130**, 022308 (2008).
- [204] C. J. Kim, S. Kota, and Y.-M. Moon, *An Instant Center Approach Toward the Conceptual Design of Compliant Mechanisms*, *Journal of Mechanical Design* **128**, 542 (2006).
- [205] M. D. Murphy, A. Midha, and L. L. Howell, *The topological synthesis of compliant mechanisms*, *Mechanism and Machine Theory* **31**, 185 (1996).
- [206] G. Ananthasuresh, S. Kota, and Y. Gianchandani, *A methodical approach to the design of compliant micromechanisms*, in *Solid-state sensor and actuator workshop*, Vol. 1994 (IEEE, 1994) pp. 189–192.
- [207] N. Hogan, *The mechanics of multi-joint posture and movement control*, *Biological Cybernetics* **52**, 315 (1985).
- [208] C. E. English, *Stiffness behaviour in two degree of freedom mechanisms.*, PhD Dissertation, Ottawa Carleton Institute for Mechanical and Aerospace Engineering, Ottawa, Canada (1999).
- [209] G. Radaelli and J. Herder, *Gravity balanced compliant shell mechanisms*, *International Journal of Solids and Structures* **118–119**, 78 (2017).
- [210] M. Fox and M. Kemp, *Interactive architecture*, 1st ed. (Princeton Architectural Press, New York, 2009).
- [211] *Robotic Building(s)*, *Next Generation Building* **1** (2014), 10.7564/14-NGBJ8.
- [212] C. A. Mattson, *Synthesis through Rigid-Body Replacement*, in *Handbook of Compliant Mechanisms* (John Wiley & Sons Ltd, 2013) pp. 109–121.
- [213] A. G. Erdman, G. N. Sandor, and S. Kota, *Mechanism design: analysis and synthesis. Vol. 1*, 4th ed. (Prentice Hall, Upper Saddle River, NJ, 2001).
- [214] J. J. Uicker, G. R. Pennock, and J. E. Shigley, *Theory of machines and mechanisms*, 4th ed. (Oxford University Press, New York, 2011).
- [215] S. Babaee, J. Shim, J. C. Weaver, E. R. Chen, N. Patel, and K. Bertoldi, *Metamaterials: 3d Soft Metamaterials with Negative Poisson's Ratio (Adv. Mater. 36/2013)*, *Advanced Materials* **25**, 5116 (2013).

- [216] A. Rafsanjani, A. Akbarzadeh, and D. Pasini, *Metamaterials: Snapping Mechanical Metamaterials under Tension* (*Adv. Mater.* 39/2015), *Advanced Materials* **27**, 5930 (2015).
- [217] N. Hu and R. Burgueño, *Buckling-induced smart applications: Recent advances and trends*, *Smart Materials and Structures* **24** (2015), 10.1088/0964-1726/24/6/063001.
- [218] J. Lienhard, S. Schleicher, S. Poppinga, T. Masselter, M. Milwich, T. Speck, and J. Knippers, *Flectofin: a hingeless flapping mechanism inspired by nature*, *Bioinspiration & Biomimetics* **6**, 045001 (2011).
- [219] A. Pirrera, X. Lachenal, S. Daynes, P. M. Weaver, and I. V. Chenchiah, *Multi-stable cylindrical lattices*, *Journal of the Mechanics and Physics of Solids* **61**, 2087 (2013).
- [220] B. H. Coburn, A. Pirrera, P. M. Weaver, and S. Vidoli, *Tristability of an orthotropic doubly curved shell*, *Composite Structures* **96**, 446 (2013).
- [221] N. G. Boddeti, X. Liu, R. Long, J. Xiao, J. S. Bunch, and M. L. Dunn, *Graphene Blisters with Switchable Shapes Controlled by Pressure and Adhesion*, *Nano Letters* **13**, 6216 (2013).
- [222] S. E. Wilding, L. L. Howell, and S. P. Magleby, *Spherical lamina emergent mechanisms*, *Mechanism and Machine Theory* **49**, 187 (2012).
- [223] J. O. Jacobsen, B. G. Winder, L. L. Howell, and S. P. Magleby, *Lamina Emergent Mechanisms and Their Basic Elements*, *Journal of Mechanisms and Robotics* **2**, 011003 (2009).
- [224] J. O. Jacobsen, G. Chen, L. L. Howell, and S. P. Magleby, *Lamina Emergent Torsional (LET) Joint*, *Mechanism and Machine Theory* **44**, 2098 (2009).
- [225] J. J. Parise, L. L. Howell, and S. P. Magleby, *Ortho-planar linear-motion springs*, *Mechanism and Machine Theory* **36**, 1281 (2001).
- [226] E. A. Peraza-Hernandez, D. J. Hartl, R. J. Malak Jr, and D. C. Lagoudas, *Origami-inspired active structures: a synthesis and review*, *Smart Materials and Structures* **23**, 094001 (2014).
- [227] L. Bowen, C. GAMES, S. Magleby, L. Howell, and R. Lang, *A classification of action origami as systems of spherical mechanisms*, *Journal of Mechanical Design, Transactions of the ASME* **135** (2013).
- [228] H. C. Greenberg, M. L. Gong, S. P. Magleby, and L. L. Howell, *Identifying links between origami and compliant mechanisms*, *Mechanical Sciences* **2**, 217 (2011).
- [229] M. Schenk, *Folded Shell Structures*, *Ph.D. thesis*, University of Cambridge, Cambridge, UK (2011).

- [230] K. A. Seffen and S. D. Guest, *Prestressed Morphing Bistable and Neutrally Stable Shells*, *Journal of Applied Mechanics* **78**, 011002 (2010).
- [231] A. M. Watt and S. Pellegrino, *Tape-spring rolling hinges*, in *Proceedings 36th Aerospace Mechanisms Symposium* (Glenn Research Center, 2002).
- [232] E. Kebabzade, S. D. Guest, and S. Pellegrino, *Bistable prestressed shell structures*, *International Journal of Solids and Structures* **41**, 2801 (2004).
- [233] S. K. Christine Vehar, *Closed-loop tape springs as fully compliant mechanisms: preliminary investigations*, in *Proceedings of ASME IDETC/CIE 2004* (2004).
- [234] B. Hassani, S. M. Tavakkoli, and N. Z. Moghadam, *Application of isogeometric analysis in structural shape optimization*, *Scientia Iranica* **18**, 846 (2011).
- [235] J. Rommers, G. Radaelli, and J. L. Herder, *Pseudo-Rigid-Body Modeling of a Single Vertex Compliant-Facet Origami Mechanism*, *Journal of Mechanisms and Robotics* **9**, 031009 (2017).
- [236] J. Rommers, G. Radaelli, and J. Herder, *A Pseudo Rigid Body Model of a Single Vertex Compliant-Facet Origami Mechanism (SV-COFOM)*, in *ASME IDETC/CIE 2016* (2016) p. V05BT07A006.
- [237] S. A. Zirbel, M. E. Wilson, S. P. Magleby, and L. L. Howell, *An origami-inspired self-deployable array*, in *Proceedings of ASME 2013 Conference on Smart Materials, Adaptive Structures and Intelligent Systems* (ASME, 2013) p. V001T01A026.
- [238] K. Kuribayashi, K. Tsuchiya, Z. You, D. Tomus, M. Umemoto, T. Ito, and M. Sasaki, *Self-deployable origami stent grafts as a biomedical application of Ni-rich TiNi shape memory alloy foil*, *Materials Science and Engineering: A* **419**, 131 (2006).
- [239] M. Schenk and S. D. Guest, *Geometry of Miura-folded metamaterials*, *Proceedings of the National Academy of Sciences of the United States of America* **110**, 3276 (2013).
- [240] T. Tachi, *Interactive Form-Finding of Elastic Origami*, in *Proceedings of the International Association for Shell and Spatial Structures (IASS) Symposium 2013, 23-27 September, Wroclaw, Poland* (International Association for Shell and Spatial Structures (IASS), 2013).
- [241] K. Saito, A. Tsukahara, and Y. Okabe, *New deployable structures based on an elastic origami model*, *Journal of mechanical design* **137**, 021402 (2015).
- [242] J. L. Silverberg, J.-H. Na, A. A. Evans, B. Liu, T. C. Hull, C. D. Santangelo, R. J. Lang, R. C. Hayward, and I. Cohen, *Origami structures with a critical transition to bistability arising from hidden degrees of freedom*, *Nature materials* **14**, 389 (2015).

- [243] J. Rommers, G. Radaelli, and J. L. Herder, *A design tool for a single vertex compliant-facet origami mechanism (sv-cofom) including torsional hinge lines*, *ASME Journal of Mechanism and Robotics* (2017).
- [244] S. Felton, M. Tolley, E. Demaine, D. Rus, and R. Wood, *A method for building self-folding machines*, *Science* **345**, 644 (2014).
- [245] C. D. Onal, R. J. Wood, and D. Rus, *Towards printable robotics: Origami-inspired planar fabrication of three-dimensional mechanisms*, in *Proceedings of IEEE International Conference on Robotics and Automation (ICRA), 2011* (IEEE, 2011) pp. 4608–4613.
- [246] D. Xu and G. K. Ananthasuresh, *Freeform Skeletal Shape Optimization of Compliant Mechanisms*, *Journal of Mechanical Design* **125**, 253 (2003).
- [247] C.-C. Lan and Y.-J. Cheng, *Distributed Shape Optimization of Compliant Mechanisms Using Intrinsic Functions*, *Journal of Mechanical Design* **130**, 072304 (2008).
- [248] E. G. Merriam, K. A. Tolman, and L. L. Howell, *Integration of advanced stiffness-reduction techniques demonstrated in a 3d-printable joint*, *Mechanism and Machine Theory* **105**, 260 (2016).
- [249] X. Lachenal, S. Daynes, and P. M. Weaver, *A non-linear stiffness composite twisting I-beam*, *Journal of Intelligent Material Systems and Structures* **25**, 744 (2014).
- [250] M. Goldfarb and J. E. Speich, *Split tube flexure*, U.S. Patent 6585445, Jul, (2003).
- [251] M. Goldfarb and J. E. Speich, *A Well-Behaved Revolute Flexure Joint for Compliant Mechanism Design*, *Journal of Mechanical Design* **121**, 424 (1999).
- [252] R. Vos, Z. Gürdal, and M. Abdalla, *Mechanism for Warp-Controlled Twist of a Morphing Wing*, *Journal of Aircraft* **47**, 450 (2010).
- [253] B. P. Trease, Y.-M. Moon, and S. Kota, *Design of Large-Displacement Compliant Joints*, *Journal of Mechanical Design* **127**, 788 (2004).
- [254] H. Alkisaiei, *Statically Balanced Compliant Walls*, *MSc thesis*, Delft University of Technology, Delft, The Netherlands (2016).
- [255] S. G. Yuen, D. T. Kettler, P. M. Novotny, R. D. Plowes, and R. D. Howe, *Robotic Motion Compensation for Beating Heart Intracardiac Surgery*, *The International journal of robotics research* **28**, 1355 (2009).
- [256] M. Khoshnam and R. V. Patel, *Robotics-assisted catheter manipulation for improving cardiac ablation efficiency*, in *Proceedings of 5th IEEE RAS/EMBS International Conference on Biomedical Robotics and Biomechatronics* (2014) pp. 308–313.

- [257] S. B. Kesner and R. D. Howe, *Force Control of Flexible Catheter Robots for Beating Heart Surgery*, *Proceedings of IEEE International Conference on Robotics and Automation (ICRA) 2011*, 1589 (2011).
- [258] D. Gelman, A. Skanes, M. Tavallaei, and M. Drangova, *Design and Evaluation of a Catheter Contact- Force Controller for Cardiac Ablation Therapy*, *IEEE Transactions on Biomedical Engineering* **PP**, 1 (2016).
- [259] H. W. R. Houwers, *Closed-loop two-fold tape spring transmissions*, *MSc thesis*, Delft University of Technology, Delft, the Netherlands (2016).
- [260] C. English and D. Russell, *Implementation of variable joint stiffness through antagonistic actuation using rolamite springs*, *Mechanism and Machine Theory* **34**, 27 (1999).
- [261] K. Oosterhuis, *Simply complex, toward a new kind of building*, *Frontiers of Architectural Research* **1**, 411 (2012).
- [262] K. Oosterhuis, *iA#5 - Robotics in Architecture* (Jap Sam Books, Heijningen, 2012).
- [263] B. Wisse, *Laevo exoskelet*, <http://en.laevo.nl/>, accessed: 2017-04-24.
- [264] *Exoskeleton Technologies: Media Lockheed Martin*, <http://www.lockheedmartin.com/us/products/exoskeleton/media.html> (), accessed: 2017-04-24.
- [265] C. J. Walsh, K. Endo, and H. Herr, *A quasi-passive leg exoskeleton for load-carrying augmentation*, *International Journal of Humanoid Robotics* **4**, 487 (2007).

Contribution to each chapter

A short description of the contribution of the author to each chapter of this dissertation is given next.

Chapter 1: Introduction

First and only author.

Chapter 2: Static balancing of an inverted pendulum with prestressed torsion bars

First author. Author wrote the article, generated the contents and conducted the experiments.

Chapter 3: Design of a compact gravity equilibrator with an unlimited range of motion

Second author. This chapter is an abstract of an article resulted from the M.Sc. research project of B.G. Bijlsma. Author was the daily supervisor of the student. Author contributed to the concept development, the analysis and thoroughly reviewed the article.

Chapter 4: Shape optimization and sensitivity of compliant beams for prescribed load-displacement response

First author. The author wrote the whole article and was responsible for all the content.

Chapter 5: A carbon fibre beam balancing a pendulum: experimental evaluation

First author. This chapter is an abstract of a full length conference paper. The author wrote the whole article, was responsible for all the content, fabricated the prototype, and conducted the experiments.

Chapter 6: A monolithic compliant large-range gravity balancer

First author. The author wrote the whole article, was responsible for all the content, fabricated the prototype, and conducted the experiments.

Chapter 7: Design and Optimization of a General Planar Zero Free Length Spring

Second author. This chapter is an abstract of an article resulted from the M.Sc. research project of A.A.T.M. Delissen. Author was the daily supervisor of the student. Author suggested the use of shape optimized beams to realize ZFLS behavior. Furthermore, the optimization was performed with a software platform developed by the author. The author also thoroughly reviewed the article.

[Chapter 8: Design and Characterization of a Linear Elastic Isotropic Meta-material with Zero Poisson's Ratio over Large Strains Using a Spring Lattice](#)
Second author. This chapter is an abstract of an article resulted from the M.Sc. research project of A.A.T.M. Delissen. Author was the daily supervisor of the student. The optimization was performed with help of a software platform developed by the author. The author also thoroughly reviewed the article.

[Chapter 9: Potential energy fields of systems with torsion stiffness](#)

First author. This chapter is an abstract of an article resulted from the M.Sc research of the author.

[Chapter 10: A lumped compliant statically balanced self-guiding straight-line mechanism](#)

Second author. This chapter is an abstract of an article resulted from a joint effort between the author and E.J. Rosenberg, with equal share in the contents and writing.

[Chapter 11: A potential energy field \(PEF\) approach to the design of a compliant self-guiding statically-balanced straight-line mechanism](#)

First author. The author wrote the whole article, was responsible for all the content, fabricated the prototype, and conducted the experiments.

[Chapter 12: Gravity balanced compliant shell mechanisms](#)

First author. The author wrote the whole article, was responsible for all the content, fabricated the prototype, and conducted the experiments.

[Chapter 13: Pseudo Rigid Body Modeling of a single vertex compliant-facet origami mechanism \(SV-COFOM\)](#)

Second author. This chapter is an abstract of an article resulted from the M.Sc. research project of J. Rommers. Author was the daily supervisor of the student. The author thoroughly reviewed the article.

[Chapter 14: A design tool for a single vertex compliant-facet origami mechanism \(SV-COFOM\) including torsional hinge lines](#)

Second author. This chapter is an abstract of an article resulted from the M.Sc. research project of J. Rommers. Author was the daily supervisor of the student. The author thoroughly reviewed the article.

[Chapter 15: Study on the large-displacement behavior of a spiral spring with variations of cross-section, orthotropy and prestress](#)

First author. The author wrote the whole article and was responsible for all the content.

[Chapter 16: Application examples](#)

Section 1: Author developed the concept, conducted the numerical simulations and wrote the text. Section 2: This section is an abstract of the M.Sc. research report of H. Alkisaie. Author was the daily supervisor of the student.

Curriculum Vitæ

Giuseppe Radaelli

21-10-1985 Born in Padua, Italy.

Education

- 1998–2004 High School
Calandlyceum, Amsterdam
- 2004–2007 B.Sc. in Mechanical Engineering
Delft University of Technology
Thesis: Dynamic behavior of the human finger
- 2007–2009 M.Sc. in Mechanical Engineering, *cum laude*
Delft University of Technology
Dept. of BioMechanical Engineering
Thesis: An energy approach to static balancing of systems with torsion stiffness
- 2013–2017 Ph.D. in Mechanical Engineering
Delft University of Technology
Dept. of Precision and Microsystems Engineering
Thesis: Synthesis of mechanisms with prescribed elastic load-displacement characteristics
Promotor: Prof. dr. ir. J.L. Herder

Professional activity

- 2009–2010 *Researcher* at Holland Container Innovations B.V.
developed innovative balancing concepts for a foldable see-container
- 2010–2013 *R&D Engineer* at InteSpring B.V.
developed a passive exoskeleton to prevent back injuries (the Laevo)
- 2013–2017 *Research Manager* at Laevo B.V. (0.2 FTE)
responsible for effectiveness validation and intellectual property

Awards

- | | |
|------|--|
| 2009 | M.Sc. cum laude |
| 2014 | Best paper award, ASME IDETC 2014 conference, Buffalo |
| 2014 | Best presentation Compliant Mechanisms Symposium, ASME IDETC 2014 conference, Buffalo |
| 2016 | (with J. Rommers) Compliant mechanisms award, ASME IDECT 2016 conference, Charlotte |

List of Publications

Journal articles

15. **G. Radaelli**, J.L. Herder, *Study on the large-displacement behavior of a spiral spring with variations of cross-section, orthotropy and prestress*, *International Journal of Solids and Structures* (submitted 2017).
14. J.P.A. Nijssen, **G. Radaelli**, C.J. Kim, J.L. Herder, *Overview and kinematic characterization of compliant shell mechanism building blocks*, *Mechanism and Machine Theory* (to be submitted).
13. A.A.T.M. Delissen, **G. Radaelli**, J.L. Herder, J.B. Hopkins, *Design and characterization of a linear elastic isotropic meta-material with zero Poisson's ratio over large strains using a spring lattice*, *Advanced Functional Materials* (to be submitted).
12. **G. Radaelli**, J.L. Herder, *A potential energy field (PEF) approach to the design of a compliant self-guiding statically-balanced straight-line mechanism*, *Mechanism and Machine Theory* **114**, 141-155 (2017).
11. J. Rommers, **G. Radaelli**, J.L. Herder, *A design tool for a single vertex compliant-facet origami mechanism (SV-COFOM) including torsional hinge lines*, *Journal of Mechanisms and Robotics* (2017).
10. H. Alkisaiei, **G. Radaelli**, J.L. Herder, H.H. Bier, L.J. Sluys, *Design of large-scale, statically balanced and compliant shell structures as deformable walls*, *Engineering Structures* (submitted 2016).
9. **G. Radaelli**, J.L. Herder, *Gravity balanced compliant shell mechanisms*, *International Journal of Solids and Structures* **118-119** 78-88 (2017).
8. B.G. Bijlsma, **G. Radaelli**, J.L. Herder, *Design of a compact gravity equilibrator with an unlimited range of motion*, *Journal of Mechanisms and Robotics* (2017).
7. A.A.T.M. Delissen, **G. Radaelli**, J.L. Herder, *Design and optimization of a general planar zero free length spring*, *Mechanism and Machine Theory* **117C**, 56-77 (2017).
6. H. Alkisaiei, **G. Radaelli**, J.L. Herder, H.H. Bier, L.J. Sluys, *Design of large-scale compliant and monolithic gravity balancers as deformable walls*, *Engineering Structures* (submitted 2016).
5. J. Rommers, **G. Radaelli**, J.L. Herder, *Pseudo-rigid-body modeling of a single vertex compliant-facet origami mechanism*, *Journal of Mechanisms and Robotics* **9**(3), 031009 (2017).
4. **G. Radaelli**, R. Buskermolen, R. Barents, J.L. Herder, *Static balancing of an inverted pendulum with prestressed torsion bars*, *Mechanism and Machine Theory* **108**, 14-26 (2017).

3. **G. Radaelli**, J.L. Herder, *Shape optimization and sensitivity of compliant beams for prescribed load-displacement response*, [Mechanical Sciences](#) **7**, 219-232 (2016).
2. **G. Radaelli**, J.L. Herder, *A monolithic compliant large-range gravity balancer*, [Mechanism and Machine Theory](#) **102**, 55-67 (2016).
1. **G. Radaelli**, J.A. Gallego, J.L. Herder, *An Energy Approach to Static Balancing of Systems With Torsion Stiffness*, [Journal of Mechanical Design](#) **133(9)**, 091006 (2011).

Peer-reviewed conference articles

10. J.P.A. Nijssen, **G. Radaelli**, J.L. Herder, C.J. Kim, J.B. Ring, *Design and analysis of a shell mechanism based two-fold force controlled scoliosis brace*, In [Proceedings of the ASME International Design Engineering Technical Conferences and Computers and Information in Engineering Conference](#), August 6-9, 2017, Cleveland, Ohio, USA.
9. J. Rommers, **G. Radaelli**, J.L. Herder, *A Pseudo Rigid Body Model of a Single Vertex Compliant-Facet Origami Mechanism (SV-COFOM)*, In [Proceedings of the ASME International Design Engineering Technical Conferences and Computers and Information in Engineering Conference](#), August 21-24, 2016, Charlotte, NC, USA. *recipient of Compliant Mechanism Award*
8. B.G. Bijlsma, **G. Radaelli**, J.L. Herder, *Design of a compact gravity equilibrator with an unlimited range of motion*, In [Proceedings of the ASME International Design Engineering Technical Conferences and Computers and Information in Engineering Conference](#), August 21-24, 2016, Charlotte, NC, USA.
7. **G. Radaelli**, J.L. Herder, *A Monolithic Compliant Large-Range Gravity Balancer*, In [Proceedings of the 14th IFToMM World Congress](#), October 25-30, 2015, Taipei, Taiwan.
6. A.G. Dunning, J.L. Stroo, **G. Radaelli**, J.L. Herder, *Feasibility study of an upper arm support based on bending beams*, In [Proceedings of the IEEE International Conference on Rehabilitation Robotics \(ICORR\)](#), August 11-14, 2015, Singapore, Singapore.
5. **G. Radaelli**, J.L. Herder, *Isogeometric shape optimization for compliant mechanisms with prescribed load paths*, In [Proceedings of the ASME International Design Engineering Technical Conferences and Computers and Information in Engineering Conference](#), August 17-20, 2014, Buffalo, New York, USA. *recipient of the Best Paper Award*
4. B.L. Rijff, J.L. Herder, **G. Radaelli**, *An Energy Approach to the Design of Single Degree of Freedom Gravity Balancers With Compliant Joints*, In [Proceedings of the ASME International Design Engineering Technical Conferences and Computers and Information in Engineering Conference](#), August 28-31, 2011, Washington, DC, USA.
3. **G. Radaelli**, R. Buskermolen, R. Barents, J.L. Herder, *Static balancing of an inverted pendulum with pre-stressed torsion bars*, In [Proceedings of the 13th World congress in Mechanisms and Machine Science](#), June 19-25, 2011, Guanajuato, Mexico.
2. E.J. Rosenberg, **G. Radaelli**, J.L. Herder, *An Energy Approach to a 2DOF Compliant Parallel Mechanism with Self-Guiding Statically-Balanced Straight-Line Behavior*, In [Proceedings of the ASME International Design Engineering Technical Conferences and Computers and Information in Engineering Conference](#), August 15-18, 2010, Montreal, Quebec, Canada.

1. **G. Radaelli**, J.A. Gallego, J.L. Herder, *An Energy Approach to Static Balancing of Systems with Torsion Stiffness*, In [Proceedings of the ASME International Design Engineering Technical Conferences and Computers and Information in Engineering Conference](#), August 15-18, 2010, Montreal, Quebec, Canada.

Patents

3. H. Alkisaiei, **G. Radaelli**, J.L. Herder, *Statically balanced compliant sound barriers*, NL2015722 (2015).
2. **G. Radaelli**, E.J. Rosenberg, M.E. Aguirre, A.C. Verkuyl, B.M. Wisse, *Wearable support structure and method of supporting a torso*, NL2011483 - WO2015041532 - US2016250062 - JP2016532528 - EP3046517 (2013).
1. **G. Radaelli**, E.J. Rosenberg, M.E. Aguirre, A.C. Verkuyl, B.M. Wisse, *Wearable pivotable structure and method for supporting a torso*, NL2011482 (2013).